Flexible and substrate-free optoelectronic devices based on III-V semiconductor nanowires

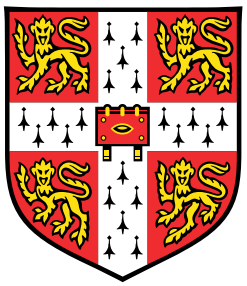

Sarwat Baig

Department of Engineering
University of Cambridge

This dissertation is submitted for the degree of
Doctor of Philosophy

Sidney Sussex College

July 2018

To Richard - my love, my rock, my everything

Declaration

I hereby declare that except where specific reference is made to the work of others, the contents of this dissertation are original and have not been submitted in whole or in part for consideration for any other degree or qualification in this, or any other university. This dissertation is my own work and contains nothing which is the outcome of work done in collaboration with others, except as specified in the text and Acknowledgments. This dissertation contains fewer than 65,000 words including appendices, bibliography, footnotes, tables and equations and has fewer than 150 figures.

Sarwat Baig
July 2018

Acknowledgements

The acknowledgements have always been my favourite part of a thesis to read. Researching and writing a dissertation in any field can feel like an impossible task sometimes - but the acknowledgements section always shows that success is possible - not when experiments go correctly (though that certainly helps!) - but when you are surrounded by dear family, friends and colleagues. Certainly, my thesis would not have been written without the help, support and kindness of several individuals, and I will be forever grateful for all that they have done for me.

Firstly, I would like to thank my supervisor, Dr Hannah Joyce - for her sheer persistance and determination in getting me through my PhD. It has been a long and difficult journey - but thanks to her sunny personality, intimidating intellect and unwavering support - we have done it! Hannah is an early career academic with an immensely bright future ahead of her. I wish her the very best, and can't wait to read about her future achievements. I would also like to thank the other Joyce group members - Greg, Lissa and Kate. It was an absolute honour to have you all at my wedding. Thank you for all the good times - in the lab, pub and while punting!

For financial support throughout the PhD, I am indebted to the Photonics CDT for full PhD funding and travel grants, and the NanoDTC, Sidney Sussex college and the ANU for generous travel grants which enabled me to attend several conferences, and travel to Canberra, Oxford and London for collaborations.

I have been incredibly fortunate to have had the chance to work with some truly exceptional scientists throughout the course of my PhD.

Special thanks to Professor Andrew Flewitt and his group - especially Dr Girish Rughoobur and Dr Kham Niang — who welcomed me into their group while Hannah was on maternity leave. They helped me and taught me so much in the cleanroom - without them I am certain that Chapter 8 would not exist.

I must also thank Professor Jagadish, Professor Michael Johnston and Dr Ioannis Papakonstantinou - for hosting me at their respective groups at the ANU, Oxford University and UCL. I got to spend 3 months living and studying in Canberra which really kick-started my PhD research. I learnt more than I ever thought I would about nanowires, Szechuan cooking and how to dodge wallabies who hop into the road when you're driving! Special thanks must also go to Dr Lan Fu, Dr Sudha Mokkapati and Dr Qian Gao for continued help and support, even on my return to

Cambridge. It was a welcome surprise to be reunited with Dr Jessica Boland at Oxford, after our stint at HP together!

Many thanks also to Professor Magnus Borgstrom at Lund University and Professor Huiyuan Liu at UCL and Dr Amalio Fernandez-Pacheco at Cambridge University for generously providing me with nanowire samples which were vital in furthering my understanding of nanowire-Parylene C thin films.

My PhD involved me spending a substantial amount of time in the cleanroom - and it is here, over laughter and commiserations over samples gained and lost, that key friendships are forged. I would like to thank the Nanoscience and CAPE cleanroom technicians - who can magically fix any machine - Roger, Duncan, Neil and Yury - and the students who shared every lab victory and defeat - Juan, Nikhil, Sarah, Jerome, Dean, Girish, Kham and Edward.

Outside the cleanroom, my time was spent in college, teaching undergrads, knitting and swimming. Friend, academics and staff of Sidney Sussex College - thank you for keeping me going through the tough times. It was a comfort to know that you are not alone and help is here if you need it. Being on the MCR committees was one of the highlights of my Cambridge experience. I thoroughly enjoyed teaching some really bright individuals when I took undergraduate supervisions - so thank you all for the opportunity, and also for keeping my theory up to scratch!

To my friends from my knitting circle, swimming and from my undergrad days at Bristol - thank you for dragging me out of the Cambridge bubble and keeping me grounded, sane and healthy. I have also been struck by the kindness of my colleagues at Oakland Innovation, where I am a very new member of the team! They have given me the support and flexibility I needed in helping me to finish my thesis, and have introduced me to the exciting new world of technology consulting.

I would not be where I am today without the limitless support and care of my darling family and in-laws. Mum, Dad, and my little sister Tasmia - I do not even know where to begin to thank you. Every step of the way, you have always been there - encouraging me to be ambitious, follow my dreams and offering much-needed advice and guidance. Jane, David and Emily - thank you for all your kindness and treating me as one of your own since day one.

Last, but by no means least, is my darling husband, Richard. Thank you for keeping me focussed, listening to my whining, giving me strength when I thought I had none left, being my LaTeX guru and making a spectacular G&T when I needed one! I love you. You are my rock, my hero, my everything.

Flexible and substrate-free optoelectronic devices based on III-V semiconductor nanowires

Sarwat Baig

III-V nanowires have been the subject of intense research interest for the past 20 years, as their unique optical and electronic properties, which arise from their nanoscale dimensions and composition, make them particularly suited for high-performance opto-electronic devices. Since epitaxial growth is on expensive, brittle, crystalline substrates, the field of flexible devices has been little explored in the context of III-V nanowires. In order to fully exploit these properties and move away from conventional wafer based electronics to flexible electronics, hybrid devices consisting of organic and inorganic components must be developed to harness the benefits from both materials systems. Embedding high performance vertically aligned III-V nanowires in a flexible matrix enables applications where there is a need for substrate-free, flexible devices. The work in this thesis looks to address this by (1) developing a repeatable method of producing nanowire-polymer thin films and (2) demonstrating how these thin films could be fabricated into different opto-electronic devices. The thin films are made by encapsulating the nanowires in Parylene C, which are then be peeled off from the growth substrate, thus retaining the vertical alignment of the nanowires. These thin films are used to fabricate a THz modulator and a solar cell. Single and multi-layer THz modulators are fabricated from nanowire-Parylene C thin films laminated together. 1,2,4,8, and 14-layer modulators are compared, with the 14-layer modulator displaying the best performance. A high switching speed (<5 ps), modulation depth (-8 dB), extinction (13%) and dynamic range (-9 dB) and broad bandwidth operation (0.1 THz–4 THz) are obtained. This surpasses the performance of several devices in the literature and presents the first THz modulator which combines a large modulation depth, broad bandwidth, picosecond time resolution for THz intensity and phase modulation, which makes it an ideal candidate for ultrafast THz communication. In addition to the THz work, the fabrication process towards a flexible solar cell is also developed. This consists of optimising the dry etching, and annealing-free contacting processes to give nanowire devices that show good ohmic IV characteristics. Following this work, a proof-of-concept Schottky barrier solar cell is fabricated using the knowledge gleaned from this development work. This preliminary device gives a conversion efficiency of 0.02% and a fill factor of 0.3, with scope for device performance improvement by using nanowires that are grown and optimised specifically for solar cell operation.

Table of contents

List of figures xv

List of tables xix

Abbreviations and symbols xxi

Publications and Conference Presentations xxvii

1 Introduction 1

1.1 Towards flexible, substrate-free III-V nanowire devices 1

1.2 Structure of thesis 2

2 III-V Nanowires: Materials Properties and Devices 5

2.1 Significance of III-V nanowires 5

2.2 III-V nanowire structures 7

2.3 Optimising nanowire geometry for light absorption 13

2.4 Nanowire devices 15

2.5 Conclusion 24

3 Flexible Nanowire Devices 27

3.1 Progress in flexible electronics 27

3.2 Choice of materials for flexible electronics 29

3.3 Nanowire alignment for flexible devices 31

3.4 Polymer encapsulation 33

3.5 Flexible nanowire devices 38

3.6 Conclusion 40

4 Experimental Methods 43

4.1 Nanowire growth 43

4.2 Flexible nanowire-polymer thin film fabrication 45

4.3 Flexible thin film characterisation 47

4.4 THz Polarisers 49

4.5 Optimising the fabrication of flexible nanowire diodes . . . 52
4.6 Nanowire device characterisation . . . 56

5 Nanowire-Parylene C Thin Films 59
5.1 Embedding nanowires in polymer . . . 59
5.2 Solution processed polymers . . . 60
5.3 CVD Polymers: Introduction to Parylene C . . . 63
5.4 Nanowire-Parylene C thin film removal . . . 65
5.5 Additional insights into Parylene C . . . 67
5.6 Towards nanowire-polymer thin film devices . . . 68
5.7 Conclusion . . . 69

6 Single-Layer Nanowire Terahertz Modulator 71
6.1 Current THz modulators . . . 71
6.2 GaAs nanowires for THz modulators . . . 73
6.3 Modulator fabrication and characterisation . . . 75
6.4 Photoconductivity response . . . 77
6.5 Rotation and photoexcitation measurements . . . 79
6.6 Improving polariser modulation depth . . . 80
6.7 Conclusion . . . 81

7 Multi-Layer Nanowire THz Polarisers 83
7.1 Towards a high speed THz communications system . . . 83
7.2 Modulator fabrication and characterisation techniques . . . 84
7.3 Rotation and temporal response . . . 86
7.4 Communications system . . . 91
7.5 Conclusion . . . 92

8 Towards Flexible Nanowire Diodes: Solar Cells and Photodetectors 93
8.1 Current nanowire diodes . . . 94
8.2 Flexible device design . . . 96
8.3 Fabrication optimisation . . . 105
8.4 Reactive ion etching . . . 106
8.5 Contact deposition . . . 110
8.6 Nanowire test device fabrication process . . . 114
8.7 Schottky barrier solar cell . . . 116
8.8 Framework for an optimal nanowire solar cell . . . 119
8.9 Conclusion . . . 121

9 Conclusion **123**
9.1 Nanowire-Parylene C thin films 123
9.2 A high performance nanowire THz modulator 124
9.3 A flexible, substrate-free nanowire solar cell 124
9.4 Towards fully integrated nanosystems 125

References **127**

Appendix A Preliminary work on a solar cell based on SAE grown nanowires **145**
A.1 SAE InP nanowire growth process 145
A.2 Suggested device fabrication process 146
A.3 Device characterisation 148

Appendix B Preliminary studies on a single nanowire photodetector **151**
B.1 Nanowire growth and single nanowire photodetector fabrication 151
B.2 Single nanowire photodetector characterisation 152

Appendix C FDTD Simulations **155**
C.1 Simulation parameters 155
C.2 Single nanowire simulations 156
C.3 Nanowire array simulations 160

Appendix D Extraction of parameters from OPTP spectroscopy data **163**

List of figures

2.1 III-V semiconductor optical and electronic properties 6
2.2 Schematic of nanowire growth, crystal structure, orientation and heterostructures 9
2.3 Schematic depicting light interaction with nanowire arrays 14
2.4 Schematic depicting photodetector behaviour and devices 16
2.5 Schematic depicting a photovoltaic cell operation and devices 19
2.6 Schematic diagram of THz modulator operation and devices 23

3.1 Schematic showing scope of flexible electronics 28
3.2 Diagram of the electronic structure of organic and inorganic semiconductors . . 31
3.3 Commonly used nanowire alignment techniques 32
3.4 Nanowire encapsulation using solution processed and CVD polymers 34
3.5 Examples of flexible nanowire devices in the literature 39
3.6 Schematic showing a general flexible fully integrated nanosystem 40

4.1 Schematic of an MOCVD system 44
4.2 Schematic of spin coating 46
4.3 Schematic of the Gorham process 48
4.4 Schematic diagrams of profilometry, SEM, AFM and EDX 50
4.5 Schematic of the nanoimprint system 51
4.6 Schematic diagram of the OPTP system 53
4.7 Schematic of the different etchers used in dry etching optimisation 54
4.8 Schematic diagrams of electron beam and thermal evaporation 55
4.9 Schematic diagram of an ITO sputter coater 56
4.10 Schematic diagram of the probe station 56
4.11 Schematic diagram of a solar simulator 57

5.1 Chemical structures of the polymers encapsulants 61
5.2 Images of solution processable nanowire-polymer thin films 62
5.3 Chemical structure of Parylene polymers 63
5.4 Parylene info 64
5.5 Mechanism of Parylene C polymerisation 65

5.6 Schematic showing Parylene C thin film removal method 66
5.7 Images and UV-Vis spectra of InP and GaAs nanowires and thin films 67
5.8 Photographs depicting perovskite degradation when protected with Parylene C . 68
5.9 Towards flexible, substrate-free nanowire devices 69

6.1 Schematic diagram of the OPTP experiment 74
6.2 GaAs nanowire growth and modulator fabrication process 75
6.3 THz time domain trace of Parylene C and quartz 76
6.4 Photoconductivity response of a single layer Parylene C modulator 78
6.5 Single layer PDMS modulator data 79
6.6 Single layer Parylene C modulator data 80

7.1 GaAs nanowire growth and modulator fabrication process 85
7.2 THz wave attenuation different between single and multilayer polarisers 85
7.3 Performance data of the PDMS multilayer polarisers 87
7.4 Performance data of the Parylene C multilayer polarisers 89
7.5 Further data on 14-layer polariser 90
7.6 Comparison of the performance of the PDMS and Parylene C polarisers. 90
7.7 Suggested high speed THz communications system 91

8.1 Band diagram for a pn junction 96
8.2 Band diagrams for ohmic and Schottky contact for an n-type semiconductor . . 100
8.3 IV curves showing ideal solar cell operation 101
8.4 Flexible photodetector fabrication process 106
8.5 IV curve of initial diode device 107
8.6 SEM images showing different RIE techniques 108
8.7 Power series for RIE 109
8.8 Band diagram and device architecture of test device 110
8.9 IV curves of control devices 111
8.10 IV curve before and after optimising the Ti/Au contact 112
8.11 IV curve before and after optimising ITO top contact 113
8.12 IV response of asymmetric nanowire test device 115
8.13 Device architecture and band structure of Schottky barrier solar cell 116
8.14 IV curves for Schottky barrier solar cell 118
8.15 Timeline showing the progress made in nanowire solar fabrication 120

9.1 Next generation substrate-free, flexible nanowire devices 125

A.1 Schematic of SAE-nanowire-Parylene C thin films 146
A.2 Comparison between parylene coated VLS and SAE nanowires. 147
A.3 EDS spectra of the parylene coated SAE nanowires 148

A.4 Schematic of selective contacting of core-shell heterostructure 149
A.5 IV curve of SAE-nanowire solar cell 149

B.1 Single nanowire photodetector fabrication 152
B.2 EDX spectra of nanowire samples after FIB milling 153
B.3 IV curve - single nanowire photodetector 153

C.1 Schematic diagram outlining FDTD simulation unit cell 156
C.2 Single nanowire GaAs simulation - nanowire length 157
C.3 Single nanowire GaAs simulation - nanowire radius 157
C.4 Single nanowire GaAs simulation - aspect ratio 158
C.5 Single nanowire InP simulation - nanowire length 159
C.6 Single nanowire InP simulation - nanowire radius 159
C.7 GaAs nanowire array simulation - reflection 160
C.8 GaAs nanowire array simulation - transmission 160

D.1 Parameter extraction from photoconductivity spectra 163

List of tables

3.1 Table comparing organic and inorganic semiconductor properties 30

4.1 RIE test parameters 54

8.1 Initial RIE test outcomes 107

Abbreviations and symbols

Roman symbols

A	Area
A	Exponential pre-factor for Arrhenius equation (Equation 2.4)
C	Solids concentration in the formulation
C_i	Initiator concentration
C_m	Monomer concentration
D	Detectivity
D^*	Specific detectivity
dB	Decibel
$d_{parylene}$	Parylene C layer thickness
d	Nanowire diameter
$D_{e,h}$	Diffusion coefficient for electrons, holes
D_i	Diffusivity
E_a	Activation energy
$E_{fn,fp}$	Fermi level for n,p doped material
E_g	Band gap
E_{on}	Electric field transmitted through sample with photoexcitation
E_{off}	Electric field transmitted through sample without photoexcitation
ΔE	Photoinduced change in THz transmission
F	Applied field
FF	Fill factor
eFF	Emperical fill factor
ff	Effective areal fill factor
Δf	Bandwidth
G	Photoconductive gain
G_{energy}	Gibbs free energy
g	Photoelectric gain
h	Planck's constant
h	Film height (Equation 3.2)
I	Current
I_L	Light generated current
I_{mp}	Current at maximum power point
I_{pc}	Photocurrent arising from change in photoconductivity
I_N	Detector noise current
I_s	Reverse saturation current

I_{sc}	Short circuit current
i	Complex number
J_{pc}	Photoinduced current density
$k_{\parallel}$	Absorption coefficient for light polarisation parallel to nanowire axis
$k_{\perp}$	Absorption coefficient for light polarisation perpendicular to nanowire axis
$k(T)$	Rate constant
Kn	Knudsen number
k_p	Kinetic rate constant for propagation
k_d	Kinetic rate constant for dissociation
k_t	Kinetic rate constant for termination
L	Nanofeature length
l	Nanowire length
$L_{e,h}$	Diffusion length for electrons, holes
m_e^*	Electron effective mass
n	Ideality factor (Equation 8.41)
N	Charge carrier density (Appendix D)
n,p	Charge carrier density for electrons, holes
$\Delta n, p$	Change in carrier numbers for electrons, holes
n_{atoms}	Number of atoms
N_A	Number of acceptors
N_D	Number of donors
N_{DC}	Number of detected carriers
NEP	Noise equivalent power
N_i	Intrinsic carrier concentration
N_P	Photoexcited carrier density
$n_{parylene}$	Frequency dependant complex refractive index of the Parylene C
N_{Ph}	Number of absorbed photons
N_{photon}	Number of photons absorbed by the material at a specific depth
N_s	Number of photons at the surface of the material
P_{abs}	Absorbed power
P_{in}	Power input to cell
P_{opt}	Incident optical power
p	Partial pressure of a component
p_0	Equilibrium partial pressure of a component
q	Elementary charge
r, θ, z	Cylindrical polar co-ordinates (Equation 3.1)
R	Gas constant
r	Nanofeature radius
r_react	Rate of reaction
R_{mat}	Reflectance
R_λ	Responsivity
R_d	Differential resistance
S	Non-depleted cross section surface of the nanowire
sccm	Standard cubic centimeters per minute
SILAR	Surface ionic layer adsorption and reaction

T	Temperature
t	Time
ΔT	Photoinduced change in THz transmission (Appendix D)
V	Voltage
V_0	Built-in potential
V_{mp}	Voltage at maximum power point
V_{nw}	Volume of nanowire
V_{oc}	Open circuit voltage
v	Carrier drift velocity
v	Velocity (Equation 3.1)
v_i	Mean gas velocity
w	Depletion width thickness
$[W]$	Partial pressure of component W (Equation 2.3)
w	Moles of component w (Equation 2.3)
$x_{p,n}$	Depletion width thickness on p,n side of the junction
x	Material thickness

Greek symbols

α	Absorption coefficient
α, a	Fitting constants for spin coating modelling (Equation 3.2)
γ	Momentum scattering rate
γ_i	Sticking probability
ε	Electric field strength
ε	Dielectric constant of nanowire (Equation 6.1)
ε_0	Dielectric constant of environment (Equation 6.1)
ε_0	Vacuum permittivity
ε_r	Relative permittivity
η	Power conversion efficiency
η_e	External quantum efficiency
η_i	Internal quantum efficiency
η^*	Effective carrier photogeneration quantum efficiency
η_v	Viscosity
θ	Angle
λ	Wavelength
$\mu_{e,h}$	Carrier mobility for electrons, holes
μ_l	Chemical potential of the liquid component
μ_s	Chemical potential of the solid component
μ_v	Chemical potential of the vapour component
$\Delta\mu_c$	Chemical potential difference
ν	Frequency
ν_0	Initial spin velocity
ρ	Density
σ	Photoconductivity
$\Delta\sigma$	Photoinduced change in photoconductivity (Appendix D)
σ_{dark}	Photoconductivity with no illumination

σ_{light} Photoconductivity under illumination

$\Delta\sigma$ Change in photoconductivity arising from illumination

$\tau_{e,h}$ Carrier lifetime for electrons, holes

τ_t Carrier transit time

ϕ Incident photon power

ϕ Thiele modulus (Equation 3.6)

ϕ_{evap} Evaporation rate

ω Angular frequency

ω_0 Resonant frequency

ω Angular velocity (Equation 3.1)

Chemical abbreviations

AlGaAs Aluminum gallium arsenide

AsH_3 Arsine

Au Gold

BCB Benzocyclobutene

CH_4 Methane

CdS Cadmium sulfide

CdSe Cadmium selenide

CIGS Copper indium gallium selenide

Cr/Au Chromium gold

CZTS Copper zinc tin sulfide

DEZn Diethylzinc

GaAs Gallium arsenide

GaInAs Gallium indium arsenide

GaInAsP Gallium indium arsenide phosphide

GaInP Gallium indium phosphide

GaN Gallium nitride

GaP Gallium phosphide

H_2O_2 Hydrogen peroxide

H_2O Water

HCl Hydrochloric acid

HMDS Hexamethyldisilazane

InAs Indium arsenide

InGaAs Indium gallium arsenide

InP Indium phosphide

InSb Indium antimonide

ITO Indium tin oxide

$K_2Nb_8O_{21}$ Potassium niobate

MoS_2 Molybdenum disulfide

$(NH_4)_2S$ Ammonium sulfide

Pd Palladium

PDMS Polydimethyl siloxane

PEDOT:PSS Poly(3,4-ethylenedioxythiophene): poly(styrene sulfonate)

PET Poly(ethylene terephthalate)

PI Poly(imide)

PMMA Poly(methyl methacrylate)

PUE Poly(urethane)

PVA Poly(vinylalcohol)

PVP Poly(vinylpyrollidone)

P3HT Poly(3-hexylthiophene-2,5-diyl)

PH_3	Triphenylphosphine
Si	Silicon
SiH_4	Silane
SiO_2	Silica
SiO_x	Silica (varying stoichiometry)
SiN_x	Silicon nitride (varying stoichiometry)
Spiro-OMeTAD	N2,N2,N2',N2',N7,N7,N7',N7'-Octakis(4-methoxyphenyl)-9,9'-spirobi[fluorene] -2,2',7,7'-tetraamine
TCO	Transparent conducting oxide
Ti/Au	Titanium/gold
TMIn	Trimethylindium
TiO_2	Titanium dioxide
Zn	Zinc
ZnO	Zinc oxide

Acronyms

AFM	Atomic force microscopy
ALD	Atomic layer deposition
AM0	Air mass 0
AM1	Air mass 1
AM1.5	Air mass 1.5
ANU	Australian National University
CB	Conduction band
CNME	Crossed nanowire modulator element
CVD	Chemical vapour deposition
DI	Deionised
EBL	Electron beam lithography
EDX	Energy dispersive X-ray spectroscopy
FDTD	Finite difference time domain
FET	Field effect transistor
FIB	Focussed ion beam
HOMO	Highest unoccupied molecular orbital
IR	Infra-red
LED	Light emitting diode
LPCVD	Low pressure chemical vapour deposition
LUMO	Lowest unoccupied molecular orbital
MOCVD	Metal-organic chemical vapour deposition
MOVPE	Metal-organic vapour phase epitaxy
MPP	Maximum power point
MSM	Metal-semiconductor-metal
NREL	National renewable energy laboratory
NW	Nanowire
OPTP	Optical pump–Terahertz Probe
PCB	Periodic boundary conditions
PECVD	Plasma enhanced chemical vapour deposition
PML	Perfectly matched layers

PV	Photovoltaic
RF	Radio frequency
RIE	Reactive ion etching
RPM	Rotations per minute
SAE	Selective area epitaxy
SEM	Scanning electron microscope/microscopy
TFSF	Total-field scattered-field
UV	Ultraviolet
UV-Vis	Ultraviolet-visible
VB	Valence band
VLS	Vapour-liquid-solid
VPE	Vapour phase deposition
WZ	Wurtzite
ZB	Zincblende

Publications and Conference Presentations

Publications

[1] **S. Baig**, J. Boland, D. Damry, H. Hoe Tan, C. Jagadish, H. Joyce, M. Johnston. *An ultrafast switchable terahertz polarization modulator based on III-V semiconductor nanowire*, NanoLetters, 17, **4**, 2603-2610 (2017).

[2] **S. Baig**, J. Boland, D. Damry, H. Hoe Tan, C. Jagadish, M. Johnston, H. Joyce *Choice of polymer matrix for a fast switchable III-V nanowire terahertz modulator*, MRS Advances, 1, 1-6 (2017).

[3] H. Joyce, **S. Baig**, P. Parkinson, C. Davies, J. Boland, H. Hoe Tan, C. Jagadish, L. Herz, M. Johnston. *The influence of surfaces on the transient terahertz conductivity and electron mobility of GaAs nanowires*, Jourrnal of Physics D: Applied Physics, 50, **22**, 224001 (2017).

[4] H. Joyce, J. Boland, C. Davies, **S. Baig**, M. Johnston. *A review of the electrical properties of semiconductor nanowires: insights gained from terahertz conductivity spectroscopy*, Semiconductor Science and Technology, 31, **10**, 103003 (2016).

Selected conference presentations

Oral presentations are indicated with an asterix '*', all others are poster presentations. Presentations were given by Sarwat Baig, unless otherwise indicated.

[1] ***S Baig**, J. Boland, D. Damry, H. Hoe Tan, C. Jagadish, M. Johnston, **H. Joyce (speaker)** *Modulation of terahertz polarization on picosecond timescales using polymer-encapsulated semiconductor nanowires*, CLEO:Science and Innovations, San Francisco, USA (2017).

[2] **S Baig**, G. Rughboor, Z, Li, Q. Gao, L. Fu, C. Jagadish, I. Papakonstantinou and H. Joyce *Towards a flexible photodetector fabricated from polymer nanowire films*, Nanowire week, Lund, Sweden (2017).

[3] *__S Baig__, J. Boland, D. Damry, H. Hoe Tan, C. Jagadish, H. Joyce, M. Johnston. *A fast switchable terahertz modulator based on III-V semiconductor nanowires*, MRS, Boston, USA (2016).

[4] *__S Baig__, J. Boland, D. Damry, H. Hoe Tan, C. Jagadish, H. Joyce, M. Johnston. *A fast switchable III-V nanowire terahertz modulator*, Photon16, Leeds, UK (2016).

Chapter 1

Introduction

III-V nanowires have been the subject of intense research interest for the past 20 years. Their unique materials, optical and electronic properties, which arise from their nanoscale dimensions and chemical composition, make them particularly suited for high performance opto-electronic devices [1–8]. In recent years, there has been a general shift from wafer-based electronics towards flexible electronics where devices can be designed to be conformable, rugged and durable [9–13]. Since epitaxial growth of nanowires is on expensive, brittle, crystalline substrates, the area of flexible electronics has been little explored in the context of III-V nanowires. In order to fully exploit nanowire properties in this novel research area, devices consisting of organic and inorganic components must be developed to harness the benefits from both materials systems.

1.1 Towards flexible, substrate-free III-V nanowire devices

Moore's law predicts that the number of transistors on an integrated circuit roughly doubles every two years [14]. However, as the performance of silicon is pushed to its limits, there has been a demand for other semiconductor materials [1, 7, 15]. III-V nanowires are an interesting alternative to silicon as, depending on the III-V stoichiometry, they possess high electron mobility, carrier lifetime and direct band gap [6, 16, 17]. As a result, they can be used to fabricate devices with better performance than their thin film equivalents [1–5].

Intense research activity in nanowire growth, device fabrication and computer modelling has advanced our knowledge and led to impressive progress in each of these three areas [2, 18, 19]. Computational methods have improved our understanding of III-V nanowire behaviour and have thus helped to optimise nanowire growth parameters for efficient device design [20–24]. Tight control of nanowire growth parameters has meant that precise III-V stoichiometries, nanowire diameters, lengths and pitches can be achieved, and high purity, defect-free nanowires can be grown [25–27]. Research into device design has developed fabrication processes to produce high performance nanowire devices, both built directly on their growth substrate or built on receiver substrates [5, 28–33].

For novel innovative applications for nanowire devices, new processing techniques must be developed to form enabling technologies for these devices [34–38]. One interesting - yet little studied - route is to embed high performance vertically aligned III-V nanowires in a flexible matrix. This approach allows for the move away from conventional wafer based electronics, to flexible, substrate-free devices. This is especially important for applications where the nanowires must be removed from the growth substrate.

The work in this thesis commences with an investigation in how solution processed and chemical vapour deposition (CVD) polymers may be used to encapsulate nanowires to form robust thin films which, when removed from the growth substrate, can be used for further device fabrication. I then use these thin films to fabricate two, very different, opto-electronic devices - single and multilayer THz modulators and a Schottky barrier solar cell. By forming these robust nanowire-polymer thin films, proof-of-concept substrate-free devices were able to be successfully demonstrated.

1.2 Structure of thesis

This thesis consists of 8 further chapters. A review of the literature and current state of the art is given in Chapters 2 and 3.

In Chapter 2, I introduce III-V nanowires and discuss their significance in the field of next generation opto-electronic devices. I give an overview of their materials, optical and electronic properties, explain why they are particular suited for use opto-electronic devices and highlight notable examples of growth, modelling and device fabrication research.

In Chapter 3, I introduce the field of flexible electronics and why this new form factor is an enabling technology for innovative and exciting applications for III-V nanowires. I discuss how flexible nanowire devices give rise to whole host of novel devices, and outline the challenges faced in the fabrication of such devices.

Chapters 4-8 describe the research I have undertaken during the PhD. Chapter 4 is a comprehensive overview of all the experimental techniques used in this thesis, ranging from nanowire growth, to detailed device fabrication recipes.

In Chapter 5, the investigation into substrate-free flexible nanowire devices begins by demonstrating how, by using a CVD polymer, robust, reproducible and flexible nanowire-polymer thin films were fabricated. The fabrication process is compared to equivalent thin films made from solution processed polymers, the study showed that using a CVD polymer was far superior. It must be noted that findings from Chapter 5 are of utmost importance with respect to the rest of the thesis, as it underpins the results described in the subsequent chapters.

Chapters 6, 7 and 8 make use of these flexible nanowire thin films by using them for device fabrication. In particular, these Chapters showcase the adaptability of these thin films, are they have been used to make very different devices.

Chapters 6 and 7 describe the fabrication of a ultra-fast THz modulator. Chapter 6 describes the fabrication and characterisation of a single layer THz modulator, where the modulation depth is limited by the level of pumping. The only way to improve the modulation depth of these polarisers is to increase the areal density of the nanowires, using the lamination technique developed in Chapter 7. Here, the thinness of the nanowire-parylene films enable as many as 14 films to be laminated together. An equivalent device was made from poly(dimethyl siloxane) (PDMS) films, which were considerably thicker, hence only 4 layers could be laminated together.

Chapter 8 demonstrates a fabrication process towards a flexible nanowire diodes, for solar cell and photodetector applications. I carried out extensive work in optimising a fabrication process for nanowire test devices, which involved developing dry etching and annealing-free contact deposition techniques. This resulted in the fabrication of a proof-of-concept a Schottky barrier solar cell, with scope for fabricating a solar using using axial pn or pin junction nanowires.

Finally, in Chapter 9, I consider they key outcomes from the project as a whole. I conclude by outlining suggestions for further work and offer an outlook in the future of substrate-free flexible III-V nanowire devices.

Chapter 2

III-V Nanowires: Materials Properties and Devices

In this chapter I have evaluated the impact of III-V nanowires on the field of optoelectronics. This chapter begins by discussing how the optical and electronic properties of III-V nanowires mean that they are well suited for applications in high performance optoelectronic devices. Important research breakthroughs, such as fine control of nanowire growth, device fabrication and theoretical modelling to aid device design and better understand the quantum behaviour of these materials, are cited to show how they have all directly contributed to great progress of the field. A brief overview of the best nanowire devices reported to date in the published literature is given, with key focus on nanowire modulators, photodetectors and solar cells, as these are devices of interest in this thesis. Finally, I conclude this chapter by offering my future outlook for nanowire devices: the emergence of flexible nanowire array devices.

2.1 Significance of III-V nanowires

Nanowires are defined as high aspect ratio nanoscale structures with small diameters (100s of nanometres) compared to their length (on the order of micrometres). Nanowires have been a topic of intense research for the past 20 years as they exhibit very different behaviour to their bulk material and thin film counterparts, resulting in nanowires devices which have higher performance than that of thin film devices of equivalent area [1–5].

This performance enhancement is due to their nanoscale dimensions and chemical composition, which gives rise to unique electrical and optical properties [6]. When fabricated as high density 'forest-like' arrays, light trapping and light scattering between the nanowires results in enhanced absorption of light, resonant mode effects and absorption and scattering cross sections larger than their physical cross section [16]. The high aspect ratio of nanowires can also result in confined transport of electrons/photons/phonons along the length of the nanowire, resulting in devices with single photon sensitivity and polarisation sensitive effects [17, 42]. Figure 2.1(b)

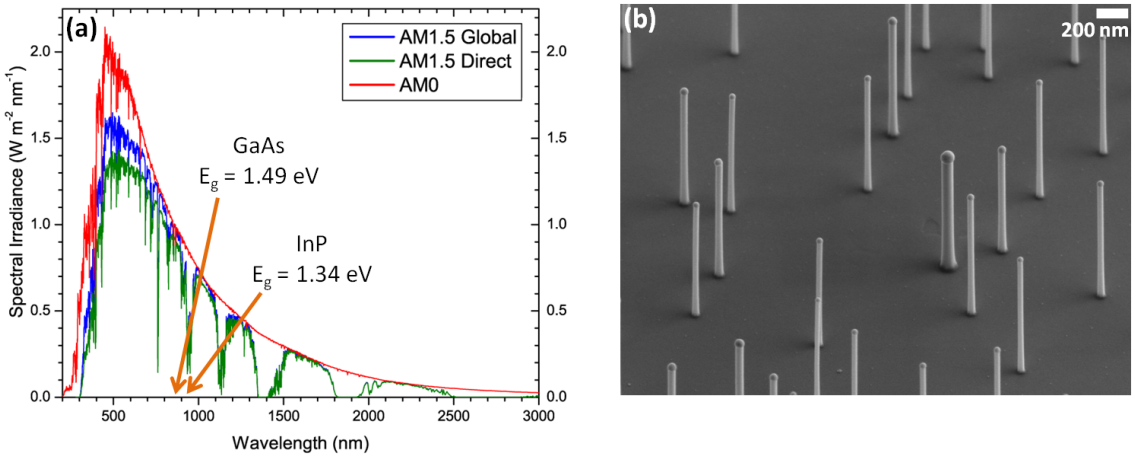

(c)

Nanowire	Surface recombination velocity [S/(cm s^{-1})]	Electron mobility (μ /cm^2 V^{-1} s^{-1})	Electron lifetime (τ /ps)	Band gap (E_g /eV)
GaAs	5.4 x 10^{-5}	1200 - 3000	1-5	1.49
InP	170	120 – 660	1100 - 1300	1.34

Fig. 2.1: Overview of III-V semiconductor optical and electronic properties. (a) Graph depicting the solar radiation spectrum for direct light, with the band gaps for GaAs and InP clearly marked. Image used from [39]. (b) SEM image of GaAs nanowires. (c) Table depicting optical and electronic properties of GaAs and InP - the two III-V materials of interest in this thesis [2, 40, 41]

shows an SEM (scanning electron microscope) image of nanowires grown on a substrate, where their high aspect ratio structure can be clearly seen.

The use of nanowire structures also gives rise to novel materials systems. Normally, depositing layers of thin films made from different materials with different lattice constants is difficult due to lattice mismatch between the layers. This causes strain and defects, which form traps for unwanted electron-hole recombination [23]. However, when nanowires are used, the diameter can be radially expanded and contracted to accommodate lattice mismatch - thus allowing lattice mismatched materials to be combined in heterostructures not otherwise possible with planar materials [7, 8].

III-V compound semiconductor nanowires (named as they are grown from group III and V elements) are of particular interest due to their direct band gaps and high charge carrier mobilities which makes them particularly suited for optoelectronic devices. Figure 2.1(a) depicts the solar radiation spectrum for direct light. AM refers to the "'air mass"' coefficients which determine the optical path length through the atmosphere. AM0 (air mass zero) refers to the spectrum taken outside of the atmosphere, AM1 (air mass one) is the spectrum taken at sea level with the sun directly overhead and AM1.5 (air mass 1.5) refers to a thickness of 1.5 atmospheres, when the sun is at an angle, and is used for the (densely populated) mid-latitude locations [39]. GaAs and InP, for example, have band gaps well matched to the solar spectrum and have found use as photovoltaic devices [25, 40]. Different III-V compounds have different properties such as

band gaps, electron mobilities and surface recombination velocities, hence different nanowire materials are suited for different devices. Further optical and electronic property parameters of InP ans GaAs can be found in Figure 2.1(c).

Nanowires are inherently versatile structures that can be engineered to maximise device performance. Several nanowire homostructures and heterostructures have been demonstrated in the literature as fine control of nanowire doping and III/V stoichiometry is now possible following intense research in this area. The crystal structure of III-V nanowires can also be specified by changing the growth conditions, resulting in producing crystal phases in nanowires that an unstable in bulk form [25]. Furthermore, the band gaps of III-V materials can be tuned depending on their stoichiometry [5].

It is not unreasonable to suggest that III-V nanowires have revolutionised the field of opto-electronic devices. Use of these nanoscale materials have pushed the field in new and exciting directions, and given the scope for devices that were previously not possible - including photodetectors with single photon sensitivity, high performance photovoltaics and nanowire-biological cell integration, to name but a few [2, 18, 19]. Nanowire growth methods - which have enabled high purity, defect free nanowires to be grown reproducibly [25, 26] - and theoretical modelling methods - which explain unusual nanowire behaviour and aid device design [21, 23] - have been integral to the progress made in nanowire devices.

2.2 III-V nanowire structures

Nanowire growth parameters dictate nanowire purity, quality and crystal structure which in turn affects their optical and electronic properties. Nanowires with defects give rise to trap states where unwanted recombination can occur. In addition, fine control of doping density, crystal structure, nanowire spacing, height and diameter is required as these parameters need to be specifically engineered towards different device applications. Consequently, there has been intense research studying nanowire growth mechanisms, recipes and methodologies in order to produce high quality, reproducible nanowires which have been engineered to provide optimal device performance[21, 25, 26, 43].

Nanowire fabrication methods can be initially divided into bottom up and top down synthesis. Both methods have been extensively used in the literature, each with their own merits and limitations.

Top-down synthesis involves depositing a metal pattern onto a III-V wafer and dry etching to wafer. The metal mask blocks the etching process, and thus this method produces nanowires. While top-down fabrication uses straightforward, standard cleanroom processing, the nanowire quality is dependant on the wafer quality, which is difficult to guarantee through the depth of the wafer and it is difficult obtain uniform etching - tapered nanowires are common.

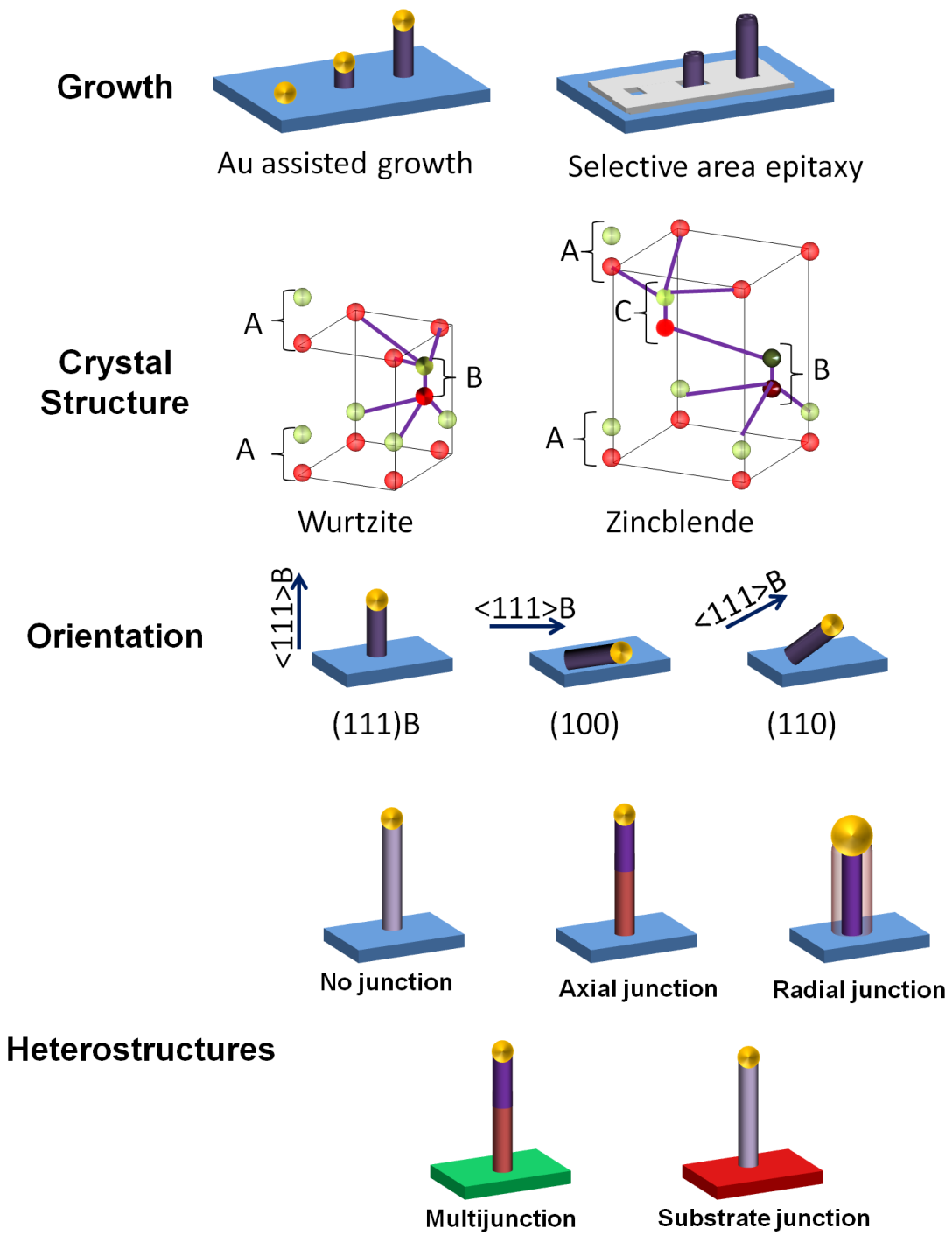

Fig. 2.2: Figure depicting various nanowire structures. Caption continues on next page.

Fig. 2.2: (Previous page.) Growth: Au-assisted MOCVD and SAE MOCVD were the two growth techniques used for the nanowires in this thesis. Au-assisted growth involves the deposition of gold seed particles with catalyses the nanowire growth at these points. SAE is a gold free method and makes use of a dielectric mask to from precisely ordered nanowire arrays. Crystal structure: III-V nanowires form wurtzite (bulk material) and zincblende (nanowire and bulk) crystal structures. Wurtzite forms an "'ABAB"' repeating structure, whereas Zincblende forms an "'ABCABC"' repeating structure. Orientation: The nanowire growth direction is determined by the crystal direction of the substrate. Here, the 111B direction is depicted for the (111)B, (100) and (110) oriented growth substrates. Homostructures: Nanowire homostructures are all made for the same compound semiconductor. Through doping - various structures can be formed. A doped or undoped nanowire can be grown with no junction within the nanowire, dopant can be changed during growth to form an axial structure, where the p section follows the n section, or a radial structure could be formed when p material encapsulates the previously grown n material. Heterostructures: Nanowire homostructures are made from different compounds - the nanowire geometry relaxes the strain between material growth of differing lattice constants. It is possible to grow materials of varying band gaps axially, resulting in a multijunction solar cell, or to grow a nanowire on a lattice mismatched substrate such as III-V on silicon.

Bottom-up synthesis involves growing nanowires layer by layer from percursor materials. Bottom-up synthesis can be further divided into two main methods: templated-directed and free-standing growth [5, 25, 44].

Templated-directed growth occurs where the nanowire grows in a pre-defined mould which forces the nanowire into a shape that is the relief of the mould. While this technique offers a relatively simply mechanism for nanowire growth, the nanowire dimensions are limited by the lithographic methods used to fabricate the moulds [45].

Free-standing growth occurs when nanowires are grown outwards from a single nucleation point where the nanowire growth direction is oriented on a growth substrate. The reactor conditions are used to encourage growth in one direction, and suppress growth in all directions. As demonstrated in the literature, different nanowire growth methods can be used [46–48].

Vapour phase epitaxy (VPE) is one of the most common techniques used for nanowire growth. VPE growth is carried out by precipitating out material from a supersaturated vapour phase. VPE is a versatile method with great scope for optimisation - vapour phase precursors are commonly available, which gives rise to several materials choices. VPE process conditions (gas flow rates/temperature/pressure) can be controlled which gives fine control of nanowire growth[49].

Metal-organic chemical vapour phase deposition (MOCVD) is a subtype of VPE where organo-metallic precursors are flowed into a reactor using a high purity carrier gas. The precursors decompose into atomic elements needed for the nanowire, thus enabling the nanowires to grow epitaxially [50].

MOCVD can be used in conjunction with particle assisted growth and selected area epitaxy - which are methods used to define the growth substrate in order to direct nanowire growth, as shown in Figure 2.2. MOCVD grown nanowires were used in the devices demonstrated in this thesis as it is possible to obtain high purity, device specific nanowires[51].

Selective area epitaxy (SAE) — also known as oxide assisted growth uses a patterned dielectric layer to enhance one dimensional growth. A thin dieletric layer is deposited onto a nanowire substrate, and holes are patterned into it exposing the III-V substrate underneath. The nanowires grow where the holes are, and do not grow on the dielectric layer [43].

Alternatively, using a catalyst seed particle — often a gold nanoparticle — acts as a single nucleation point for one dimensional growth. Therefore, the nanowires only grow where there is a gold nanoparticle seed. The gold nanoparticles are either pre-fabricated and deposited onto the substrate using spin coating, drop casting or by evaporating a thin (1 nm) layer of gold and heating the substrate to cause gold to nucleate and form small nanoparticles. Pre-fabricated nanoparticles are the preferred way to do this as this offers fine control of particle size. In any case, both methods result in an 'array' of identically oriented nanowires[24].

Gold nanoparticle assisted III-V nanowire growth occurs via a complex vapour-liquid-solid (VLS) process, named as such, as the mechanism involves a vapour phase precursor, a liquid alloy and the subsequent solid crystal growth. The organo-metallic precursors decompose and form an alloy with the gold nanoparticle. This alloy becomes supersaturated, and III-V material precipitates out, layer by layer, to form a nanowire. The mechanisms underpinning the nanowire growth rate are complex and can depend on the ratio of the III and V precursors, mass transport (movement of material through the gas phase), surface effects (diffusion of compounds formed on surfaces) and chemical reactions (decomposition of precursors, adduct formation and adsorption/desorption of active species). The doping level *in situ* is carefully controlled by flowing in a gas phase dopant with respect to the gas phase ratio of the precursors. The doping density can also be tuned to give optimum device performance, and increased doping results in a decrease in carrier mobility [52] In addition, as shown in Figure 2.2, the orientation of the nanowire growth substrate also dictates the growth direction of the nanowire[**?**].

Nanowire growth can be controlled by studying the thermodynamic (likelihood of reaction occurring) and kinetic (rate of reaction) factors. A summary of the governing equations given by Dick is given below [26]. The thermodynamic conditions are mostly dependant on the chemical potentials of the various components. For vapour phase growth, a stable, steady-state non-equilibrium condition is established by the continuous replenishing of vapour-phase materials, resulting in a constant chemical potential difference.

$$\Delta\mu_c = \mu_v - \mu_s = RTln(\frac{p}{p_0}) \tag{2.1}$$

where, $\Delta\mu_c$ is the chemical potential difference, R is the gas constant, and $\frac{p}{p_0}$ refers to the ratio of the partial pressure of the component in the gas phase and equilibrium partial pressure of that component over the crystalline material at the given growth conditions. It must be noted that this expression refers to one-component systems. Growth of III-V compound semiconductors are considered to be binary or tertiary systems, and as such, the analysis of their growth parameters is correspondingly more complex.

In general, the thermodynamic requirements of μ_v, μ_l, μ_s (the chemical potentials of the vapour, liquid and solid components respectively) to drive the reaction in the direction nanowire growth are given in Equation 2.2. This means growth of the crystal (solid component) needs to be the lowest energy, and therefore most energetically favourable route forward [26].

$$\mu_v > \mu_l > \mu s \tag{2.2}$$

When considering the kinetic aspects for a multistep chemical reaction, the slowest step is defined as the rate limiting step. For a chemical reaction, the rate r_{react} can be defined as

$$r_{react} = k(T)[W]^w[X]^x \tag{2.3}$$

where $[W]$ denotes the partial pressure of W and w denotes the number of moles of the component. The coefficient $k(T)$ is known as the rate constant and is defined by the Arrhenius relation:

$$k(T) = Ae^(E_a/RT) \tag{2.4}$$

The activation E_a is the kinetic barrier that must be overcme in order for the reaction to move forward. As can be shown by equation 2.4, the rate of a chemical reaction has an exponential dependence on temperature. This is useful, as growth conditions can be tweaked to ensure crystal growth is favourable over other side reactions such as parisitic base growth, that may limit desired crystal growth. Indeed, for layer growth to occur, the Gibbs free energy G_{energy} per unit area of absorbed layer must decrease with the adsorbed number of atoms n_{atoms} per unit area. If this condition is not met, then island growth of the adsorbate material over the substrate (i.e. thin film, rather than nanowire growth) will be favourable:

$$\mu = \frac{dG_{energy}}{dn_{atoms}} \tag{2.5}$$

Changing the stoichiometry of the III-V results in the growth of different compound semiconductors, which gives rise to tunable band gap thus allowing for specific absorption in the electromagnetic spectrum. This is especially important for applications such as spectral specific photodetectors and multijunction solar cells, enabling absorption in key parts of the spectrum[53].

The nanowire crystal structure can also be controlled by growth conditions. III– V nanowires can exhibit two crystal structures – cubic zincblende (ZB) and hexagonal wurtzite (WZ). Unit cells of both crystal structures are given in Figure 2.2. The ZB structure is found in bulk material, whereas both the WZ and ZB structures are found in nanowires [5, 33]. The WZ side-facet has lower surface energy, whereas the ZB has lower lattice energy. The high surface-area-to-volume ratio of nanowires can mean that the WZ phase is energetically more favourable. Control of the crystal structure is particularly important as this dictates the band structure of the nanowire, and therefore the electronic and optical properties. Furthermore, changes in crystal structure within a nanowire — polytypism — results in twin defects and stacking faults which form potential wells and barriers and act as scattering sites [25].

Polytypism occurs due to the similarities in growth direction for both crystal forms. As shown in Figure 2.2, zincblende growth occurs in the $<\bar{1}\bar{1}\bar{1}>$ direction, whereas wurtzite growth occurs in the $<000\bar{1}>$ direction, both of which are closely related. Zincblende exhibits a repeating pattern of ABCABC, where wurtzite has a repeating pattern of ABAB. As nanowires are grown epitaxially, this small change in the sequence of the layers can induce growth of a different crystal phase [26]. Joyce *et al* demonstrated the growth of phase pure nanowires by varying the proportion of III/V precursors and the growth temperature [25].

Epitaxial nanowire growth can be used to design device specific heterostructures. Axial and radial homostructures, depicted in Figure 2.2, are named as such because the components in an axial structure are grown vertically, one on top of the other, whereas the radial structure components are grown in a core-shell configuration, with each subsequent material growth completely encapsulating the previous material [54].

For solar cells and photodetectors, the main advantage of a radial junction over an axial junction is that the direction of light absorption is orthogonal to the direction of carrier collection, thus decoupling the two processes. As the nanowire diameter is typically less than the carrier diffusion length, efficient charge collection still occurs, meaning that lower purity materials may be used, reducing the overall cost and relaxing the processing conditions [23]. However, selectively contacting the core and the shell without inadvertently contacting both and short circuiting the device is challenging, whereas axial structures are easier to contact when adding top and bottom contacts [48].

Epitaxial growth of lattice mismatched materials has allowed III-V-on-silicon devices where the junction is formed between the III-V nanowire and the Si substrate, and multijunction devices where nanowires of different band gaps are grown axially and the junction is formed within the nanowire length. These growth of these structures, and their subsequent fabrication into proof-of-concept devices has been frequently demonstrated in the literature [28–32]. These devices have the added advantage of potentially being able to combine high performance III-V materials onto silicon substrates for integration with existing semiconductor devices.

2.3 Optimising nanowire geometry for light absorption

Nanowires experience light scattering, trapping and enhanced absorption effects, as shown in Figure 2.3, which can enhance their device performance [6]. The light absorption and scattering characteristics of a nanowire array varies according to nanowire length, spacing and diameter [21]. Therefore, these parameters can be adapted to increase light absorption. As shown repeatedly in the literature, nanowire structures absorb more light than expected - which in turn also results in a higher performance than that of a thin film device of equivalent area [55]. Nanowires also demonstrate polarisation specific absorption depending on their orientation with respect to incident light. This can be attributed to the dielectric contrast between the nanowire and its surroundings, and because the wavelength of light is larger than the nanowire dimensions [56].

Optimal light absorption occurs at a certain thickness.The absorption coefficient α describes how much a material absorbs light, and therefore how likely an electron transition from the valence band to the conduction band is, at a given wavelength where h is Planck constant, ν is the light frequency and E_g is the band gap [57].

$$\alpha = (h\nu - E_g)^{1/2}. \tag{2.6}$$

The number of photons N_{photon} absorbed by a material at a specific depth is given by

$$N_{photon} = N_s e^{-\alpha x}, \tag{2.7}$$

where N_s is the number of photons at the surface of the material and x is the material thickness.

The unusual absorption effects seen with nanowires cannot be accounted for with commonly used approximations such as ray optics (interaction of light rays with different media) and the Beer-Lambert law (relating the transmittance of light to the absorbance of the medium). Ray optics does not consider the quantum effects when light interacts with a feature that is smaller than the wavelength of light. The Beer-Lambert law requires several conditions to be valid, two of which are that no scattering occurs in the medium and that the light source used is monochromatic - both of which are not valid for nanowire devices. As a result, there has been considerable research effort in building models to deduce how, and why nanowires devices interact with light[2, 58].

Wallentin *et al* demonstrated this deviation of nanowire behaviour and proceeded to develop an advanced model to explain the interaction of light with the nanowires. They fabricated a single nanowire InP solar cell and found that their experimentally measured short circuit current (I_{sc}) was 6 times higher than that predicted by the ray optics limit and showed a photocurrent response much high than that of a thin film device of equal area. They developed an electromagnetic

optical model, which they used to design their nanowires to improve solar cell performance. The lengths of the p,i and n doped segments were then carefully designed to ensure efficient carrier collection. As shown in Wallentin's work, the length of the n segment of the pin structure is crucial to device performance [2].

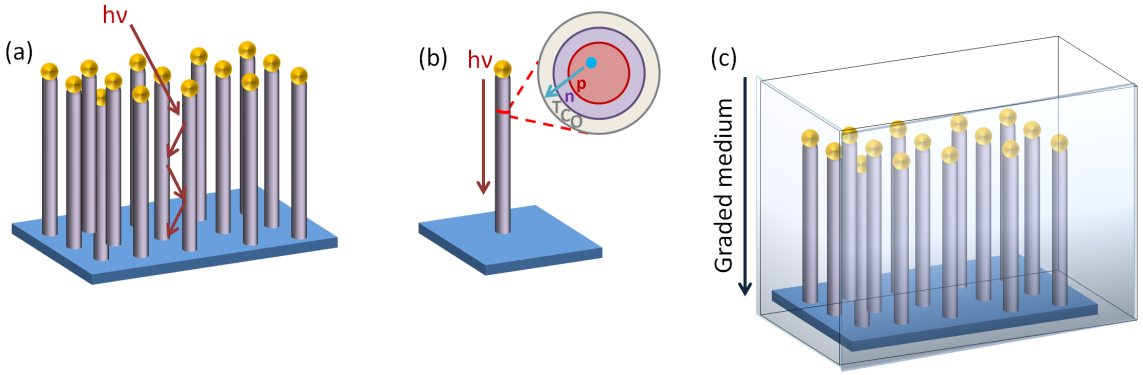

Fig. 2.3: Schematic diagrams depicting (a) light trapping, (b) light absorption and carrier collection and (c) graded medium approximation in nanowires.

Sandhu *et al* found that this enhanced absorption is also attributed to waveguiding within the nanowire. This was only valid at diameters less than 500 nm for solar spectrum wavelengths — this absorption enhancement broke down at larger nanowire diameters and the nanowires behaved more like bulk material [20].

Li *et al* found that for a core shell GaAs nanowire solar cell device, a nanowire diameter of 160 nm, pitch of 291 nm and length of 2 µm was found to be optimum for light absorption and carrier generation [21, 22]. LaPierre investigated two solar cell devices; GaAs nanowires grown on a GaAs substrate and GaAs nanowires grown on a silicon substrate. He found a diameter of 180 nm and spacing of 350 nm between nanometers and length up to 5 µm gave optimum device performance [23].

Finite Difference Time Domain (FDTD) simulations are used to model how nanostructures interact with light as this method is based on finding solutions to Maxwell's equations. The electric field and the magnetic field vectors are solved in an instance of time, as the modelling is done in the time domain. The process is continued for a subsequent instances of time until the desired electromagnetic behaviour is found. The FDTD method also takes into account the waveguiding and light scattering effects of the nanowires. The FDTD method was used effectively by Li *et al* and LaPierre *et al* to design their solar cell devices. Modelling nanowire arrays is undertaken by designing a single nanowire unit cell, and applying Bloch (or periodic) boundary condition to simulate a nanowire array.

Enhanced absorption in nanowire arrays can also be explained by Maxwell-Garnett effective medium approximation. In nanowires with small spacing, the array essentially has a effective refractive index close to air. This index matching results in less scattering thereby increasing

absorption of light, as shown in (c) [24, 57].

In addition to the well-documented work on ordered arrays, there has been intriguing work carried out on the light absorption properties of random arrays of nanowires. This work suggests that random nanowire arrays may enhance light absorption as ordered arrays result in light reflections from the nanowires and the substrate constructively and deconstructively interfering periodically, resulting in periodic reflections. Removing this long range order removes this periodicity and reduces the corresponding reflections [45]. This has also been observed by Siddique *et al* who found that the remarkable anti-reflective properties on the wing of a glasswing butterfly arose from the random array of nanopillars on the wing surface [59]. This is challenging to model as simulations rely on symmetry of a smaller unit cell to reduce computing time. For random arrays, a large unit cell is required. This would also be difficult to reproduce the exact simulation results in a device.

It is clear to see in this section that a thorough understanding of light interaction and carrier transport in nanowires is vital when designing nanowire structures. In addition, ideal nanowire dimensions can change depending on their intended application. Therefore careful consideration of nanowire geometry is required when growing nanowires for specific high-performance device.

2.4 Nanowire devices

As shown in the previous section, progress in MOCVD nanowire growth research has enabled high purity, well defined nanowires to be realised, which may be optimised for optimum device performance. The flexibility has resulted in the fabrication of high performance nanowire devices in a range of fields - photovoltaics [2, 8], photodetectors [60], lasers [61, 62], LEDs [63–65] as well as III-V on silicon devices [4, 66] have all been successfully fabricated. Furthermore, nanowires have also been used in creative applications such water splitting [67, 68], thermoelectric devices [17, 69, 70], light modulators [71, 72] and have been interfaced with biological cells [73].

Indeed, it is clear to see that nanowires show great promise in future research in a wide variety of fields owing to their ability to be engineered precisely for a specific device application. As can be seen the scope of nanowire engineering is huge. This gives rise to several possibilities for device fabrication. For brevity, a literature review on the three devices which are fabricated in this thesis - photovoltaics, photodetectors and modulators - is described below.

2.4.1 Photodetectors

A photodetector is device where the electrical current changes with light absorption. This change in current can be used to detect light. As shown in Figure 2.4, when light is incident onto a III-V

nanowire, electron-hole pairs are generated, which contributes to a change in conductivity - also known as *the photoconductivity*. A more detailed explanation of the photodetector operation can be found in Section 8.1.2. Photodetectors have found to be invaluable in a variety of applications, ranging from next generation communications and computing, to sensors as 'eyes' in robotic insects for monitoring applications [58, 74–77]. In general, a successful photodetector needs to have high sensitivity, signal-to-noise ratio, spectral selectivity, speed and stability [74]. These performance metrics are dependant on the photosensitive semiconductor used. As a result, photodetectors made from a variety of high-performance materials with different sensitivities and spectral ranges have been demonstrated in the literature, ranging from 2D materials such as MoS_2 [78] and graphene to perovskites, ZnO nanowires, quantum dot structures and organic polymers such as PEDOT:PSS.

Perovskite-based photodetectors have the benefit of high sensitivities, though they are unstable in air and water without proper encapsulation [79]. Dou *et al* demonstrated a solution-processed perovskite photodetector with detectivity of 2 x 10^{12} Jones at 550 nm under -100 mV bias, which is comparable with vacuum grown perovskites [80].

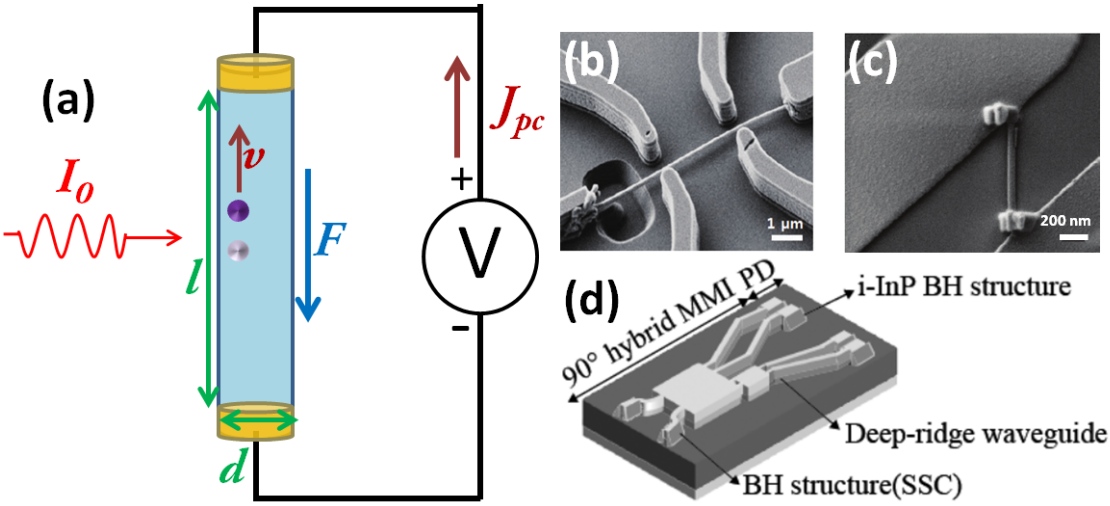

Fig. 2.4: (a) Schematic depicting photoconductivity in nanowires. When illuminated by incident light *Io*, electron-hole pairs are generated. This results in photoinduced current density J_{pc}. F refers to the electric field along the current direction, v is the charge carrier drift velocity, l and d refer to the nanowire length and diameter respectively [57]. (b) SEM image depicting a nanowire 'bridge' geometry for a single nanowire photodetector [77]. (c) SEM image depicting horizontal single nanowire photodetector [58].(d) Schematic depicting the integration of a nanowire photodetector into a compact coherent receiver [81]. Images reproduced with permission from [57, 58, 77, 81].

2D semiconductor photodetectors can also be solution-processed or grown using a CVD method. Heterostructures can be formed between different 2D material layers without the worry of lattice mismatch due to Van de Waals's interactions between the different layers [82]. However, graphene photodetectors suffer from high dark current due to its zero band gap

electronic structure, which impacts on its photosensitivity [83]. MoS_2, while having a high sensitivity under low illumination suffers from slow response time (temporal resolution on the order of s) [84]. Black phosphorus has a faster response time (ms) but suffers from thermal and light instability, make fabrication and device lifetimes challenging [85, 86].

Photodetectors based on quantum dots can be engineered for spectral selectivity by varying the composition of the quantum dot itself [87, 88]. High temperature droplet epitaxy techniques for quantum dots are normally used for compound semiconductors such as GaAs and CdS [89, 90]. This can be expensive, hence solution processing is an alternative fabrication pathway [91]. CdS quantum dots functionalised with ligands so they can be solution processed were able to achieve high detectivity of $1x10^{13}$ Jones [92]. Graphene quantum dots can be tuned through edge functionalisation, resulting in high responsivities 8.61 A W^{-1} at low temperatures of 150 K [93].

Nanowire structures have also been used for photodetectors, with spectral sensitivity ranging from UV to THz. For example, $K_2Nb_8O_{21}$ nanowires have been used for UV detection [94], CdSe nanowires are used for white light detection for broadband detection applications [95] and carbon nanotubes have been used for THz detection [96]. Hybrid nanostructured devices have also been demonstrated, to combine the strengths of the various nanostructures available. A high responsivity graphene-quantum dot photodetector where the spectral selectivity of the device can be tuned by varying the size of the quantum dots has been demonstrated [97]. ZnO nanowire arrays grown on silicon have demonstrated a broadband photodetector - the ZnO nanowires act as an anti-reflective medium as well as absorbing short wavelengths and Si absorbs longer wavelengths [98].

III-V nanowires are prime candidates for photodetectors as they exhibit high light sensitivity due to their small dimensions and large surface-to-volume ratio [24], polarisation dependent absorption due to their anisotropic geometry [42, 56] and spectral selective detection depending on the compound semiconductor used [99]. GaAs, InGaAs and AlGaAs exhibit ultrafast carrier dynamics which have been used for high speed photodetectors [100, 101]. III-nitride nanowires are used for UV detection [102] and InAs, InSb and InGaAs have all been used for IR detection [103]. Nanowire photodetectors can be initially divided into two classes: single nanowire devices and nanowire array devices.

Single nanowire devices are fabricated by depositing the nanowires via solution or mechanical processing. The nanowires are located using electron microscopy and contacts are then applied using electron beam lithography followed by metallisation. For the most part, nanowires are horizontally aligned [57, 75, 102–104], though there have been examples in the literature of a vertically aligned single nanowire device by planarising a nanowire array using PMMA and using a conductive AFM time to carry out IV characterisation [105]. Single nanowires devices are inherently useful as they allow for detailed studies of carrier dynamics [106]. Single nanowires may also be used in applications such as single photon detection [18]. However, these devices

are labour intensive as they require fabrication on a per-nanowire basis. Each nanowire needs to be painstakingly located on the substrate using electron microscopy, followed by electron beam lithography and contact deposition, which are not scalable processes.

Photodetectors fabricated from nanowire arrays can result in increased photoconductive gain and several more devices per chip [107–109]. Nanowire arrays photodetectors are fabricated by planarising the nanowires by depositing a polymer, and etching back the excess to expose the nanowire tips. Transparent indium tin oxide (ITO) top and reflective back Ti/Au gold contacts are then applied. The nanowire in question is either singly doped, or doped to form a junction within the nanowire, or between the nanowire and the substrate. Separation of charge carries occurs due to the PN junction, and the ohmic contact at either end allows for efficient carrier collection. An ohmic contact is essential in this device to provide low resistance contacts and therefore efficient collection of photogenerated carriers [103, 108, 110].

However, due to Fermi level pinning caused by surface states on the nanowire, forming ohmic contacts can be challenging. For this reason, an alternative device architecture has been demonstrated - a metal-semiconductor-metal (MSM) structure. This makes used of a Schottky contact on one side of the nanowire, and using a metal which forms an ohmic contact on the other side of the nanowire. This structure makes use of the Schottky contact to separate the charge carriers, whilst the ohmic contact once again allows for efficient collection of the charge carriers [75, 98, 100, 104, 105].

An avalanche photodiode is a variant of the MSM structure which relies on large Schottky barriers formed on either side of the nanowire. The presence of large Schottky contact enables a large electric field to be applied, which induces the ‘avalanche’ effect. This occurs when the presence of a large electric field allows the semiconductor to accelerate the charge carriers to a sufficiently high energy that they can generate additional electron-hole pairs through collisional ionisation. Use of a large Schottky barrier enables this process to happen at high voltages before breakdown of the Schottky barrier occurs. This device structure results in high gain and photon recycling as one photon can produce many electron-hole pairs [18, 111].

In conclusion, it is clear to see that nanowire photodetectors with high spectral selectivity, photoconductive gain, photosensitivity, stability and low dark current have been repeatedly demonstrated in the literature. The next steps for high performance nanowire photodetectors seem to be focussed on growth, to produce purer and higher quality starting materials [24], innovative device architectures to integrate nanowires into real world devices [81], single photon detectors [18] and multispectral detectors where the nanowire diameter is varied across the sample, as an alternative to using lattice mismatched materials [58], and flexible photodetectors [112].

2.4.2 Photovoltaics

Photovoltaic devices convert light energy to electrical energy which can then be used to power an external load. Firstly, incident photons with energy greater than the material band gap are absorbed to create electron-hole pairs. If the carriers recombine before they are collected at the electrodes, then the light-generated electron-hole pair is lost and no current or power can be generated. Therefore a pn junction is used to prevent this recombination by spatially separating the electrons and the holes. A built-in potential exists at the pn junction - this results in the minority carriers being swept across the junction where it is now a majority carrier. If the solar cell is short-circuited, the light-generated carriers flow through the external circuit.

As with photodetectors, III-V nanowires have also shown promise in photovoltaic applications due to light trapping in nanowire arrays resulting in enhanced absorption, high conversion of photons to charge carriers (external quantum efficiency), high power conversion efficiency and their direct band gap in solar spectrum.

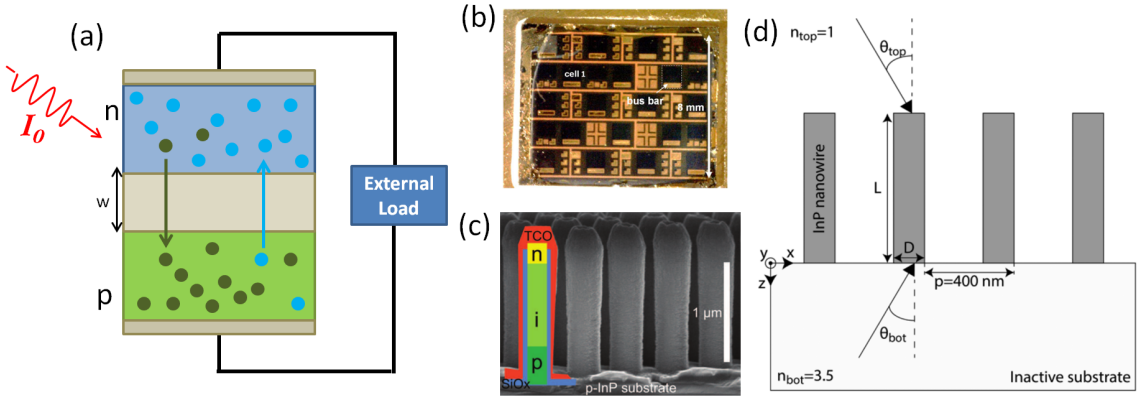

Fig. 2.5: Schematics, photographs and diagrams depicting solar cell operation, devices, architecture and light interaction (a) Schematic depicting a photovoltaic cell with a pn junction structure. Electron hole pairs and generated with incident light. The minority carriers are swept across the junction where they can be collected when connected to a load. (b) Photograph of a typical solar cell device [113]. (c) SEM imaging depicting a nanowire grown with a PIN axial junctions, to be used as a solar cell [2]. (d) Schematic depicting the 2D cross section of a nanowire array/ θ_{top} and θ_{bottom} refer to the propagation direction of light in the top and bottom regions, which have refractive indices n_{top} and n_{bottom} of 1 and 3.5. The nanowire diameter D and length L are set, and the nanowires are arranged in a square pattern with a period p of 400 nm. An azimuth angle ϕ of 0°indicates that light propagates in the x-z plane; an azimuth angle of ϕ of 90°indicates light propagates in the y-z plane. Schematic adapted from [114].

Solar cells have been demonstrated in the literature for several years with silicon dominating product sales owing to its competitive $\$/W$. This is partially due to the maturity of the semiconductor industry which keeps the price of silicon low, and partly due to government policy and subsidies towards renewable energy. However, owing to silicon's indirect band gap and low absorption coefficient, the Shockley-Queisser limit for the efficiency of silicon solar

cells is around 33%, which devices fast reaching this limit [115]. As a result, there has been intense research into other materials and device architectures which have the ability to break the Shockley-Queisser limit [1, 7, 15]. Currently, a multijunction III-V thin film solar cell under light concentration (GaInP, GaAs; GaInAsP, GaInAs) holds the record for power conversion efficiency at 46±2% [116]. III-V multijunction solar cells also hold to record efficiency for unconcentrated light at 38.8±2% and the best efficiencies for thin film GaAs and InP solar cells are 28.8±0.9% and 24.2±0.5%, respectively. Therefore, materials which are comparable to III-V materials are copper indium gallium selenide (CIGS) 21.7±0.7% and perovskite 19.7±0.6%. Other device systems such as quantum dot solar cells, and devices which make use of upconversion and downconversion effects to boost efficiency [15, 117].

Perovskite solar cells can be fabricated from solution processing techniques or vacuum deposition processes. Generally, the latter offers better quality films with improved morphology but without the cost benefits of solution processing. Indeed, the solution phase fabrication of perovskite nanowires has also been demonstrated, giving rise to perovskite nanowire solar cell with power conversion efficiency of 14.7% [118, 119]. However, as stated previously, perovskite solar cells suffer from toxicity and stability issues which limits their potential applications [79, 120].

Quantum dot solar cells can be fabricated in a variety of ways from quantum dot colloidal formulations. The solution may be deposited via spin coating, drop casting, chemical bath, separated using electrophoretic deposition or the quantum dots may be grown using the SILAR (surface ionic layer adsorption and reaction). Quantum dot solar cells are kinetically driven (rather than field driven as pn junction based solar cells are) and require fast transport of the photogenerated electrons in the quantum dot to the acceptor material which is often TiO_2 (titanium dioxide). Though devices architectures have been modified to avoid losses of photogenerated carriers by adding blocking layers to suppress back electron transfer and using hole scavengers, the efficiency just is not as high as the other architectures described. At the time of writing, the best certified power conversion efficiency for a quantum dot solar cell was 11.6% [121]. Quantum dot solar cells can also make use of effects such as multiple exciton generation, hot electron capture and upconversion to harvest more photons for photocurrent [122].

Thin film chalcogenide solar cell such as CIGS and CZTS (copper zinc tin sulfide) had demonstrated promising performances of 21.7% and 10.2%. However, CIGS contain indium, and given scarcity of indium and it's predicted increase in price due to the displays industry, alternative materials such as CZTS have been investigated. CZTS substitutes In for Zn which is much more abundant. However, as this is an emerging technology, further development is required for CZTS solar cells to increase their power conversion efficiency to become comparable to CIGS devices [123].

III-V-on-silicon devices have yielded impressive performance figures. The work carried out by Holm *et al* has showed that III-V nanowires grown on a silicon substrate to create a

multijunction solar cell, yielding an efficiency of 10.2 % [8]. Yao *et al*demonstrated axial GaAs-on-Si solar cells with an efficiency of 7.58 % and an ideality factor of 2.2 [124]. Several growth and device fabrication challenges are encountered with III-V devices including well-controlled nanowire growth and doping on a lattice mismatched substrate, preventing mis-fit dislocations and abnormal growth orientation. To mitigate this, there is often a critical diameter at which the nanowire must be grown to.

III-V nanowire array solar cells are looking extremely promising [125]. The best reported efficiency of a III-V nanowire solar cell was demonstrated by Aberg *et al.* who fabricated a GaAs nanowire array solar cell achieving an efficiency of 15.3% where the axial pn junctions only covered 13% of the surface area [113]. Similarly, van Dam et al have demonstrated an InP nanowire array solar cell with an efficiency of 17.8%. The absorption of the nanowires was enhanced by using a layer of self-aligned nanoparticle on the TCO, which caused forward scattering of light.[126]. Wallentin *et al*, have demonstrated a InP nanowire array solar cell where the nanowires covered 12 % of the surface but managed to achieve 83 % of the photocurrent density of a thin film device [2].

In general, the fabrication process of single nanowire and nanowire array solar cells is similar throughout the literature. Single nanowire solar cells tend to be fabricated in a very similar way to photodetectors — the nanowires are dispersed onto a substrate, located using electron microscopy followed by patterning the electrodes using electron beam lithography follows by metallisation. Single nanowire photovoltaics have been useful in carrying out proof-of-concept studies into device performance and materials properties of the nanowires [20, 29, 127].

However, nanowire arrays offer more potential as a means towards large area devices. Nanowire array devices tend to be fabricated as follows: growth substrates are patterned, either by selective area epitaxy [44], substrate conformal imprint lithography [113] or nanoimprint lithography [128] to clearly define the nanowire spacing and diameter. The nanowires are then grown epitaxially, to define the nanowire lengths and to form axial or radial junctions. The nanowire array is planarised with a polymer such as benzocyclobutene (BCB), SiO_2, then etched back to reveal the nanowire tips. Top and bottom contacts can then be added. Generally the top contact tends to be a transparent conducting oxide (TCO) such as ITO, though other TCOs have been used such as graphene [129] and aluminium zinc oxide. The back contact tends to be a variant of an alloyed gold contact, the most common being Ti/Au [124].

There have been a fewer reports of other device architectures, such as Schottky barrier solar cells and hybrid nanowire-polymer devices. Schottky barrier solar cells, similar to the photodetectors utilise the Schottky barrier for charge separation [129]. Hybrid nanowire-polymer solar cells use a conducting p-type polymer such as spiro-OMeTAD [119] or P3HT to form a junction with the n doped nanowire. However, by and large, forming the junction within the nanowire, or forming a junction between the nanowire and the substrate is the most commonly

used approach.

In conclusion, it is clear to see that III-V materials have proven to form excellent photovoltaic devices, so far. III-V nanowire solar cells, in particular, are looking extremely promising with devices achieving high efficiencies whilst covering a small fraction of the surface area of thin films device. There has been new research investigating larger scale methods of patterning to form well defined arrays, as commonly used methods for lab-scale devices such as selective area epitaxy rely on electron beam lithography which is not scalable. However, patterning methods based on nanoimprint lithography are potentially scalable and are only limited by the size of the wafer accepted by the nanoimprint machine. There are also general fabrication challenges such as forming high quality contacts and reducing the contact resistance, as there will now be several points between the nanowire tips and the metal contact in an large area array device, as well as selectively contacting the core and shell components to avoid shorting a radial junction device [7].

2.4.3 THz modulators

A modulator is a device which transmits and blocks signals between a signal emitter and signal receiver. In the case of nanowire THz modulators, these work similarly to a wire grid polariser - absorbing radiation polarised parallel to the long axis of the nanowire, and transmitting radiation polarised perpendicular to the long axis of the nanowire.

Terahertz (THz) radiation, lying between the infrared and microwave regions of the electromagnetic spectrum (0.1 to 10 THz) has been of intense interest due to enormous potential in a variety of applications, ranging from biological and medical sciences to non-destructive evaluation, security, and ultrafast computing [132–134]. Initial progress in the field was hampered by a lack of intense sources of THz radiation [135, 136], but in the past 20 years huge advances have been made in THz generation [137–143] and detection [132, 144–148], materials characterisation [149–153] and non-invasive medical imaging [154, 155]. Despite these significant developments, one application that has still not been realized is high-speed THz communication, due to the lack of THz modulators available.

Though III-V nanowires are not widely used as the active component in THz modulators, several other materials systems have been investigated. Depending on which property of light is controlled, THz modulators can come in different forms. The intensity [156, 157], phase [72, 158], or spatial position of the transmission and reflection coefficients of the THz electric field [159, 160] can all be modulated using different devices.

Early THz modulators mainly focused on modulation of THz intensity, with devices based on two-dimensional electron-gas (2DEG) structures [161, 162], birefringent liquid crystals [163, 164] and static THz polarizers [165–168]. Recently, THz modulation has also been re-

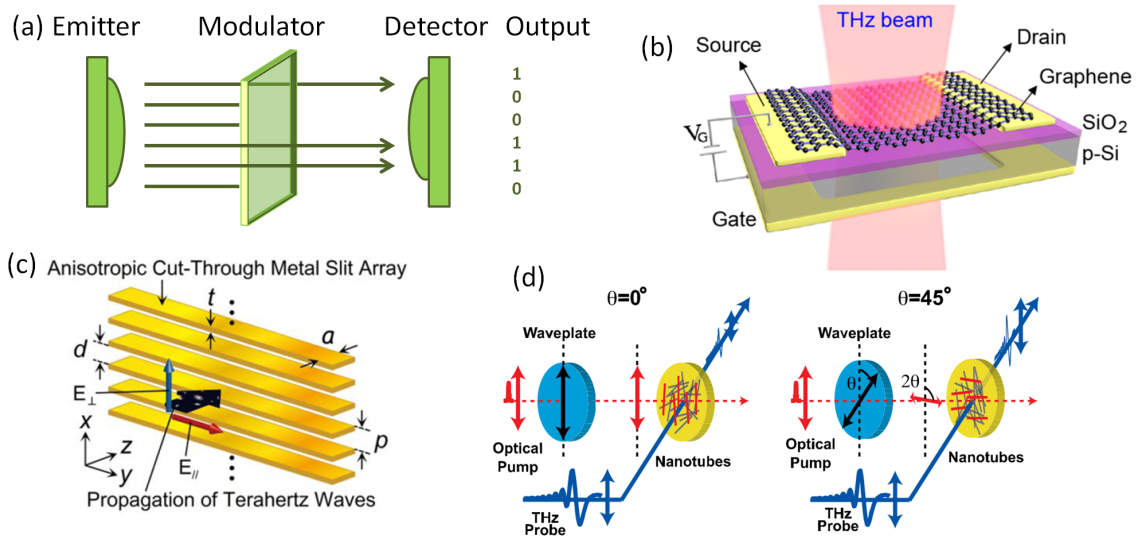

Fig. 2.6: (a) Schematics and diagrams depicting THz systems. (a) General schematic of a THz communication. An emitter is used to generate THz signal. The modulator is used to encode information into the THz wave and produce binary information by absorbing and transmitting the wave. A detector is used to read the binary information. (b) Schematic showing the device architecture of a graphene-based THz modulator [130], (c) Schematic showing the device architecture of a metamaterial-based THz modulator [131]. (d) Schematic showing how the orientation of the optical pump affects the transmission of the THz wave for a carbon nanotube-based THz modulator [72].

alised with metamaterials [156, 158, 159, 167, 169–173], optical cavities [174, 175], graphene [176–178] and carbon nanotubes [72, 179, 180], each with their own merits and weaknesses.

For high speed THz communications, fabricating a polariser with a high modulation depth and fast switching speed and to have a broad bandwidth is desirable. A high modulation depth is needed so there is a big difference in absorption between the absorbing and transmitting states to ensure a high signal-to-noise ratio. A fast switching speed is the time needed to change between the absorbing and transmitting state which needs to be fast enough for high speed communications. Broad bandwidth is also needed to ensure that the modulator can be used for as much of the THz frequency range as possible.

Metamaterial-based THz modulators have achieved high modulation depths, with Karl *et al.* [181], demonstrating a dynamic range of over 20 dB and Chen *et al.* showing a modulation depth of $\sim 50\%$ [169, 182]. However, these THz modulators suffer from low bandwidth, with optimal operation only at a designated wavelength, as well as limited switching speeds with microsecond temporal resolution.

THz amplitude modulators based on Fabry-Perot semiconductor cavity designs have also been demonstrated, with a modulation depth of $\sim 90\%$, yet only microsecond switching speeds [175]. Recently, Liu *et al.* have demonstrated THz modulation with close to 100% modulation depth

by utilizing the evanescent wave in a total internal reflection setup coupled with a conductive interface to enhance attenuation of THz radiation [183].

With the aim of improving switching speeds, graphene-based modulators have been shown to improve performance, by utilising intraband absorption to obtain a modulation depth of $\sim 16\%$ and nanosecond modulation time [176]. By utilising a total internal reflection geometry, the modulation depth of these graphene-based modulators could be improved up to 70% per reflection [184]. Furthermore, carbon-nanotube based THz polarisers have also been demonstrated. Ren *et al.* [179] fabricated static carbon nanotube THz polarizers by depositing aligned nanotubes onto a sapphire substrate and reported an extinction ratio of 10 dB in the optical and THz range, whereas Kyoung *et al.* [180] demonstrated an extinction ratio of 37 dB by using a carbon nanotube stack fabricated from aligned nanotube arrays to produce static THz polarizers.

However, in order to realise ultrafast THz communication, modulation times on the order of picoseconds are required. Carbon nanotube–polymer based modulators can offer such high switching speeds, yet at the cost of modulation depth. Docherty *et al.* [72] demonstrated an ultrafast switchable carbon nanotube THz polariser, which could be optically controlled and was capable of polarization and intensity modulation of THz radiation with a time resolution on the order of 1 ps, although it suffered from a low modulation depth of around -27 dB.

Thus, there is still a need for the development of a practical THz modulator with a high modulation depth and picosecond switching speeds, which can be electrically or optically controlled and can be easily integrated into current silicon-based technology. III-V nanowires could be used as when photoexcited, the charge carriers in the conduction band interact with the THz wave, resulting in attenuation. When the nanowire is not photoexcited, the THz wave is transmitted through. Given that the carrier lifetimes for several III-V materials is of picosecond timescale, this would also gives the potential for ultra fast switching speeds, as the polariser is only active when the nanowire is photoexcited. To continue in the same fashion as above, removing the nanowires from the substrate and embedding them in a flexible polymer offers a promising way to fabricate a novel THz modulator.

2.5 Conclusion

In conclusion, it is clear to see that advances in nanowire growth, theoretical work and device fabrication have led to impressive progression in the field of III-V nanowire devices. Research into these distinct areas has led to greater understanding into nanowire geometries needed for efficient device design, tight control of nanowire growth parameters needed to grow these high purity and well-defined nanowires, and finally - developing the best way to utilise these nanowires in high performance devices.

Collaboration and knowledge sharing between the different groups at respected institutions around the world who hold specialist expertise in these different research areas has been integral to the rate at which the field has moved forward. This is clearly indicative by the breadth of publications — a review of the literature has shown several remarkable examples of nanowire devices with impressive performance data. Nanowires have further shown their adaptability and applicability as, depending on the optical and electrical properties of the nanowire used, a wide range devices may be fabricated — including photodetectors, solar cells, modulators, LEDs, nanogenerators.

However, while nanowire devices are still limited to substrate based growth and fabrication, the applications of such devices will also remain limited. The following chapter addresses the use of flexible electronics, and how this may enable flexible, substrate-free nanowire devices - an area that has been relatively little explored to date. Moving nanowire research into flexible electronics could potentially be the next step into realising full scale commercialization of nanowire devices.

Chapter 3

Flexible Nanowire Devices

Following on from the discussion of III-V nanowire properties and devices in chapter 2, this chapter addresses why flexible nanowire devices is an enabling technology for next generation device applications. This chapter begins by giving a brief overview on the progress of flexible electronics, and the scope and outlook of such technology. I then highlight important literature investigating the properties of organic and inorganic electronic materials and explained why combining organic polymers and III-V nanowires would be beneficial for device design. A review of the recent literature is presented on current flexible nanowire devices, which details common device fabrication techniques and best device performance to date. I conclude the chapter by proposing a fabrication method towards a flexible nanowire device, and present how I plan on adapting existing processes and overcoming fabrication challenges in order to successfully fabricate a flexible, substrate-free vertically aligned nanowire-polymer device.

3.1 Progress in flexible electronics

Flexible electronics, a field distinct from conventional wafer based electronics, describes the incorporation and/or fabrication of electrical components from 'soft materials', giving rise to devices that may be bent, twisted or shaped[13, 37, 185, 186]. The term 'form factor' has been utilised in hardware design to describe the size, shape and specification of electronic components[187]. For example, research into nanotechnology has enabled the development of ever smaller form factors, thus coinciding with Moore's law[4, 6, 28, 188]. Research into flexible electronics has enabled the feasibility of new, bendable, stretchable form factors[35, 36, 189].

Such research arose from the need to create devices with functionality that was just not possible from wafer-based electronics. Examples in the literature include rewritable Braille displays (or haptic displays, as they are otherwise known) which need dynamic and changeable raised dots that lie flush from the screen surface, and then can be flattened in order to refresh the page; military equipment which can withstand field use in harsh environments; and smart textiles, where electronics are woven into the fabric itself has been used to heat or cool the user,

was well as for fashion and aesthetic reasons. Given the scope, and the need, for novel devices and applications using this new form factor, it is reasonable to suggest that more and more ingenious and clever applications will come to light - ranging from displays, implantable medical devices and energy harvesting devices to sensing devices, e-paper and smart textiles [9–13]. Furthermore, flexible electronics are potentially a cost effective method to manufacture electrical devices through the use of existing fast throughput processes such as roll-to-roll coating, solution processing and direct contact printing, whilst still maintaining the performance and the product lifetime of wafer based electronics[190–192].

Fig. 3.1: Schematic showing scope of flexible electronics. Numerous advances in the field and enabled several interesting applications - displays, wearable electronics, biomedical implants, energy storage & harvesting and sensing. Image adapted from [193–197]

It is interesting to note how the scope and aims of flexible electronics research has changed over the past 10 years. In a review article written by Sun, just over 10 years ago in 2007, they stated that the future of flexible electronics was to return to macroelectronics systems, rather than miniaturising further. This paper was written at a time where semiconductor device research was heavily focussed on miniaturisation of electrical components for ‘nanoelectronics’. Flexible

electronics were seen as a lower performance, but inexpensive alternative to wafer-based nano-electronics, and the cost trade-off was worth the drop in performance [9]. Conversely, a recent review written by Liu in 2015 - is of the opinion that flexible electronics now seeks to create robust, flexible nanoelectronics with the aim of developing fully integrated 'nanosytems' which consists of several nanodevices including a nano-power source, generator, detector etc to form fully integrated systems [112]. This is partly due to advances in device fabrication and thin film handling which has made combining several nanoscale devices onto a flexible substrate possible.

Flexible electronics which match the performance of their wafer-based counterparts whilst improving robustness and cost effectiveness will form the next generation of electronic devices. This will also be coupled with other technological advances in complementary fields such as sensing, low cost nanofabrication, sustainable electronic waste materials recovery and upcycling, as well as communications and connectivity to form a network of interconnected devices - resulting in an 'Internet of Things' connected world [198].

3.2 Choice of materials for flexible electronics

Choice of materials is fundamental in ensuring the success of flexible electronics, as this dictates the functionality of the device, and how well it copes under environmental factors such as mechanical stress and extremes of temperature, as well as the optical and electrical performance [10, 192, 199]. Electronic devices - flexible or not - all consist of conductors, semiconductors and insulators. Organic polymers, that form the basis of many flexible electronic devices, tend to form an amorphous structure consisting of long chains of hydrocarbons which are weakly bonded together by Van de Waals interactions. This means these long chains are able to slide past each other, resulting in an inherently flexible structure[4]. This is very different to inorganic materials which tend to form crystalline structures where electrostatic interactions between the ions hold the ions in definitely positions - resulting in inherently brittle solids[23]. However, inorganic nanostructures may be incorporated into flexible electronics by embedding them in polymers.

Organic materials are generally considered to be more cost effective than their inorganic counterparts due to lower materials costs and their ability to be dispersed in solvents to form inks suitable for high throughput printing processes such as roll-to-roll coating[187]. Inorganic materials are generally more expensive due to the cost of growth precursors, substrates and specialist growth equipment under non room temperature and pressure conditions[58]. In addition, materials engineering to tune optical and electronic properties would need to be carried out via inorganic synthesis through the growth process [52]. However, with the high cost also comes better device performance; it has been found that the performance of organic materials

does not match the performance of their inorganic counterparts due to their inherent materials properties, as shown in Table 3.1 [200–202].

Semiconductor	Mobility (μ / $cm^2V^{-1}s^{-1}$)	Lifetime (τ/s^{-1})
P3HT	$10^{-3} - 10^{-4}$	10^{-4}
PPV	$10^{-1} - 10^{-2}$	10^{-3}
GaAs	10^{3}	10^{-12}

Table 3.1: Table comparing organic and inorganic semiconductor properties [200–202]

Conductivity arises in metallic conductors from metallic bonding where there are free electrons available for conduction. In organic materials, atoms are covalently bonded which results in their lower conductivity as there is a lack of free electrons available for conduction. Conductive polymers tend to be conjugated chemical structures, where there is a presence of alternating single and double bonds. This bonding structure has overlapping p-orbitals which results in delocalisation of electrons which are free for conduction. However, from the literature it seems that the dependence of conductivity on polymer morphology is still not well understood, and further work is needed to gain a better understanding. Examples of conductors used as electrodes in flexible devices include PEDOT:PSS, graphene, carbon nanotubes and noble metals[82, 203–205].

Organic and inorganic semiconductors both require n doping and p doping (reductive and oxidative doping in organic semiconductors) to form n-type and p-type semiconductors. As shown in Figure , the electronic structure of organic semiconductors is analogous to inorganic semiconductors with the highest occupied molecular orbital (HOMO) and lowest occupied molecular orbitaL (LUMO) correspond to the valence band and conduction band respectively. Lower mobility values for organic semiconductors is attributed to the disorder in organic materials. Examples of semiconductors used to form a junction in flexible electronics include semiconducting polymers, silicon, III-V materials and 2D materials [206].

Insulators used in flexible devices include, silicon nitride, silicon dioxide, and elastomers such as poly(dimethyl siloxane) (PDMS) [9]. These can act as a dielectric layer, or as an encapsulant to protect brittle and delicate crystalline inorganic nanostructures from degradation from mechanical stress, moisture, oxygen and light [9, 112, 207].

In order to make truly robust, flexible devices that possess high electrical and optical performance, a different approach is needed: devices made from both organic and inorganic components which harnesses the benefits of both materials systems. As stated in Chapter 2, III-V nanowires possess excellent mechanical stability, electrical and optical properties which make them ideal candidates for incorporation into flexible devices. However, such a device is not trivial to fabricate, and developing fabrication methods for high quality is challenging. Therefore,

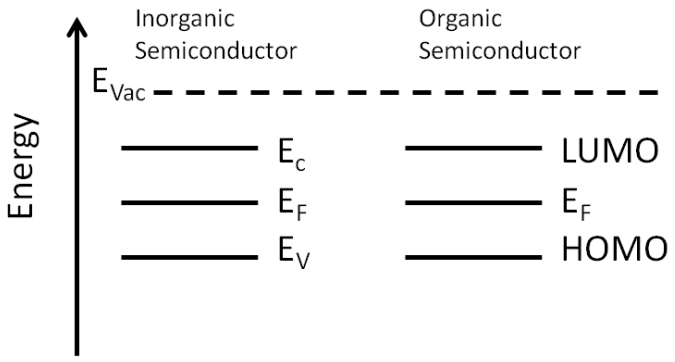

Fig. 3.2: Schematic showing the electronic structure of organic and inorganic intrinsic semiconductors. The HOMO and LUMO in organic semiconductors are analogous to the valence and conduction bands respectively.

flexible nanowire devices is an active field of research with various innovative proof-of-concept devices being published in the literature.

3.3 Nanowire alignment for flexible devices

Fabrication of flexible nanowire devices starts with nanowire alignment. This can be achieved though nanowire growth process, or by an alignment process following removal from the substrate. In the literature, five main methods have been frequently demonstrated - nanowire growth on a flexible substrate; spin coating of nanowire formulations; contact printing of nanowires; post-growth nanowire alignment (i.e Langmuir-Blodgett)[203, 208–210]. There have been several flexible nanowire devices demonstrated in the literature in several applications including transistors, photodetectors, solar cells, and logic circuits. Key examples in the literature highlighted in this section.

Firstly, nanowires may be grown on a flexible substrate. However, this has shown to yield poor quality nanowire growth where the nanowires are improperly aligned and exhibit polytypism.

Cui *et al.* demonstrated the growth of gold-seeded zinc oxide (ZnO) nanowires on thinned glass, polystyrene and polyethylene foils [211]. The gold seed particles were deposited using the Langmuir-Blodgett techniques, which allows the nanoparticles to self assemble into a single ordered layer [210]. However, a hydrothermal growth method is used, at a temperature of 90°C in order to prevent heat degradation of the plastic substrate. This method is unsuitable for III-V nanowires has higher growth temperatures are required for MOCVD, in order to provide high quality nanowires. Furthermore, a crystalline substrate is needed to dictate the growth orientation of the nanowires [212].

Mohseni *et al.* demonstrated the growth of InGaAs nanowires on flexible graphene substrates using direct Van de Waals epitaxy - where an epilayer grows between the graphene and the InGaAs nanowires, thus relaxing the lattice matching requirements. Mohseni uses an InAs

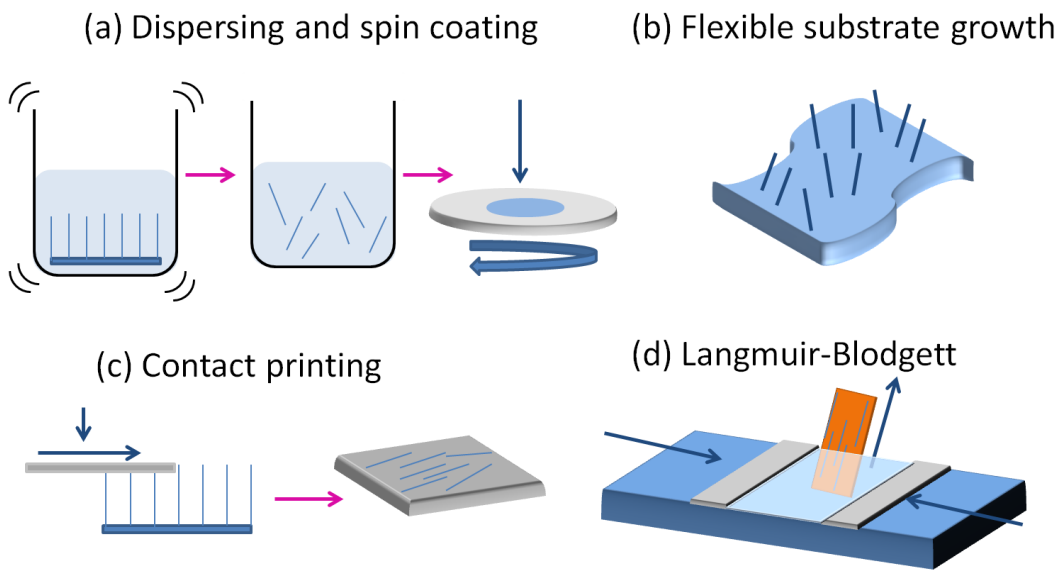

Fig. 3.3: Commonly used nanowire alignment techniques. (a) Nanowires grown on wafers may be sonicated in solvent/water/polymer to form dispersions, the resultant dispersion is spin coated and dried/heated to remove the solvent/polymerise the polymer. (b) Nanowires may also be grown on a flexible substrate - though as this substrate is not crystalline, the growth direction of the nanowires cannot be controlled. (c) Contact printing involves sliding a receiver substrate across the nanowire substrate - the shearing movement allows the nanowires to be removed from their growth substrate and be aligned planar on the receiver substrate (d) Langmuir-Blodgett consist of a water bath, where a film of the nanowire dispersion is dropped on the surface and compressed. A receiver substrate is submerged in the film, and removed at a controlled rate in order to align the nanowires on the substrate.

epilayer to seed the growth of the nanowires. While a successful photovoltaic cell was made from these nanowires, it must be noted that these nanowires were not phase pure [208].

Flexible devices based on nanowires, nanotubes and 2D materials have been built on flexible silicon foils, using similar fabrication processes to wafer based electronics. The production of such foils is through chemical thinning of standard wafers which is needlessly wasteful and inefficient. Furthermore, the resultant devices are not truly robust [213].

An alternative to flexible substrate growth is to prepare nanowire formulations for solution processing. Nanowire formulations are prepared by growing the nanowires using one of the growth methods described in Chapter 2, or by aerotaxy (substrate-free nanowires are grown in a flow-through reactor using an aerosol of Au nanoparticles and gaseous precursors, which are then collected onto a wafer using an electric field [214]). The nanowire wafer is then sonicated in organic solvent to release the nanowires from the wafer and disperse the nanowires in the organic solvent. This nanowire suspension can then be used to disperse the nanowires in a suitable polymer, or can be directly spin coated onto another substrate. This produces a thin film with a randomly oriented though highly connected network of nanowires [203].

Electrodes made from silver nanowires from a mesh which allows for low resistance films [215]. However, these unaligned nanowire meshes are unsuitable for high performance optoelectronic devices - therefore alignment techniques such as microfluidics and blown bubble films are used to to obtain planar aligned nanowires [216, 217].

It is also possible to transfer nanowires to a receiver substrate without the aid of solvents through dry transfer [218], contact printing [207] and differential roll printing [209]. An adhesive tape or an intermediate receiver substrate may also be used to facilitate the transfer. Finished nanowire devices can also be transferred in this way too, though their performance suffers after the transfer [207]. Electrospinning aligned nanowire-polymer mats using oriented electrodes can also be used to align nanowire films, though this then poses issues with contacting the nanowires through the polymer [219].

The work of Han *et al* and Sun *et al* both used contact printing to transfer nanowires onto flexible organic polymer substrates for subsequent device fabrication [36, 37]. However, these methods yield planar nanowires and does not produce vertically aligned nanowires needed for high performance devices.

3.4 Polymer encapsulation

After the alignment step, nanowires can then be coated with a polymer and peeled off to remove from the receiver substrate, resulting in a thin film that encapsulates the nanowires. Two main types of polymer could be used as the encapsulant: solution processable polymers and chemical vapour deposition (CVD) polymers - each with their own merits and limitations. Both routes are suitable for flexible nanowire device development [189, 220].

3.4.1 Solution processed polymers

Solution processed polymers are those which can be dissolved in an organic solvent, making it suitable for printing and coating. The polymer formulation frequently contains the monomer and some form of initiator. The initiator can be activated using heat or UV light, and causes the monomer to polymerise and resultant polymer film to harden. After polymerisation, the polymer film is ready to remove from the nanowire substrate. Solution processable materials can be optimised through formulation chemistry - while this is still a challenging process, it is relatively straightforward when compared to needing to develop a new growth process for inorganic crystalline growth. These optimised formulations can then be coated directly onto a plastic substrate for high-throughput, low cost processing [187, 221]. In addition, these polymer formulations can be reformulated, or the polymers themselves functionalised through synthetic organic chemistry to optimise the device to performance specifications.

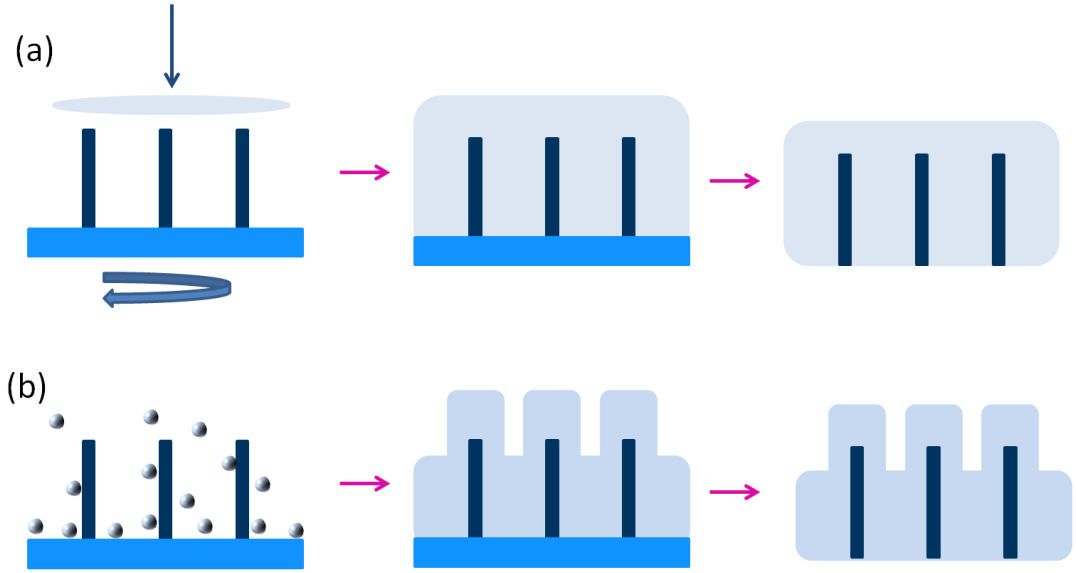

Fig. 3.4: Nanowire encapsulation using (a) solution processed and CVD (b) polymers. (a) Solution processed polymers consist of an organic/aqueous solution containing corresponding monomer and some form of initiator. The formulation is spin coated onto the nanowires substrate and allowed to polymerise, after which, the polymer film can be removed from the nanowire substrate. (b) CVD polymers are vaporised in a furnace to crack them into smaller, reactive species in the gas phase. These reactive species adsorb onto the nanowire surface where they undergo polymerisation and form a thin film, which can then be removed from the substrate.

Commercially available photoresists such as Cyclotene 3022-57 (BCB) and Shipley S1808 are frequently used to planarise nanowires when fabricating devices that remain on the growth substrate. These photoresists cannot be removed from the substrate as they form a hard, brittle film which have strong adhesion to the substrate [48, 222].

PDMS has been used extensively in the literature to make thin films using silicon nanowires [22]. PDMS is readily available, cost-effective, and straightforward to formulate and polymerise. However, fine control of the formulation and surface chemistry is needed is order to form high quality thin films. Understanding the surface interaction between the polymer, the solvent in which is it dissolved in and the nanowire is crucial as nanowires have such a high surface-to-volume ratio [223]. The wetting properties of the polymer solution needed to be optimised in order to ensure the formulation adequately fills the voids between the nanowires. Failure to do so would result in short circuiting the device between the top and bottom contacts [17].

Finally, the polymer needs to encapsulate the polymers well, yet be easily removed from the growth substrate. While PDMS has been frequently used to embed nanowires, it is not easily removed. Often, a razor blade needs to be used, which results in damaging the thin film and scratching the growth substrate [22].

Spin coating is frequently used to optimise polymer formulations prior to scaling up for larger area coating. Spin coating parameters need to be considered to ensure uniformity of the coating, as the act of spin coating and the capillary forces between the wet nanowires can cause

the nanowires to clump or to change their vertical orientation and fall over [220]. Spin coating is a mature process, extensively used in the electronics industry. However, it must be noted that spin coating results in wastage - generally only 2-5% of formulation ends up being coated on the substrate - the rest is flung off during the spin coating process.

The final film thickness and quality is determined from the viscosity of the solution, the weight percentage loading of the polymer, the spin speed at which the formulation is deposited on the substrate and the mixture of solvents used. From a practical perspective, spin curves are obtained by spin coating formulations of different viscosities and different spin speeds to produce a matrix of samples, and plotting the measured film thickness against spin speed. This gives a curve with an exponential dependence of film thickness on spin speed: The faster the spin speed, the thinner the film. Due to the ease of acquiring this process data, theoretical analyses of spin coating are often neglected. Nevertheless, it is useful to consider the factors which affect spin coating.

Emslie *et al.* proposed a spin coating approximation where they made several assuptions: no evaporation of solvent, an infinite horizontal rotating plane so there is no gravitational component, a thin liquid layer so that differences in gravitational potential normal to the surface are negligible, the radial velocity is small enough that Coriolis force can be neglected and the liquid is Newtonian. A detailed analysis of this derivation is given in their paper[224]. Using cylindrical polar co-ordinates (r, θ, z), the balance between viscous and centrifugal forces per unit volume of Newtonian fluid is given by

$$-\eta_v \frac{d^2 v}{dz^2} = \rho \omega^2 r, \tag{3.1}$$

where η_v is the viscosity, ρ is the density, ω is the angular velocity and v is the velocity. If we consider that the height h of the film is equal to z, then integrating equation 3.1 and solving the resultant differential equation gives the following expression for the height of the film:

$$h = ae^{-\alpha^2 r^2}, \tag{3.2}$$

where h is the film height, α and a are fitting constants. The exponential term leads to a flattening of film height with time t, which is seen in practical spin coating as allowing the film to settle results in a more uniform film thickness. Of course, such an approximation is not applicable for non-Newtonian fluids, and solvent evaporation has a great effect on film quality and thickness and therefore needs to be included in analyses of spin coating. Including evaporation into the analysis, as calculated by Sahu *et al.* gives the following expression for the final film height h

$$h = \frac{3C^3(t)\nu_0\phi}{2(1-C(t))\omega^2} \tag{3.3}$$

where C is the solids concentration in the formulation, ν_0 is the initial spin velocity and ϕ_{evap} is the evaporation rate. There are several other approximations for Newtonian fluids, solvent

mixtures, shear stress conditions in the same paper - showing the complexity of spin coating analysis[225].

To summarise, solution processed polymers have been frequently used in the electronics industry as a low-cost, high-throughput method of fabrication. Different coating methods have been used, including spin coating, dip coating, gravure coating and bead coating to name but a few. Careful control of polymer formulation is needed to ensure the quality of the thin film. Solution processed polymers tend to be used as planarising films - forming a clean, flat layer in which to conduct subsequent processing steps on to. However, surface tension effects from the solvents may make it difficult for the polymer formulation to penetrate the voids between the nanostructures. In this case, other polymer deposition methods may be more suitable for the coating of nanostructures.

3.4.2 CVD polymers

CVD polymers are deposited directly onto a substrate, from the vapour phase. Though CVD was traditionally used for growing semiconducting thin films [226], carbon nanotubes [204] and graphene [227], this technique has been found to deposit polymers successfully.

Polymer CVD technologies enable conformal coatings of samples with complex topographies with feature sizes on the order of nanometers. CVD polymers provide an interesting alternative to coating nanostructures using solution processed polymers. Surface tension affects arising from solvents cause non-uniformities in the coating as the capillary length of the solvent, typically on the order of 1 mm is several orders of magnitude larger than the length scale of the nanostructure.

A typical polymer CVD deposition process is depicted in Figure 3.4. First the polymer is vaporised in a furnace after which it either fragments into reactive species, or in vaporised with an initiator. The gas phase species then absorb onto the deposition surface where they undergo polymerisation and form a thin film. There are several related deposition techniques to CVD, depending on the polymer used: some examples include initiated CVD, oxidative CVD, plasma-enhanced CVD, self-initiated CVD, molecular layer deposition, vapour phase deposition and vapour phase polymerisation [228].

While vapour phase deposition removes the constraints exhibited by surface tension effects seen in solution processing, there are other parameters which need to be considered to ensure optimum quality of the conformal coating. Generally, the CVD coating process involves three main steps - transport of reactants from the vapour phase to the substrate, the ‘sticking’ of the reactant molecules to the coating substrate and the reaction of the monomer units with the surface-adsorbed growing chain via the Eley- Rideal mechanism where a gas phase molecule collides and reacts with surface bound molecule. Monomer units and radicals must adsorb to the surface at the same rate at which they are being consumed by the polymerisation reaction. A summary of the governing equations given by Baxamusa is given below[229].

To describe the transport of reactants to the surface, consider molecular flow in a pore. The diffusivity D_i based on kinetic theory is:

$$D_i = \frac{2r}{3} v_i \tag{3.4}$$

where v_i is the mean gas velocity, and r is the pore radius. In this case, transport of reactants to all surface is more difficult through smaller features - as expected for the coating of nanoscale objects. However, the transport of reactants is not the rate limiting step.

The 'sticking' of the reactant molecules to the coating substrate is process where the reactant molecules adsorb irreversibly onto the coating substrate. The likelihood of this chemisorption occurring is known as the 'sticking probability.' This process is very important to control as it dictates deposition conformality. The sticking probability should be low, as it is not desireable to have molecules absorbing freely on every surface - too high a sticking probability results in non-conformal coatings. However, there is a tradeoff, too low a sticking probability results in slow deposition rate. This is why this step is often the rate limiting step in the CVD process.

One must also consider the nature of the free radical. Bulky, stearically hindered radicals affect the sticking probability and therefore the rate of reaction. It is interesting to note that substrate temperature does not affect sticking probability, which is why sample stages tend to not be heated.

Another important considering for conformality is the Knudsen number. The mean free path - the average distance between molecular collisions varies with the inverse of pressure. For example, Parylene deposition pressure is around 100 mTorr, which results in a mean free path of nearly 1 mm. The ratio of the mean free path and feature length scale is known as the Knudsen number *(Kn)*. When Kn < 1 conformal coating occurs as molecular movement is governed by classical diffusion. When Kn > 1, a non conformal coating occurs. A Knudsen number greater than 1 can easily occur for nanoscale features. In order to circumvent this, a low sticking probability is needed.

The rate expression for the reaction between the growing polymer chains and monomer molecules can be given by:

$$rate = k_p C_m \left(\frac{f k_d}{k_t} C_i\right)^{1/2}, \tag{3.5}$$

where k_p, k_d, k_t are the kinetic rate constants for propagation, dissociation and termination steps respectively, C_m is monomer concentration and C_i is initiator concentration, f is initiator efficiency. This is dependant on the chemical potential of the reaction species, and is considered to be secondary to the process, as the rate limiting step is the sticking probability.

The Thiele modulus ϕ frequently appears in analyses of reaction diffusion problems and is defined below

$$\phi^2 = \frac{3\Gamma_i}{4}(\frac{L}{r})^2, \tag{3.6}$$

where γ_i is the sticking probability and L and r are the length and radius of the nanoscale features. The Thiele modulus includes terms for the sticking probability and the feature dimensions and represents the ratio of reaction rate to diffusion rate. Systems with a large Thiele modulus are diffusion limited (kinetic process) and those with a low thiele modulus are reaction limited (thermodynamic process). This also shows that conformal deposition is preferred with the surface reaction rate is lower than gas diffusion rate, and that conformal deposition is hindered when the aspect ratio of a feature is large - such as a nanowire.

In general, polymerisation of CVD polymers occurs through a cross-linking mechanism creating a highly linked network which is robust and resistant to solvents/acids/bases depending on the polymer used. Furthermore, deposition from the gas phase results in a highly conformal coating, which in the case of nanowire encapsulation is highly desirable as this ensures that the voids between the nanowires are filled in with the polymer [220]. Fine control of film thickness is achieved by varying the amount of precursor monomer used. Therefore CVD is an ideal method to produce reproducible thin films that can withstand further processing such as reactive ion etching (RIE) and contact deposition (electron beam evaporation) [70]. In addition, polymer deposition takes place at, or near room temperature, which avoids thermal damage to the coated substrate. This is especially important in nanowires which degrade at around 400 °C.

While CVD processes are unsuitable for high-throughput solution processing such as roll-to-roll processing, CVD processes are nonetheless scalable and relatively straightforward to integrate into existing wafer based processes [228]. CVD polymer are advantageous over solution processed polymers as the absence of solvent excludes the complications that arise from dewetting - where the polymer formulation does not wet the surface of the nanowires adequately, resulting in pin holes and defects in the film. CVD polymers are versatile and have found use as dielectric layers in semiconductor devices, functional hydrophobic or hydrophilic coatings, gas separation membranes and barrier coatings [228].

3.5 Flexible nanowire devices

Research into and engineering of various flexible nanowire devices has been frequently reported in literature. Key examples of interesting fabrication techniques and high performance devices are described in this section.

Takahashi et al demonstrate indium arsenide transistors by transferring InAs using contact printing and carrying out subsequent fabrication steps on a Si wafer coated with polyimide. The polyimide layer was later peeled off from the silicon, with the device [34]. Similarly, Kim *et al* demonstrated a flexible field effect transistor by depositing gold electrodes onto parylene,

polyimide and alumina substrates, and aligning the nanowires between the electrodes using an electric field [35]. For both methods, the devices were later coated with an encapsulation layer of poly(methyl methacrylate) (PMMA) in order to protect them, and help them adhere to the flexible substrate. Sun *et al* made use of contact printing to transfer nanowires from their growth substrate to a PDMS, polyurethane (PUE) and poly(ethylene terephthalate) (PET) substrates where they were fabricated into logic circuits [36].

InGaAs solar cells-on-graphene have been produced Mohseni *et al* using direct Van de Waals epitaxy - they obtained a power conversion efficiency of 2.51% [208]. GaAs solar cells on polyimide were produced by Han *et al*, where they were able to fabricate a devices with a power conversion efficiency of 1.6% [37].

Chen *et al* demonstrated flexible photodetectors fabricated from InP and GaP nanowire arrays. The nanowires were grown using a thermal evaporation method, dispersed in solvent then transferred using contact printing onto flexible PET subsstrates for subsequent device fabrication. They obtained a responsivity of 779.14 AW^{-1} at 2V bias [38]. Duan demonstrated a flexible single nanowire InP photodetector by dispersing n-doped InP nanowires in solvent, and spin coating them onto mica. After using electron microscopy to locate the nanowires, contact pads were patterned using photolithography. They obtained a responsivity of 1900 AW^{-1} at a bias of 1V [230].

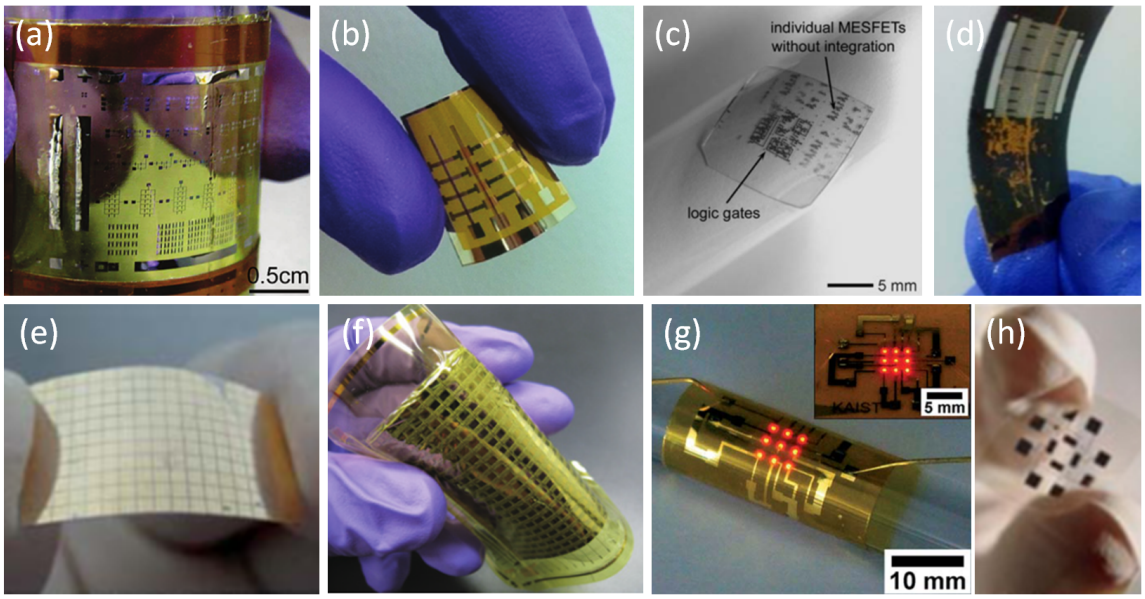

Fig. 3.5: Examples of flexible nanowire devices in the literature. Images used from: (a) InAs FET on PI substrate [34], (b) PbS FET on kapton substrate [35], (c) GaAs logic circuit on PET [36], (d) GaAs solar cell on PI [37], (e) InP photodetector on PET [38], (f) Artificial skin made from Ge/Si core-shell nanowires on Parylene C and PI [188], (g) self-powered AlGaInP nanowire LED by piezoelectric nanogenerator on PET [231], (h) silicon nanowire gas sensors on PET [218]

Chen *et al* demonstrated flexible photodetectors fabricated from InP and GaP nanowire arrays. The nanowires were grown using a thermal evaporation method, dispersed in solvent then transferred using contact printing onto flexible PET subsstrates for subsequent device fabrication. They obtained a responsivity of 779.14 A W^{-1} at 2V bias [38]. Duan demonstrated a flexible single nanowire InP photodetector by dispersing n-doped InP nanowires in solvent, and spin coating them onto mica. After using electron microscopy to locate the nanowires, contact pads were patterned using photolithography. They obtained a responsivity of 1900 A W^{-1} at a bias of 1V [230].

By changing the nanowire material used, several other opto-electronic devices can be made, depending on the electrical, optical and materials properties of the nanowire. For example, the piezoresistance observed in silicon nanowires can be used fabricate stress sensors[232]. Silicon/germanium core/shell nanowires have been used as active matrix circuitry for artificial skins [188]. Piezoelectric nanowires such as ZnO can be used to make nanogenerators [198]. Polymer nanowires have been used as sensitive gas and chemical [205]. Flexible light emitting diodes (LEDs) based on GaN nanowires have been frequently demonstrated in the literature [189].

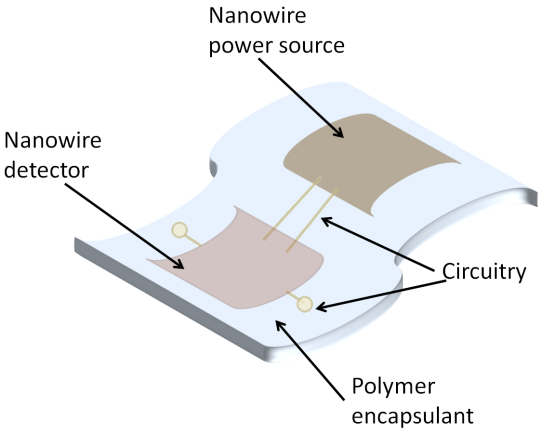

Fig. 3.6: Schematic showing a general flexible fully integrated nanosystem. This consists of a nanogenerator such as piezoelectric, photovoltaic, battery supercapacitor to drive the nanowire sensor, all embedded in a flexible polymer

Ultimately, the aim is to integrate all these discrete flexible nanodevices to form a fully integrated nanosystem. Jeong *et al* have fabricated a self-powered light emitter. The nanosystem consists of an AlGaInP LED and a piezoelectric energy harvester with the aim of creating a fully self powered system for implantable applications [231].

3.6 Conclusion

In conclusion, research interest in flexible devices has been growing steadily for the past 40 years due to the need of devices to be lightweight, portable, and bendable. This enables electronics

used in environments where traditional wafer-based electronics are unsuitable. Developments in nanostructure growth and thin film fabrication have driven the development of low cost devices without sacrificing device performance. This approach combines high performance inorganic components with flexible organic components thus harnessing the benefits of both materials systems.

While there have been several impressive examples of flexible nanowire devices discussed in literature — including highly efficient solar cells, high sensitive photodetectors and stretchable LEDs, it must be noted that the majority of these devices use planar nanowire arrays, and there is a distinct lack of flexible devices based on vertically aligned nanowires. As has been discussed in Chapter 2 — the vertical alignment of nanowires arrays is inherently important for device performance as arrays experience enhanced light scattering, trapping and absorption, as well as efficient carrier collection. This all leads to nanowire devices with higher performance than that of their thin film counterparts.

One limiting factor for truly flexible, substrate-free vertically aligned nanowire devices if the notable lack of a method to *both* encapsulate *and* cleanly remove the nanowires from their growth substrate whilst retaining their vertical alignment. The aim of this thesis is to adapt these existing design principles for nanowire devices to successfully engineer a flexible, substrate-free devices based on vertically aligned nanowires.

Chapter 4

Experimental Methods

This chapter describes the experimental techniques used to fabricate and characterise nanowire-polymer devices in this thesis.

Nanowire growth recipes for vapour-liquid-solid (VLS) InP and VLS GaAs nanowires used in later chapters are described in Section 4.1 and refer to nanowires used to Chapters 5-8. The nanowires were grown by Dr Hannah Joyce, Dr Amira Ameruddin and Dr Mykhaylo Lysevych at Professor Jagadish's lab at the Australian National University.

Polymer encapsulation methods for poly(dimethyl siloxane) PDMS, poly(urethane) PUE, poly(vinylalcohol) PVA and Parylene C are described in Section 4.2 and correspond to the results in Chapter 5. Characterisation of the nanowire-polymer thin films using scanning electron microscopy (SEM), energy dispersive X-ray spectroscopy (EDX), atomic force microscopy (AFM) and profilometry is described in Section 4.3 and are used throughout Chapters 5-8. I carried out these measurements at the University of Cambridge.

Single layer and multilayer Terahertz (THz) modulator fabrication by lamination; and characterisation using optical pump–THz probe spectroscopy (OPTP) are outlined in Section 4.4, with the results described in Chapter 5 and Chapter 7. I carried out the modulator fabrication at the University of Cambridge. Dr Jessica Boland and Mr Djamshid Djamry at Professor Michael Johnston's lab at the University of Oxford.

Section 4.5 describes the processes used to optimise and fabricate flexible nanowire test devices outlined in Chapter 8. This includes dry etching, contact deposition, thin film handling. I carried out these processes at the University of Cambridge. IV characterisation of the nanowire test devices is given in Section 4.6. Solar cell characterisation was carried out by Dr Zihyuan Li at Professor Jagadish's lab at the Australian National University.

4.1 Nanowire growth

Nanowire growth was carried out by collaborators at the Australian National University (ANU), after which the nanowires were shipped to Cambridge where they were used to make devices de-

scribed in Chapter 5,6,7 and 8. Nanowires were grown using an AIXTRON 200/4 metal-organic vapour phase (MOVPE) reactor. Vapour-liquid-solid (VLS) grown InP undoped nanowires were used for nanowire-polymer thin film fabrication in Chapter 5 and in Chapter 8 for nanowire test device optimisation and Schottky barrier solar cell fabrication. VLS grown undoped GaAs nanowires were used in Chapters 6 and 7 as Terahertz (THz) polarisers.

Metal-organic chemical vapour deposition (MOCVD) involves using gaseous precursors to deposit a thin layer of material into a growth wafer - a schematic is shown in Figure 4.1. Gases need to be ultra pure and and the amount injected into the chamber must be measured carefully in order to have fine control of nanowire growth. As described in Chapter 2, the orientation of the crystal of the growth wafer and using a nanoparticle catalyst dictates the direction in which the nanowire will grow, and will suppress growth in other directions. Precursors decompose under heat in a process called pyrolysis and the volatile organics are removed from the chamber leaving the inorganic component to bond to the substrate surface and form a new crystalline layer.

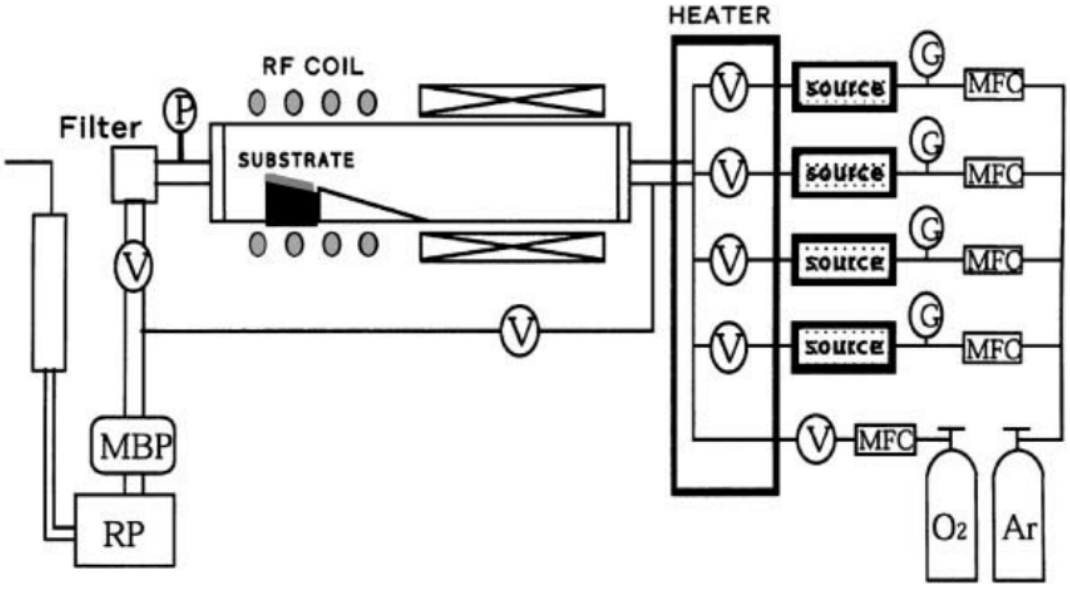

Fig. 4.1: A general schematic of an MOCVD system. Ultra pure gaseous precursors are carefully injected into the growth chamber to deposit a thin layer of material on to a growth wafer. The crystal orientation of growth wafer and using a nanoparticle catalyst dictates the direction of nanowire growth, whilst suppressing material growth in other directions. Image adapted from [233]

4.1.1 VLS — InP

InP nanowires were grown using the VLS method with 80 nm gold nanoparticles as catalysts on p+ (111)B-oriented InP substrates at 420°C using a metal-organic chemical-vapour deposition system. The growth time was 20 mins, the flow rate of PH_3 was 4.241 x10^{-3} mol/min, flow

rate of trimethyl indium (TMIn) was $1.214\,x10^{-5}$ mol/min, the V/III ratio was 349.3. These nanowires were grown by Dr Amira Ameruddin.

4.1.2 VLS — GaAs

High-density arrays of GaAs nanowires of diameter 50 nm were grown via gold-seeded horizontal flow MOCVD in the $\langle 111 \rangle$B direction at an angle of 35.3°to the GaAs $\langle 100 \rangle$ substrate. Trimethylgallium was used as the group III precursor, AsH_3 was used as the group V precursor and Au nanoparticles were used to seed the nanowire growth [25]. GaAs $\langle 100 \rangle$ substrates were treated with poly-L-lysine solution followed by a solution of colloidal Au nanoparticles 50 nm in diameter. Nanowire growth occurred at a pressure of 100 mbar and a total gas flow rate of 15 slm. Prior to growth, the substrate was annealed at 600°C under AsH_3 ambient to desorb surface contaminants. The nanowires were grown via a two-temperature process consisting of a brief 1 minute 'nucleation' step at 450°C followed by a prolonged 30 minute 'growth' step at a lower temperature of 375°C [50, 234]. These nanowires were grown by Dr Hannah Joyce and Dr Mykhaylo Lysevych.

4.2 Flexible nanowire-polymer thin film fabrication

In Chapter 5, VLS grown InP nanowire wafers were cleaved into roughly 10mm x 10mm pieces prior to being coated with polymer. Solution processed (poly(dimethyl siloxane) (PDMS), poly(urethane) (PUE), poly(vinylalcohol) PVA) and chemical vapour deposition (CVD) Parylene C polymers were used to encapsulate the nanowires to form nanowire thin films. A 5 µm layer of Parylene C was used. These films were then characterised using scanning electron microscopy (SEM) , atomic force microscopy (AFM) and UV-Vis Spectroscopy and profilometer as described in Section 4.3.

In Chapter 8, VLS grown InP nanowire wafers were cleaved into roughly 10mm x 10mm pieces prior to being coated a 3 µm layer of Parylene C. Prior to subsequent device processing, the films were then characterised using SEM, (energy dispersive X-ray spectroscopy) EDX, AFM and UV-Vis Spectroscopy and profilometer as described in Section 4.3.

In Chapters 6 and 7, VLS grown GaAs wafers were not cleaved prior to coating with Parylene C. The GaAs nanowires were coated with 5 µm of Parylene C, the wafer was scored into smaller squares, and the thin films were removed as needed. For further details, please refer to Section 4.4.

4.2.1 Solution processed polymers

All polymers and solvents were used as received without any further purification. Solvents were purchased from Fisher, all reagent grade.

Spin coating was used for polymer deposition as it is a straightforward, repeatable method of depositing thin films of polymer onto a flat substrate. As shown in Figure 4.2, a spin coater consists of a rotating stage where the sample is mounted, and the spinning motion is used to spread a thin film into the sample surface. The spin speed, acceleration and time can be controlled, though ultimately, the quality of the thin film is heavily dependant on careful formulation chemistry. All polymers was dynamically spun - where the spin coater is allowed to reach a pre-defined speed before depositing the material onto the spinning substrate. The material is spread across the substrate by centrifugal force. Generally, the faster the spin speed and the more dilute the formulation, the thinner the resultant film is.

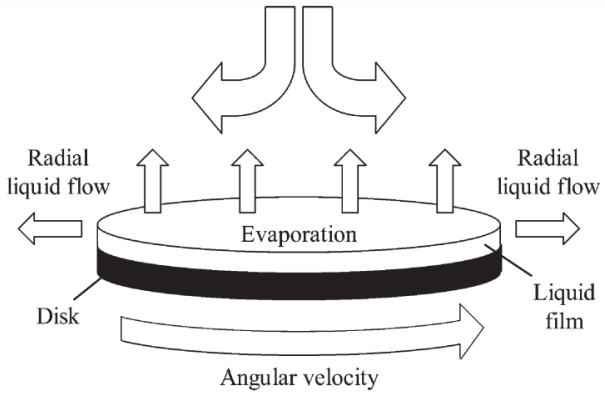

Fig. 4.2: Schematic of the spin coating technique. Solution-based material is deposited on to a spinning substrate and is spread in an even layer across the substrate by centrifugal force. Fine control of film thickness and quality is obtained from the formulation. Imaged adapted from [235].

PVA (Sigma Aldrich, $M_w = 100,000$ was mixed 5 % and 10 % (w/w) in deionised water and stirred at room temperature using a magnetic stirrer bar for 2 hours until dissolved and homogeneous PVA formulations were spin coated at 1000 - 4000 rpm using a spin coater on vertically aligned GaAs nanowire substrate. The films were then baked at 95 °C for 1 minute to remove the solvent and polymerise the film. The film was the cooled to room temperature, then removed from the substrate by loosening the edges of the film with a razor blade, then peeling off the film using tweezers.

Sylgard 184 (Dow Corning) was mixed in a proportion of 1:10 curing agent:base, as per the manufacturer's instructions. The mixture was stirred using a stirrer bar for 15 minutes until homogeneous. The formulation was used immediately for spin coating, as polymerisation starts

to occur when the curing agent is added to the base. To dilute the film, toluene was added to the base/curing agent mixture prior to stirring, and the whole mixture was stirred for 15 minutes, until homogeneous. 10% and 50% elastomer formulations in toluene (w/w) were made up. All PDMS formulations, were spin coated from 1000-4000 rpm using a spin coater on a vertically aligned GaAs nanowire substrate. The films were left to polymerise at room temperature for 24 hours, after which they were removed by loosening the edges of the film with a razor blade, before pulling off the film using tweezers.

ClearFlex90 (Smooth-On) was mixed in a 2:1 base:curing agent ratio, as per the manufacturer's instructions and stirred using a magnetic stirrer bar for 15 minutes until homogeneous. To dilute the formulation, 10 % and 50 % (w/w) formulations were made using toluene, which was added prior to stirring. then stirred for 15 minutes until homogeneous. All formulations were used immediately. The PUE formulations were spin coated at 1000-4000 rpm on to a vertically aligned GaAs nanowire substrate and were then left to polymerise at room temperature for 24 hours. The thin films were removed by using a razor blade to loosen to the edges of the thin film, which was then peeled off using tweezers.

4.2.2 CVD Polymers

Parylene C was deposited using the Gorham process which is widely used to deposit different parylenes. As shown in Figure 4.3, the Gorham process is a low pressure chemical vapour deposition (LPCVD) process[236]. Dichloro[2.2]-paracyclophane dimer (DPX C, lot 08F16015, SCS Coatings) was the dimer used. The dimer undergoes sublimation (T= 130 °C) and pyrolysis (T=650 °C) before condensing and polymerising at room temperature onto the substrate (furnace T = 690 °C, evaporation T = 170 °C). The process takes place at approximately 10^{-2} mbar. The weight of dimer was directly proportional the thickness of the film deposited. 3 g of dimer yielded a 5 µm thick film, 1.2 g yielded a 2 µm, 0.7 g yielded a 1 µm

After deposition, the film was removed by gently loosening the edge of the film from the substrate using scalpel, then peeling off the sample using tweezers to grip the edge of the polymer film - as with the other polymers. An alternative method for releasing the film was to delaminate the edge of the film using a scalpel, then submerge the film in water. After a few minutes, the film would float to the top of the water and could be dried and used.

4.3 Flexible thin film characterisation

Profilometry, SEM, AFM and EDX were all used to characterise the nanowire-polymer thin films. Schematic diagrams of each of the techniques are given in Figure 4.4

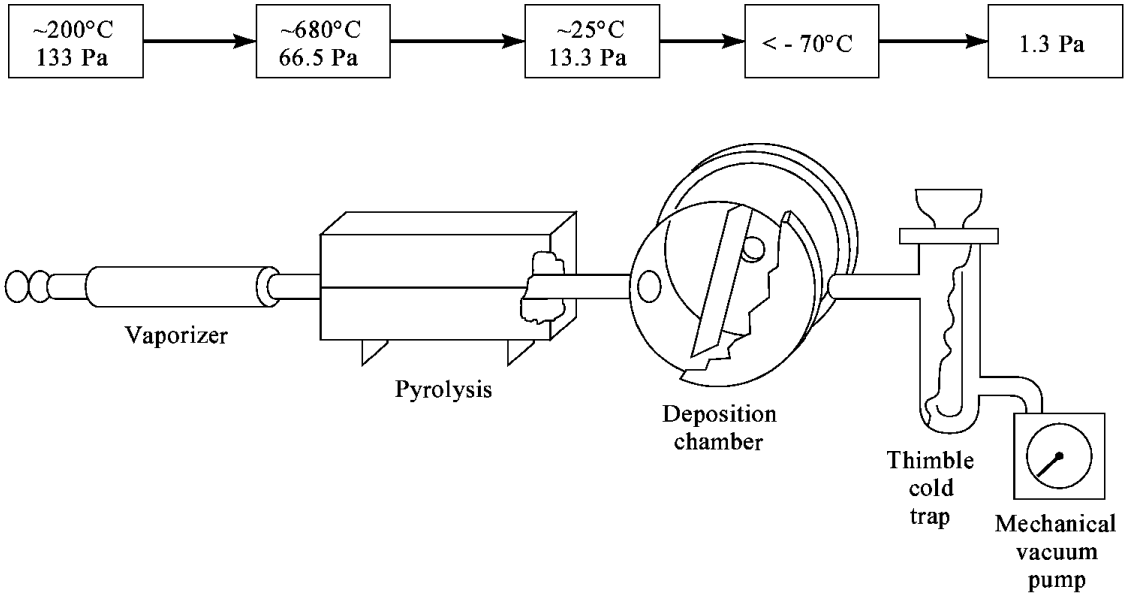

Fig. 4.3: Schematic of the Gorham process for Parylene deposition - a low pressure chemical vapour deposition process. The Parylene precursor, in dimer form undergoes sublimation and pyrolysis before condensing and polymerising at room temperature on the substrate, to form a conformal coating. Image adapted from [237]

A Dektak profilometer was used for simple thickness measurements. Parylene build up on the inside of the deposition chamber can revapourise and re-deposit, hence regular measurements were important to check the thickness of the nanowire film to ensure reproducibility for the subsequent processes. The measurement itself is straightforward: there is a fine tip which runs across the surface of the sample and assess the film roughness and thickness. Profilometry is reliable to around 100 nm after which it is sensible to use AFM.

A Bruker atomic force microscope was used to determine the surface morphology and to confirm that the parylene coating is conformal. A piezoelectric element oscillates the cantilever where an atomically sharp tip is attached to one end of the cantilever. As the tip is moved over the sample, the detector records the deflection and motion of the cantilever. The interaction between tip and sample, which occurs on the atomic scale is translated into changes of the motion of cantilever, which occurs on a larger scale. The deflection of the tip, the amplitude of the oscillation of the cantilever, or the shift in resonance frequency of the cantilever can all be used to quantify cantilever deflection. This is converted into electrical signal by the detector where the intensity of this signal will be proportional to the displacement of the cantilever. This is then converted into an image where colour represents the recorded signal

A Zeiss Sigma scanning electron microscope was used to characterise the surface morphology of the nanowires and the nanowire thin films. The flexible nanowire-polymer thin films were sputter coated with a thin layer of Au/Pd alloy (55mA, 3s) to render them conductive for the

SEM measurements. The surface of the sample is raster scanned by a focused electron beam. The electrons interact with atoms at various depths within the sample, which produce secondary electrons. The signals arising from these secondary electrons contain information about the topography of the sample. The beam's position is combined with the detected signal to produce an image. Depending on the operating conditions, SEM can achieve very high-resolution images of a sample surface, revealing details less than 1 nm in size. The in-lens detector was used for these images. An accelerating voltage of 3 kV was used for the polymer samples and 5kV used for the nanowires, to prevent charging and working distances of 4-8 mm were used for optimum resolution.

Energy dispersive X-ray spectroscopy was also used in conjunction with SEM to gain understanding of the elemental composition of the surface. X-rays are emitted when the electron beam removes an inner shell electron from the sample, causing a higher-energy electron to fill the shell and release energy. These X-Rays are related to the atomic number of the element, and hence it is possible to use these X-rays to identify the composition and measure the abundance of elements in the sample. An accelerating voltage of 1 kV was used to obtain enough signal and elemental maps were acquired for a minimum of 15 minutes, to up to 30 minutes to obtain enough information [238].

4.4 THz Polarisers

VLS grown GaAs nanowires used to fabricate single layer and multilayer THz polarisers. The polarisers were characterised using SEM (described in Section 4.3) and OPTP spectroscopy.

4.4.1 Fabrication

VLS grown GaAs nanowires (Section 4.1) were examined under the SEM, prior to polymer coating, to establish the general orientation of the nanowires. This direction was marked on the back of the wafer. PDMS and Parylene C were used to encapsulate the nanowires.

The PDMS used was undiluted and was mixed according to the manufacturer's instructions (10:1 base: curing agent) and was spin coated onto the nanowire wafers at 250 rpm, then baked at 150°C for 5 minutes, to yield 300 µm films of PDMS.

A 5 µm layer of Parylene C was coated using the Gorham process in a PSD 2010 LabCoter2 chamber [242]. The polymer thin films were peeled off from the substrate and these films were divided into equal sized segments using a razor blade to form 10 mm $\times$ 10 mm squares. These individual squares were measured as single layer modulators.

Multiple layer samples were fabricated by layering nanowire-Parylene C thin films together whilst carefully preserving the alignment of the nanowires and laminating these layered thin

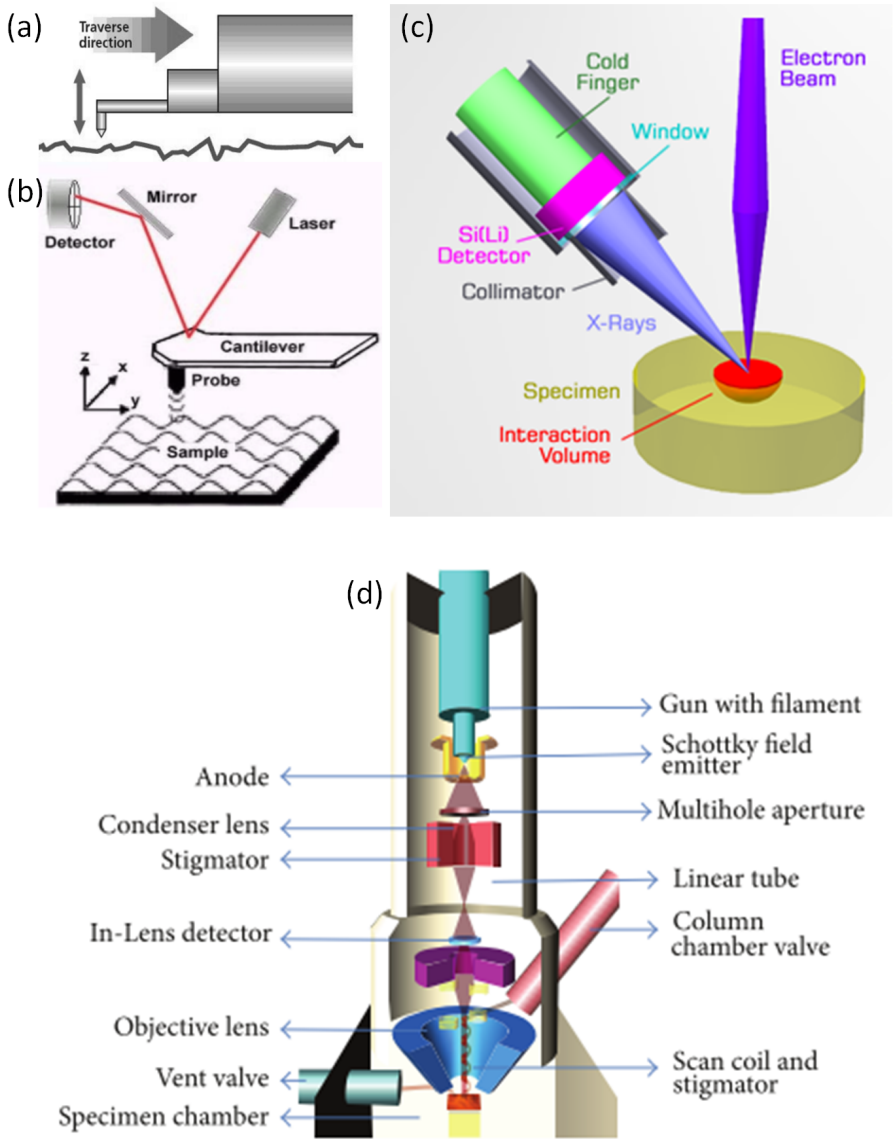

Fig. 4.4: Schematic diagrams of profilometry, SEM, AFM and EDX, which were used to characterise the nanowire-polymer thin films. (a) Profilometry — a fine tip scans the sample surface to assess the film roughness/thickness . (b) AFM — a piezoelectric element oscillates a cantilever with an atomically sharp tip. The deflection and motion of the tip corresponds to the surface morphology of the sample, which is ultimately converted into an image. (c) EDX — X-rays are emitted when the electron beam interacts with the sample electrons, which are characteristic to the atomic number of the element, this enabling identification of the composition and relative abundance of elements in the sample. (d) SEM - the surface of a conductive sample is raster scanned by a focused electron beam, which produces secondary electrons that contain information about the topography of the sample. This can be used to produce an image. Images adapted from [238–241].

films at 120° C and 20 bar using an Obducat nano-imprinter, depicted in Figure 4.5. Nanowire polarisers consisting of 1, 4, 8 and 14 layers were fabricated and characterised. This was to eliminate any air gaps which may be detrimental to modulator performance, and for ease of handling.

The PDMS-nanowire thin films did not need to be hot bonded as the PDMS thin films are inherently tacky due to Van de Waals interactions and therefore the films bonded together without the need for hot bonding. However, given the thickness of the PDMS films, only 1,2,3 and 4 layer films could be fabricated. Films thicker than 4 layers were mechanically unstable.

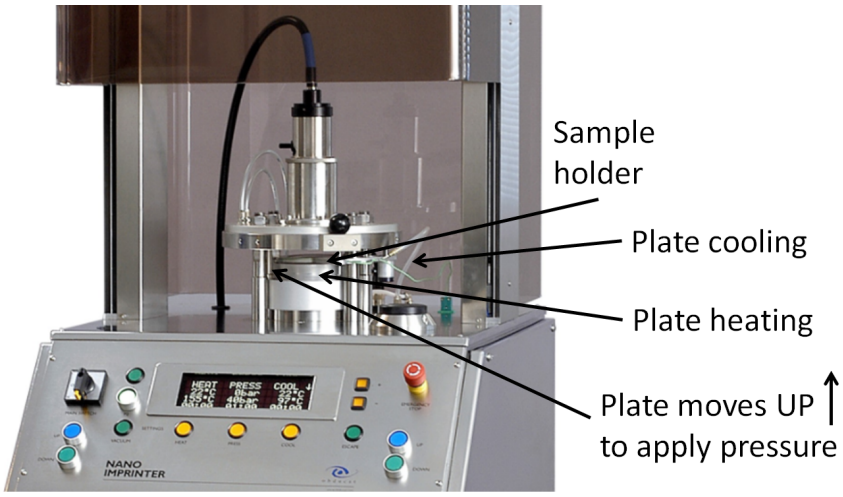

Fig. 4.5: Schematic of the nanoimprint system laminate the Parylene stacks together. The Parylene stacks were mounted between the two parallel plates, which are able to come into contact with each other. Heat and pressure were then applied to the Parylene stack through these parallel plates, resulting in lamination of the film. Image was adapted from [243].

4.4.2 Optical-Pump–Terahertz-Probe Spectroscopy

Firstly, all the experiments were carried out under vacuum to avoid any absorption of the THz radiation by atmospheric water vapour and the nanowire modulators were placed in the OPTP system, such that the long axes of the constituent nanowires were oriented vertically. These measurements were carried out by Dr Jessica Boland and Mr Djamshid Djamry.

A schematic diagram of the OPTP system is depicted in Figure 4.6. An amplified Ti:Sapphire laser with an average power of 4 W was used to generate 35 fs pulses at a 5 kHz repetition rate and centre wavelength of 800 nm. Each pulse was separated into 3 paths: 590 microJ/pulse was used as an optical pump with a beam width of 5 mm to photoexcite the nanowire polarisers; 200 microJ/pulse was used to generate the THz probe pulse by optical rectification in a 2 mm $\langle 110 \rangle$ GaP crystal, giving a THz beam width of less than 1 mm at the nanowire film; and 1.6 microJ/pulse to act as a gate beam for electro-optical sampling of the THz field via a 200 μm $\langle 110 \rangle$ GaP crystal.

OPTP was used to measure the transmission of the electric field of the THz probe pulse through the nanowires, E, as a function of frequency. The electric field transmitted through the sample without photoexcitation (at equilibrium) is given by E_{off} and with photoexcitation as E_{on}. The photoinduced change in THz transmission through the nanowires is denoted as $\Delta E = E_{\text{on}} - E_{\text{off}}$. I define $t = 0$ to be the pump–probe delay at which $-\Delta E/E_{\text{off}}$ is maximum [50]. The THz electric field was measured using a balanced photodiode circuit and a lock-in amplifier referenced to a chopper at 2.5 kHz in the THz generation beam, while the optical pump-induced change in the THz electric field was measured using a second lock-in amplifier reference to a chopper at 125 Hz in the optical pump beam.

In order to assess modulator performance and establish E_{off} and E_{on} I measured $\frac{\Delta E_{on}}{E_{off}}$ as a function of pump polarisation. The polarisation of the photoexcitation beam was rotated, while fixing the orientation of the nanowire modulator and the THz beam. The polarisation of the photoexcitation beam is selected via a half-wave plate. By rotating the half-wave plate by an angle of θ, the polarisation of the optical pump beam was altered by an angle of 2θ. Thus, by rotating the half-wave plate by 45°, the optical pump beam was rotated from vertical polarisation to horizontal polarisation.

In order to assess the switching speed, $\frac{\Delta E_{on}}{E_{off}}$ was measured as a function of pump probe delay. The long axis of the nanowires in the modulator, the photoexcitation beam and the THz beam were all aligned. For both experiments we also varied the fluence to investigate the fluence dependence on modulator performance. In order to obtain a range of fluences up to 280 μJ cm^{-2}, the optical pump beam was attenuated using neutral density filters.

In order to assess the broadband response of the modulators $\frac{\Delta E_{on}}{E_{off}}$ was measured as a function of THz frequency.

4.5 Optimising the fabrication of flexible nanowire diodes

VLS grown InP nanowires used to develop the fabrication method for a flexible substrate-free nanowire solar cell. The dry etching, this film handling and contact deposition steps were optimised, and the test devices were characterised using a probe station.

4.5.1 Dry etching

Dry etching was used to selectively remove the Parylene C, to expose the nanowire tips ready for contacting. Dry etching generally works by using an radio frequency (RF) source to generate, in this case, oxygen plasma (though, depending on the material that needs to be etched, different process gases may be used).

The oxygen plasma accelerates high energy ions which strike the substrate and either remove the material using a physical process (the force of hitting the sample forcibly knocks out and removes the surface molecules) or a chemical process (the ion hits sample, reacts with the surface

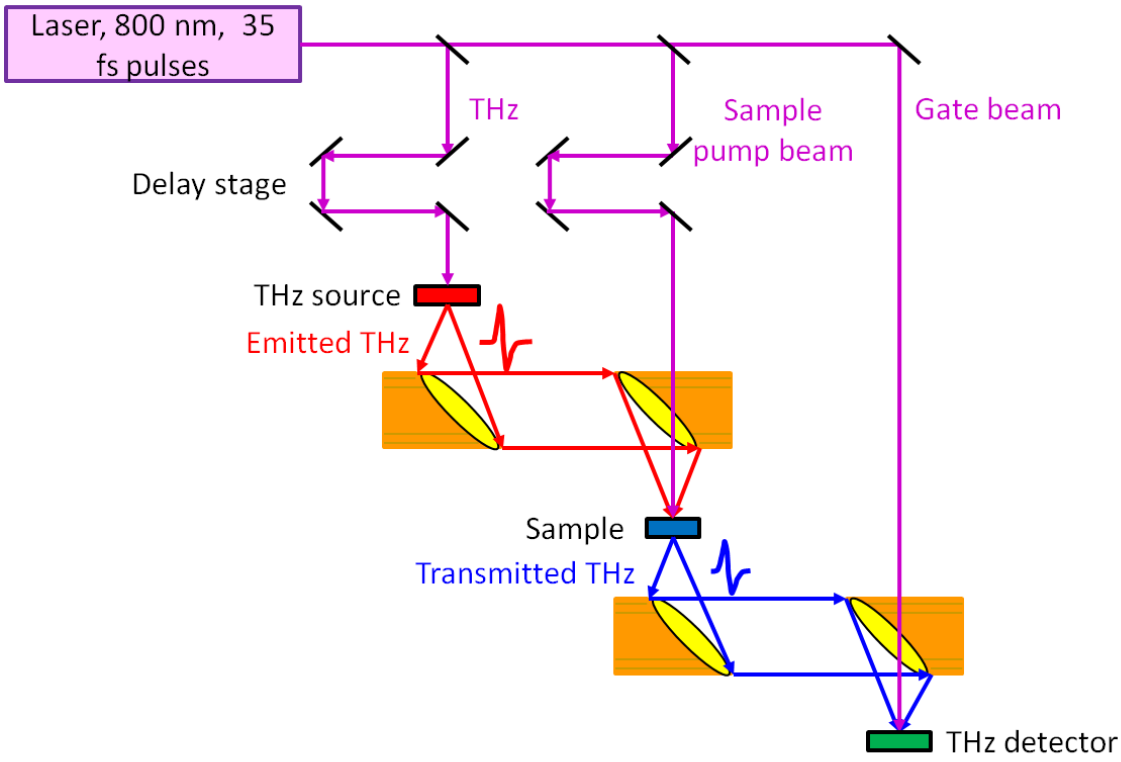

Fig. 4.6: Schematic diagram of the OPTP system used to characterise THz polarisers. An amplified Ti:Sapphire laser was used to generate femtosecond pulses. Each pulse was separated into 3 paths: an optical pump to photoexcite the nanowire polarisers, a pulse to generate the THz probe pulse by optical rectification, and a pulse to act as a gate beam for electro-optical sampling of the THz field.

molecules and the new compounds diffuse away). Whether the physical or chemical removal process occurs depends on the chamber conditions: process pressure, gas type used, gas flow rate, reactive ion etching (RIE) power and etching time.

For this study, Philips RIE, Diener etcher and the Barrell etcher were all tested to determine which system was the best to use for the fabrication process. The Diener and the Barrell etchers are both simple oxygen plasma systems, the Philips is a reactive ion etching system which allows for greater control of parameters - as outlined in Table 4.1. In addition, the electrode shapes were different for all three etching systems, which also affected the degree of anisotropy achieved in the etching, as shown in Figure 4.7. The oxygen plasma etching machines (Barrel and Diener etcher) have a curved electrodes, where as the Philips RIE uses a flat electrode.

4.5.2 Bottom contact deposition

Thermal evaporation and electron beam evaporation were used for bottom contact deposition.

Cr/Au contacts were used for initial devices, and was deposited using thermal evaporation. As shown in Figure 4.8(b), the metal target is heated by passing a large current through a resistive

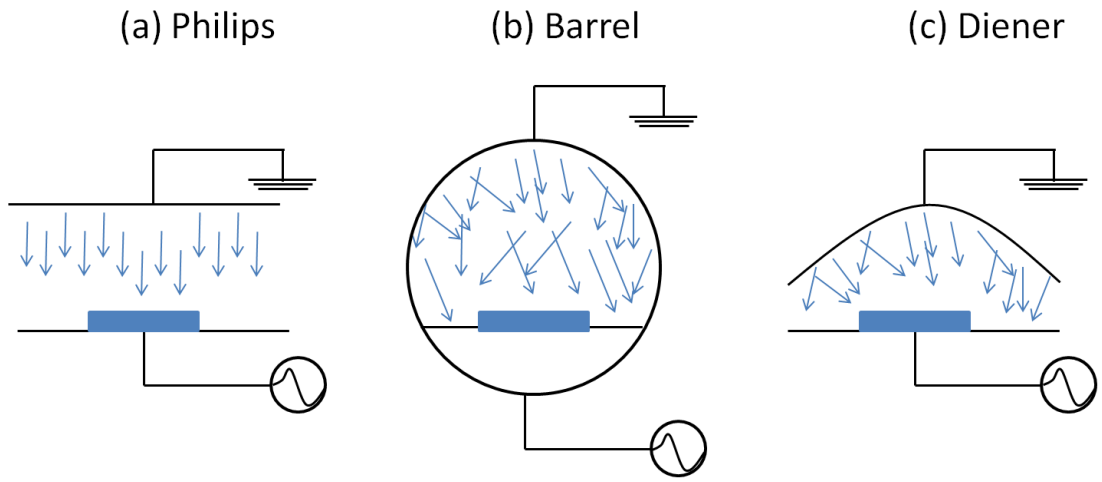

Fig. 4.7: Schematic of the etching regimes obtained from the different etchers tested in dry etching optimisation. (a) Phillips RIE - which offered greater level of control of parameters and anisotropic etching. (b) Barrel etcher and (c) Diener etcher both gave isotropic etching.

Etcher	**Parameters**	**Electrode**	**Etching regime**
Diener	Time, power	Curved	Isotropic
Barrell	Time	Curved	Isotropic
Philips	Time, power, gas flow rate, process pressure	Flat	Anisotropic

Table 4.1: Table summarising the outcomes of the initial RIE tests. Different etchers resulted in different etching regimes. It was found that the Philips RIE gave the best results, going forward.

basket containing a metal source. The metal evaporates and is deposited onto the substrate. Fine control of the deposition rate and final metal thickness is controlled by adjusting the applied voltage. 10 nm of chromium followed by 100 nm of gold was applied as contacts. However, as the contacts could not be annealed, a cleaner deposition process was needed to make high quality contacts.

Electron beam evaporation was then used for Ti/Au contacts. As shown in Figure 4.8(a), an electron beam is used to heat up a crucible containing the source metal, which is also evaporated and deposited in a controlled manor on the substrate. The deposition chamber was pumped overnight to achieve a pressure of 5 x 10^{-7} Torr to ensure the chamber was as clean as possible to offer higher quality metal thin films. The deposition rate for the Ti and the Au was 0.1 Å/s was used for the Ti, a rate of 1 Å/s was used for the gold deposition, to ensure uniform deposition. 10 nm Ti and 100 nm Au were deposited and the contacts were not annealed.

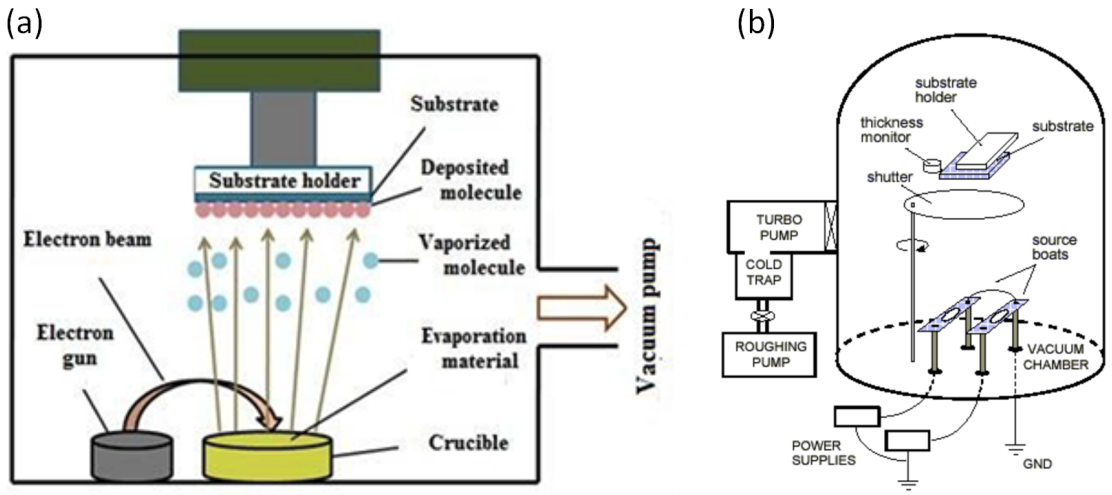

Fig. 4.8: Schematic diagrams of (a) electron beam and (b) thermal evaporation. (a) Electron beam evaporation was used to deposit Ti/Au contacts. An electron beam is used to heat up a crucible containing the source metal, which is evaporated and deposited in a controlled manor on the substrate. Adapted from [244]. (b) Thermal evaporation was used to deposit Cr/Au contacts. A metal target is heated by passing a large current through a resistive basket containing a metal source. The metal is evaporated and deposited in a controlled manor on the substrate. Adapted from [245]

4.5.3 Thin film handling

After bottom contact deposition, the thin film was peeled off from the substrate and backed onto a tacky PDMS slide to ensure the sample remained flat from top contact deposition. The edges of the sample were isolated with kapton tape, to prevent short circuiting of the device.

The tacky glass slide was prepared by mixing PDMS (Sylgard 184, Dow Corning) according to the manufacturer's specification (10:1 base: curing agent) and spin coating at 500 rpm to create a thin film on the glass slide. This was then baked at 180 °C for 2 minutes on a hotplate to polymerise. The PDMS glass slide was activated using oxygen plasma (Diener etcher, 2 minutes) which activated the surface and provided a tacky coating which allowed the nanowire thin film to be backed onto it and lay flat.

4.5.4 Top contact deposition

The nanowire tips were passivated, then coated with an indium tin oxide (ITO) top contact. For passivation optimisation, hydrochloric acid (HCl, reagent grade, Sigma, 37%), and ammonium sulfide ($(NH_4)_2S$, reagent grade, Fisher, 20% in H_2O was used. HCl was diluted to 10% 20% and 50% of the 37% concentration with deionised (DI) water and the nanowires were etched for 30s, 1min, 2min. $(NH_4)_2S$ was diluted 10:1 in H_2O:$(NH_4)_2S$ and were etched for 1min, 2min, 5min, 7min. After etching, the nanowires were rinsed with DI water and left to dry out on a hotplate at 40°C for 5 minutes. The passivation and rinsing steps were carried out immediately before loading the nanowire samples into the evaporation chamber, to ensure the oxide layer

would not form again. The effect of passivation was investigated once the contacts had been applied and the sample's IV curve could be measured.

For top contact deposition, ITO was deposited via sputter coating. Gas molecules hit a target where material is ejected and deposited onto a substrate as shown in 4.9. The recipe used was for 100 nm of ITO was 30 sccm Ar, for 1072 seconds at 50 W, with a 300 s pre-sputter time.

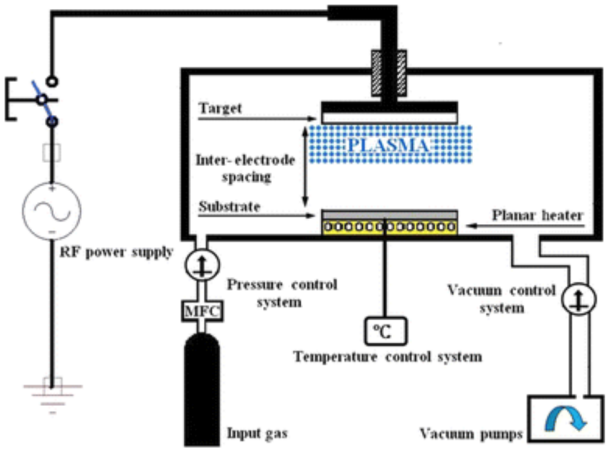

Fig. 4.9: Schematic diagram of an ITO sputter coater. High energy gas molecules hit an ITO target where material is ejected and deposited in a controlled manner onto a substrate. Adapted from [246]

4.6 Nanowire device characterisation

Characterisation of the test devices were carried out in Cambridge. IV curves were measured by backing the Ti/Au side of the test device to copper tape and the dark current was measured using a Cascade probe station. The positive and negative terminals were applied to the Ti/Au and ITO sides respectively. Care was taken to lower the probes gently onto the thin film to avoid puncturing and therefore short circuiting the device. A compliance of 1 mA was used for safety.

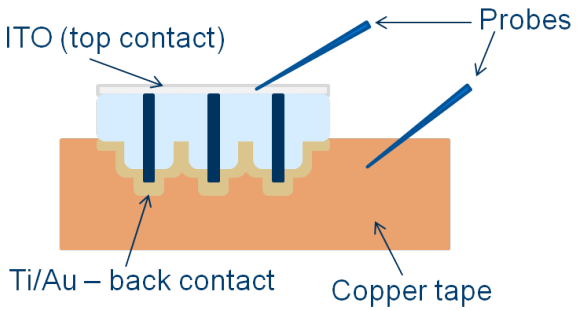

Fig. 4.10: Schematic diagram of the probe station used to characterise the nanowire test devices. The nanowire devices were backed onto copper tape, and the positive terminal was placed on the copper tape, the negative terminal was placed on the ITO side to measure the dark IV curves.

The Schottky barrier solar cell was shipped to Australia and the characterisation was carried out by Dr Ziyuan Li. The samples were measured using an Oriel solar simulator under AM 1 sun with a spot size of 11 µm. Samples were backed onto copper tape for ease of measurement (Ti/Au side).

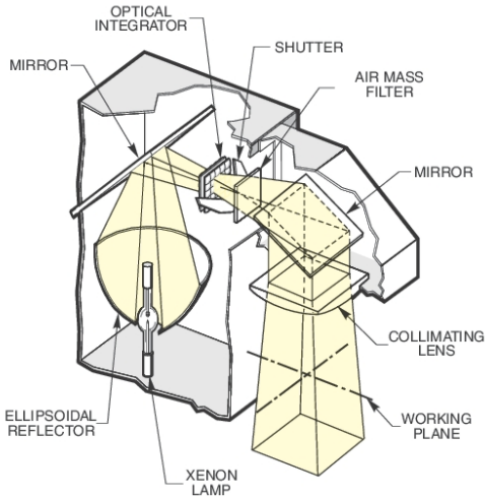

Fig. 4.11: Schematic diagram of a solar simulator used to characterise the Schottky barrier solar cell. Adapted from [247]

Chapter 5

Nanowire-Parylene C Thin Films

This chapter addresses how I fabricated and characterised the III–V nanowire–Parylene C thin films. A brief overview of why pre-existing techniques of flexible nanowire device fabrication is given, followed by a summary of the uses, limitations and benefits of solution processed polymers and chemical vapour deposition polymers. I present my results on coating vapour-liquid-solid (VLS) grown nanowires with several solution processable polymers (poly(dimethylsiloxane) (PDMS), poly(urethane) (PUE) and poly(vinylalcohol) (PVA) and Parylene C and find that the nanowire-Parylene C thin films give the best results. The Parylene family of polymers - their chemical vapour deposition (CVD) process, the mechanism of polymerisation (free radical addition) - are then all discussed to show why they are suited for this application. Preliminary work on encapsulating selective area epitaxy (SAE) grown nanowires is also discussed. I concluded the chapter by stating why Parylene C was particularly suited for device fabrication and detail how these thin films were used to make devices described in Chapters 6, 7 and 8. This chapter was an integral part of this thesis as it demonstrated a key concept: this straightforward method of producing nanowire-polymer thin films makes it possible to fabricate a variety of flexible devices, simply by varying the choice of nanowire material used.

5.1 Embedding nanowires in polymer

As discussed in chapters 2 and 3, while nanowire on-substrate devices have been demonstrated frequently throughout the literature [23], there has been a noticeable lack of high performance, flexible, substrate-free nanowire devices [112]. Several difficulties arise when attempting the fabrication of these devices - embedding, growing or dispersing the nanowires in a flexible material, forming high quality, low resistance contacts and ensuring these devices are sufficiently robust. Whilst various methods have been demonstrated they all have limitations. Dispersing nanowires in polymer and coating the formulation onto a flexible substrate does not make use of the carefully grown vertical nanowire alignment which is highly beneficial for high performance devices [52, 215]. Electrospinning aligned nanowire-polymer mats only maintains nanowire

alignment if the nanowire diameter is a similar to that of the electrospun fibre - the fibre diameter essentially forces the nanowires to orient in the same direction [219]. Vertically aligned nanowires grown on a flexible substrate are limited to low temperature growth which may impact on the quality of the nanowire [212]. Developing a method of embedding the nanowires in a polymer matrix that is easy to remove from the substrate without leaving an organic residue behind, does not contribute to transmission losses, maintains the vertical alignment of the nanowires and is flexible would be an immense contribution to the field, as to our knowledge, no method has been found which adequately fulfils all of these criteria. Use of the polymer as an encapsulant also has the added benefit of protecting to the delicate nanowires from damage, acting as an insulating layer between the top contact and bottom contact, thus preventing short circuiting of the device and could potentially enable reuse of the expensive growth substrate [248].

Choice of encapsulation polymer relies on its materials properties to retain its flexibility. Commercially available photoresists such as Cyclotene 3022-57 (benzocylcobutene (BCB)) and Shipley S1808 are frequently used to planarise nanowires, but these are brittle and cannot be lifted off the substrate [48, 222]. Given that they are designed to form highly level, robust coatings, it is evident that these are not suitable materials for flexible device fabrication. Chapter 3 addressed the difference between chemical vapour deposition (CVD) and solution processed polymers. To summarise, CVD polymers are deposited in the gas phase and form a highly conformal coating, solution processed polymers are deposited in the solution phase and form highly planar films. Both types of polymers have their merits and weaknesses, and both require careful control of deposition parameters to form high quality thin films.

5.2 Solution processed polymers

The following solution processable organic polymers were used to fabricate nanowire-polymer thin films: poly(dimethyl siloxane) (PDMS), poly(urethane) (PUE) and poly(vinyl alcohol) (PVA) [249]. Vapour-liquid-solid (VLS) grown InP nanowires were used for these tests due to their straightforward growth process. No time consuming electron beam lithography (EBL) step is required to pattern the surface, hence several wafers could be grown in quick succession allowing ample samples for optimising this process. The polymers were chosen due to their mechanical flexibility, ease of reformulation (all require common laboratory solvents to disperse) and their transparency in the visible range, in order to minimize losses that arise due to encapsulation. As shown in Figure 5.1, the chemical structures of each polymer are very different. As a result, each polymer exhibits very different wetting and adhesion properties on InP nanowires, which in turn effects the quality of the thin film.

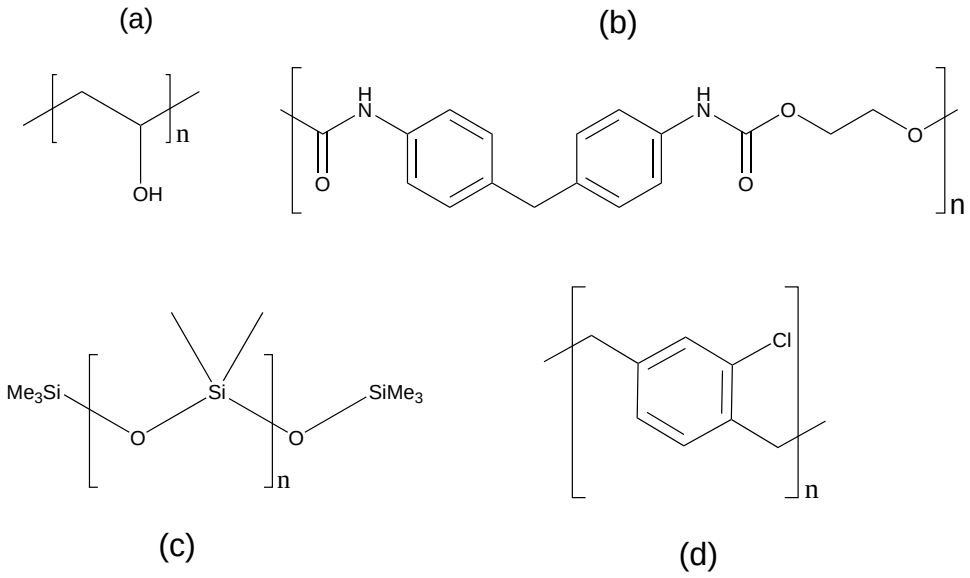

Fig. 5.1: Chemical structures of the polymers used to make polymer–nanowire freestanding thin films: (a) Poly(vinylalcohol) (PVA) (b) Poly(urethane) (PUE) (c) Poly(dimethyl siloxane) (PDMS) (d) Parylene C

PDMS (Sylgard 184) is commercially available as a two part kit; a base and curing agent. These were mixed to together in the manufacturer's recommend ratio, and diluted to required concentration with toluene as PDMS is too viscous to spin coat into a thin film. The resultant formulation was spin coated onto the nanowires, then polymerised at room temperature. PDMS has a low surface energy and normally does not adhere well to surfaces - indeed, it is these low adhesion properties with results in its common use as a casting resin. It was found that using the 50% dilution and spin coating at 1000 rpm (rotations per minute) gave a thickness of around 2.2µm$\pm$0.1µm. While it was found that it was easy to control the thickness and viscosity of the PDMS through reformulation, once polymerised the adhesion of the PDMS to the surface was so great that it could not be removed - contrary to its usual behaviour. This increased adhesion is thought to arise from the high surface area of the nanowires which resulted in stronger interactions with the PDMS and therefore higher surface adhesion. In the process of removing the PDMS thin film, the substrate shattered (remnants of the shattered substrate are clearly visible in the polymer thin film in Figure 5.2) - the polymer films need to have an easy, repeatable lift off process - which was not possible for PDMS. For this reason, PDMS was deemed to be unsuitable.

PUE exhibits similar elastomeric properties to PDMS, despite their different chemical structure. PUE is also commercially available as a two part kit; a base and curing agent. These are mixed to together in the manufacturer's recommend ratio, diluted to the correct thickness, spin coated onto the nanowires, then heated to polymerise. Depositing a 50% dilution at 1000 rpm gave a thickness of around 1.9µm$\pm$0.1µm. Similar to PDMS, this was difficult to remove due to its adhesion to the nanowire substrate, but also, it had more of an elastic quality than the

other polymers. Consequently, removing the thin film by using tweezers stretched the film and reduced the quality of the films isolated as this would most likely increase the spacing between the nanowires. As stated previously, the polymer films need to have an easy, repeatable lift off process - which was not possible for PUE. For this reason, PUE was deemed to be unsuitable.

PVA is available in powder form and is water soluble. Depositing the 10% formulation at 1000 rpm gave a thickness or 2µm±0.1µm. It was found that the PVA film did not have much adhesion when spin coating onto the substrate, and was easily lifted off and embedded the nanowires well. However, as PVA is water soluble it was found to degrade over time from ambient moisture in the atmosphere. When freshly fabricated, the film was pliable and elastic - on ageing, it became brittle. Furthermore, it is only possible to make a formulation with a maximum concentration of 15% wt/wt,thus limiting the film thickness possible. Even though nanowire-polymer thin film devices will eventually be encapsulated, PVA was considered to be not robust enough and was also deemed unsuitable.

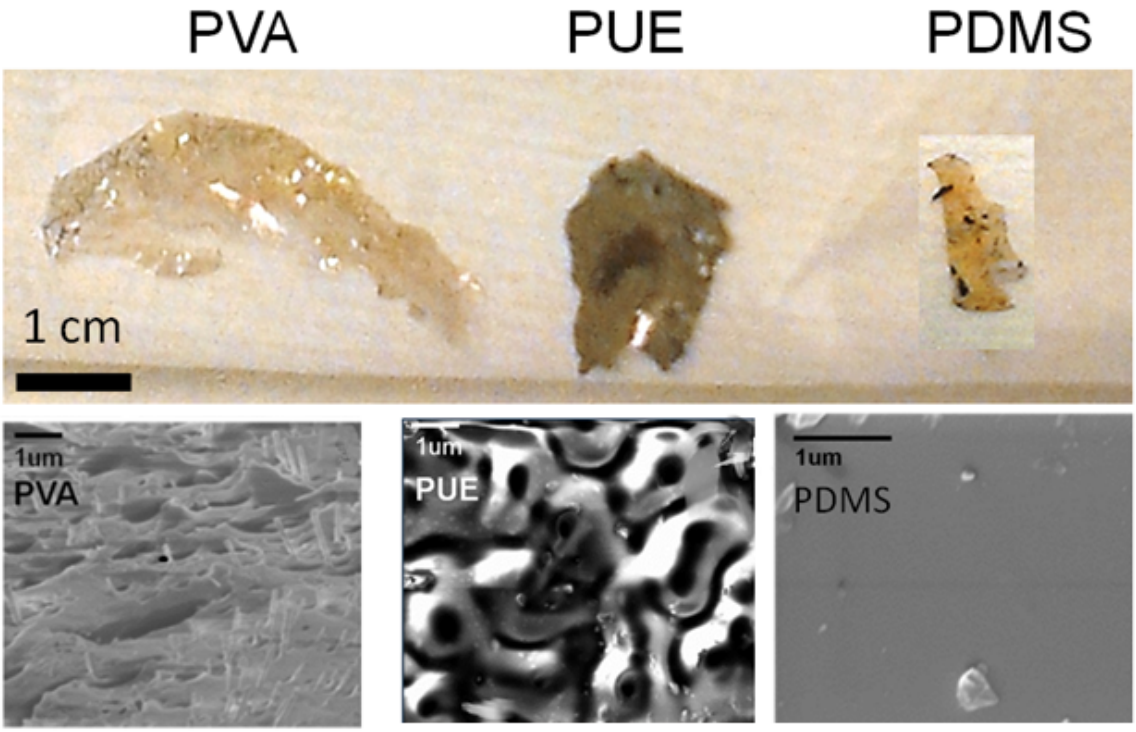

Fig. 5.2: Photographs and SEMs of various solution processable nanowire-polymer thin films. From left to right: PVA, PUE and PDMS. While it was straightforward to formulate, coat and remove the PVA thin film, the quality of the film is very pitted due to dewetting effects, and it was found that the PVA film did degrade with time due to its water solubility. On removing the PUE film, stretching of the film was observed due to the elastic property of the PUE. The PUE film formed interesting domains at low magnifications, but on higher magnification formed planar looking thin films. PDMS also formed planar thin films and both elastomers were easy to formulate and spin coat, though not easy to remove.

5.3 CVD Polymers: Introduction to Parylene C

Parylene C was the only CVD polymer to be tested. It is a π-conjugated polymer, which belongs in the family of polymers known as "'Parylenes"' which are based on chemical structures known as *para-xylenes*. There are four Parylenes that are commercially available, as shown in Figure 5.3: Parylene N (no substituents), Parylene C (one -Cl group), Parylene D (two -Cl groups) and Parylene HT (fluorinated) [250]. Parylene N, Parylene C and Parylene D may be used in lab based Parylene coaters. Parylene HT requires higher processing temperatures that are not possible in their conventional lab-based machines and samples need to be sent to the manufacturer (SCS) for coating. Parylene C is the most widely used of all the Parylenes due to its processing advantages and materials properties. Traditionally used in in the electronics industry to encapsulate electrical components, as it is a highly insulating and robust coating which does not leave an organic reside, Parylene C has found use in a variety of applications as a dielectric layer and as an encapsulant.

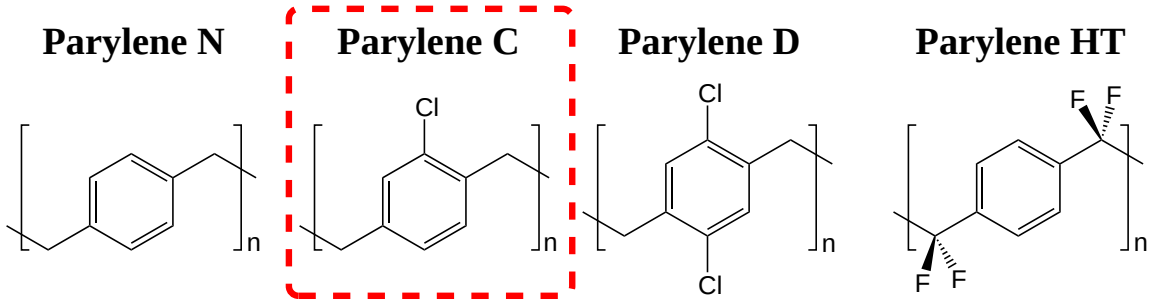

Fig. 5.3: Chemical structures of commercially available parylenes. From left to right: Parylene N (no substituents), Parylene C (one -Cl group), Parylene D (two -Cl groups) and Parylene HT(fluorinated). Parylene C (highlighted in red dashed lines) was used to fabricate the thin films.

Parylene C was used to encapsulate the nanowires in this thesis due to its wide availability, relatively fast deposition rate compared to the other parylenes and optical clarity ($\sim$ 99 % visible light transmission)[250].

Parylene C has a deposition rate of 5µm/hour whereas Parylene N has a much slower deposition rate of 1µm per hour.

Data on the visible light transmission taken by Jeong *et al.* is given in Figure **??**. As can be shown, Parylene C has close to 99% light transmission for much of the visible and infrared part of the spectrum, meaning that it is suitable for opto-electronic devices. However, as is common with several other organic molecules and polymers, absorption peaks are seen in the deep UV. This explains why Parylene C will eventually break down with prolonged exposure to UV light - an inherent problem with organic materials. There are several commercially available solutions that exist including UV blocking and UV absorbing layers, which are frequently used to protect organic material from UV light[250]. Parylene C also has favourable mechanical properties which makes is suitable for flexible device applications. Parylene C has a Young's modulus of 2.6 GPa, tensile strength of 68 MPa and a linear coefficient of thermal expansion of 3.5 x

10^{-5} / °C [251]. Figure 5.4(b) shows bend radii of 130 µm - 420 µm, depending on the device architecture have been measured by Lee *et al.*. Devices consisting of Parylene C (P), metal (M) and alumina (A) layers have been fabricated and the bend ratios measured. The device architecture as well as the direction the sample is bent is important to consider. 'In' refers to the top layer of Parylene C being on the inside of the curvature, 'out' refers to the top layer of Parylene C being on the outside of the curvature. Adding the alumina layer increased the minimum bend diameter[252].

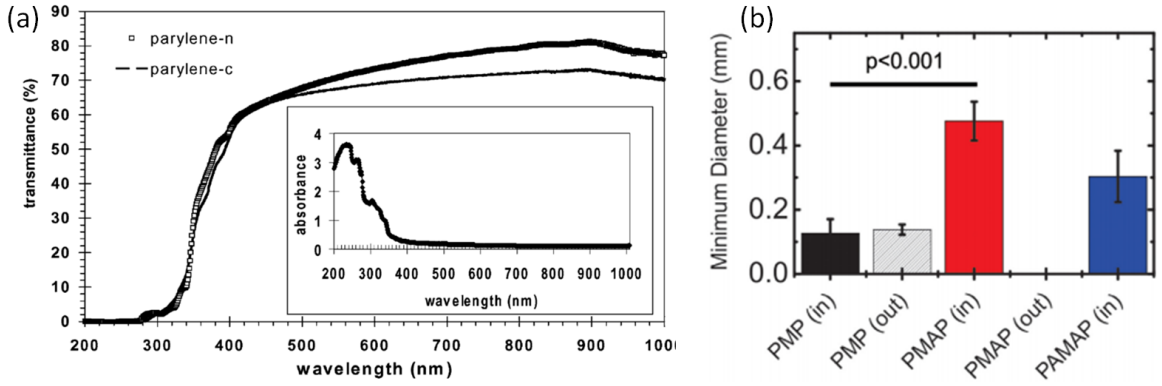

Fig. 5.4: Data on the optical and mechanical properties of Parylene C. (a) Visible transmission spectrum of Parylene C shows close to 99% light transmission in the visible range, making it suitable for use in opto-electronic devices [250]. Bend ratio measurements of Parylene C devices. P refers to Parylene, M refers to metal and A refers to alumina layers. In/out refer to the direction the device has been bent - 'in' means the last (i.e. top) layer of parylene is on the inside of the curvature, 'out' means the top layer of Parylene C is on the outside of the curvature.[252].

Parylenes where first synthesised in 1947, though their use did not become widespread until the Gorham process was developed - the method in which Parylenes are deposited. The Gorham process is a variant on chemical vapour deposition [242]. Parylene precursors are available in a powder form, which is then vaporised, cracked, then deposited as thin film through a free radical addition mechanism, described below.

The mechanism of Parylene polymerisation is depicted in Figure 5.3. Parylene precursors are available as a dimer, which is vaporised at 120° C and cracked at 690° C (1) to form a highly reactive diradical species which acts as the initiator (2a). Its cycloalkene resonant form is shown in (2b). Polymerisation takes place via free radical addition through two different pathways: (3) the diradical reacts with the cycloalkene species which rearranges to form another diradical, and (4) where two diradicals react forming a single bond between the aliphatic substituents. The reaction continues and forms polymeric Parylene C, outlined in red and shown as a repeating unit (5). Parylene C is an extremely conformal coating as it is deposited in a vapour form, and due to the reactivity of the diradical species. As a result, the vapour infiltrates the tiny voids between the nanowires where it forms the thin film and therefore and encapsulates the nanowires well. This is especially important as any gaps in the parylene coating could cause shorting of the device. It must also be noted that the thickness of the Parylene C coating is directly proportional

to the amount of precursor dimer material - a thickness/dimer weight plot is shown in Figure 5.5(g) - offering fine control and reproducible thin film thickness.

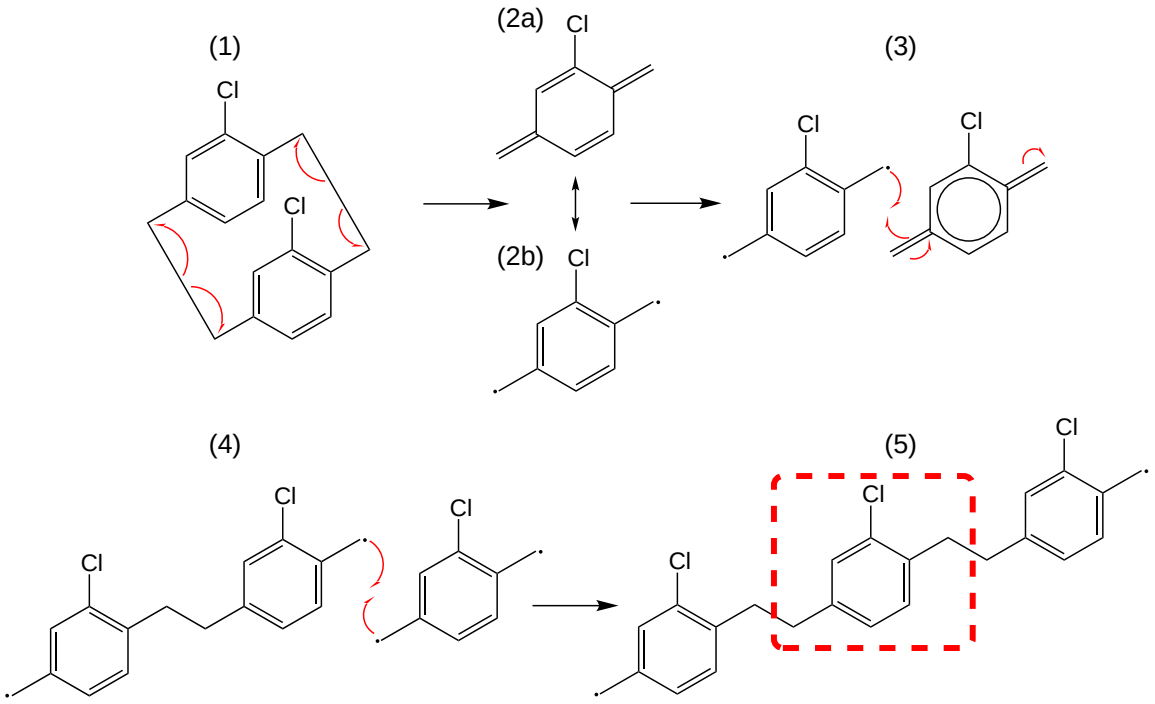

Fig. 5.5: Mechanism of parylene polymerisation: free radical addition. The Parylene C dimer precursor is vaporised and cracked (1) to form a diradical species (2a) and cyclo-alkene resonant form (2b). Polymerisation takes place. (3) shows one pathway, where the diradical reacts with the cyclo-alkene species to produce another radical species. (4) shows an alternative pathway where two diradicals react to form a single bond between the aliphatic substituents. The reaction continues and forms polymeric Parylene C, outlined in red and shown as a repeating unit (5).

5.4 Nanowire-Parylene C thin film removal

Once Parylene C is coated onto the VLS grown nanowires, it is straightforward to obtain a free standing thin film. To remove the thin film, I simply ran a scalpel around the edge of the sample to loosen the edges of the Parylene C coating. This is important, as conformal Parylene C coating covers the top, sides, and underneath the sample. Once the edges have been loosened it is then possible, using a pair of sharp tweezers, to gently peel away the nanowire thin film from the substrate. Films thinner than 1 µm are difficult to remove as they are very delicate and tear easily, though it is possible to remove them by soaking in (deionised) DI water. This causes the Parylene C film to swell and delaminate from the substrate.

Figure 5.5 details the full nanowire-Parylene C thin film fabrication process, which was ultimately used in Chapters 6,7 and 8. After nanowire growth (a) the nanowires are coated with Parylene C (b) and then carefully removed from the substrate yielding a clean substrate (c) and nanowire-Parylene C thin film (d). Note the SEM image (c) which depicts the wafer after thin

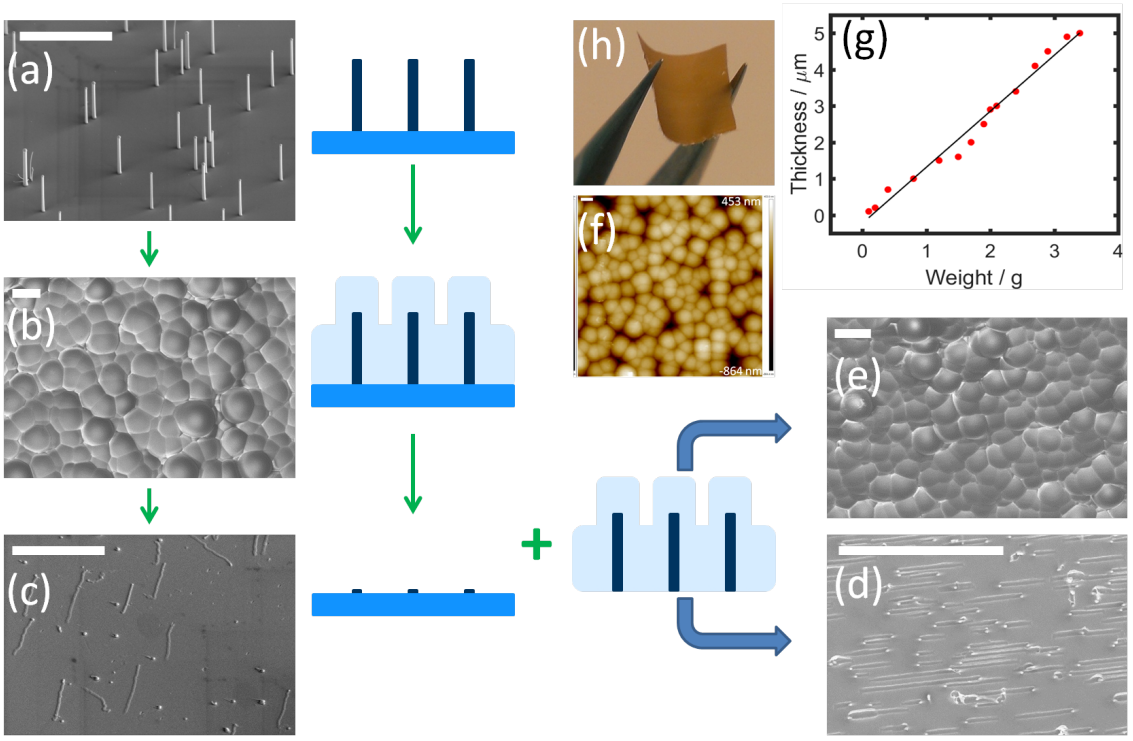

Fig. 5.6: Schematic and SEM images showing Parylene C thin film removal. First, nanowires are grown on a substrate (a) then coated with Parylene C (b). The thin film is removed yielding a clean growth substrate (c) and a polymer thin film (h). The top of the thin film is textured as shown in the SEM (e) and AFM (f) images, due to the conformal parylene coating. In comparison, the underside of the film is relatively smooth due to contact with the substrate(d). The thickness of the Parylene C thin film is dependant on the amount of dimer precursor used, as shown by the thickness/dimer weight plot (g).

film removal. There are no nanowires remaining on the substrate except for planar parasitic growth defects and tiny (10 nm) nanowire stubs, and no polymer residue. Due to the conformal nature of Parylene C coating, the top and underside of the film look different. The top of the film as shown in the scanning electron microscope (SEM) (e) and atomic force microscope (AFM) (f) images has a textured surface as the Parylene C has coated the top and sides of the nanowires and has a therefore has a matt appearance. Conversely the underside of the film is much smoother due to the contact with the substrate, and it is possible to see the nanowire tips in the SEM (d), and understandably has a shiny appearance as there is less texture. Furthermore, it is possible to see slight rips in the film, likely causes by the nanowire causing resistance and breaking when removed from the substrate (h) is a photograph showing a free standing nanowire-Parylene C thin film — GaAs nanowires were embedded in Parylene C.

SEM images, thin film photographs and UV-Vis spectra are shown in Figure 5.6. SEM images (a) and (b) show VLS grown GaAs and InP nanowires respectively. Photograph (c) shows the blue dashed box as the InP thin film, the red dashed box shows the GaAs thin film, and the green dashed box shows Parylene C (no nanowires), which is optically transparent. The UV-Vis

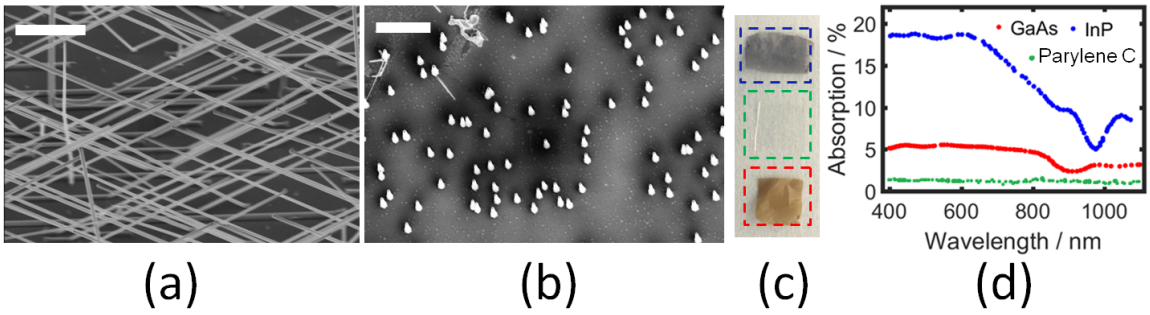

Fig. 5.7: SEM images of (a) GaAs and (b) InP nanowires, prior to Parylene C coating. (c) Photograph of nanowire-Parylene C thin films: InP (blue dashed box), GaAs (red dashed box) and Parylene C (no nanowires - green dashed box). (d) UV-Vis spectra showing the absorption of InP (blue) and GaAs (red) nanowire-Parylene C thin films compared with Parylene C thin films (green).

absorption spectra shows that absorption of the GaAs thin film is far less than that of the InP films.

5.5 Additional insights into Parylene C

The work discussed in this chapter give an excellent base for a systematic study regarding Parylene C thin film removal. As mentioned briefly, it was much easier to removed SAE nanowires with wider spacing, compared to those grown in a higher density configuration. Furthermore, throughout the course of my PhD I have had the opportunity to work with collaborators who were interested in applying this technique to their own nanowires. I found that I was unable to remove nanowires which were large diameter (over 500 nm), small spacing (less than 400 nm), had parasitic base growth (commonly seen in nanowires grown using molecular beam epitaxy) and selective area epitaxy where SiN_x masks were used (instead of SiO_x). This is by no means a systematic study, but anecdotal evidence which would provide the basis for a systematic study. Therefore, it would be very interesting to carry out and define the parameter space for the Parylene C technique. It would be interesting to further investigate this space and quantify the usefulness and adaptability of Parylene C through optical characterisation techniques, and indeed if other CVD polymers would actually be a better candidate.

Parylene C is also an interesting candidate for a moisture barrier layer. To test the encapsulating properties of Parylene C, quartz discs were coated with perovskite, then encapsulated with Parylene C. Perovskites, rather than nanowires, were a good candidate for these degradation tests, as when exposed to moisture and UV, the perovskite films rapidly degrade. This change can be easily seen as the brown perovskite thin film changes to a yellow colour. In Figure 5.8 samples 1, 2, 3, 4, refer to perovskite thin films coated with 100 nm, 500 nm, 1 µm, 5 µm of Parylene C, respectively. The samples were then left in a class 10,000 cleanroom, under ambient

pressure, temperature and moisture conditions. Initial experiments show that films as thin as 100 nm prolong the lifetime of the perovskite by around 6 weeks, and thicker films for much longer. It would be interesting to conduct a study with perovskite test devices and see if their lifetime is increased by adding the Parylene films.

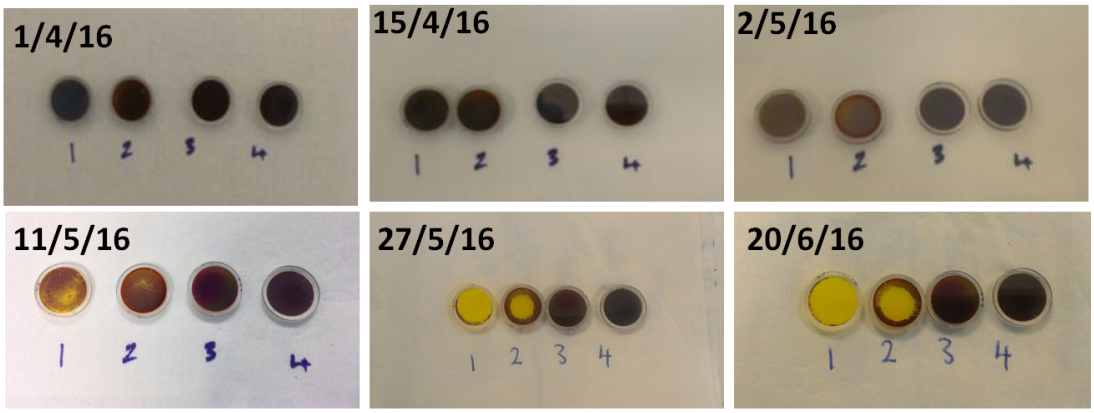

Fig. 5.8: Photographs depicting perovskite degradation when protected with Parylene C. Samples 1, 2, 3, 4, refer to perovskite thin films coated with 100 nm, 500 nm, 1 µm, 5 µm of Parylene C, respectively

5.6 Towards nanowire-polymer thin film devices

Once removed, the thin films can then be made into opto-electronic devices. I have used VLS grown GaAs nanowires to fabricate single layer Terahertz (THz) modulators (Chapter 6) and multilayer THz modulators (Chapter 7); and VLS grown InP nanowires to develop the fabrication of a flexible solar cell/photodetector (Chapter 8). This showcases the versatility of such a technique which has been missing from the literature - simply by replacing the nanowire used, different devices can be fabricated. Indeed, it is possible to make use of different nanowires that are particularly suited for certain applications [253].

While the development of this encapsulation process is a step forwards towards the fabrication of opto-electronic devices, there are still several other fabrication steps to optimise. Selective etching to expose the nanowire tips for contacting, passivation of the nanowire surface, formation of low resistance ohmic contacts, thin film handling are all issues that are addressed in upcoming chapters.

Furthermore, this encapsulation technique broadens the scope of substrate-free nanowire devices in a variety of applications. ZnO nanowires may be used as nanogenerators through their piezo electric or thermoelectric devices. Other III-V nanowires may be used in other opto-electronic devices such as photodetectors, lasers, multijunction solar cells and light emitting diodes (LEDs). Indeed, applications for THz may also be extended and it may be possible to fabricate substrate-free THz generators and detectors too. This method may also be used for conducting nanowires to fabricate contacts or insulating nanowires to form composite materials.

Removal of the nanowires from the substrate could enable reuse of the growth substrate, resulting in a step forward for commercially viable nanofabrication techniques, and for ultimately creating an integrated nanosystem on several nanowire devices. Simulation work investigating optimum nanowire parameters for light absorption are given in Appendix C.

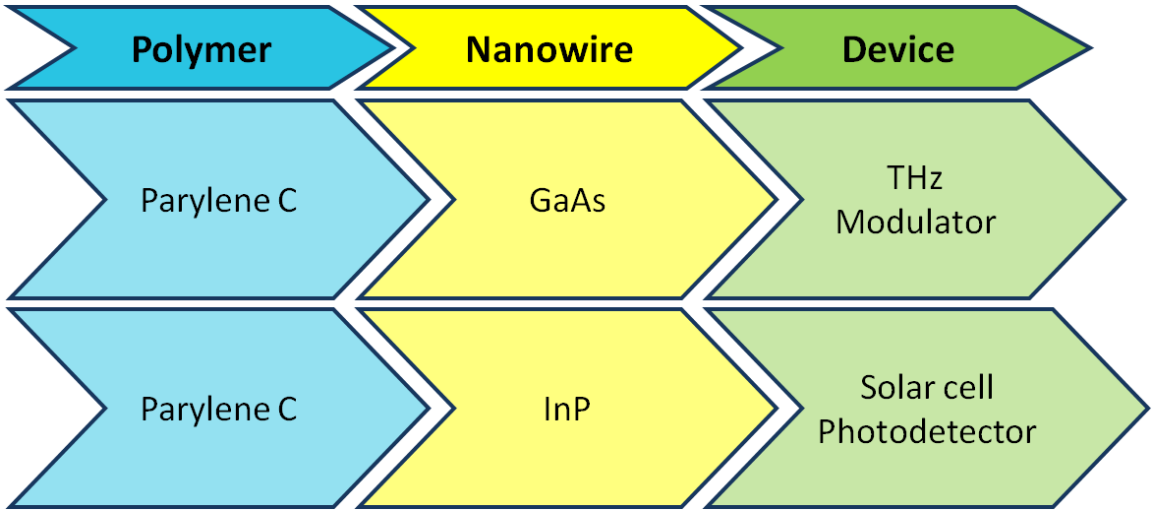

Fig. 5.9: Schematic depicting the breadth of flexible substrate-free nanowire device fabrication enabled by the straightforward encapsulation method showcased in this Chapter. By simply varying the nanowires embedded in parylene, a whole host of other devices may be fabricated - this can include piezoelectric and conductive nanowires too.

This chapter is integral to the rest of the thesis. By using a simple method of producing polymer-nanowire thin films, it is possible to fabricate a variety of flexible devices, simply by varying the choice of nanowire material.

5.7 Conclusion

In conclusion, I have successfully demonstrated that fabrication of Parylene C-nanowire thin films. This chapter shows the optimisation process using solution processed polymers and have found that they were unsuitable in producing nanowire-polymer thin films. The polymerisation mechanism and properties of Parylene C explain why its chemistry is key to successfully forming free standing vertically aligned nanowire-polymer thin films. The resultant thin films were characterised using profilometry, SEM and AFM, which showed the morphology of the films, as well as the clean substrate after thin film removal. The optical properties of the thin films were also determined using UV-Vis spectroscopy.

Chapter 6

Single-Layer Nanowire Terahertz Modulator

This chapter describes the design, fabrication and characterisation of an ultrafast switchable Terahertz (THz) polariser based on aligned GaAs nanowires. When photoexcited, GaAs nanowires transiently absorb THz radiation - this absorption is not seen when the nanowires are not photoexcited, and the THz wave is transmitted through the sample. As this is, to our knowledge, the first demonstration of GaAs nanowires used as a THz modulator, the literature review briefly investigates materials used in previous THz modulators and compared their merits and limitations in terms of ease of fabrication, modulation depth, and switching speed. The GaAs nanowires were grown by Dr Hannah Joyce and Dr Mykhaylo Lysevych at Professor Jagadish's group at the ANU. Modulator design and fabrication using GaAs nanowire coated with Parylene C and PDMS was carried out in Cambridge. Modulator characterisation using Optical Pump—Terahertz Probe (OPTP) spectroscopy was carried out by Dr Jessica Boland and Mr Djamshid Damry at Oxford University. It was found that using the poly(dimethyl siloxane (PDMS) and Parylene C for single layer GaAs nanowire-Parylene C thin films did not make a difference (at this stage) to the device performance and THz absorption of both modulators was limited by the photoexcitation fluence.

The modulators demonstrated an ultrafast switching time of around 1 ps though the extinction was around 1.8 % and are capable of broad bandwidth between 0.1 THz and 4 THz by showing their photoconductivity response. While the modulation depth is low, the ultrafast switching speed is extremely promising.

6.1 Current THz modulators

The Terahertz (THz) frequency range is located between the infrared and microwave regions of the electromagnetic spectrum (0.1-10 THz) [133]. Whilst huge advances have been made in THz generation [137] and detection [144] in the past 20 years, an ultrafast switchable THz modulator has not been demonstrated. This is crucial in the development of high speed THz

communications as components capable of encoding information into the THz waveform are essential to drive the technology forward [254].

At present, the development of practical THz modulators is an active field of research with many different approaches being investigated. Depending on which property of light is controlled, different materials are used to fabricate THz modulators. Material systems which vary the intensity [156, 157], phase [72, 158], or spatial position of the transmission and reflection coefficients of the THz electric field [159, 160] have all been demonstrated.

Early work shows THz modulators which vary the intensity of the THz wave based on two-dimensional electron-gas (2DEG) structures [161, 162], birefringent liquid crystals [163, 164] and static THz polarisers [165–168].

High performance THz modulators have now been fabricated using metamaterials [156, 158, 159, 167, 169–173], optical cavities [174, 175], graphene [176–178, 255] and carbon nanotubes [72, 179, 180], each with their own merits and limitations.

Metamaterial-based THz modulators have achieved high modulation depths, with Karl *et al.* [181], demonstrating a dynamic range of over 20 dB and Chen *et al.* showing a modulation depth of $\sim 50\%$ [169, 256]. However, these THz modulators suffer from low bandwidth, with optimal operation only at a specific wavelength, as well as limited switching speeds with microsecond temporal resolution.

THz amplitude modulators based on Fabry-Perot semiconductor cavities have achieved a modulation depth of $\sim 90\%$, though only microsecond switching speeds [175]. Liu *et al.* have demonstrated THz modulation in a silicon device, with close to 100% modulation depth by utilizing the evanescent wave in a total internal reflection setup coupled with a conductive interface to enhance attenuation of THz radiation [183]. Through careful material choice the THz modulator could be optimised as only low sheet conductivities ($\sim$12 mS) are required to obtain a high modulation depth, the broadband response and switching speed is dependant on the frequency-dependent conductivity response of the material.

Since metamaterial and Fabry-Perot based THz modulators lack high switching speeds, graphene-based and carbon nanotube-based modulators have been developed as an alternative.

Graphene THz modulators improve performance by utilising intraband absorption to obtain a modulation depth of $\sim 16\%$ and nanosecond modulation time [176]. In addition, the modulation depth of these graphene-based modulators could be improved up to 70% per reflection [184] by using a total internal reflection geometry.

THz polarisers fabricated from carbon nanotubes have also been demonstrated by Ren *et al.* by depositing aligned nanotubes onto a sapphire substrate and reported an extinction ratio of 10 dB in the optical and THz range and Kyoung *et al.* who used a carbon nanotube stack fabricated from aligned carbon nanotube arrays to achieve an extinction ratio of 37 dB [179, 180]. However, picosecond switching speeds are required for ultrafast THz communication applica-

tions. Carbon nanotube–polymer based modulators can offer high switching speeds, though at the cost of modulation depth as shown by Docherty *et al.* [72]. This carbon nanotube–polymer THz modulator could be optically controlled and was capable of polarisation and intensity modulation of THz radiation with a switching speed of $\sim$1 ps, although it suffered from a low modulation depth ($\sim$-27 dB).

As discussed above, whilst metamaterial and Fabry-Perot based THz modulators can offer a high modulation depths and carbon nanotube and graphene based THz modulators can offer high switching speeds, neither materials systems can offer both. In order to realise high speed THz communications there is still a need for the development of a THz modulator with a straightforward fabrication process, high modulation depth, picosecond switching speeds, capable of electrical or optical control and can be easily integrated into current silicon-based technology.

6.2 GaAs nanowires for THz modulators

Practically, III–V nanowires have been considered for use in THz applications due to their high electron mobilities and their ability to be integrated with silicon devices [257]. GaAs nanowires, in particular, are ideal candidates for THz modulation, as they exhibit a direct band gap, high absorption coefficient and tunable opto-electronic properties, such as carrier lifetimes and mobility [150, 253].

It is the inherent geometric anisotropy of semiconductor nanowires that enables a polarized photoexcitation pulse to induce transient modulation of the polarization and intensity of the transmitted THz pulse. Specifically, the dielectric mismatch between the zincblende nanowire and the surrounding Parylene C medium allows an electric field to penetrate the nanowire if the field is polarized parallel to the nanowire axis, but strongly suppresses penetration of electric field components oriented perpendicular to the nanowire axis according to Equation 6.1 where $k_{\parallel}$ and $k_{\perp}$ refer to absorption coefficient for light polarisation parallel and perpendicular to nanowire axis respectively, and ε and ε_0 refer to the dielectric constants of the nanowire and surrounding environment respectively [57, 258].

$$\frac{k_{\parallel}}{k_{\perp}} = \left| \frac{\varepsilon + \varepsilon_0}{2\varepsilon_0} \right|^2 \tag{6.1}$$

As a result, nanowires exhibit strong linear polarization anisotropy in response to photoexcitation. Photoexcitation is most effective if the optical pump is polarized parallel to the nanowire axis, but minimally effective if the pump is polarized perpendicular to the nanowire axis. The absorption of THz radiation also strongly depends on the polarization of the THz pulse relative to the nanowire orientation. The plasmon modes that propagate longitudinally along the nanowire axis are responsible for plasmonic THz absorption signatures between 0.1 and 4 THz: these modes strongly absorb components of the THz electric field parallel to the nanowire axis

[41]. In all OPTP (optical pump—terahertz probe) experiments reported here, the THz pulse was polarized parallel to the nanowire axes, which is the configuration that gives the strongest absorption, and therefore modulation, of the THz pulse in the range of 0.1 to 4 THz. A schematic diagram of the OPTP experiment is given in Figure 6.1.

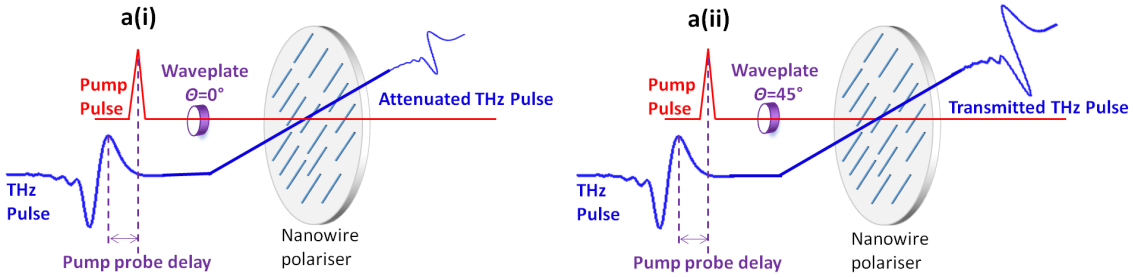

Fig. 6.1: Schematic diagrams of the OPTP experiment. The nanowires are oriented vertically and the incident THz electric field is vertically polarized. A half-wave plate rotates the polarization of the 800 nm photoexcitation pump beam by 2θ, where θ is the angle between the vertical and the waveplate axis. The pump beam selectively photoexcites nanowires that are aligned with their long axes parallel to the polarization of the pump beam. The THz pulse is then absorbed by the photoexcited nanowires. (i) When $2\theta = 0°$, the nanowires are aligned with the polarization of the pump beam, so are photoexcited and rendered conductive, leading to maximum THz absorption. (ii) When $2\theta = 90°$ the nanowires are orthogonal to the polarization of the pump beam, so the incident pump pulse does not photoexcite the nanowires effectively and consequently the pump does not significantly change the THz transmission properties of the nanowires, leading to minimum THz absorption.

In contrast, any component of the THz pulse that is polarized perpendicular to the nanowire axis will be transmitted with minimal photoinduced modulation. As 2θ increases to 90°, the optical pump beam polarization becomes orthogonal to the nanowires and only a minimal density of free charge carriers are photogenerated in the nanowires. Consequently, when $2\theta = 90°$ the THz radiation is barely attenuated, regardless of the polarization of the incident THz radiation. Therefore, by controlling the polarization of the incident optical pump beam, it is possible to modulate the intensity and polarization of the THz wave passing through the nanowire sample.

Therefore GaAs nanowire can offer a practical alternative to other THz modulation techniques discussed above, and is also capable of modulating the intensity and polarisation of the THz radiation. This allows for an increase in information that can be encoded on the THz wave and the realization of high-speed THz communication.

In order to make full use of the excellent properties of the GaAs nanowires, they need to be removed from the substrate and embedded in a flexible polymer which is capable of transmitting the photoexcitation and the THz pulse, to minimise interference with nanowire performance. As explained in Chapter 5, PDMS is a solution processed polymer, whereas Parylene C is a chemical vapour deposition (CVD) polymer - hence both have different wetting and therefore film forming capabilities. Both polymers are transparent to THz radiation and visible light, can

be removed from the substrate fairly easily (though this is more straightforward for Parylene C than it is for PDMS) and can be coated and removed whilst retaining the alignment of the nanowires. Hence, both polymers were deemed suitable for device fabrication.

6.3 Modulator fabrication and characterisation

Nanowire growth is described in detail in Chapter 4. To summarise: high-density arrays of GaAs nanowires which were 50 nm in diameter were grown via gold-seeded metal-organic chemical vapour deposition (MOCVD) using a two-temperature process that gives high uniformity in nanowire diameter, a twin-free zincblende structure and high charge carrier mobilities [259]. The GaAs nanowires were grown by Dr Hannah Joyce and Dr Mykhaylo Lysevych at Professor Jagadish's group at the ANU.

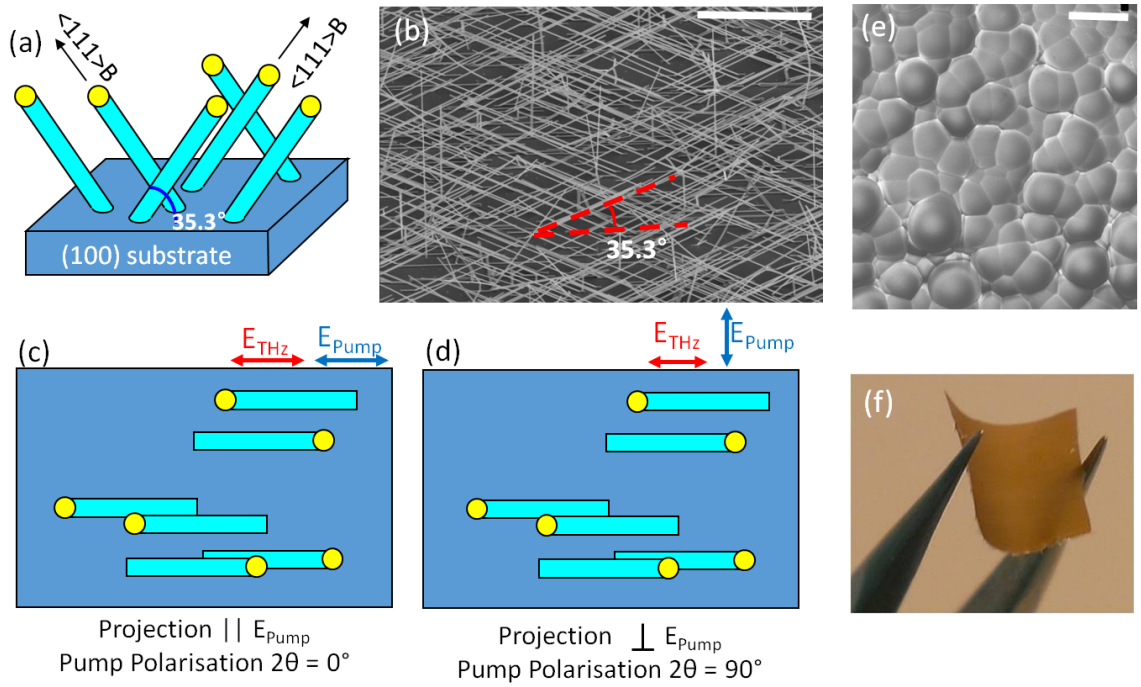

Fig. 6.2: (a)Schematic diagram illustrating the 3-dimensional geometry of the ⟨111⟩B oriented nanowires grown on the (100) substrate. (b) SEM image of the ⟨111⟩B oriented nanowires grown on the (100) substrate, with the orientation and angle of growth (35.3° to the substrate) marked on. This was imaged at a substrate tilt of 40°. (c, d)Schematic diagram showing the projections of the nanowires onto the (100) plane. The THz and pump polarisation directions both lie within this plane. The polarisation of the pump, either parallel (c) or perpendicular (d) is defined relative to the projection of the nanowires on the (100) plane. (e) SEM image showing the nanowires after coating with conformal Parylene C. (f) Photograph of a GaAs nanowire—Parylene C thin film. The scale bars in the SEM images show 500 nm.

A suitable polymer was needed to encapsulate the nanowires. Figure 6.3 shows the time domain trace of a transmitted THz pulse through a quartz substrate coated 5 µm of Parylene

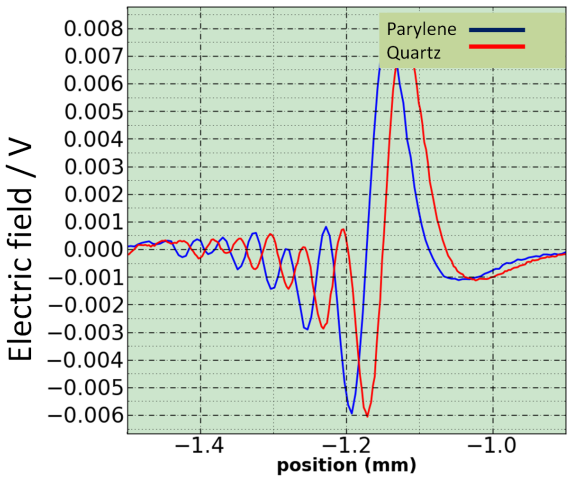

Fig. 6.3: Time domain trace of a transmitted THz pulse through parylene on quartz and a quartz reference. The parylene layer produces a slight phase shift due to the film thickness, but negligible absorption compared to the reference quartz substrate.

C, and a bare quartz substrate as a reference. The spectrum shows that the Parylene C layer produces a slight phase shift due to the film thickness, but negligible absorption compared to the reference quartz substrate. Therefore, this was deemed suitable for coating the GaAs nanowires, as it was important to choose a matrix that this not cause losses through unwanted absorption of THz pulse.

To assess the potential of these Parylene C coated GaAs nanowire polarisers for THz modulation, their photoconductivity and THz transmission were measured via OPTP spectroscopy. A brief summary is given here - for further detail, please refer to Chapter 4. A Ti:sapphire regenerative amplifier laser was used to generate femtosecond pulses which were used as a source for THz generation, THz detection and optical photoexcitation of the nanowires. Modulator characterisation using Optical Pump—Terahertz Probe (OPTP) spectroscopy was carried out by Dr Jessica Boland and Mr Djamshid Damry at Oxford University.

From a practical perspective, nanowires aligned planar to the nanowire substrate were needed. Growing nanowires vertically using a (111)B substrate then flattening them such that they lay planar to the substrate proved difficult to ensure the alignment of nanowires was retained in the flattening process. The nanowires preferentially grow in the two $\langle 111 \rangle$B directions that lie at angles of 35.3°to the (100) substrate plane, as shown in Figure 6.2(a) and (b). When projected onto the (100) plane then $\langle 111 \rangle$B directions appear parallel, and the nanowires may be thought of as lying almost ‘flat’ to the substrate. Figure 6.2 (c) and (d) shows the plan view SEM image of the nanowires grown on the substrate and illustrates the parallel orientation of the nanowires projected onto the (100) plane. It is this projection of the nanowires onto the (100) plane that is relevant in the operation of the polariser as the THz and pump polarisation directions lie in the (100) plane. Therefore the polarisation directions are described relative to the nanowire

projection onto the (100) plane. The nanowires height above the substrate plane is not considered in this analysis. It can be seen that the nanowires have a highly directional quality and are well-aligned.

The GaAs nanowire wafers were coated with a 5 µm layer of Parylene C using the Gorham process [242] in a PSD 2010 LabCoter2 chamber. Figure 6.2(e) and (f) show a scanning electron microscope (SEM) image of the Parylene C coated nanowires and a photograph of the resultant thin film respectively. The PDMS samples were fabricated by preparing the PDMS according to the manufacturer's specifications and spin-coated - for more detail, please refer to Chapter 4. The nanowire-polymer thin films were peeled off from the substrate and these films were divided into equal sized segments using a razor blade to form 10 mm × 10 mm squares. These single layer modulators were then characterised using OPTP as described below.

The transmission of the electric field of the THz probe pulse through the nanowires, E, can then be measured as a function of frequency. The electric field transmitted through the sample without photoexcitation (at equilibrium) is given by E_{off}. Upon photoexcitation, free charge carriers are generated in the nanowires and these carriers interact with the THz wave to reduce the transmission to E_{on}. The photoinduced change in THz transmission through the nanowires is denoted as $\Delta E = E_{\text{on}} - E_{\text{off}}$. The value of $-\Delta E/E_{\text{off}}$ is then proportional to the photoinduced conductivity of the nanowires and directly related to the photoexcited free carrier concentration. For convenience, $t = 0$ is the pump–probe delay at which $-\Delta E/E_{\text{off}}$ is maximum [41].

In this OPTP system, the polarisation of the photoexcitation beam is selected via a half-wave plate. Figure 6.2 shows a schematic diagram of the experimental setup, with the cases for $\theta = 0^\circ$ (a(i)) and $\theta = 45^\circ$ (a(ii) depicted. By rotating the half-wave plate by an angle of θ, the polarisation of the optical pump beam was altered by an angle of 2θ. Thus, by rotating the half-wave plate by 45°, the optical pump beam was rotated from vertical polarisation to horizontal polarisation. The nanowires-in-Parylene C samples were placed in the OPTP system, such that the long axes of the constituent nanowires were oriented vertically.

6.4 Photoconductivity response

Figures 6.4(a, b) respectively plot the photoconductivity response of the nanowires embedded in Parylene C, when the pump beam is polarised parallel and perpendicular to the nanowires. The photoconductivity response is greatest when the pump is polarized parallel to the nanowires (Figure 6.4(a)) and negligible when the pump is polarized perpendicular to the nanowires (Figure 6.4(b)). The photoconductivity response exhibits a Lorentzian lineshape characteristic of a plasmon response. A Drude–plasmon response was fitted to the data. A detailed derivation is given in Appendix D.

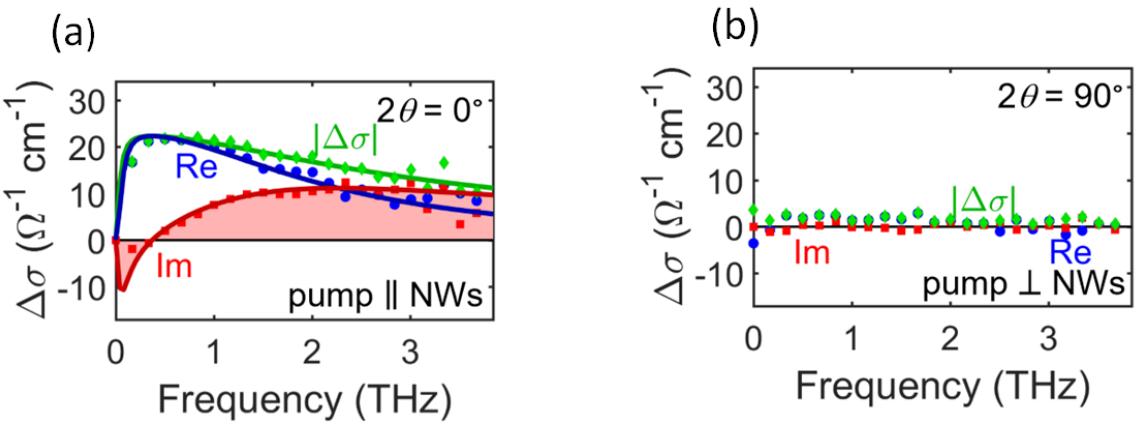

Fig. 6.4: (a)(b) Frequency-dependent photoconductivity response of nanowires embedded in Parylene C after photoexcitation with the pump beam polarised (a) parallel and (b) perpendicular to the nanowire axis. Blue circles, red squares and green diamonds represent the real part, imaginary part and magnitude of the photoconductivity, respectively. Lines represent fits to the conductivity modelled by a Drude-plasmon response.

The photoconductivity $\Delta\sigma$ in Figure 6.4 was extracted from the OPTP measurements of $\frac{\Delta E}{E}$. Previous work within Professor Johnston's group detailing the calculations and derivations can be found in the following references [41, 260]. The nanowires are considered to be embedded within a surrounding Parylene C layer of thickness, $d_{parylene}$ and to have an effective areal fill factor, f. The qualities were measured from the SEM images of the nanowires on the growth substrate (as we assume they would have all been lifted off by the Parylene C).

The complex conductivity of a plasmon resonance is given by

$$\sigma = \frac{iN_P e^2 \omega}{m_e^*(\omega^2 - \omega_{0,N_P}^2 + i\omega\gamma)} \tag{6.2}$$

where N_P is the photoexcited carrier density, e is the electronic charge, m_e^* is the electron effective mass in GaAs, ω_0 is the resonant frequency and γ is the momentum scattering rate. The scattering rate was determined by fitting Equation 6.2 to the data in Figure 6.3-a(i) then converted to electron mobility μ using

$$\mu = \frac{e}{m_e^*\gamma} \tag{6.3}$$

In this manner I extracted an electron mobility of 1800 $\mathrm{cm^2V^{-1}s^{-1}}$ for the GaAs nanowire samples indicative of the excellent electronic properties of the nanowires. The magnitude of the photoconductivity ($\Delta\sigma$) is significant and extends across the measurement bandwidth (0.1 to 4 THz). The broad spectrum of the photoconductivity response of the GaAs nanowire–Parylene C layer indicates its potential as a broadband THz polariser.

6.5 Rotation and photoexcitation measurements

To investigate the effect of the polarisation of the optical pump beam on the THz modulation, the ratio of the transmission under photoexcitation to the transmission at equilibrium, $E_{on}/E_{off} = 1 + \Delta E/E_{off}$, is plotted as function of polarisation angle, 2θ for both the PDMS and Parylene C polarisers. This experiment was performed at a range of photoexcitation fluences from 6–280 μJ cm^{-2}.

Figures 6.5 depicts the PDMS data and Figure 6.6 depicts the Parylene C data. Fits to the data show a cosine-squared relationship between the THz transmission and 2θ, as expected from Malus' Law for transmission through a polariser [72] for both polymers. At $2\theta = 0°$ and $2\theta = \pm 180°$, when the polarisation of the optical pump beam is aligned parallel to the nanowire axis, a minimum in the THz transmission (maximum THz absorption) is observed. As the polarisation angle is rotated, the THz transmission increases to reach a maximum at $2\theta = \pm 90°$ when the optical pump beam is polarized perpendicular to the nanowire axis.

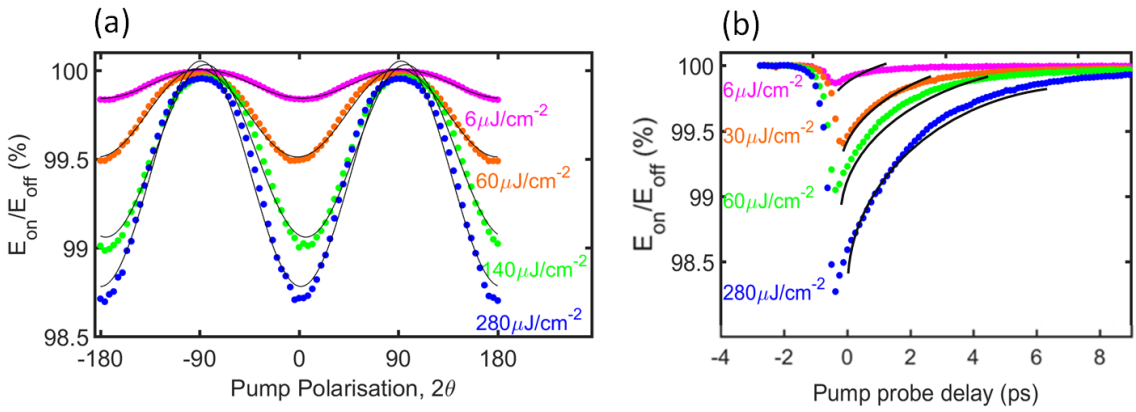

Fig. 6.5: Performance data for the PDMS based modulator. (a) THz transmission, E_{on}/E_{off}, through the photoexcited single-layer nanowire polarisers as a function of polarisation angle (2θ) of the photoexcitation pulse. Photoexcitation was performed with pump fluences between 6 and 280 µJ cm^{-2} and data in (b) were measured with the pump–probe delay at $t = 0$ ps at which $-\Delta E/E_{off}$ is maximum. Solid black lines represent squared-cosine fits according to Malus's Law. (b) THz transmission, E_{on}/E_{off}, through the single-layer polariser as a function of time after photoexcitation with pump fluences between 6 and 280 µJ cm^{-2} with the pump polarised parallel to the nanowire long axes ($2\theta = 0°$). The solid black lines are fits describing monoexponential decay of the photoconductivity at early times after photoexcitation.

From these rotation scans, it is possible to deduce the modulation depth and dynamic range. The modulation depth is defined as the value of $-\Delta E/E_{off}$ reached when the pump is polarized parallel to the nanowires ($2\theta = 0°$) and the dynamic range was defined as the relative difference in THz transmission when the pump is polarized at angles of $2\theta = 90°$ and $2\theta = 0°$. For this single-layer Parylene C coated GaAs nanowire polariser at the highest investigated fluence (280 µJ cm^{-2}), the modulation depth was found to be -17.4 ± 0.1 dB corresponding to extinction of $\sim 1.82 \pm 0.04\%$, and the dynamic range was determined as -18.8 ± 0.1 dB. These values

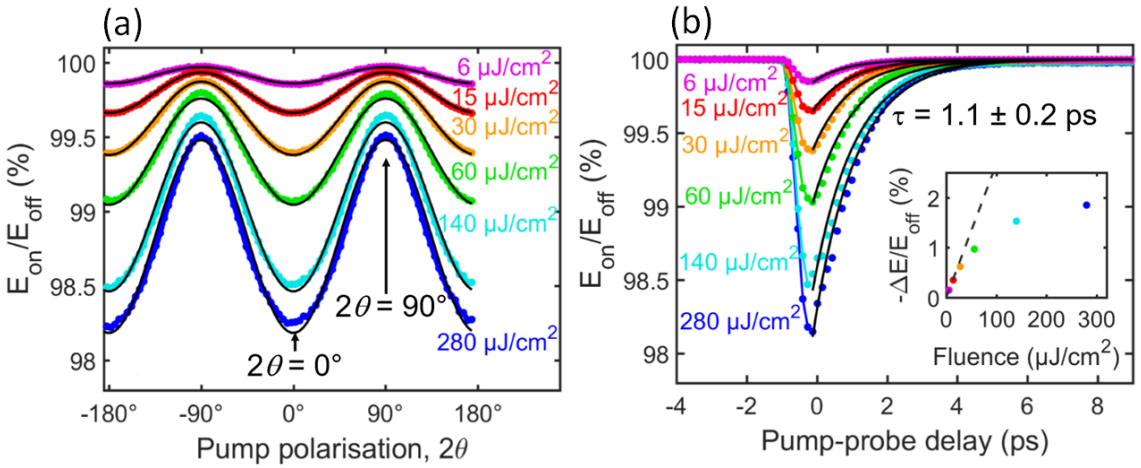

Fig. 6.6: Performance data for the Parylene C based modulator. (a) THz transmission, E_{on}/E_{off}, through the photoexcited single-layer nanowire polarisers as a function of polarisation angle (2θ) of the photoexcitation pulse. Photoexcitation was performed with pump fluences between 6 and 280 μJ cm^{-2} and data in (b) were measured with the pump–probe delay at $t = 0$ ps at which $-\Delta E/E_{off}$ is maximum. Solid black lines represent squared-cosine fits according to Malus' Law. (b) THz transmission, E_{on}/E_{off}, through the single-layer polariser as a function of time after photoexcitation with pump fluences between 6 and 280 μJ cm^{-2} with the pump polarized parallel to the nanowire long axes ($2\theta = 0°$). The solid black lines are fits describing monoexponential decay of the photoconductivity at early times after photoexcitation. The inset in (b) shows the maximum photoinduced change in THz transmission, $-\Delta E/E_{off}$, equivalent to modulation depth, as a function of pump fluence. The dashed line in the inset shows the expected values if photoconductivity scaled linearly with pump fluence. Data in the inset were measured with the pump–probe delay at $t = 0$ ps and the half-wave plate angle at $2\theta = 0°$.

exceed those reported for other polarisers with comparable switching speeds; namely carbon nanotube-based polarisers [72]

The switching speed of the GaAs polariser was determined by measuring the THz transmission as a function of time after photoexcitation at the same range of fluences (between 6-280 μJ cm^{-2}), as shown in Figure 6.6(b). For all fluences, a sharp rise in photoconductivity within 1 ps was observed followed by a rapid decay attributed to trapping of free carriers at the GaAs nanowire surface. A monoexponential function was fitted to the decays over the first 5 ps, from which the photoconductivity decay lifetime extracted. The photoconductivity lifetime was found to be of the order of a picosecond, 1.1 ± 0.2 ps, with the initial photoconductivity, which is related to modulation depth, increasing with fluence.

6.6 Improving polariser modulation depth

At this stage, there is very little difference in performance between the two polymer matrices. The inset of Figure 6.6(b) shows that the maximum photoinduced change in transmission,

$-\Delta E/E_{\text{off}}$, increases only sublinearly with photoexcitation fluence and saturates towards the highest fluences. This phenomenon arises due to two effects: (1) carrier–carrier scattering and (2) conduction band filling. Carrier–carrier scattering arises because as photoexcitation fluence increases, the charge carrier density increases and therefore carrier–carrier scattering mechanisms become more pronounced. This additional scattering reduces the charge carrier mobility and consequently limits the photoconductivity of the nanowires. Conduction band filling occurs at highest photoexcitation fluences and results in a shift of the absorption edge according to the Burstein-Moss effect and may reduce the absorption coefficient of the GaAs nanowires at the photoexcitation energy. Both phenomena result in limiting the photoconductivity of the nanowires.

Therefore the modulation depth cannot simply be increased by correspondingly increasing the fluence indefinitely. What is needed is a modulator which a greater areal density of nanowires available for photoexcitation, which would improve the performance of the polarisers. Chapter 7 describes how this was achieved through the fabrication of multi-layer modulators.

6.7 Conclusion

In summary, I have fabricated and characterised an ultrafast THz modulators based on GaAs nanowire-Parylene C and GaAs nanowire-PDMS thin films via a straightforward fabrication process. The modulation depth, extinction and dynamic range exceed values measured for ultrafast carbon nanotube-based THz polarisers, and picosecond switching has also been achieved. The modulation depth and dynamic range increased with increasing photoexcitation fluence, but eventually saturates at the highest fluences. This places a limit on the performance of the polarisers as the fluence cannot be indefinitely increased in order to obtain a high modulation depth or dynamic range.

Chapter 7

Multi-Layer Nanowire THz Polarisers

This chapter extends the work carried out in Chapter 5, which demonstrated proof-of-concept Terahertz (THz) polarisation modulators based in GaAs nanowire-Parylene C and GaAs nanowire-poly(dimethyl siloxane) (PDMS) thin films. In order to improve the extinction of the modulators, the areal density of the nanowires needed to be increased. This was achieved by fabricating multilayer polarisers where several nanowire-polymer thin films were bonded together. Due to the thickness of the PDMS layers, it was only possible to stack 4 layers, which showed a small improvement in performance. As the GaAs thin films were much thinner, it was possible to bond as many as 14-layers together - thus dramatically increasing the areal density at the performance of the multilayer modulators compared to the single layer modulators. For the nanowire-Parylene C thin films, 1,4,8, and 14-layer modulators were fabricated, the number of layers limited only to the nanowire wafers available at the time. As described previously the GaAs nanowires were grown by Dr Hannah Joyce and Dr Mykhaylo Lysevych at Professor Jagadish's group at the ANU. Modulator design and fabrication using GaAs nanowire coated with Parylene C and PDMS was carried out in Cambridge. Modulator characterisation using Optical Pump—Terahertz Probe (OPTP) spectroscopy was carried out by Dr Jessica Boland and Mr Djamshid Damry at Oxford University. The performance characteristics of the 14-layer modulator was as follows: switching speed (<5 ps), modulation depth (-8dB), extinction (13%), dynamic range (-9 dB). The modulators remained capable of broad bandwidth for THz modulation between 0.1 THz and 4 THz which surpasses the performance of several devices in the literature and presents the first THz modulator which combines not only a large modulation depth but also a broad bandwidth and picosecond time resolution for THz intensity and phase modulation. This makes it an ideal candidate for ultrafast THz communication [42].

7.1 Towards a high speed THz communications system

Chapter 6 describes how, for single layer modulators, the maximum photoinduced change in transmission, $-\Delta E/E_{\text{off}}$, saturates towards the highest fluences due to carrier–carrier scattering

and conduction band filling. Because of this saturation and because of the difficulties in achieving very high fluences in practical communications systems, other avenues of obtaining high modulation depths needed to be investigated. In order to realise a high speed Terahertz (THz) communications system, the dynamic range, modulation depth and extinction ratio need to be improved. In order to overcome this performance limit, a modulator with a greater areal density of nanowires available for photoexcitation is needed. Increasing the areal density of nanowires at the nanowire growth stage is impractical. Another way is to layer the thin films, whilst being careful to retain overall nanowire alignment to ensure efficient photoexcitation, as described below.

7.2 Modulator fabrication and characterisation techniques

The nanowire growth and polymer coating processes are described in detail in Chapter 4. The GaAs nanowires were grown by Dr Hannah Joyce and Dr Mykhaylo Lysevych at Professor Jagadish's group at the ANU. When fabricating the multilayer polarisers, it is important to ensure that the nanowire alignment is maintained throughout the stack. Prior to coating the nanowires with polymer, the nanowire wafers were examined using scanning electron microscopy (SEM) to establish the general orientation of the nanowires - this direction was marked on the back of the wafer. The GaAs nanowire wafers were then coated with Parylene C and poly(dimethyl siloxane) PDMS as described in Chapter 4. The thin films were peeled off from the substrate and these films were divided into equal sized segments using a razor blade to form 10 mm $\times$ 10 mm squares. The nanowire-Parylene C thin films laminated together whilst carefully preserving the alignment of the nanowires as described in Chapter 4. Nanowire polarisers consisting of 1, 4, 8 and 14-layers were fabricated and characterised. The nanowire-PDMS thin films were bonded without the need for hot bonding as the PDMS thin films are inherently tacky due to Van de Waals interactions. However, given the thickness of the PDMS films, only 1,2,3 and 4 layer films could be fabricated. Films thicker than 4 layers were mechanically unstable.

To assess the potential of these parylene-coated GaAs nanowire polarisers for THz modulation, their photoconductivity and THz transmission were measured via optical pump–terahertz probe (OPTP) spectroscopy - this is described in detail in Chapters 4 and 5. Modulator characterisation using Optical Pump—Terahertz Probe (OPTP) spectroscopy was carried out by Dr Jessica Boland and Mr Djamshid Damry at Oxford University.

To recapitulate - the electric field transmitted through the sample without photoexcitation (at equilibrium) is given by E_{off}. The photoinduced change in THz transmission through the nanowires is denoted as $\Delta E = E_{\text{on}} - E_{\text{off}}$. The value of $-\Delta E/E_{\text{off}}$ is then proportional to the photoinduced conductivity of the nanowires and directly related to the photoexcited free carrier concentration. For convenience, $t = 0$ is the pump–probe delay at which $-\Delta E/E_{\text{off}}$ is maximum [41]. The polarisation of the optical pump beam was altered by an angle of 2θ by rotating the

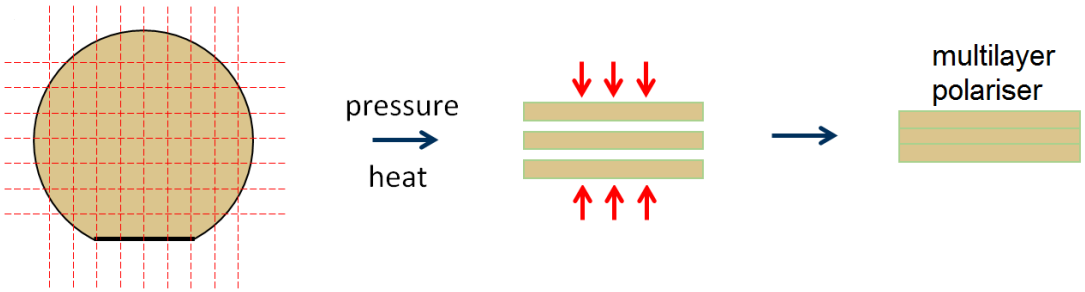

Fig. 7.1: (a) Schematic diagram illustrating the fabrication process of the multilayer polarisers. First, the nanowire wafer is coated in either PDMS (spin-coated) or Parylene C (CVD). The thin films are dissected into equal size segments are carefully removed, one by one, from the growth substrate. The thin films are then layered, ensuring the alignment of the nanowires is maintained through the stack. The Parylene C stacks were then laminated under heat and pressure to increase the robustness of the multilayer polariser. The PDMS stacks did not require hot bonding and formed robust stacks through layering.

half-wave plate by an angle of θ. Thus, by rotating the half-wave plate by 45°, the optical pump beam was rotated from vertical polarisation to horizontal polarisation. The nanowires-in-parylene samples were placed in the OPTP system, such that the long axes of the constituent nanowires were oriented vertically.

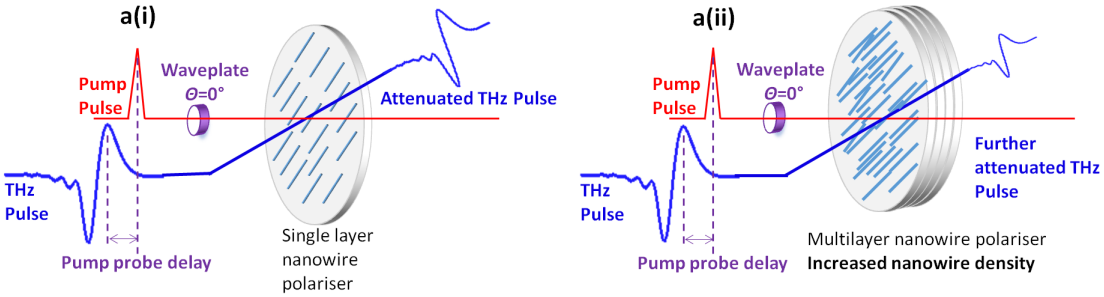

Fig. 7.2: a(i) and a(ii) Schematic diagrams of the OPTP experiment, showing the difference in THz pulse attenuation between the single layer and multilayer polarisers. The nanowires are oriented vertically and the incident THz electric field is vertically polarised. A half-wave plate rotates the polarisation of the 800 nm photoexcitation pump beam by 2θ, where θ is the angle between the vertical and the waveplate axis. The pump beam selectively photoexcites nanowires that are aligned with their long axes parallel to the polarisation of the pump beam. The THz pulse is then absorbed by the photoexcited nanowires. Increasing the area density of the nanowires results in many more nanowire being photoexcited and therefore interacting with the THz wave. This results in stronger attenuation of the THz wave.

As shown in Figure 7.2 the number of layers of polymer-nanowire thin films constituting the polariser was increased in order to increase the modulation depth and extinction ratio without increasing the photoexcitation fluence. As the number of layers is increased, there is an increase in the effective areal density of photoexcited nanowires that interact with the THz pulse. This should lead into a increase in the transient THz absorption which should in turn result in an

increase in modulation depth, dynamic range and extinction.

Modulators consisting of 1,2,3, and 4 layers were made using the PDMS-nanowire thin films. It was not possible to add any more layers, as each single layer was 300 µm thick, so more than 4 layers made the stacks mechanically unstable. However, given the thinness of the GaAs nanowire-Parylene C thin films, it was possible to fabricate modulators consisting of 1,4,8, and 14-layers. The number of layers was purely limited to the number of nanowire wafers available at the time. A picosecond switching time should still be possible with the 14-layer polarisers as the thinness of the 5 µm GaAs nanowire-Parylene C thin films should minimise any dispersion effects which would cause temporal smearing of the transient response.

7.3 Rotation and temporal response

Figure 7.3(a) shows the THz transmission as a function of the optical pump polarisation angle for the PDMS multilayer samples at the highest fluence investigated ($280\,\mu\mathrm{J\,cm^{-2}}$). Similar to the single-layer sample, the THz transmission through the multilayer samples followed the cosine-squared dependence on 2θ described by Malus' Law. Figure 7.3(b) shows the THz transmission ($\frac{E_{on}}{E_{off}}$) as a function of time after photoexcitation as a function of time after photoexcitation. It was found that the modulation depth increased when adding more nanowire-PDMS layers, but lead to slight peak broadening and therefore lengthening of the lifetime. However, given the thickness of the PDMS layer led to mechanically unstable nanowire polariser, and it was not possible to laminate more layers together.

As the Parylene C thin films are so much thinner than the PDMS thin films, it was possible to layer many more thin films together and still maintain the mechanical stability of the multi-layer nanowire polariser. Figure 3(a) shows the transmission of the THz electric field (without nanowire photoexciation), measured across the bandwidth from 0.1 - 4 THz, through vacuum and through 1,4,8,14-layer samples. It was seen that increasing the number of parylene layers, up to 14-layers, is associated with insertion losses of less than 35% across the measurement bandwidth from 0.1 to 4 THz. Figure 7.3(b) shows the THz transmission as a function of the optical pump polarisation angle for the PDMS multilayer samples at the highest fluence investigated ($280\,\mu\mathrm{J\,cm^{-2}}$). Similar to the single-layer sample, the THz transmission through the multilayer samples followed the cosine-squared dependence on 2θ described by Malus' Law.A large increase in modulation depth and extinction is observed with increasing number of nanowire layers. For the single layer sample (Chapter 4), the extinction was less than $\sim 2\%$, but the THz modulation becomes more obvious with increasing number of layers with the best performance seen for the 14-layer nanowire sample. As stated before, the observed increases in extinction, modulation depth and dynamic range are attributed to the increased areal density of

photoexcited nanowires absorbing THz radiation in the multilayer samples. This is why the use of Parylene C as a nanowire encapsulant is key to the success of the polarisers - it is possible to dramatically increase the areal density of nanowires, by layering up several parylene-nanowire thin films. This is not possible with the PDMS, as only a 4 layer modulator could be fabricated.

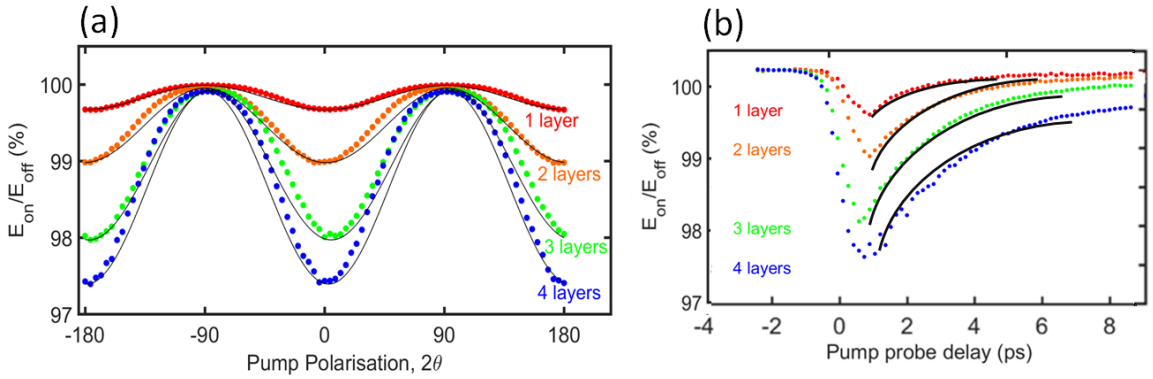

Fig. 7.3: Performance data of the PDMS multilayer polarisers. (a) THz transmission, $E_{\text{on}}/E_{\text{off}}$, through the photoexcited 1-layer, 2-layer, 3-layer and 4-layer PDMS-based polarisers as a function of angle of polarisation (2θ) of the photoexcitation pulse, with a photoexcitation pump fluence of 280 μJ cm^{-2}. Solid black lines represent squared-cosine fits, according to Malus's Law. (c) THz transmission, $E_{\text{on}}/E_{\text{off}}$, through the photoexcited 1-layer, 2-layer, 3-layer and 4-layer PDMS based polarisers as a function time after photoexcitation. The pump was polarised parallel to the nanowire long axes ($2\theta = 0°$) and a photoexcitation pump fluence of 280 μJ cm^{-2} was used. The solid black lines are fits describing monoexponential decay of the photoconductivity at early times after photoexcitation.

The temporal dynamics of modulation were measured for all multilayer samples, with Figure 7.4(b) showing the THz transmission ($\frac{E_{on}}{E_{off}}$) as a function of time after photoexcitation and Figure 7.4(d) showing the photoinduced change in transmission ($\frac{-\Delta E}{E_{off}}$) as a function of time after photoexcitation. By fitting monoexponential functions to the data in Figure 7.4, the decay time constants were extracted for each multilayer sample. The decays were seen to slow with increasing number of nanowire layers, with time constants of 1.1 ± 0.2 ps for the single-layer sample and 3.5 ± 0.3 ps for the 14-layer sample (also shown above with the PDMS samples). Slight curvature of the thicker polarisers, and internal reflections due to air gaps unintentionally incorporated between multiple layers, may be responsible for broadening the transient response of the thicker polarisers. Dispersion effects may occur if the photoexcitation pulse and the THz pulse propagate at slightly different speeds in the polariser, which would result in the observed smearing out of the transient response. The effect of dispersion should, however, be small due to the low thickness (less than 100 microm) of the polarizers, given each GaAs nanowire-Parylene C is less than 10 µm thick. Despite the observed slowing of the transient decay with increasing number of layers, the decay is still on the order of picoseconds even for the thickest 14-layer sample. Therefore the 14-layer polariser maintained picosecond switching speeds while improv-

ing modulation depth significantly.

For the highest fluence of $280\,\mu J\,cm^{-2}$, the extinction ($13.5 \pm 1\%$) was comparable to other graphene and metamaterial-based THz modulators. The modulation depth was measured as -8 dB with a dynamic range of -9 dB. This modulation depth represents a vast improvement over the ultrafast carbon-nanotube based THz polariser described in previous work [72]. What is particularly promising is that the inset of Figure 7.4(c) shows that the modulation depth achieved depends almost linearly on the number of layers constituting the polarisers. This means that there is no obvious saturation of $-\Delta E/E_{\text{off}}$ with increasing number of layers up to the maximum number investigated, 14. This result suggests that this type of polariser could be improved even further by increasing the number of nanowire layers fabricated into the THz polariser. Given that the 14-layer one was only limited to the availability of nanowires wafers at the time, and the thinness of the GaAs nanowire-Parylene C thin films, several layers could potentially be added.

7.3.1 Polarisation response of the 14-layer polariser

I examined the 14-layer nanowire polariser in further detail as it exhibited the best performance. In addition, I also considered its behaviour to be representative of multilayer samples. Figure 7.5(a) shows the dependence of THz transmission on the polarisation of the pump beam at different photoexcitation fluences. Similar to the single-layer polariser, the modulation depth increases sublinearly with increasing photoexcitation fluence (Figure 7.5(b)) and its performance is therefore also limited by the photoexcitation fluence.The modulation data of Figures 7.3, 7.4 and 7.5 were obtained by measuring the transmission of the peak of the THz pulse.

The modulation of the THz peak is broadly representative of the performance of the polariser across the measurement bandwidth, but analysis of the peak alone does not allow us to assess the frequency-dependence of the modulation. To assess the spectral dependence of the photoinduced modulation and the modulation bandwidth achieved by the 14-layer polariser across the frequency range from 0.1 to 4 THz, the entire transmitted THz pulse was measured and Fourier analysis was performed. Figure 7.5(c) shows the photoinduced change in THz transmission, equivalent to the modulation depth, across the measured frequency range for the cases when the photoexcitation pulse is polarised parallel ($2\theta = 0^\circ$, blue dots) and perpendicular ($2\theta = 90^\circ$, pink dots) to the nanowires. When the photoexcitation pulse was polarised perpendicular to the nanowire axis, the photoresponse was minimal throughout the measurement bandwidth. In contrast, when the pump was polarised parallel to the nanowires, strong extinction between 9 and 15% was observed across the entire measurement bandwidth. This indicates that the polariser has achieved broad bandwidth modulation of the THz transmission.

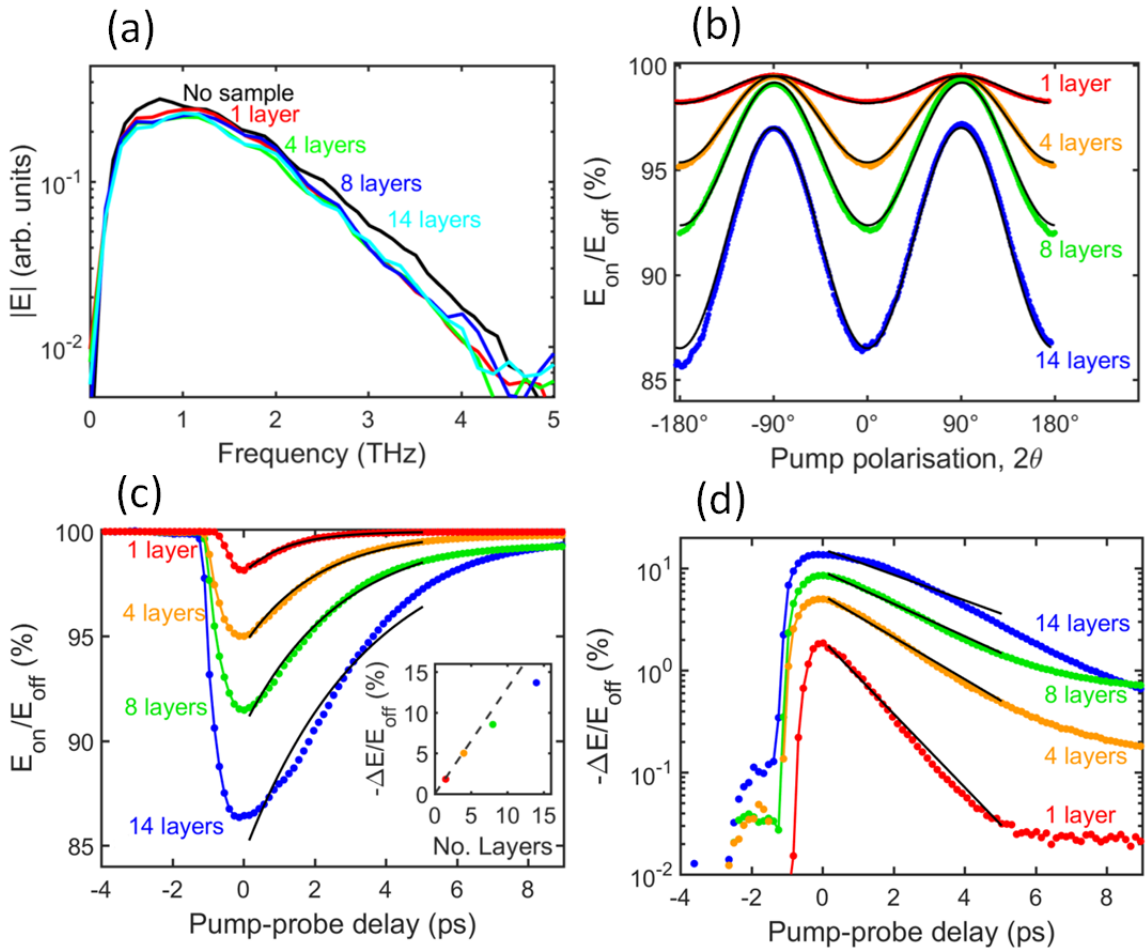

Fig. 7.4: (a) THz electric field transmitted through vacuum and through the 1,4,8,14-layer samples. (b) THz transmission, $E_{\mathrm{on}}/E_{\mathrm{off}}$, through the photoexcited 1-layer, 4-layer, 8-layer and 14-layer nanowire polarisers as a function of angle of polarisation (2θ) of the photoexcitation pulse. Solid black lines represent squared-cosine fits, according to Malus's Law. (c) THz transmission, $E_{\mathrm{on}}/E_{\mathrm{off}}$, through the photoexcited 1-layer, 4-layer, 8-layer and 14-layer polarisers as a function time after photoexcitation. (d) Photoinduced change in transmission, $-\Delta E/E_{\mathrm{off}}$, through the same polarisers plotted on a logarithmic ordinate axis. The lines represent single exponential decays fitted to the experimental data, with time constants of 1.2 ps, 2.1 ps, 2.7 ps and 3.5 ps for the 1-layer, 4-layer, 8-layer and 14-layer polarisers, respectively. The inset in (c) shows the maximum photoinduced change in THz transmission, $\Delta E/E_{\mathrm{off}}$, equivalent to modulation depth, as a function of the number of layers constituting the polariser. All data were taken with the photoexcitation pulse polarised parallel to the nanowire axes ($2\theta = 0°$) and with a photoexcitation pump fluence of 280 μJ cm^{-2}. Data in the inset were measured with the pump–probe delay at $t = 0$ ps.

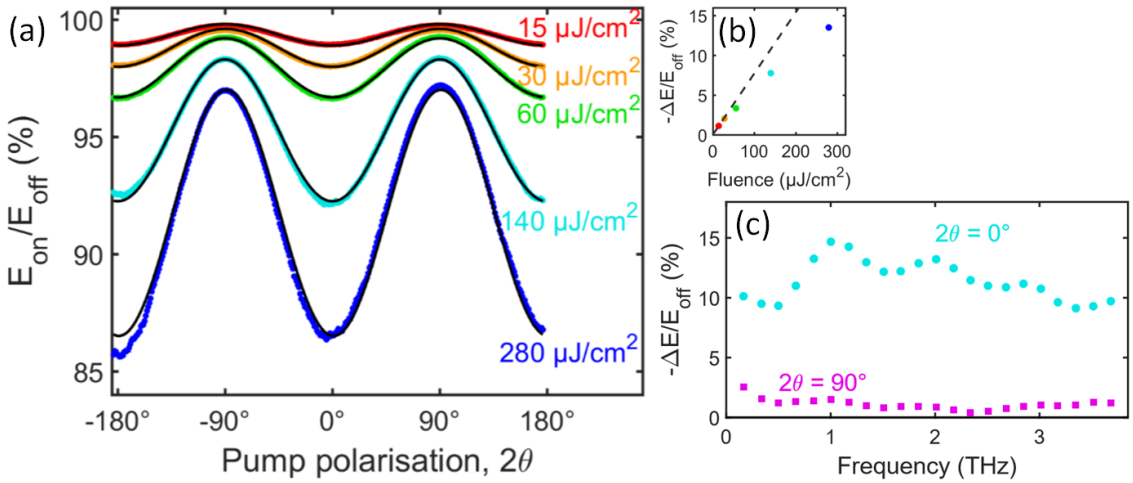

Fig. 7.5: (a) THz transmission, E_{on}/E_{off}, through the 14-layer polariser as a function of angle of polarisation (2θ) of the photoexcitation pulse after photoexcitation with pump fluences of 15, 30, 60, 140 and 280 μJ cm^{-2}. (b) Photoinduced change in transmission, $-\Delta E/E_{off}$, equivalent to modulation depth, as a function of pump fluence for a 14-layer polariser. The dashed line shows the expected values if the photoconductivity scaled linearly with pump fluence. Data was measured with the pump-probe delay at $t = 0\,ps$ and a half wave plate angle at $2\theta = 0°$. Data in (a) and (b) were measured with the pump–probe delay at $t = 0$ ps at which $-\Delta E/E_{off}$ is maximum. (c) Frequency-dependence of the modulation depth, $-\Delta E/E_{off}$, achieved by the 14-layer polariser. Data were taken with the photoexcitation pulse polarised parallel to the nanowire axes ($2\theta = 0°$, cyan circles) and perpendicular to the nanowire axes ($2\theta = 90°$, magenta squares) with a photoexcitation pump fluence of 280 μJ cm^{-2}.

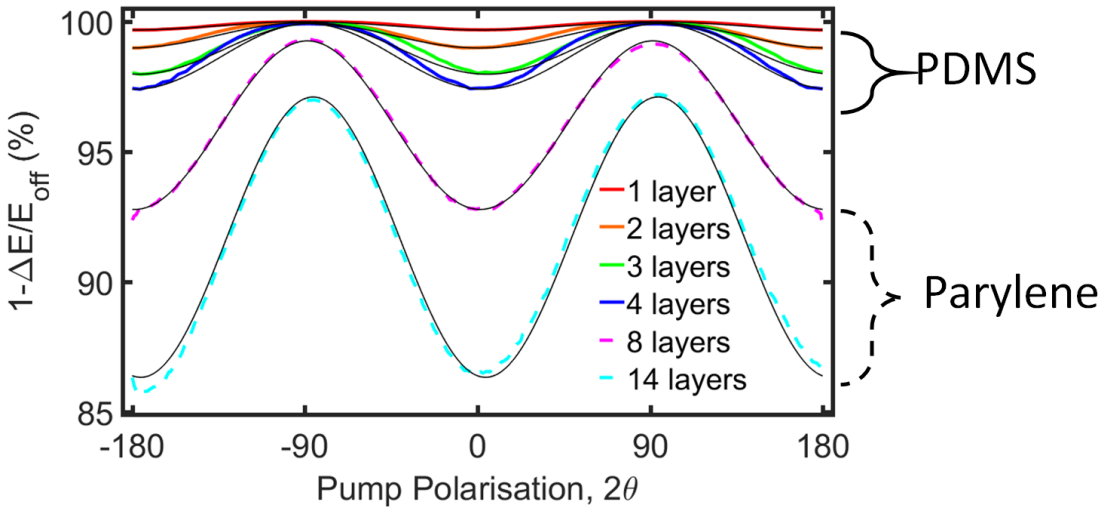

Fig. 7.6: Comparison of the performance of the PDMS and Parylene C polarisers. The PDMS performance data is depicted by the solid coloured lines, the Parylene C performance data is given by the dotted coloured lines. It is clear to see that by increasing the number of layers, the polariser performance dramatically improves. As the Parylene C thin films were thin enough, several more layers could be laminated together thus greatly increasing the areal density of the nanowires and the photoexcitation response of the nanowires.

7.4 Communications system

There is also much scope for further development and improvement of these polarisers. It is thought that the future generations of the modulators could be improved by using the same fabrication process, and instead changing the properties of the nanowires. For example, the nanowire electronic characteristics could be modified via doping, shell-coating, or wrapping in π-conjugated polymers [261], the carrier lifetimes and therefore switching speeds can be controlled. Furthermore, it would be interesting to investigate other nanowire materials systems, both III-V semiconductors and beyond. In addition, nanowire alignment is very important for a high performing device, so optimising the growth recipe further would also in turn provide scope to increase nanowire performance. Furthermore, the modulation depth and extinction continued to increase almost linearly as the number of layers was increased to 14. This observation suggests that further improvements to this type of multilayer nanowire polariser will be possible by increasing the number of layers and by improving the nanowire alignment and density further. Ease of fabrication means that thinner layers of Parylene C could be deposited, or even different Parylenes/other CVD polymers could be used to realise this.

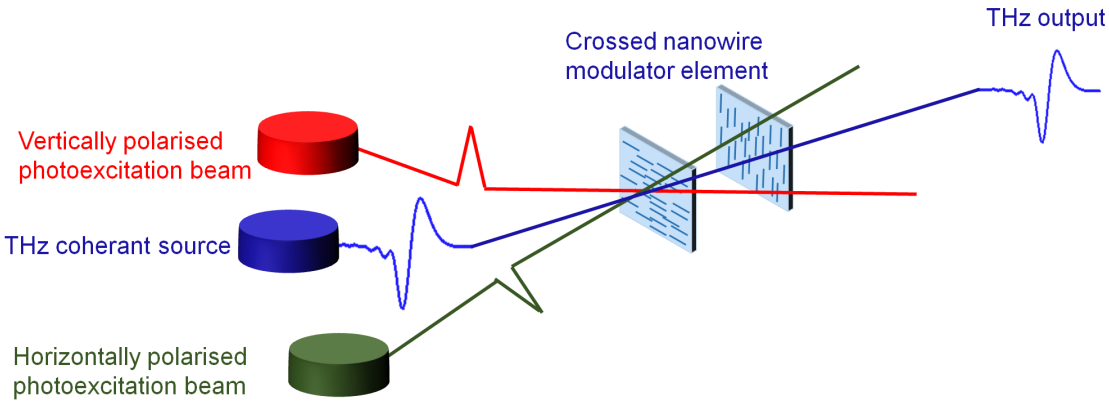

Fig. 7.7: Schematic of a suggested high speed THz communications system. Vertically and horizontally aligned nanowires are arranged to form a CNME. Two linearly polarised photoexcitation beams that are aligned vertically (depicted in red) and horizontally (depicted in green) are used to photoexcite the horizontally and vertically aligned films of nanowires. When both are photoexcited, the CNMEs act has crossed polarisers and in theory no THz is transmitted. When both are not photoexcited, the THz wave passes through. The photoexcitation laser sources can be programmed with a given output, and the resulting THz output can then be detected.

Ultimately, however, an ultrafast THz communications system could be achieved by using these multilayer polarisers. By utilising two nanowire polarisers orientated perpendicular to each other, and increasing the number of layers, a modulation depth close to 100% could also be achieved, with THz radiation attenuated in both polarisation directions. This is depicted with a schematic in Figure 2.7. Vertically and horizontally aligned nanowires thin films are arranged to form a crossed nanowire modulator element (CNME). Two linearly polarised photoexcitation

beams that are aligned vertically (depicted in red) and horizontally (depicted in green) are used to photoexcite the horizontally and vertically aligned films of nanowires. The red and green are for illustrative purposes and bear no significance to the photoexcitation wavelength used. When both the vertical and horizontal aligned nanowires are photoexcited, the CNMEs act has crossed polarisers and in theory, the THz wave will not be transmitted. When both the vertical and horizontal nanowire elements are not photoexcited, the THz wave passes through. The photoexcitation laser sources can be programmed with a given output which dictates the activation of the CNMEs, and the resulting THz output can then be detected.

7.5 Conclusion

In summary, I have fabricated and characterised an ultrafast THz modulator based on GaAs nanowire-Parylene C thin films. The modulator demonstrated a carrier lifetime of approximately 1ps, allowing for picosecond switching speeds needed for next generation ultrafast THz communications applications. The modulator operates over a broad bandwidth between 0.1 THz and 4 THz, which is the highest bandwidth recorded to date for THz modulation. By fabricating a 14-layer polariser the extinction increased from $\sim 2\%$ to over $\sim 13\%$ when compared to a single layer GaAs nanowire-Parylene C modulator. In addition, the modulation depth was improved from from 17 dB to -8 dB and the dynamic range was improved from from -18.8 dB to -9 dB respectively. These values are comparable to those observed for graphene-based THz modulators and surpass those for any previous modulators based on nanostructures, such as unaligned carbon nanotubes. In addition, these modulators have a simple fabrication process: the nanowires are coated with Parylene C, the resultant thin film is then dissected into even sized pieces and several layers are laminated together using a hot bonding process, ensuring the directionality of the nanowires is maintained throughout the stack.

Chapter 8

Towards Flexible Nanowire Diodes: Solar Cells and Photodetectors

This chapter described the research undertaken to develop the fabrication process for flexible nanowire solar cells and photodetectors.

A brief discussion on the semiconductor physics of III-V materials was given to understand the reasoning behind flexible diode design. Photodetectors and photovoltaic devices are devices based on diodes, operated in different quadrants of the IV curve. The bulk of this chapter was focussed on the work carried out on optimising the fabrication process of these nanowire devices. As the nanowire-Parylene C thin film process had already been discussed extensively in Chapter 4, and was only mentioned briefly in this chapter. The InP nanowires used in this thesis were grown by Dr Amira Ameruddin, in Professor Jagadish's lab at the Australian National University. The nanowires were shipped to Cambridge for device fabrication processes that I carried out, which are described in this Chapter. A dry etching process, designed to selectively remove the Parylene C and leave the nanowire tips ready for contacting was developed. Three different machine systems were tested: the Diener etcher, Barrel etcher, and Phillips RIE, with the best technique taken forward for subsequent device processing. Ohmic contact formation then required further optimisation as high temperature annealing (the process typically used for alloyed contacts) could not be used due as Parylene C degrades when exposed to high temperature. Clean chamber processing and surface passivation were used to form sufficient ohmic contacts. On optimising these processes, a simple Schottky barrier solar cell was fabricated, with a power conversion efficiency of 0.02%. The Schottky barrier solar cell was characterised by Dr Zihyuan Li at Professor Jagadish's lab at the Australian National University.

The findings in this chapter have pushed the field of flexible nanowire solar cells in a new direction, by demonstrating an early stage, substrate-free device on InP nanowires that were not yet optimised for solar cell devices. To conclude this chapter, I outlined the further work needed to yield the first, truly substrate-free, flexible nanowire solar cell.

8.1 Current nanowire diodes

The basic definition of a diode is a semiconductor device which allows current flow primarily in one direction [262]. Depending on the device architecture and materials choice, diodes have found use in several applications such as rectifiers, signal limiters, voltage regulators, switches, signal modulators, signal mixers, oscillators, as well as photovoltaic devices and photodetectors - the two devices of interest in this thesis [263]. Using nanowires to fabricate photodetectors and photovoltaic devices offers scope to both improve device performance through favourable light absorption and charge carrier properties, and extend device capabilities to applications where rigid wafer- based electronics are unsuitable. For the purpose of the discussion in this chapter, it was deemed that the photodetector and photovoltaic device would share the same device architecture, but be operated in different quadrants of the IV curve. A solar cell is operated in the fourth quadrant as it is generating power, a photodetector is operated in the third quadrant in reverse bias to keep the reverse saturation current low to enable light detection. These concepts are discussed in further detail later in this section.

8.1.1 Nanowire solar cells

Increasing world population, energy demand and dwindling fossil fuel sources coupled with greater public awareness of the environmental impact of fossil-based fuels have all driven research into alternative, green and renewable energy sources [264]. The solar power received by the earth from the sun is several orders of magnitude higher than our current power demands. Indeed, the energy received by the earth from the sun in one hour could provide 80% of the energy that was consumed globally in 2008 [54]. Therefore, photovoltaic (PV) devices have the potential to partially replace current energy technologies that rely on carbon-based fuels. Uptake of solar cells has been slow as they provide a more expensive $/W than fossil fuel technology. Government tariff incentives have been used worldwide in an effort to increase the usage of solar cells. While it is always beneficial to have buy-in and confidence in a form of a government subsidy, ultimately, this is not a long-term solution for sustaining the energy demand. Silicon solar cells have dominated the world market for PV technology, in an effort to minimise the cost of PV devices, despite their low conversion efficiencies and high installation cost. In addition, silicon solar cells are fast approaching the theoretical limit of their efficiency - the Shockley-Queisser limit, which is defined as the maximum theoretical efficiency for a single p-n junction solar cell under ideal conditions [115]. For a silicon solar cell, the Shockley-Queisser limit would be a power conversion efficiency of 34%.

III-V materials are ideal candidates for photovoltaic applications as their band gaps fall in the peak of the solar spectrum. Furthermore, their electrical and optical properties gives rise to the possibility of breaking the Shockley-Queisser limit [115]. Sharp have produced an National Renewable Energy Laboratory (NREL) certified, concentrated multijunction (InGaP/GaAs/InGaAs)

solar cell with a power conversion efficiency of 37.9% [116]. However, multijunction solar cells are complex and expensive to fabricate and face issues with lattice mismatch between the layers. Furthermore, concentrator equipment can also be expensive, bulky and requires a specialist cooling system to prevent the solar cell from being damaged through overheating.

Nanowire array solar cells offer an alternative platform to thin film photovoltaic devices, with intense research focussing on nanowire growth, theoretical modelling and device fabrication [125]. Nanowire arrays benefit from light trapping and scattering effects which in turn lead to increased light absorption. Furthermore, their high aspect ratio structure lends themselves to thin junctions and therefore efficient carrier collection, as explained in Chapter 2. At the time of writing, the best reported efficiency of a GaAs nanowire array solar cell was 15.3% [113], and 17.8% for an InP solar cell [126]. As explained in Chapters 3 and 5, while wafer scale electronics provide sufficient functionality for several important applications, the brittle and delicate nature of the crystalline growth wafers limits their use in other applications.

Flexible solar cells, on the other hand, would give rise to PV usage in novel applications and industries. Such solar cells may be fabricated by embedding vertically aligned nanowires in a flexible polymer matrix and fabricating a device from the resultant thin film. Flexible solar cells may enable several interesting photovoltaic coatings on vehicles, buildings, windows, or even integration into garments. This is where the real value of flexible nanowire photovoltaics lies: a simple, cost effective way to embed highly efficient but potentially expensive nanowire PV into other objects for energy harvesting. The work in chapter aims to develop a fabrication process to build such a device.

8.1.2 Nanowire photodetectors

Over the past 50 years, progress in semiconductor devices have completely transformed the performance, and therefore the usage and uptake of electronic devices. Photodetectors - one of the most important optoelectronic devices - convert light into electrical signals and have found important use in numerous applications, from sensing/detection to communications. The accurate detection of light across the electromagnetic spectrum - UV, Visible, IR, THz - is critical for several applications. As demands on device performance, speed, operation and cost continue, new methods are sought to find increasingly smaller, more efficient and sensitive photodetectors.

III-V materials are also ideal candidates for photodetectors. By having fine control of the III/V stoichiometry during the growth process, their band gap may be engineered to detect light at specific wavelengths. Furthermore, their nanoscale dimensions and material purity enables high sensitivity and low dark current needed for single photon detection - vital in quantum computing applications.

On-substrate nanowire photodetectors have been extensively demonstrated in the literature - both as single nanowire and nanowire arrays architectures. Flexible nanowire photodetectors have also been demonstrated - but similar to flexible solar cell - there has been a distinct lack of

vertically-aligned, substrate-free devices. Flexible photodetectors increases device engineering possibilities and allows for the integration of photodetectors into flexible, moldable rugged devices, large area devices, as well as integrated nanosystems which were previously out of reach. The work in this chapter hopes to develop a fabrication process to enable this technology.

8.2 Flexible device design

Solar cells and photodetectors based on a pn junction can essentially have the same diode-based device structure, and are treated as such in this Section. Fabricating such a device is not a trivial matter, and therefore thorough understanding of both the semiconductor physics and materials properties are needed to optimally design a flexible nanowire solar cell.

8.2.1 Current flow in a pn junction

In the literature, pn and pin junction structures are used for wafer based nanowire solar cells. As shown in Figure 8.1, when p and n material are brought into contact, a depletion region of width w is formed. The concentration gradient causes the diffusion of electrons from the n side (an area of a high concentration of electrons) to the p side (an area with a low concentration of electrons). This results in a lack of electrons and holes either side of the junction - resulting in a depletion region.

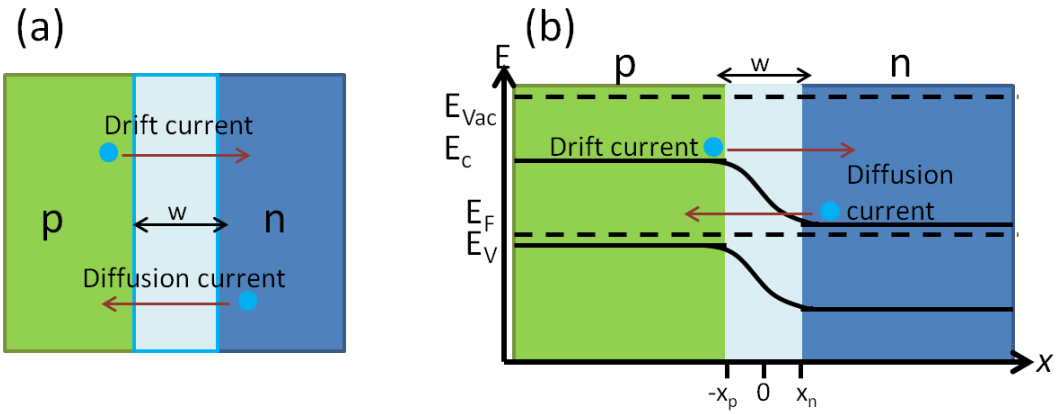

Fig. 8.1: Schematic diagram for (a) a pn junction and (b) the band diagram for a pn junction depicting the formation of the depletion layer and the direction of the drift and diffusion currents

The built in potential V_0 arises from the depletion region, and is given by:

$$qV_0 = E_{fn} - E_{fp}, \tag{8.1}$$

where E_{fn} and E_{fp} refer to the Fermi levels of the n and p doped material respectively and q is elementary charge. V_0 may also be written as

$$V_0 = \frac{kT}{q} ln(\frac{N_A N_D}{n_i^2}), \tag{8.2}$$

where k, T refer to the Boltzman constant and temperature, and N_A, N_D and n_i refer to the concentration of acceptors, concentration of donors and the intrinsic carrier concentration respectively.

The overall depletion region width w is the sum of the depletion widths either side of the junction x_p and x_n.

$$w = x_p + x_n, \tag{8.3}$$

and can also be written as

$$w = (\frac{2\varepsilon_0 \varepsilon_r V_0}{q})^{1/2} [(\frac{N_A}{N_A N_D + N_D^2})^{1/2} + (\frac{N_D}{N_A N_D + N_A^2})^{1/2}], \tag{8.4}$$

where $\varepsilon_0, \varepsilon_r$ refer to vacuum and relative permittivity.

In materials that are heavily doped or metallic, a depletion region does not form as the voltage drop is essentially screened by a large number of free carriers. The depletion region forms on the side with less doping, and consequently a lower number of free carriers.

As shown in Figure 8.1, the diffusion current arises from the diffusion of majority carriers (i.e. electrons travelling from the n to the p side, and holes travelling from the p to the n side). Drift current refers to minority carriers that are swept across the junction by the electric field arising from the depletion region (holes are swept from the n side to the p side, and electrons from the p side to the n side) where they become minority carriers and have a smaller chance of recombining before being collected by the electrodes.

As described in Chapter 2, the pn junction may be formed axially or radially. Axial structures are more straightforward to contact then radial structures, where selective etches need to be carried out to selectively contact the p and the n portions of the nanowires [48]. Radial structures, however, are believed to offer high performance devices as the thickness of the doped layers can be very thin - much less than the diffusion length of the minority carrier, which reduces the chance of unwanted recombination and to ensure maximum carrier collection [23].

8.2.2 Light generated current

Current flow in a pn junction can be deduced from the Continuity equation (equation 8.5), which describes the change in carrier number with time $\frac{\delta(\Delta p)}{\delta t}$, $\frac{\delta(\Delta n)}{\delta t}$ and considers the carrier lifetime $\tau_{h,e}$ for electrons and holes respectively, the diffusion current and the drift current. $\mu_{h,e}$ and $D_{h,e}$ refer to the carrier mobility and diffusion coefficient for electrons and holes respectively. We assume that there are negligible fields outside the depletion region, no recombination occurs

in the depletion region due to the lack of carriers, the injected minority carrier concentration (carriers arriving from across the junction) is much less than the majority carrier concentration, and that there is an abrupt junction. The Continuity equation for holes is

$$\frac{\delta(\Delta p)}{\delta t} = -\frac{\Delta p}{\tau_h} - \mu_h \varepsilon \frac{\delta(\Delta p)}{\delta x} + D_h \frac{\delta^2(\Delta p)}{\delta x^2}. \tag{8.5}$$

A high performance solar cell requires that light generated minority carriers are swept across the junction and collected by the electrodes before they have the chance to recombine. This means that materials with a long minority carrier lifetime and diffusion length are desired. This is achieved through the growth of high purity, defect free III-V material and thin layer thicknesses. However, III-V materials need to be of a minimum thickness to absorb enough light to produce light generated carriers. In addition, high doping densities naturally increase the amount of carriers, but also increases the amount of defects and trap states. As always, there is a tradeoff between the different parameters, in order to design the highest performing cell possible.
The Continuity equation can therefore be used to calculate the reverse saturation current I_s:

$$I_s = A[e(\frac{D_e}{L_e})\frac{n_i^2}{N_A} + q(\frac{D_h}{L_h}) + \frac{n_i^2}{N_D}], \tag{8.6}$$

where A refer to the area, D_e, L_e, D_h, L_h refer to the diffusion coefficient and diffusion length of electrons and holes respectively.

In reverse bias, the depletion width gets wider, and so in principle there should not be any current arising from majority carriers diffusion across the junction as the barrier (i.e. depletion width) is too high. However, in practice the reverse saturation current arises from diffusion of minority carriers (holes from n side) into the depletion region where they recombine with electrons that are in traps and defects. These carriers are thermally generated and move across the depletion region under reverse bias. As unwanted recombination also gives rise to an increased reverse saturation current, I_s can be seen as a measure of device quality and therefore a loss of photo generated charge carriers at the defects due to recombination. The key here is to ensure excellent quality III-V materials. The current of a diode (without illumination) is

$$I = I_s(exp(\frac{qV}{kT}) - 1). \tag{8.7}$$

The light generated current I_L modifies the I-V relationship to

$$I = I_s(exp(\frac{qV}{kT}) - 1) - I_L. \tag{8.8}$$

Solar cell operation is where a pn junction is illuminated, the curve is shifted downwards in the y direction, as the direction of the light generated current flows in the opposite direction to the diffusion current. When light is shone on the junction, new electron hole pairs are formed.

The newly formed holes on the n side and electrons on the p side are swept across the junction where they become majority carriers, so they can contribute to light generated current before recombining. If the newly generated minority carrier recombines before it drifts across the junction and is collected by the electrode, then it it is wasted. Therefore, it is important to ensure the minority carriers are swept across the junction by the electric field. Finally, the power P is defined as $P = IV$, so as the voltage increases, the power increases too.

8.2.3 Efficient carrier collection

In order to get efficient carrier collection, ohmic contacts must be formed between the metal and semiconductors. Typically, an alloyed Ti/Au contact is used on the p side, and ITO is used as the top contact on the n side. As shown by the band diagrams in Figure 8.2, the current flows freely in both directions for an ohmic contact. In a Schottky contact however, the current can only flow in one direction due to the presence of a potential barrier. For an n-type semiconductor, the work function of the metal ϕ_m needs to be less than than the work function of the semiconductor ϕ_{sc} to form an ohmic contact.

While this gives a useful basis in device design, in reality complications arising from Fermi level pinning and surface states may not give expected results. Therefore, passivation and clean processing steps are vital to ensure high quality,ohmic contact formation between the metal and semiconductor material.

8.2.4 Figures of merit for solar cells

There are several standard figures of merit used to describe and therefore compare solar cell performance. Figure 8.3 shows the short circuit current and the open circuit voltage. The short circuit current I_{sc} is where the voltage is $V = 0$, and depends on the current generated from light generated carriers. Generally, an increase in light generated carriers is an increase in the short circuit current. The open circuit voltage V_{oc} is where the current $I = 0$, and is an indication of the maximum voltage available from the solar cell. Generally high I_{sc} and V_{oc} are indicative of good solar cell performance. The maximum power point (MPP) is read at the maximum current I_{mp} and maximum voltage V_{mp} before increasing the forward bias causes an overall decrease in current. This is marked in Figure 8.3. As $P = IV$, maximising I and V results in a higher MPP.

The fill factor can be described how much the IV curves fills the maximum power point range, and is given by

$$FF = \frac{I_{mp}V_{mp}}{I_{sc}V_{oc}}, \tag{8.9}$$

where the red area in Figure 8.3 is $I_{sc}V_{oc}$ and the yellow area is $I_{mp}V_{mp}$. A fill factor nearing 1, is indicative of ideal solar cell performance.

The power conversion efficiency η is where P_{in} the power into the cell is divided by the power output of the cell. Efficient carrier collection at the electrodes is important in achieving a

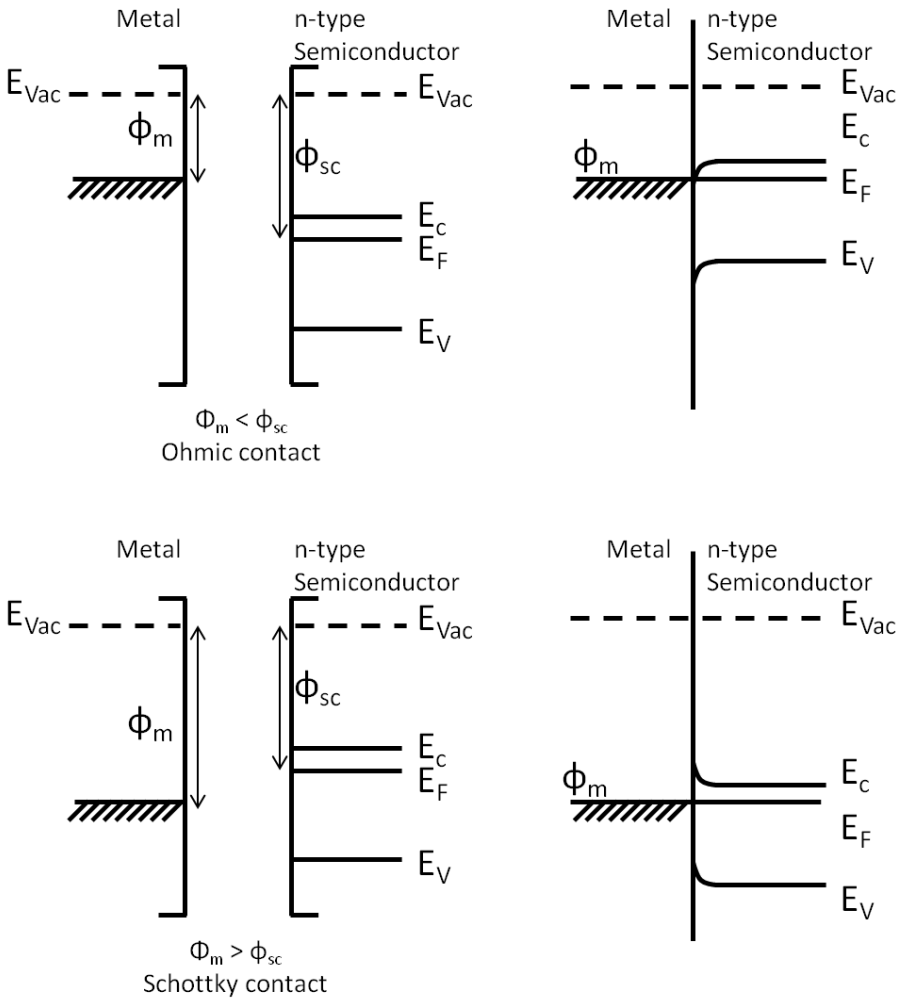

Fig. 8.2: Band diagrams for an ohmic and Schottky contact formation between a metal and an n-type semiconductor. For an n-type semiconductor, the work function of the metal ϕ_m needs to be less than than the work function of the semiconductor ϕ_{sc} to form an ohmic contact.

high power conversion efficiency:

$$\eta = \frac{V_{oc} I_{sc} FF}{P_{in}}. \tag{8.10}$$

8.2.5 Theory of photoconductive behaviour

Photoconductivity is defined as the change in electrical conductivity when the photoconductive material is under illumination [101]. As a result photoconductive materials have been used to detect light [265]. A summary of the detailed derivation described by Soci *et al.* is given below[57].

The intrinsic photoconductivity σ is defined as

$$\sigma = en\mu, \tag{8.11}$$

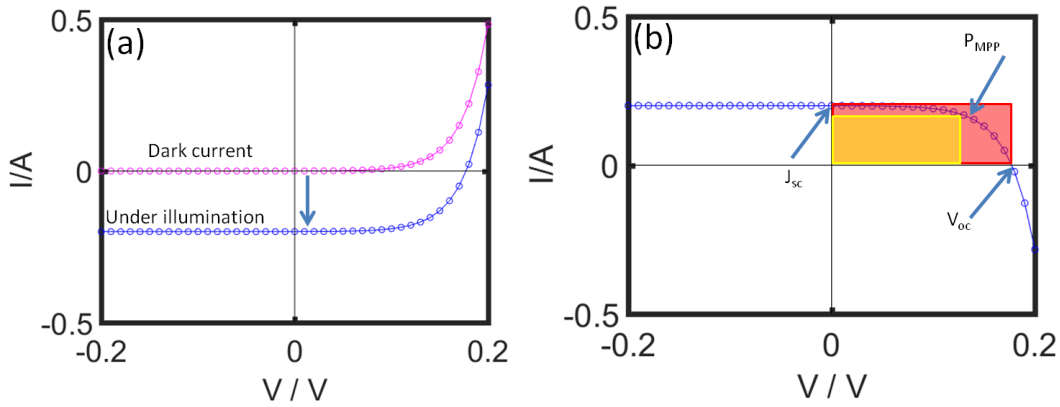

Fig. 8.3: IV curves showing ideal solar cell operation. (a) shows how the IV curve shifts down due to light generated current I_L. (b) shows the y axis flipped as per convention when the diode is generating energy. The short circuit current I_{sc}, open circuit voltage V_{oc} and maximum powerpoint *MPP* are all marked. The fill factor *FF* is calculated by dividing the red area $I_{sc}V_{oc}$ by the yellow area $I_{mp}V_{mp}$.

where e is the electronic charge, n is the charge carrier density (for simplicity, in this discussion only the photoconductivity arising from electrons is considered) and μ is the carrier mobility. In the presence of an applied field however, the carrier drift velocity needs to be taken into consideration. The current arising from this applied field is defined as

$$I = \sigma FS. \tag{8.12}$$

The applied field F is defined as $F = V/l$ where V is the applied voltage and l is the nanowire length. If we define the carrier drift velocity v as $v = \mu F$ and S as the non depleted cross section surface of the nanowire, and incorporate equation 8.11 then equation 8.12 becomes

$$I = en\mu FS, \tag{8.13}$$

which simplifies to

$$I = envS. \tag{8.14}$$

Under illumination, the electrical conductivity changes due the the optical generation of free carriers. The change in conductivity was be defined as the *photoconductivity* $\Delta\sigma$ and is defined as

$$\Delta\sigma = \sigma_{light} - \sigma_{dark}, \tag{8.15}$$

where σ_{light} may be expressed as

$$\sigma_{light} = e(n+\Delta n)(\mu+\Delta\mu). \tag{8.16}$$

As shown in equation 8.11, the intrinsic conductivity σ also depends on carrier mobility μ and charge carrier density n, so equation 8.16 becomes

$$\Delta\sigma = e(\mu\Delta n + n\Delta\mu + \Delta n\Delta\mu). \tag{8.17}$$

For the purpose of this discussion, we can assume that $\Delta\mu$ is small and therefore these terms can be considered negligible. It can be assumed that $\Delta\sigma$ can now be written as

$$\Delta\sigma = e(\mu\Delta n). \tag{8.18}$$

From equation 8.12, we can deduce that the photocurrent I_{pc} arising from $\Delta\sigma$ is

$$I_{pc} = \Delta\sigma FS, \tag{8.19}$$

and by substituting $\Delta\sigma$, equation 8.19 becomes

$$I_{pc} = e(\mu\Delta n)FS. \tag{8.20}$$

Assuming steady state conditions and constant illumination 8.20 can be modified to

$$I_{pc} = eF\mu\left[\frac{4}{\pi ld^2}(P_{abs}/\hbar\omega)\tau S\right], \tag{8.21}$$

where the absorbed power P_{abs} is defined as

$$P_{abs} = \eta^* P_{opt}, \tag{8.22}$$

and P_{opt} is the incident optical power, ω is the optical frequency, η^* is the effective carrier photogeneration quantum efficiency.
The optical generation rate g_d which defines how many free carriers are generated under illumination is

$$g_d = \eta^*(\frac{P_{opt}/\hbar\omega}{V_{nw}}), \tag{8.23}$$

where V_{nw} is the nanowire volume, defined as the volume of a cylinder $V_{nw} = \pi ld^2/4$ where l and d are the nanowire length and diameter, respectively. Substituting V_{nw} gives

$$g_d = 4\eta^*(\frac{P_{opt}/\hbar\omega}{\pi ld^2}). \tag{8.24}$$

Photoexcited carriers eventually relax to the ground state - the time in which this happens is the photoexcited carrier lifetime, τ. Under steady state conditions, and assuming constant

illumination, $\Delta n(t)$ — the change in carrier density — is constant and can be written as

$$\Delta n(t) = g_d \tau. \tag{8.25}$$

8.2.6 Photodetector figures of merit

Photodetectors are operated in the fourth quadrant, where the device is under reverse bias. The results in increasing the width of the depletion region such that very few carriers are able to diffuse across the junction. This essentially 'turns off' the depletion current, so any current change viewed arises only from photogenerated carriers. High performance photodetectors therefore must be able to absorb photons efficiently, have a high collection probability and low dark current.

Several figures of merit can be used to quantify photodetector performance. The responsivity R_λ is described as the generated photocurrent per Watt of incident photon power, and can be expressed as

$$R_\lambda = \frac{I_{pc}}{\phi A}, \tag{8.26}$$

where ϕ is the incident photon power, A is the area. R_λ can also be expressed as

$$R_\lambda = \eta_e g(q\lambda/hc), \tag{8.27}$$

where η is the external quantum efficiency, λ is the photon wavelength, q is the elementary charge, c is the speed of light and h is the Planck constant. η_e, the external quantum effiency, is the fraction of incident photons that generate electron-hole pairs which contribute to photocurrent:

$$\eta_e = \eta_i(1 - R_{mat})(1 - exp(^{-\alpha x})), \tag{8.28}$$

where η_i is the internal quantum efficiency, R_{mat} is the reflectance of the material, α is the absorption coefficient of the material and x is the material thickness. For III-V materials, the optimum light absorption occurs when the x is on the order if $1/\alpha$ (around 1 µm). However, thinner layers allow for fast carrier transit time and increased response speed. As can be seen, it is a trade of between external quantum efficiency and response speed.

Photoelectric gain g, is the number of electron-hole pairs which pass between the detector electrodes per photon absorbed,

$$g = \frac{\tau}{\tau_t}, \tag{8.29}$$

where τ_t is the carrier transit time before it reaches the detector electrodes. If $\tau > \tau_t$ it means that the photogenerated carriers are able to reach the detector electrodes before recombination occurs, and can therefore be cycled around the photodetector circuit again, leading to higher photoconductivity.

The detectivity D is defined as the inverse of NEP (noise equivalent power)

$$D = \frac{1}{NEP}, \tag{8.30}$$

where

$$NEP = \frac{I_N}{R_\lambda} \tag{8.31}$$

and I_N is the detector noise current. The noise in a photodetector normally arises from thermal noise (arising from fluctuation of carrier population) or shot noise (arises from random arrival of carriers to the detector electrodes).

The specific detectivity D^* is the detectivity D normalized to 1 cm^2 and 1 H bandwidth assuming the noise is proportional to $(A\Delta f)^{1/2}$, where Δf is the bandwidth

$$D^* = \frac{R_\lambda (A\Delta f)^{1/2}}{I_N}. \tag{8.32}$$

I_N is defined as

$$I_N = (2eI_s\Delta f + \frac{4kT\Delta f}{R_d})^{\frac{1}{2}}, \tag{8.33}$$

where R_d is the differential resistance. Substituting I_N into equation 8.32 gives

$$D^* = \frac{R_\lambda (A\Delta f)^{1/2}}{(2eI_s\Delta f + \frac{4kT\Delta f}{R_d})^{\frac{1}{2}}} \tag{8.34}$$

The photoconductive gain G of a photodetector can be defined as ratio of detected carriers N_{DC} per absorbed photos N_{Ph}

$$G = \frac{N_{DC}}{N_{Ph}}. \tag{8.35}$$

Detected carriers are assumed to be those with contribute to photocurrent and so $N_{DC} = I_{pc}/e$. The absorbed photons can also be defined as $N_{Ph} = P_{Abs}/\hbar\omega$ hence equation 8.36 can modified to

$$G = \frac{I_{Pc}/e}{P_{Abs}/\hbar\omega}. \tag{8.36}$$

Nanowire photodetectors typically have high photoconductive gain as they possess high mobility due to advances in nanowire growth techniques. This has allowed for high purity, defect-free nanowires to be grown. Furthermore, nanowire arrays enhance photon absorption due to light trapping and scattering within the array.

8.3 Fabrication optimisation

The bulk of the work in this Chapter has been focussed on optimising the fabrication process for a flexible nanowire solar cell. Previously published work on non-flexible nanowire array devices have shown that such devices are generally fabricated as follows: growth substrates are patterned, either by electron beam lithography [44], substrate conformal imprint lithography [113] or nanoimprint lithography [128] to clearly define the nanowire spacing and diameter. The nanowires are grown epitaxially, to define the nanowire lengths and to form semiconductor junctions. The nanowire array is planarised with a polymer, then etched back to reveal the nanowire tips after which a transparent top and metallic bottom contacts are deposited and annealed [124]. There have also been reports of other device architectures, such as Schottky barrier solar cells which use Schottky contact between one of the metals and the semiconductor for for charge separation [129], and hybrid nanowire-polymer devices which use a conducting 'p-type' polymer such as spiro-OMETAD [119] or P3HT to form a junction with the n doped nanowires.

This has formed a good basis for the design of a flexible nanowire solar cell fabrication process. The steps are outlined in Figure 8.4. Firstly, the nanowires are grown vertically on a substrate (step (1)) and encapsulated using Parylene C (step (2)). The Parylene C is then selectively etched using reactive ion etching (RIE) (step (3)) to expose the nanowire tips for contacting. A Ti/Au top contact (step 4) was applied using electron beam (EB) evaporation. The thin film was then carefully removed from the substrate and backed onto a carrier substrate to deposit an indium tin oxide (ITO) top contact (step (5)) using sputter coating.

Given the need to carefully engineer each process step, vapour-liquid-solid (VLS) grown undoped InP nanowires were used for the optimisation process, as they are relatively straightforward to grow in wafer scale amounts, when compared to selective area epitaxy (SAE) grown nanowires. As several samples had to be made to fully characterise and understand the parameter space at each step, nanowires which were in plentiful supply were deemed to be the most useful at this stage. The InP nanowires used in this Chapter were grown by Dr Amira Ameruddin, in Professor Jagadish's lab at the Australian National University. Nanowire arrays specially optimised and grown for high performance solar cells could then be used at a later stage, once each of the fabrication steps was optimised.

A study of the materials choice of the polymer were considered in Chapter 5. Of the polymers tested, Parylene C was found to be the optimum polymer matrix. For a detailed discussion of the suitability of Parylene C as a polymer matrix, please refer to Section 5.3. To summarise: Parylene C was found to sufficiently encapsulated the nanowires so they retained their vertical alignment, yet did not adhere too firmly to the growth substrate, to allow for easy lift off and formed a robust, pin-hole free thin film. Parylene C is also robust to solvents, acids, and mechanical stress and can therefore withstand subsequent device processing steps and protect the delicate nanowires.

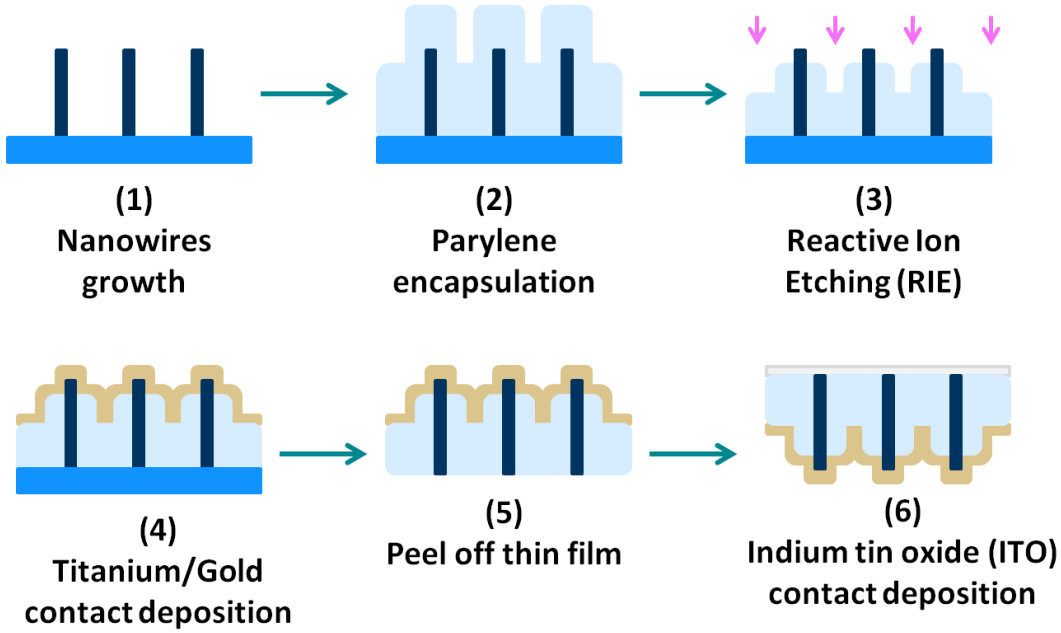

Fig. 8.4: Schematic diagram showing vertically aligned nanowire array flexible photodetector fabrication. (1) Vertically grown nanowires are grown on a substrate. (2) The nanowires are encapsulated using Parylene C. (3) The Parylene C is selectively etched back using RIE to expose the nanowire tips ready for contacting. (4) Ti/Au is deposited using electron beam lithography, creating the back contact. (5) The device is then removed from the growth substrate, and turned over. (6) ITO is deposited using sputter coating to create a top contact

Parylene C also useful electrical and optical properties - it is insulating, which is helpful in avoiding short circuiting between the top and bottom contacts, and has close to 99% transmission of visible light and hence does not hinder the light absorbing properties of the nanowires.

Figure 8.5 shows an early device made using the fabrication process described in Figure 8.4. The IV characteristics show that the contact is rectifying, and the current is low - therefore further optimisation was needed. Section 8.4 describes how the dry etching process was optimised, to selectively and repeatably remove the correct amount of Parylene C from the nanowires. This was to expose the nanowire tips for contacting. Section 8.5 describes top and bottom contact deposition, ohmic contacting and thin film handling. Section 8.6 outlines the optimised fabrication process for the test devices.

8.4 Reactive ion etching

Having successfully encapsulated the nanowires in Parylene C and removed them from the substrate (please refer to Chapter 4 for further details), a precise and repeatable dry etching technique was needed to selectively remove the Parylene C to expose the nanowire tips, ready for contacting. Dry etching has been frequently used in the literature to selectively remove photoresist and other polymers to expose the nanowire tips when fabricating on-substrate devices [266]. Initial work investigated the use of three different etching systems: Diener etcher, Barell etching

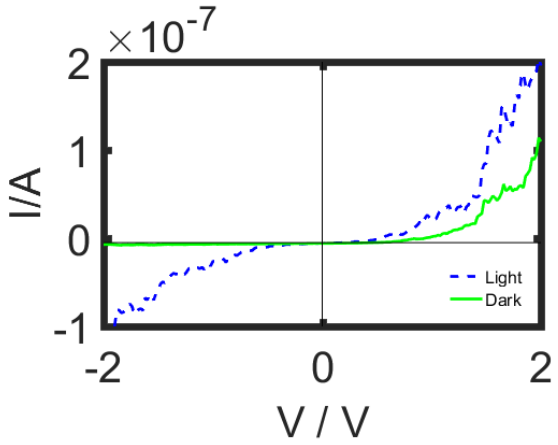

Fig. 8.5: IV curve showing the IV characteristics of a diode early in the optimisation process. Though the IV response shows the device has not been short circuited, the rectifying response shows the formation of a Schottky barrier.

and Philips RIE, which had different electrode systems, different levels of sophistication and therefore parameter control, and access to different gases, as outlined in Table 8.1.

The Diener etcher was a purely oxygen system, had a curved electrode and offered control of the power and etch time. The Barrell etcher had a curved electrode, could only adjust the etch time and was also an oxygen system, but also had access to methane. The Philips RIE had a flat electrode, had access to oxygen, trichloromethane, sulfur hexafluoride and argon and it was possible to adjust the chamber pressure, gas flow rate, etching time and etching power. It must be noted that access to different gases is important as general chamber conditions have a big effect on the etching regimes in dry etching. Using a system with access to CH_4 may result in different chamber conditions to a purely oxygen system. It is for this reason why dry etching equipment often has restrictions on gas usage and material of the sample to be etched.

Etcher	Etching regime	Outcome
Diener	Isotropic	Unsuitable
Barrell	Isotropic	Unsuitable
Philips	Anisotropic	Suitable

Table 8.1: Table summarising the outcomes of the initial RIE tests. Different etchers resulted in different etching regimes. It was found that the Philips RIE gave the best results, going forward.

The power and the time were the only variables which could be investigated for the Diener etcher. The gas rate, process pressure and power were all arbitrary units. Long etch times (range used was between 10 minutes to 40 minutes at 100 % power) were needed to remove the Parylene C as shown in Table 8.1. However long etch times also damaged the nanowires and ultimately removed them from the substrate, as shown by the lower density of nanowires seen in the SEM image. It was also observed that the chamber heated up with longer etch times, which may have contributed to nanowire degradation. Finally, the act of venting may have also blown off some of

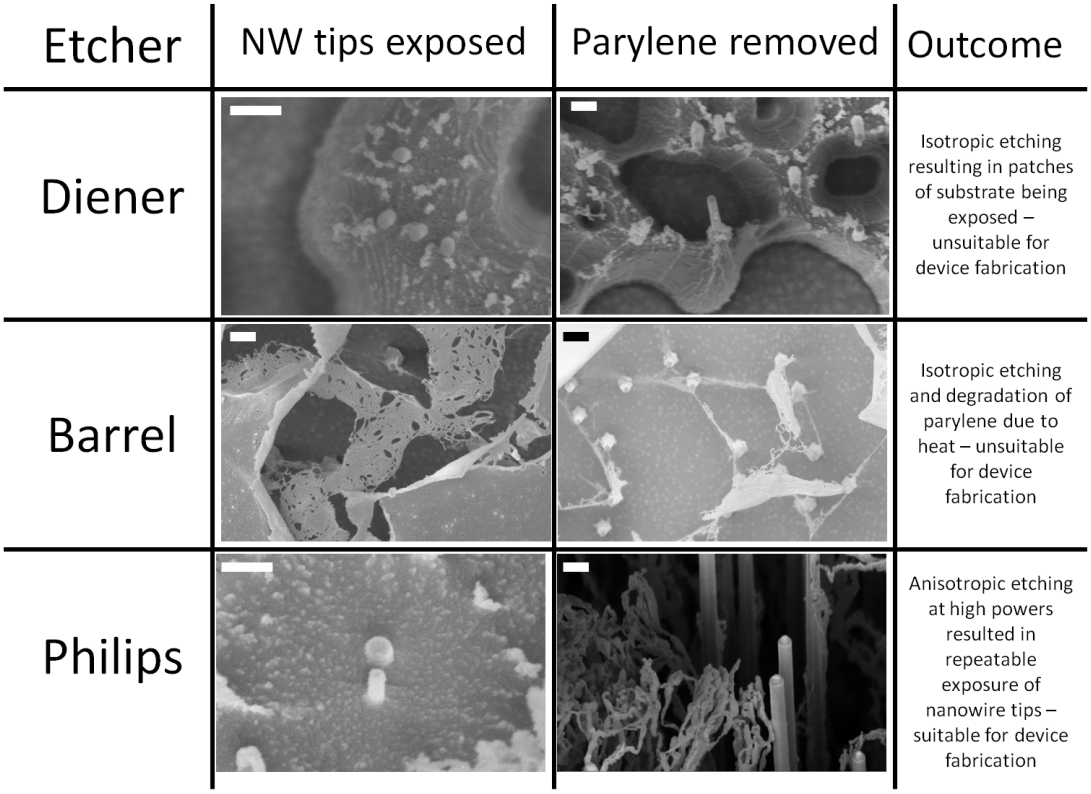

Fig. 8.6: SEM imaging showing different etching techniques. The Diener, Barrel and Philips etcher were used. The diener and barrel etchers showed isotropic etching regimes, making these techniques unsuitable for further device fabrication. The Philips RIE showed anisotropic etching, and was suitable to continue with device fabrication. Scale bar shows 100 nm.

the nanowires off the growth substrate. The etching was also found to be isotropic and therefore the Diener etcher was deemed unsuitable for device fabrication.

The time was the only variable that could be investigated using the Barrell etcher. The gas flow rate, process pressure and power were pre-set and were all given in arbitrary units. The Barrell etcher had a much faster etch rate than the Diener etcher - this was attributed to the rapid heating of the chamber after only a few minutes of etching. As a result, it was difficult to gain fine control of thin film etching and therefore unsuitable for device fabrication.

The Philips RIE offered the most scope for optimisation, as the process pressure, time, RIE power and gas flow rate could all be controlled. Varying the power and the time was sufficient to offer fine control of etching. The etching regime was found to be anisotropic for all powers and times tested. As shown in Figure 8.6, longer etch times simply and cleanly removed more Parylene C without damaging the nanowires underneath. Oxygen was used as the process gas. Interestingly, when the RIE power was varied, two different etching regimes were observed (Figure 8.7). At lower etching powers, the Parylene seemed to be removed in a layer-by-layer in what could be a chemical etching mechanism. As Parylene C is vapour deposited layer-by-layer via free radical addition, it seemed to be removed in the same fashion in which it was deposited. While this is useful in devices where thin layers of Parylene C need to be carefully removed, this

type of etching was not useful in exposing nanowire tips. This is because Parylene C coating in conformal, and removing Parylene C layer-by-layer results in the whole overall thin film becoming thinner. What is actually required is the Parylene C to be anisotropically removed from the top of the film only, thus exposing the nanowire tips. As the etching power increased, this etching regime appeared to have changed to a physical etch, where only material from the top of the thin film was removed. As the etching power increase, this is much more apparent. Using the highest RIE power possible (300 W) for 2 minutes results in 300 nm of nanowire tips exposed.

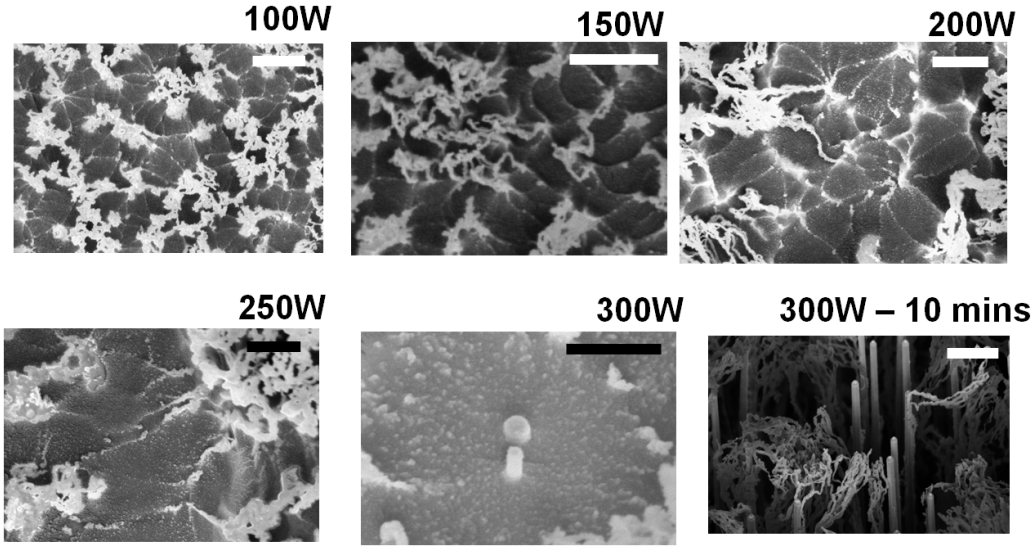

Fig. 8.7: SEM images showing nanowires encapsulated in Parylene C etched using RIE at a range of RIE power, from 100 W to 300 W for two minutes (with the exception of the 10 minute sample). Lower powers show the polymer is removed layer-by-layer, resulting in a pitted surface. Etching at higher powers shows more complete removal of polymer, resulting in a smoother texture, overall and a exposing of the nanowire tips

In conclusion, it was found the using the Philips RIE gave the most desirable results. The Diener etcher required long etching times to remove the Parylene C and was not selective enough between the Parylene C and the InP, resulting in nanowire damage. The Barrel etcher has a high etch rate and also heated up during the process, which made it difficult to obtain fine control of etching and therefore film thickness. Both the Diener etcher and the Barrel etcher had several pre-set variables, and so could not be efficiently optimised to provide the best etching conditions. The Philips RIE, on the other hand, could offer fine control of etching parameters as the time, gas flow rate, RIE power and process pressure could all be varied. It was found that high power regimes offered the best anisotropic etching whilst maintaining etching selectivity between the polymer and the nanowire. For this reason, the Philips RIE protocol was taken forward for subsequent device fabrication.

8.5 Contact deposition

After optimising the dry etching process, the next step was to optimise top and bottom contact deposition. Ohmic contact formation is required to ensure efficient carrier collection. A transparent top contact ITO) and bottom contact (Ti/Au) were optimised.

A band diagram of the proposed test device is given in Figure 8.8. As can be seen, this configurations does not include any pn or pin junction between the top and bottom contacts. Therefore, the measured IV curve would show the IV characteristics of an ohmic contact. Although the nanowires were grown to be nominally intrinsic, in reality they are most likely slightly n-type [267]. Forming ohmic contacts is notoriously difficult with nanowires, due to Fermi level pinning. This is normally circumvented by annealing the contacts - however, annealing could not be used due to process incompatibility with the Parylene C.

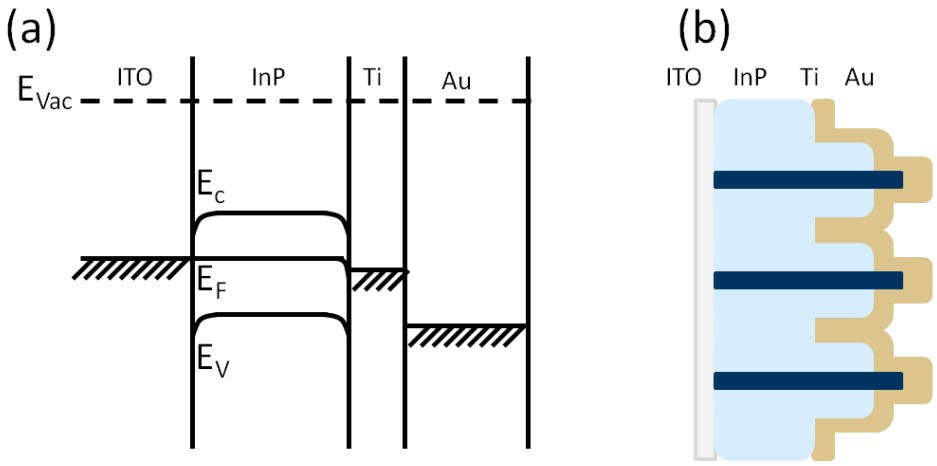

Fig. 8.8: Band diagram and device architecture of test device, which consisted of a nanowires providing a short circuit between the Ti/Au and ITO contacts, which would display ohmic IV behaviour and thus enables simple determination if ohmic contact formation had been achieved. Work functions of the following materials are as follows: ITO - 4.26 eV [268], intrinsic InP, 5.05 eV [269], Au - 5.3 eV, Ti 4.33 eV, Pd - 5.22 eV [270]

8.5.1 Control samples

During contact optimisation, different control samples were used:

For initial experiments, symmetrical devices were used where both the top and bottom contact material were the same. For example - when optimising Ti/Au deposition, test devices were fabricated with both the top and bottom contacts made from Ti/Au. Similarly, when optimising ITO deposition, test devices were made where both the top and bottom contacts were made using ITO. Focussing on each contacting process separately allowed each to be optimised independently. The devices were backed onto copper tape and were characterised using a Cascade probe station.

In addition - when testing the nanowire contacts, it was important to ensure that the current was definitely flowing through the nanowires and not short circuiting. To guard against this, two control samples were fabricated, as shown in in Figure 8.9. Sample (1) consisted of a layer of Parylene C with no nanowires, that had undergone the same RIE process, then 'contacted' with ITO and Ti/Au. The Parylene C is a dielectric, and hence no current should be seen - this was confirmed by the IV curves. Sample (2) consisted of a layer of gold, followed by a layer of ITO, with no Parylene C or nanowires in between. This was to simulate the current response of a short circuited test device. This was confirmed by the IV curves which showed an ohmic response. The compliance of the probe station was set to 100 mA for safety. These IV curves are representative of the IV curves of other control samples made for subsequent device fabrication

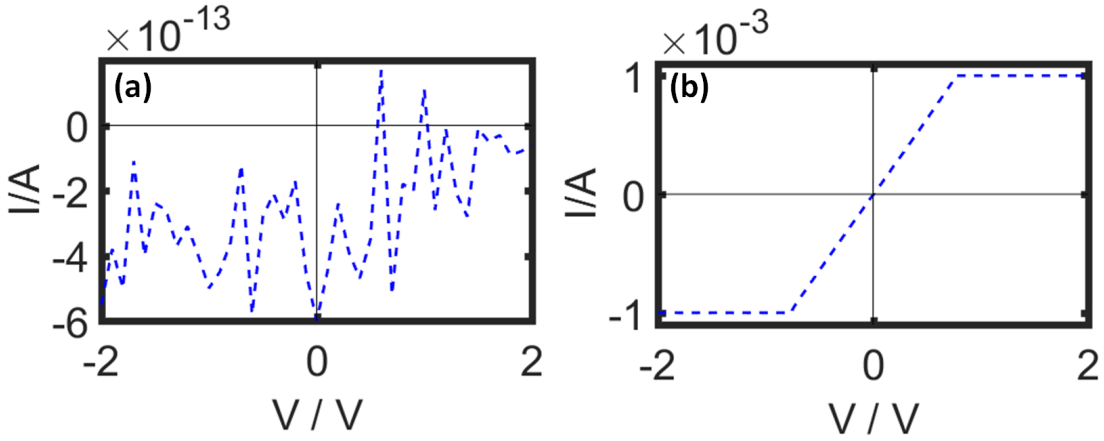

Fig. 8.9: In order to ensure current flow was through the nanowire and not short circuiting, two control samples were fabricated. (1) consisted of a layer of Parylene C which had undergone the same RIE process, then contacted with ITO and Ti/Au and (2) A layer of gold, followed by a layer of ITO. As can be seen, (1) showed virtually no current, showing the Parylene C was acting as a dielectric between the two contacts and (2) shows high current and ohmic response.

8.5.2 Bottom contact deposition

Metal contact deposition was carried out using electron beam evaporation as described in Chapter 4.Ti/Au top contact is the standard contact used in the literature and has been extensively used in III-V devices [21, 28, 222]. Ti/Au contacts are alloyed using an annealing process in order to provide better contact with the nanowires. However, annealing typically takes place at 350 - 400° C - and such a high temperature destroys the Parylene C thin films. Rapid thermal annealing - where samples are annealed very quickly at high temperature was attempted - but this also severely degraded the Parylene C and caused discolouration of the film. The Parylene C film also became brittle and extremely thin, and therefore could not be removed cleanly from the substrate.

As the contacts on this device could not be annealed, other avenues needed to be explored. Overnight pumping of metal deposition chambers to a lower pressure resulted in a cleaner environment for contact deposition. Careful control of the rate of deposition was also used to improve contact quality. Figure 8.10 shows the difference in performance for an (a) unoptimised device which showed rectifying behaviour, and an (b) optimised device which shows good ohmic characteristics. It was found that pumping overnight, and using a deposition rate of 1 Å/s and 0.1 Å/s for the Ti and Au gave good results.

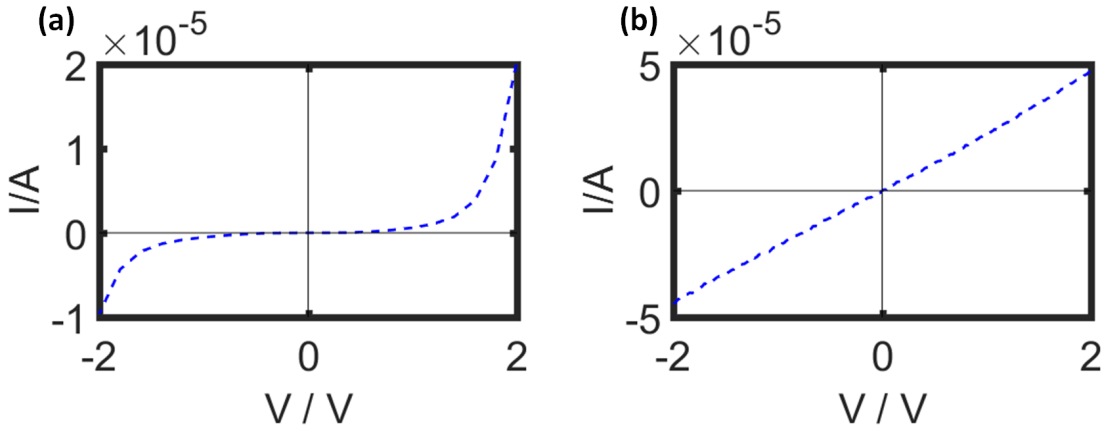

Fig. 8.10: IV curves before (a) and after (b) optimising the Ti/Au bottom contact. Using annealed contacts was not possible, hence ultra clean chamber conditions and fine control of deposition parameters were used to obtain an ohmic contact as shown in (b).

8.5.3 Thin film handling

After bottom contact deposition, the thin film was carefully peeled off. After reactive ion etching, the Parylene C film would have been on the order of 2 µm thick and therefore very delicate and difficult to remove without tearing. After several attempts, it was found that the best way to carry this out was to thoroughly loosen the Parylene C layer by running a razor blade around the edges. Any resistance to removing the thin film caused by adhesion around the edges was sufficient to tear the Parylene C. After loosening the film, it was then slowly and carefully peeled off using sharp tweezers. For subsequent processing, it was important that the film lay flat and did not buckle to ensure uniform metal deposition. Thin Parylene C films have a tendency to buckle and curl once peeled off, partly due to the direction in which peeling off takes place. For ITO deposition, the thin film needed to be flipped over to expose the uncontacted side.

The InP nanowire-Parylene C thin film was backed onto a glass slide coated with a thin layer of PDMS. Activating the PDMS coated glass slide using oxygen plasma treatment renders the surface hydrophilic. This results in the InP nanowire-Parylene C thin film lying flat on the surface, assisted by Van-de-Walls interactions between the two surface. After backing the film onto the PDMS slide, the edges of the film were reinforced with kapton tape. This had two

benefits - the kapton tape made it much easier to remove the InP nanowire-Parylene C thin film from the slide later on and it masked the edges from the ITO, preventing short circuiting the device.

8.5.4 Top contact deposition

ITO was used as the transparent top electrode - which has been repeatedly demonstrated in the literature - and was deposited using sputter coating.

ITO contacts cannot be annealed, therefore other avenues needed to be explored to improve device performance. Figure 8.11 shows a test device where the ITO was deposited at 10-5 mTorr, which shows rectifying behaviour. Passivating the nanowire tips with NH_4S improved the performance of the device (Figure 8.11b) which showed ohmic behaviour

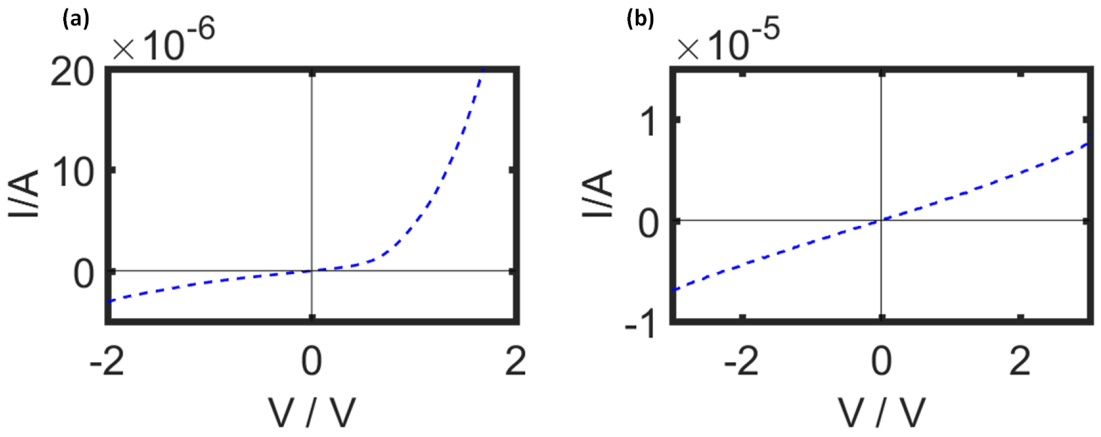

Fig. 8.11: IV curve before (a) and after (b) optimising the ITO top contact. Use of passivation and ultra clean chamber conditions enabled ohmic contact formation as shown in (b).

Given nanowire structures have a high surface-to-volume ratio, and that surfaces are more reactive than bulk material, it is important to consider surface effects when designing devices. InP has a surface recombination velocity of 170 cm/s whereas GaAs has a surface recombination velocity of 54,000 cm/s, hence passivation is much more important for GaAs [2, 253]. This is especially important for nanowires due to their high surface to volume ratio. The impact of the surface on device performance is substantial as dangling bonds on the surface can lead to deep level traps and defects resulting in unwanted recombination. It has been shown that passivating the nanowire surface results in high quality contacting formation, resulting in better device performance [265].

Fermi level pinning is known to be an issue hindering ohmic contact formation in III-V materials. The formation of a native oxide layer coupled with the presence of dangling bonds gives rise to surface states, which can result in Fermi level pinning and unexpected Schottky contact formation [248, 271].

According to Schmitt *et al.* the native oxide is formed predominantly from In_2O_3 with trace amounts of In_2O_3, $InPO_4$, and $InPO_3$. Typically, this native oxide layer is on the order of a few nm's thick and can be removed with a gentle acid etch. In the case of In_2O_3, HCl is used - as shown in equation 8.38

$$In_2O_3 + 6\,HCl \longrightarrow 2\,InCl_3 + 3\,H_2O \tag{8.37}$$

Indium (III) chloride ($InCl_3$) is formed which is water soluble and therefore washed away after etching. Literature has shown that hydrofluoric acid (HF) and hydrochloric acid (HCl) have been used to remove the native oxide layer on InP nanowires. Careful control of the acid molarity is needed to ensure a controlled oxide etch rate [272].

However, removing the oxide layer does not solve the whole problem, as the dangling bonds must be capped, to prevent the oxide layer from reforming, the nanowires needs to be passivated. This where the nanowires are coated with a material to cap the dangling bonds. Common passivating agents are other III-V layers, acids and ammonium sulfide. It must be noted that, in this case, Parylene C does not passivate the nanowire surface due to the presence of the native oxide layer for both GaAs and InP nanowires, which is not removed prior to Parylene coating.

Ammonium sulfide ($(NH_4)_2S$) has frequently used in the literature been used to passivate nanowire surface the surface by capping the dangling bonds with sulfur species [248]. Ammonium sulfide also has the added benefit of removing the oxide layer and and passivating the nanowire surface in one etch step, through a substitution reaction. When dissolved in water, $(NH_4)_2S$ dissociates to form NH_3 and $NH_4(SH)$. The $NH_4(SH)$ reacts with any InP dangling bonds and In_2O_3 to form sulfide species.

$$(NH_4)_2S_{(aq)} \longrightarrow NH_3 + (NH_4)SH \tag{8.38}$$

$$In_2O_3 + NH_3 + 3\,(NH_4)SH \longrightarrow In_2S_3 + NH_3 + 3\,(NH_4)OH \tag{8.39}$$

8.6 Nanowire test device fabrication process

After optimising the process steps described in Sections 8.3–8.5, the nanowire test device fabrication process is outlined as follows:

Nanowire growth InP nanowires were grown using the VLS method as described in Section 4.1.1

Parylene encapsulation The nanowires were coated with 3µm of Parylene C, as described in Section 4.2.2

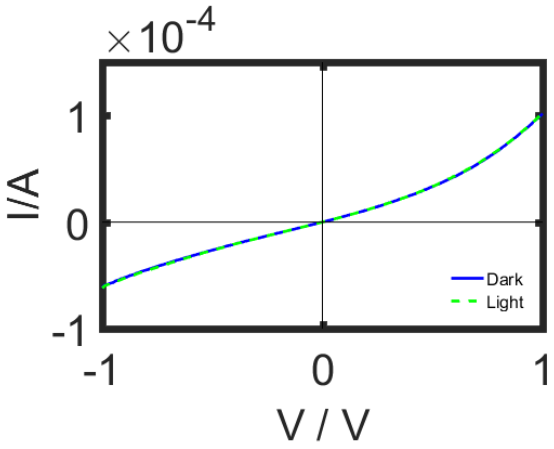

Fig. 8.12: IV response of asymmetric nanowire test device after optimising the Ti/Au and ITO contacts, which showed that a good ohmic contact had been formed.

Dry etching The Parylene C was selectively etched back using the Phillips RIE. The etching conditions were 50 sccm oxygen, pressure 150 mTorr, 300 W power for 2 minutes. Prior to etching, the chamber was cleaned for 5 minutes, at the same process conditions, in order to pre-condition the chamber and provide consistent results

Bottom contact deposition Ti/Au contacts were then deposited using electron beam evaporation. The chamber pressure was achieved by pumping overnight to 10^{-7} Torr A deposition rate of 0.1 Å/s was used for the Ti, a rate of 1Å/s was used for the gold deposition, to ensure uniform deposition. 10 nm Ti and 100 nm Au was deposited.

Thin film removal After top contact deposition, the thin film was carefully removed from the substrate by loosening the Parylene C layer by running a razor blade around the edges, peeling off the thin film using sharp tweezers, then flipped over to expose the uncontacted side.

Passivation The nanowire samples were dipped in ammonium sulfide (diluted 1:10 alkali:water)

Top contact deposition The thin film was backed onto a glass slide coated with a thin layer of PDMS, with the edges isolated with kapton tape. An ITO top contact was deposited by using sputter coating. The process recipe to give 100 nm of ITO was 30 sccm Ar, for 1072 seconds at 50 W, at 10^{-3} Torr, with a 300s pre sputter time. The base pressure was achieved by pumping overnight to 10^{-6} Torr.

Characterisation The test devices where backed onto copper tape (Ti/Au side) for characterisation using a probe station

8.7 Schottky barrier solar cell

After optimising the fabrication process using undoped InP VLS grown nanowires, the next step was to fabricate a solar cell using specially designed nanowire arrays. However, these nanowires were still under development and growth parameters had yet to be optimised. For this reason, alternative solar cell structures were investigated - including a Schottky barrier architecture. A thin layer of an Au/Pd alloy was sputtered on top of the nanowires prior to top contact formation. This was chosen as the alloy would allow a sufficiently low work function, while preventing the gold from delaminating from the surface. Indeed this structure gave a mixture of an axial and radial junction, whereby the metal coats both the tip and the sidewalls of the nanowires, as shown in Figure 8.13.

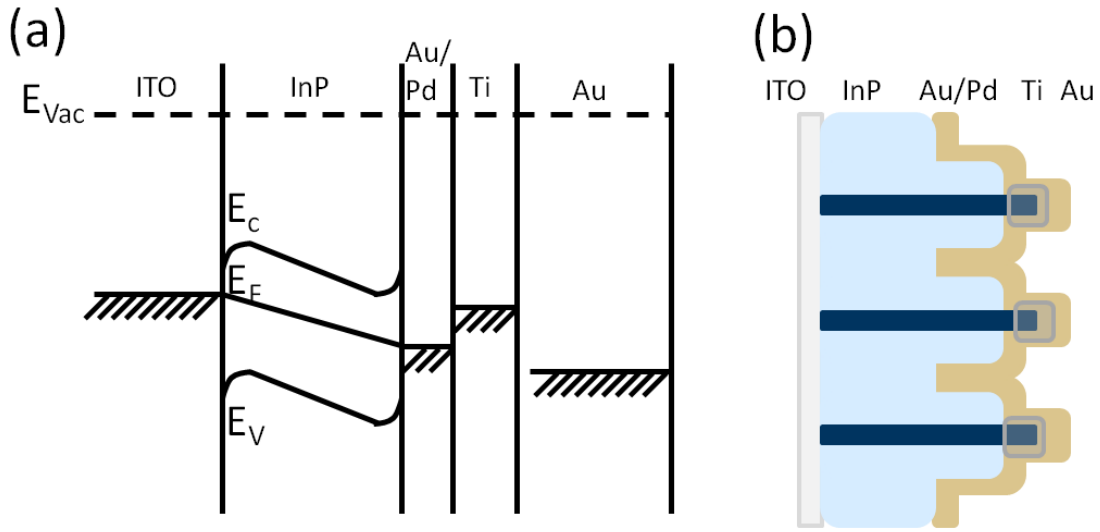

Fig. 8.13: Device architecture and band structure of Schottky barrier solar cell. An Au/Pd alloy was sputtered onto the nanowire tips to form the Schottky contact. ITO top and Ti/Au bottom contacts were used as previously described.

The fabrication process is given below:

Nanowire growth InP nanowires were grown using the VLS method as described in Section 4.1.1

Parylene encapsulation The nanowires were coated with 3 µm of Parylene C, as described in Section 4.2.2

Dry etching The Parylene was selectively etched back using the Phillips RIE. The etching conditions were 50 sccm oxygen, pressure 150 mTorr, 300 W power for 2 minutes. Prior to etching, the chamber was cleaned for 5 minutes, at the same process conditions, in order to pre-condition the chamber and provide consistent results

Schottky contact formation Au/Pd was sputter coated at 10^{-3} mbar at 55 mA for 3 s, to give a 1 nm thick coating.

Bottom contact deposition Ti/Au contacts were then deposited using electron beam evaporation. The chamber pressure was achieved by pumping overnight to 10^{-7} Torr A deposition rate of 0.1 Å/s was used for the Ti, a rate of 1Å/s was used for the gold deposition, to ensure uniform deposition. 10 nm Ti and 100 nm Au was deposited.

Thin film handling After top contact deposition, the thin film was carefully removed from the substrate by loosening the Parylene C layer by running a razor blade around the edges, peeling off the thin film using sharp tweezers, then flipped over to expose the uncontacted side. The thin film was backed onto a glass slide coated with a thin layer of PDMS, with the edges isolated with kapton tape.

Passivation The nanowire samples were dipped in ammonium sulfide (diluted 1:10 alkali:water)

Top contact deposition An ITO top contact was deposited by using sputter coating. The process recipe to give 100 nm of ITO was 30 sccm Ar, for 1072 seconds at 50 W, at 10^{-3} Torr, with a 300 s pre sputter time. The base pressure was achieved by pumping overnight to 10^{-6} Torr.

Characterisation The Schottky barrier solar cell was characterised using a solar simulator by Dr Zihyuan Li at Professor Jagadish's group at the Australian National University.

8.7.1 Schottky barrier solar cell performance

It was found that at very low voltages (between -0.1 and 0.1 V, it was possible to see a small photocurrent, and therefore able to extract solar cell performance parameters. The Schottky barrier solar cell was characterised by Dr Zihyuan Li at Professor Jagadish's lab at the Australian National University.

The ideal diode equation is

$$I = I_s[exp(qV/nkT)] - 1 \tag{8.40}$$

Taking the natural log of both sides and rearranging yields

$$ln(I) = \frac{qV}{nkT} + ln(I_s) \tag{8.41}$$

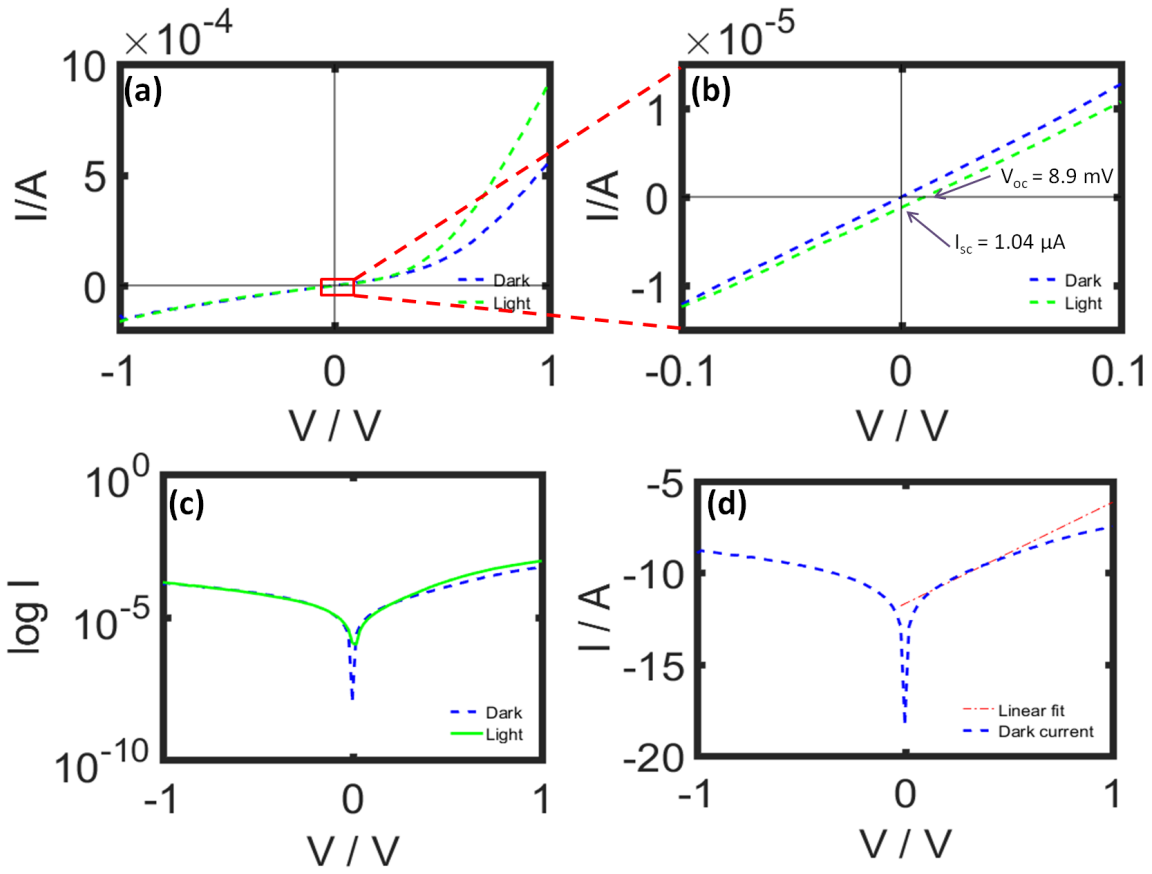

Fig. 8.14: IV curves for Schottky barrier solar cell. (a) and (b) depict the IV curves showing the V_{oc} and I_{sc}. (c) and (d) show the logarithmic plot with (d) showing the straight line fitting.

By fitting the linear part of the log plot in Figure 8.14, it is possible to extract the reverse saturation current I_s from the y intercept c and the ideality factor n from the gradient m.

$$\begin{aligned} y &= mx + c, \\ c &= ln(I_s) \\ m &= \frac{qv}{nkT} \\ n &= \frac{q}{mkT} \end{aligned} \tag{8.42}$$

n is calculated to be 6.9 and I_s is 8.36x10^{-6}. The high ideality factor and reverse saturation current suggest that the sub-optimal performance i partly due to defects and unwanted recombination, and could be improved by optimising nanowire growth and device fabrication. Having calculated n and I_s, it is possible to calculate the fill factor and power conversion efficiency. The devices were exposed to an irradiance of 1 sun (around 1000 W/m^{-2}). The spot size was 11 µm in diameter, and therefore an area of 9.5 x 10^{-11}m^2. The incident power over the area of the spot size is $1000\pi r^2$. Hence $P_{in} = 9.5033x10^{-8}\,W$

There are two ways to calculate the fill factor - empirically or from graphical data. The fill factor is essentially a way to demonstrate how 'ideal' the device is, and how close it is to an ideal

diode. The empirical fill factor eFF is given as

$$eFF = \frac{v_{oc} - ln(v_{oc} + 0.72)}{v_{oc} + 1} \tag{8.43}$$

where v_{oc} is the normalized V_{oc}. v_{oc} can be calculated from

$$v_{oc} = \frac{q}{nKT} V_{oc} \tag{8.44}$$

The fill factor FF calculated from raw data is given as

$$FF = \frac{I_{mp} V_{mp}}{I_{sc} V_{oc}} \tag{8.45}$$

The power conversion efficiency is calculated using the empirical fill factor and the calculated fill factor.

$$\eta = \frac{V_{oc} I_{sc} FF}{P_{in}} \tag{8.46}$$

The empirical fill factor was found to be 0.2966, whereas the fill factor from raw data was found to be 0.2701. The respective power conversion efficiencies were 0.027% and 0.026% respectively.

8.8 Framework for an optimal nanowire solar cell

The key objective of this work carried in this chapter was to develop the fabrication process for a flexible, substrate-free nanowire solar cell. This was not a trivial process as there were several considerations that had to be made for flexible devices, which were not needed for on-substrate counterparts. For example - careful choice of polymer which could both encapsulate the nanowires and facilitate their easy removal from the growth substrate whilst maintaining their vertical alignment was needed; avoiding high temperature processing and needing to develop a process for non-alloyed contacts; and skilled thin film handling to ensure the devices were not damaged through buckling and tearing during the multistep fabrication process.

Figure 8.15 shows how much progress has been made in terms of the development stages towards a flexible solar cell. Firstly, the study carried out in Chapter 5 was extremely valuable in explaining why CVD polymers may be a better candidate than solution processed polymers. The study in this Chapter has investigated the development of repeatable dry etching process, a method of forming good non-alloyed contacts and skilled thin films handling to form a working nanowire test device which showed ohmic IV characteristics, and a proof-of-concept, early stage Schottky barrier solar cell device. The next step for this project would be to use the knowledge gleaned and developed thus far to fabricate a nanowire array solar cell. A start into this study is given in Appendix A.

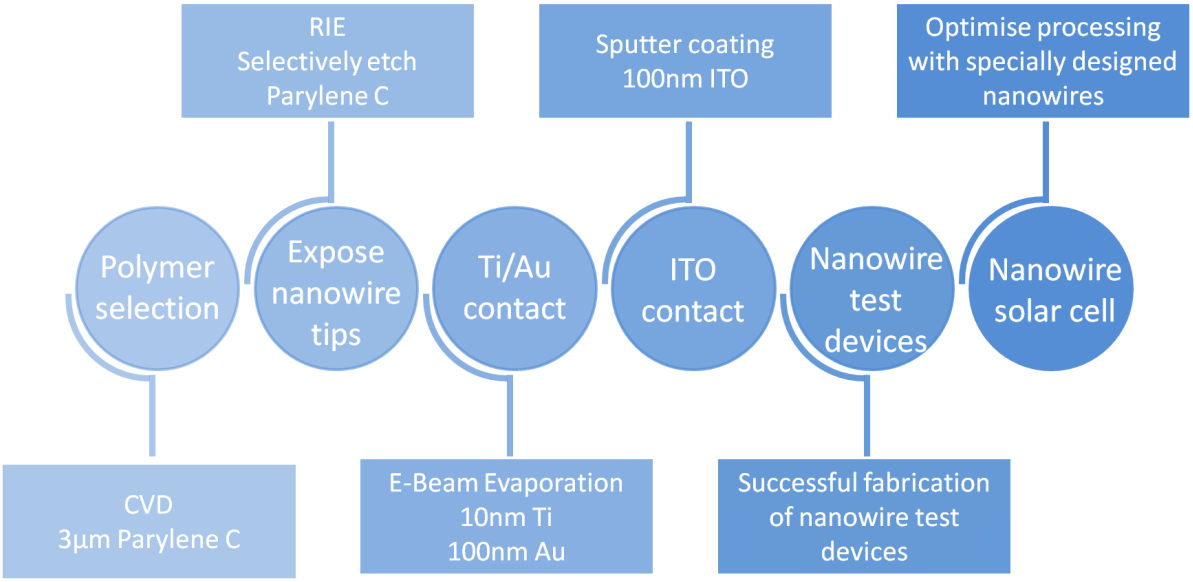

Fig. 8.15: Timeline showing the progress made in nanowire solar fabrication. The lighter coloured circles indicate the work carried out in this thesis, the darker coloured circles indicate work that will be undertaken. This highlights the level of progress has been important in the journey towards fabricating a flexible, substrate-free nanowire solar cell.

While the efficiencies of the device measured in Section 8.7 and fill factors are low, and the reverse saturation current is high, it must be taken into consideration that while the undoped VLS InP nanowires used were useful for process optimisation, these nanowires were not designed for use in solar cells. Undoped nanowires have a far lower free carrier concentration, resulting in fewer free carriers that can contribute to current flow. VLS grown nanowire are also much more sparsely arranged on the substrate when compared to SAE grown nanowires, resulting in sub-optimal light trapping and light absorption. It is thought that using specially engineered nanowires for solar cells would dramatically increase device performance.

There is great scope for future work with this project. As a proof-of-concept device has been fabricated, the next step would be to carry out these experiments with SAE grown nanowires which have been specially engineered for solar cell devices. There would some refining to carry out when using these new nanowires - such taking care not to over-etch the Parylene C to ensure that the n and p portions of the axial PIN junction nanowire are selectively contacted.

It would also be interesting to investigate if the contacting process could be improved further. While Ti/Au non alloyed contacts described in this chapter worked sufficiently well, evaporating another layer of indium has shown to give better contact between the metal and the InP. Indium tin oxide (ITO) is frequently used as the top contact in nanowire solar cells [273]. However, for flexible devices, it is unsuitable as it is brittle and cracks easily [186]. While this was useful as an investigative tool for a proof-of-concept device - it would be useful to carry out a study on other transparent conductors. These include graphene [274], aluminium zinc oxide (an alternative transparent conductive oxide) [275], or even an organic polymer such as PEDOT:PSS [192].

Improved thin film handling protocols will also be key to successful device fabrication, in order to ensure minimal damage happens to the device during processing. The film thickness is on the order of a few microns, meaning the devices will be extremely delicate and liable to tear and crumple with improper handling.

Finally, given the versatility of the fabrication process, it would be straightforward to substitute other III-V nanowires for other application. For example, certain III-V compounds have short photocarrier lifetimes, giving rise to the potential of ultrafast nanowire photodetectors. Compounds with different band gaps could be used for photodetectors with different spectral sensitivities. Avalanche photodetectors and potentially multijunction solar cells could also be fabricated using this method. Initial studies into developing a fabrication process for a solar cell made from SAE nanowires, and a photodetector are discussed in Appendix A and Appendix B. respectively.

8.9 Conclusion

In conclusion, the fabrication process towards a flexible solar cell was developed. After carrying out a study on the choice of encapsulating polymer (Chapter 5), subsequent solar cell device fabrication steps could then be optimised.

The dry etching process was optimised to selectively remove the Parylene C to expose the nanowire tips ready for contacting. Three different systems were tested - Diener etcher, Barrel etching and Philips RIE, each varying levels of sophistication and complexity. It was found that the Philips RIE was the most suited for this process and it offered the most flexibility and control with the process parameters and allowed for highly controlled, reproducible anisotropic etching.

Following this development, the top and bottom contacting techniques were studied, with the aim being to fabricate a test device which showed ohmic IV behaviour. Symmetrical devices (where both the top and contact were made from the same material) were used to study this as this allowed focus on optimising one contacting process, before focussing on the next. It was found that annealing processes normally required for metallic contacts could not be used for these devices as the Parylene C degrades. Instead the focus was on using very clean chamber conditions and careful control of the deposition parameters to ensure high purity contacts were deposited. Passivating the nanowire tips with ammonium sulfide, clean chamber conditions and careful control of deposition parameters resulted in good quality ITO contacts being formed.

Following this, a simple Schottky barrier solar cell was the fabricated using the processes developed here. This preliminary device gave an conversion efficiency of 0.02% and a fill factor of 0.3. To our knowledge, this is the first proof-of-concept demonstration of a fully flexible, substrate-free solar cell based on vertically aligned III-V nanowires. The work carried out in this chapter has pushed the field in a new direction and contributed towards the development of truly substrate-free, flexible nanowire devices.

Chapter 9

Conclusion

In this thesis, I have both developed a practical, reproducible method to produce robust, nanowire thin films using Parylene C as the polymer-based encapsulant, whilst retaining the vertical alignment of the nanowires. I then showed how these thin films could be used to make different flexible, substrate-free devices by changing the nanowire that was embedded within. I used these thin films to successfully fabricate an ultra-fast THz modulator and a proof-of-concept Schottky barrier solar cell. This chapter summarises the key results and outcomes from chapters 5–8, before providing an outlook on the future of flexible, substrate-free nanowire devices.

9.1 Nanowire-Parylene C thin films

Chapter 5 described the study into suitable polymer encapsulants for nanowire-polymer thin films. In this chapter I carried out the optimisation process for thin film fabrication using solution processed and CVD polymers, and found that Parylene C gave the best results. Parylene C forms conformal coatings as it is deposited in the vapour phase, which means it fully encapsulates the nanowires. As nanowires have such a high surface area-to-volume ratio, Parylene C has better adhesion to the nanowires then it does to the substrate, resulting in robust thin films that can be easily removed from the substrate whilst maintaining the all important vertical alignment of the nanowires.

It is important to highlight that the work discussed in this chapter formed the basis of the results achieved in the subsequent chapters. Without successfully fabricating these thin films, it would not have been possible to fabricate the THz polarisers (Chapter 6, Chapter 7) and the solar cell (Chapter 8). Therefore, I am confident that these robust nanowire thin films are an enabling technology for substrate-free, vertically aligned nanowire devices.

9.2 A high performance nanowire THz modulator

Chapters 6 and 7 described the fabrication and characterisation of nanowire THz modulator based on GaAs nanowire-Parylene C thin films. The investigation started by focussing on a single GaAs nanowire-Parylene C thin film. This modulator demonstrated a carrier lifetime of approximately 1 ps, a broad bandwidth between 0.1 THz and 4 THz and an extinction of 2%. Modulator performance was limited by the excitation pulse fluence - hence the areal density of the nanowires needed to be increased.

This was carried out by fabricating polarisers consisting of several GaAs nanowire-Parylene C thin films laminated together. As many as 14 layers were laminated together using this technique. The extinction of the 14-layer polariser increased from $\sim 2\%$ to over $\sim 13\%$ when compared to a single layer modulator. Furthermore, the modulation depth was improved from from 17 dB to -8 dB and the dynamic range was improved from from -18.8 dB to -9 dB. Indeed, 14 layers were used only due to the availability of the wafers. In actual fact, several further layers could have been added. This lamination technique is key to the high performance of the modulator, as the areal density of the GaAs nanowires could be dramatically increased very easily.

These performance values are comparable to those observed for graphene-based THz modulators and surpass those for any previous modulators based on nanostructures, such as unaligned carbon nanotubes. It should be noted that these modulators allow for picosecond switching speeds needed for next generation ultrafast THz communications applications, and operate at the highest bandwidth recorded to date for THz modulation.

9.3 A flexible, substrate-free nanowire solar cell

Chapter 8 described the work undertaken to optimise the fabrication process for a flexible, substrate-free solar cell, made from InP nanowire-Parylene C thin films.

Firstly, the dry etching process using the Philips RIE was optimised etch the InP nanowire-Parylene C thin films. This selectively removed the Parylene C to expose the InP nanowire tips ready for contacting. The top and bottom contacting techniques were then optimised on nanowire test devices to obtain an ohmic contact. As it was not possible to use annealed contacts due to the thermal instability of the Parylene C, very clean chamber conditions were used to form high quality contacts. Ti/Au and ITO were used for the bottom and top contacts respectively.

A proof-of-concept Schottky barrier solar cell was fabricated using the insight gained when developing the fabrication process for the nanowire test devices. This preliminary device gave a power conversion efficiency of 0.02% and a fill factor of 0.3. It must be noted that these nanowires were not optimised for solar cell applications, and performance could be significantly improved if specially optimised nanowires were used for device fabrication.

9.4 Towards fully integrated nanosystems

In Chapter 3, I commented on how the scope and aims of flexible electronics research has changed over the past 10 years. Flexible electronics, once viewed as a lower performance, but cheaper alternative to wafer-scale electronics, has now become a contender in its own right. As flexible devices becomes more stable and reliable and as fabrication techniques continue to be developed and refined, the next step for flexible electronics to move on from discrete, individual devices to fully integrated 'nanosystems' consisting of several nanodevices integrated onto the same substrate. Though the task of developing nanosystems is ambitious, a well established nanowire and flexible electronics community - where collaboration and knowledge sharing is common practice and encouraged will enable the successful realisation of this technology.

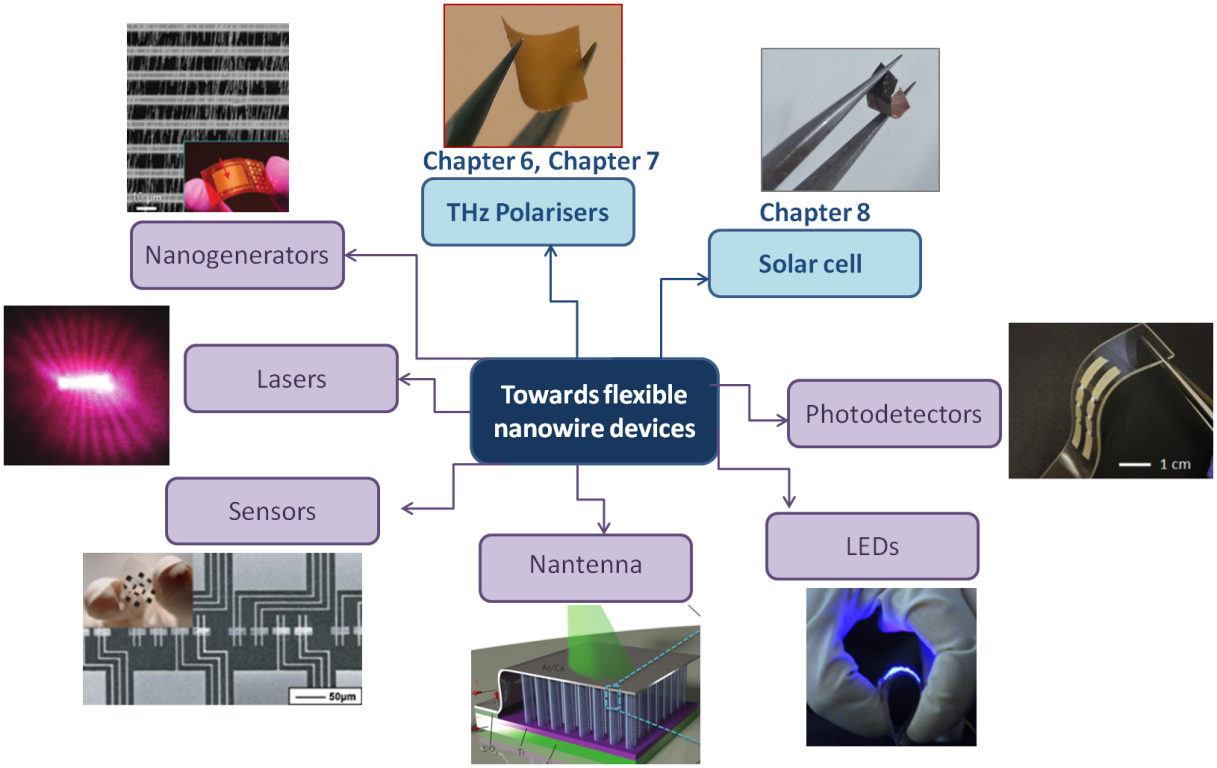

Fig. 9.1: Schematic diagram showing how by varying the semiconducting material and by using different nanowires, a whole host of different flexible, substrate-free devices may be made from nanowire-Parylene C thin films. Images using with permission from the following references. There is incredible scope for a large variety of devices, ranging but certainly not limited to a nanogenerator [198], laser [62], sensor [205], nantenna [276], LED [189] and photodetector [76]

At the time of writing, insights gained from a review of the literature indicated that a key limiting step has been the lack of truly robust nanowire-polymer thin films, that could retain the vertical alignment of the nanowires, whilst being easy to remove from the substrate and being able to withstand the harsh conditions of subsequent device processing. The work undertaken in this thesis brings the concept of nanosystems a little closer as flexible, substrate-free devices may be fabricated separately, then fitted onto a receiver substrate and interconnected.

This thesis has clearly demonstrated (a) robust nanowire-Parylene C thin film fabrication (b) successful fabrication of two very different substrate-free flexible opto-electronic devices and perhaps most importantly (c) the potential of these thin films to be used to fabricate a whole host of next generation opto-electronic devices thus showing the scope of research yet to be undertaken. Figure 9.1 shows that, by changing the semiconductor nanowire material, a whole host of devices may be fabricated from nanowire-Parylene C thin films.

References

[1] L. Wen, Z. Zhao, X. Li, Y. Shen, H. Guo, *et al*. "Theoretical analysis and modeling of light trapping in high efficicency GaAs nanowire array solar cells." *Appl. Phys. Lett.* **99**, 143116 (2011).

[2] J. Wallentin, N. Anttu, D. Asoli, M. Huffman, I. Aberg, *et al*. "InP nanowire array solar cells achieving 13.8% efficiency by exceeding the ray optics limit." *Science* **339**, 1057 (2013).

[3] M. Yao, N. Huang, S. Cong, C.-Y. Chi, M. A. Seyedi, *et al*. "GaAs nanowire array solar cells with axial p-i-n junctions." *Nano Lett.* **14**, 3293 (2014).

[4] Y. Huang, and C. M. Lieber. "Integrated nanoscale electronics and optoelectronics: Exploring nanoscale science and technology through semiconductor nanowires." *Pure Appl. Chem.* **76**, 2051 (2004).

[5] N. P. Dasgupta, J. Sun, C. Liu, S. Brittman, S. C. Andrews, *et al*. "25Th Anniversary Article: Semiconductor Nanowires–Synthesis, Characterization, and Applications." *Adv. Mater.* **26**, 2137 (2014).

[6] M. Yang, P. Yan, R. Fardy. "Semiconductor nanowires, what's next?" *Nano Lett.* **10**, 1529 (2011).

[7] A. Kandala, T. Betti, and A. Fontcuberta i Morral. "General theoretical considerations on nanowire solar cell designs." *Phys. Status Solidi* **206**, 173 (2009).

[8] J. V. Holm, H. I. Jørgensen, P. Krogstrup, J. Nygård, H. Liu, *et al*. "Surface-passivated GaAsP single-nanowire solar cells exceeding 10% efficiency grown on silicon." *Nat. Commun.* **4**, 1498 (2013).

[9] Y. Sun, and J. A. Rogers. "Inorganic semiconductors for flexible electronics." *Adv. Mater.* **19**, 1897 (2007).

[10] S. Yun, S. Park, B. Park, S. K. Park, H. Prahlad, *et al*. "Polymer-Based Flexible Visuo-Haptic Display." *IEEE Trans. Mech.* **19**, 1463 (2014).

[11] Y. Chen, J. Au, P. Kazlas, A. Ritenour, H. Gates, *et al*. "Electronic paper: Flexible active-matrix electronic ink display." *Nature* **423**, 136 (2003).

[12] D. Zhang, M. Miao, H. Niu, and Z. Wei. "Core-spun carbon nanotube yarn supercapacitors for wearable electronic textiles." *ACS Nano* **8**, 4571 (2014).

[13] A. M. Gaikwad, A. M. Zamarayeva, J. Rousseau, H. Chu, I. Derin, *et al*. "Highly stretchable alkaline batteries based on an embedded conductive fabric." *Adv. Mater.* **24**, 5071 (2012).

[14] G. E. Moore. "Cramming more components onto integrated circuits." *Electronics* **38**, 1 (1965).

[15] M. C. Beard, J. M. Luther, and A. J. Nozik. "The promise and challenge of nanostructured solar cells." *Nat. Nanotechnol.* **9**, 951 (2014).

[16] S. K. Kim, X. Zhang, D. J. Hill, K. D. Song, J. S. Park, *et al*. "Doubling absorption in nanowire solar cells with dielectric shell optical antennas." *Nano Lett.* **15**, 753 (2015).

[17] A. I. Hochbaum, and P. Yang. "Semiconductor nanowires for energy conversion." *Chem. Rev.* **110**, 527 (2010).

[18] J. Zhang, M. A. Itzler, H. Zbinden, and J.-w. Pan. "Advances in InGaAs / InP single-photon detector systems for quantum communication." *Light. Sci. Appl.* **4**, 1 (2015).

[19] A. Tan, R. Chawla, G. Natasha, S. Mahdibeiraghdar, R. Jeyaraj, *et al*. "Nanotechnology and regenerative therapeutics in plastic surgery: The next frontier." *J. Plast. Reconstr. Aesthetic Surg.* **69**, 1 (2016).

[20] S. Sandhu, Z. Yu, and S. Fan. "Detailed balance analysis and enhancement of open-circuit voltage in single-nanowire solar cells." *Nano Lett.* **14**, 1011 (2014).

[21] Z. Li, Y. C. Wenas, L. Fu, S. Mokkapati, H. H. Tan, *et al*. "Influence of Electrical Design on Core – Shell GaAs Nanowire Array Solar Cells." *IEEE* **5**, 854 (2015).

[22] H. Park, K. Seo, and K. B. Crozier. "Adding colors to polydimethylsiloxane by embedding vertical silicon nanowires." *Appl. Phys. Lett.* **101**, 193107 (2012).

[23] R. R. LaPierre, A. C. E. Chia, S. J. Gibson, C. M. Haapamaki, J. Boulanger, *et al*. "III-V nanowire photovoltaics: Review of design for high efficiency." *Phys. Status Solidi RRL* **7**, 815 (2013).

[24] A. D. Mallorquí, E. Alarcón-lladó, E. Russo-averchi, F. Matteini, V. G. Dubrovskii, *et al*. "III – V nanowire arrays : growth and light interaction." .

[25] H. J. Joyce, J. Wong-Leung, Q. Gao, H. Hoe Tan, and C. Jagadish. "Phase perfection in zinc blende and wurtzite III- V nanowires using basic growth parameters." *Nano Lett.* **10**, 908 (2010).

[26] K. A. Dick, P. Caroff, J. Bolinsson, M. E. Messing, J. Johansson, *et al*. "Control of III-V nanowire crystal structure by growth parameter tuning." *Semicond. Sci. Technol.* **25**, 024009 (2010).

[27] "www.advmat.de." **27**, 2015 (2015).

[28] B. Tian, X. Zheng, T. J. Kempa, Y. Fang, N. Yu, *et al*. "Coaxial silicon nanowires as solar cells and nanoelectronic power sources." *Nature* **449**, 885 (2007).

[29] C. M. Tian, B., Kemps, T. Lieber. "Single nanowire photovoltaics." *Chem. Soc. Rev.* **38**, 16 (2009).

[30] Y. C. Kong, D. P. Yu, B. Zhang, W. Fang, and S. Q. Feng. "Ultraviolet-emitting ZnO nanowires synthesized by a physical vapor deposition approach." *Appl. Phys. Lett.* **78**, 407 (2001).

[31] M. Heurlin, P. Wickert, F. Stefan, M. T. Borgstr, K. Deppert, *et al*. "Axial InP Nanowire Tandem Junction Grown on a Silicon Substrate." *Nano Lett.* **11**, 2028 (2011).

[32] C. Colombo, M. Heiss, M. Gratzel, and A. Fontcuberta i Morral. "Gallium arsenide p-i-n radial structures for photovoltaic applications." *Appl. Phys. Lett.* **94**, 173108 (2009).

[33] Y.-B. Wang, L.-F. Wang, H. J. Joyce, Q. Gao, X.-Z. Liao, *et al*. "Super deformability and Young's modulus of GaAs nanowires." *Adv. Mater.* **23**, 1356 (2011).

[34] T. Takahashi, K. K. Takei, K. E. Adabi, Z. Fan, A. M. Niknejad, *et al*. "Parallel Array InAs Nanowire Transistors for Mechanically Bendable, Ultrahigh Frequency Electronics." *ACS Nano* **4**, 5855 (2010).

[35] D. K. Kim, Y. Lai, T. Vemulkar, and C. R. Kagan. "Flexible, low-voltage and low-hysteresis PbSe nanowire field-effect transistors." *ACS Nano* **5**, 10074 (2011).

[36] Y. Sun, H.-s. Kim, E. Menard, S. Kim, I. Adesida, *et al*. "Printed arrays of aligned GaAs wires for flexible transistors, diodes and circuits on plastic substrates." *Small* 1330–1334 (2006).

[37] N. Han, Z.-X. Yang, F. Wang, G. Dong, S. Yip, *et al*. "High-performance GaAs nanowire solar cells for flexible and transparent photovoltaics." *ACS Appl. Mater. Interfaces* **7**, 20454 (2015).

[38] G. Chen, B. Liang, Z. Liu, G. Yu, X. Xie, *et al*. "High performance rigid and flexible visible-light photodetectors based on aligned X(In,Ga)P nanowire arrays." *J. Mater. Chem. C* **2**, 1270 (2014).

[39] C. Honsberg, and S. Bowden. "Standard solar spectra." (2018). https://www.pveducation.org/pvcdrom/appendices/standard-solar-spectra.

[40] R. R. LaPierre. "Numerical model of current-voltage characteristics and efficiency of GaAs nanowire solar cells." *J. Appl. Phys.* **109**, 034311 (2011).

[41] H. J. Joyce, J. L. Boland, C. L. Davies, S. A. Baig, and M. B. Johnston. "A review of the electrical properties of semiconductor nanowires : insights gained from terahertz conductivity spectroscopy." *Semicond. Sci. Technol.* **31**, 1 (2016).

[42] S. A. Baig, J. L. Boland, D. A. Damry, H. H. Tan, C. Jagadish, *et al*. "An ultrafast switchable terahertz polarization modulator based on III-V semiconductor nanowires." *Nano Lett.* **17**, 2603 (2017).

[43] S. Mokkapati, D. Saxena, Q. Gao, H. H. Tan, and C. Jagadish. "III-V semiconductor nanowire lasers." (2014).

[44] Q. Gao, D. Saxena, F. Wang, L. Fu, S. Mokkapati, *et al*. "Selective area epitaxy of pure wurtzite InP nanowires: High quantum efficiency and room-temperature lasing." *Nano. Letts.* **14**, 5206 (2014).

[45] M. Marus, A. Hubarevich, H. Wang, A. Smirnov, X. Sun, *et al*. "Optoelectronic performance optimization for transparent conductive layers based on randomly arranged silver nanorods." *Opt. Express* **23**, 6209 (2015).

[46] D. Dalacu, K. Mnaymneh, J. Lapointe, X. Wu, P. J. Poole, *et al*. "Ultraclean emission from InAsP quantum dots in defect-free wurtzite InP nanowires." *Nano Lett.* **12**, 5919 (2012).

[47] T. Rieger, S. Heiderich, S. Lenk, M. I. Lepsa, and D. Grützmacher. "Ga-assisted MBE growth of GaAs nanowires using thin HSQ layer." *J. Cryst. Growth* **353**, 39 (2012).

[48] J. A. Czaban, D. A. Thompson, and R. R. Lapierre. "GaAs Core - Shell Nanowires for Photovoltaic Applications 2009." *Nano Lett.* **9**, 148 (2009).

[49] K. a. Dick. "A review of nanowire growth promoted by alloys and non-alloying elements with emphasis on Au-assisted III-V nanowires." *Prog. Cryst. Growth Charact. Mater.* **54**, 138 (2008).

[50] H. J. Joyce, Q. Gao, H. H. Tan, C. Jagadish, Y. Kim, *et al*. "Twin-free uniform epitaxial GaAs nanowires grown by a two-temperature process." *Nano Lett.* **7**, 921 (2007).

[51] H. J. Joyce, Q. Gao, H. H. Tan, C. Jagadish, Y. Kim, *et al*. "III-V semiconductor nanowires for optoelectronic device applications." *Prog. Quantum Electron.* **35**, 23 (2011).

[52] A. Nowzari, M. Heurlin, V. Jain, K. Storm, A. Hosseinnia, *et al*. "A comparative study of absorption in vertically and laterally oriented InP core-shell nanowire photovoltaic devices." *Nano Lett.* **1**, 1 (2015).

[53] F. Qian, S. Gradečak, Y. Li, C. Y. Wen, and C. M. Lieber. "Core/multishell nanowire heterostructures as multicolor, high-efficiency light-emitting diodes." *Nano Lett.* **5**, 2287 (2005).

[54] T. J. Kempa, R. W. Day, S.-K. Kim, H.-G. Park, and C. M. Lieber. "Semiconductor nanowires: a platform for exploring limits and concepts for nano-enabled solar cells." *Energy Environ. Sci.* **6**, 719 (2013).

[55] R. R. LaPierre. "Theoretical conversion efficiency of a two-junction III-V nanowire on Si solar cell." *J. Appl. Phys.* **110**, 014310 (2011).

[56] J. Wang, M. Gudiksen, X. Duan, Y. Cui, and C. Lieber. "Highly Polarized Photoluminescence and Photodetection from Single Indium Phosphide Nanowires." *Science* **293**, 1455 (2001).

[57] C. Soci, A. Zhang, X.-Y. Bao, H. Kim, Y. Lo, *et al*. "Nanowire photodetectors." *J. Nanosci. Nanotechnol.* **10**, 1430 (2010).

[58] R. LaPierre, M. Robson, K. Azizur-Rahman, and P. Kuyanov. "A review of III – V nanowire infrared photodetectors and sensors." *J. Phys. D: Appl. Phys.* **50**, 123001.

[59] R. H. Siddique, G. Gomard, and H. Hölscher. "The role of random nanostructures for the omnidirectional anti-reflection properties of the glasswing butterfly." *Nat. Commun.* **6**, 6909 (2015).

[60] W. Y. Weng, S. J. Chang, C. L. Hsu, T. J. Hsueh, and S. P. Chang. "A Lateral ZnO Nanowire Photodetector Prepared on Glass Substrate." *J. Electrochem. Soc.* **157**, K30 (2010).

[61] W. Wei, Y. Liu, X. Zhang, Z. Wang, and X. Ren. "Evanescent-wave pumped room-temperature single-mode GaAs/AlGaAs core-shell nanowire lasers." *Appl. Phys. Lett.* **104**, 223103 (2014).

[62] D. Saxena, S. Mokkapati, P. Parkinson, N. Jiang, Q. Gao, *et al*. "Optically pumped room-temperature GaAs nanowire lasers." *Nat. Photonics* **7**, 963 (2013).

[63] R. Konenkamp, R. C. Word, and C. Schlegel. "Vertical nanowire light-emitting diode." *Appl. Phys. Lett.* **85**, 6004 (2004).

[64] E. Lai, W. Kim, and P. Yang. "Vertical nanowire array-based light emitting diodes." *Nano Res.* **1**, 123 (2008).

[65] J. Bao, M. a. Zimmler, F. Capasso, X. Wang, and Z. F. Ren. "Broadband ZnO single-nanowire light-emitting diode." *Nano Lett.* **6**, 1719 (2006).

[66] M. Hopkinson, T. Martin, and P. Smowton. "III–V semiconductor devices integrated with silicon." *Semicond. Sci. Technol.* **28**, 090301 (2013).

[67] P. Lio, C., Tang, J., Chen, H. M., Liu, B., Yang. "A Fully Integrated Nanosystem of Semiconductor Nanowires for Direct Solar Water Splitting." *Nano Lett.* **13**, 2989 (2013).

[68] A. Standing, S. Assali, L. Gao, M. a. Verheijen, D. van Dam, *et al*. "Efficient water reduction with gallium phosphide nanowires." *Nat. Commun.* **6**, 7824 (2015).

[69] A. Khitun, A. Balandin, and K. L. Wang. "Modification of the lattice thermal conductivity in silicon quantum wires due to spatial confinement of acoustic phonons." *Superlattices Microstruct.* **26**, 181 (1999).

[70] A. Abramson, W. Kim, S. Huxtable, H. Yan, Y. Wu, *et al*. "Fabrication and Characterization of a Nanowire/Polymer-Based Nanocomposite for a Prototype Thermoelectric Device." *J. Microelectromechanical Syst.* **13**, 505 (2004).

[71] Y. Ma, N. Sun, R. Zhang, L. Guo, Y. She, *et al*. "Integrated color filter and polarizer based on two-dimensional superimposed nanowire arrays." *J. Appl. Phys.* **116** (2014).

[72] C. J. Docherty, S. D. Stranks, S. N. Habisreutinger, H. J. Joyce, L. M. Herz, *et al*. "An ultrafast carbon nanotube terahertz polarisation modulator." *J. Appl. Phys.* **115**, 13 (2014).

[73] R. Elnathan, M. Kwiat, F. Patolsky, and N. H. Voelcker. "Engineering vertically aligned semiconductor nanowire arrays for applications in the life sciences." *Nano Today* **9**, 172 (2014).

[74] H. Chen, H. Liu, Z. Zhang, K. Hu, and X. Fang. "Nanostructured Photodetectors : From Ultraviolet to Terahertz." *Adv. Mater.* **28**, 403 (2016).

[75] X. Yan, B. Li, Y. Wu, X. Zhang, X. Ren, *et al*. "A single crystalline InP nanowire photodetector." *Appl. Phys. Lett* **109**, 053109 (2016).

[76] C. Yan, J. Wang, X. Wang, W. Kang, M. Cui, *et al*. "An intrinsically stretchable nanowire photodetector with a fully embedded structure." *Adv. Mater.* **26**, 943 (2014).

[77] W.-R. Lee, H. Ko, D.-I. Cho, K.-I. Koo, and J.-M. Seo. "A Review of Nanotechnology for Highly Sensitive Photodetectors for Vision Sensors of Insect-like Robots A Review of Nanotechnology for Highly Sensitive Photodetectors for Vision Sensors of Insect-like Robots." *Sensor. Mater.* **27**, 465 (2016).

[78] Y. Xie, B. Zhang, S. Wang, D. Wang, A. Wang, *et al*. "Ultrabroadband MoS_2 photodetector with spectral response from 445 to 2717 nm." *Adv. Mater.* **29**, 1605972 (2017).

[79] H. S. Jung, and N. G. Park. "Perovskite solar cells: From materials to devices." *Small* **11**, 10 (2015).

[80] L. Dou, Y. M. Yang, J. You, W.-h. Chang, G. Li, *et al*. "Solution-processed hybrid perovskite photodetectors with high detectivity." *Nat. Commun.* **5**, 1 (2014).

[81] N. Inoue, H. Yagi, R. Masuyama, T. Katsuyama, Y. Yoneda, *et al*. "InP-based Photodetector Monolithically Integrated with 90 Hybrid for 100 Gbit / s Compact Coherent Receivers." *SEI Tech. Rev.* **1**, 66 (2014).

[82] X. Wang, and X. Gan. "Graphene integrated photodetectors and opto-electronic devices — a review." *Chin. Phys. B* **26**, 034201 (2017).

[83] F. Xia, H. Wang, D. Xiao, M. Dubey, and A. Ramasubramaniam. "Two-dimensional material nanophotonics." *Nat. Publ. Gr.* **8**, 899 (2014).

[84] O. Lopez-sanchez, D. Lembke, M. Kayci, A. Radenovic, and A. Kis. "Ultrasensitive photodetectors based on monolayer MoS_2." *Nat. Nanotechnol.* **8**, 497 (2013).

[85] H. Liu, Y. Du, Y. Deng, and P. D. Ye. "Chem Soc Rev." *Chem. Soc. Rev.* **44**, 2732 (2015).

[86] M. Engel, M. Steiner, and P. Avouris. "Black Phosphorus Photodetector for Multispectral, High-Resolution Imaging." *Nano Lett.* **24**, 2 (2014).

[87] S. H. Asadpour, Z. Golsanamlou, and H. R. Soleimani. "Infrared and terahertz signal detection in a quantum Dot nanostructure." *Physica E.* **54**, 45 (2013).

[88] Q. Zhang, J. Jie, S. Diao, Z. Shao, Q. Zhang, *et al*. "Solution-processed graphene quantum dot deep-UV photodetectors." *ACS Nano.* **9**, 1561 (2015).

[89] H. Kim, S.-Y. Ahn, S. Kim, G. Ryu, J. H. Kyhm, *et al*. "InAs / GaAs quantum dot infrared photodetector on a Si substrate by means of metal wafer bonding and epitaxial lift-off." *Opt. Express* **25**, 17562 (2017).

[90] J. Wu, S. Chen, A. Seeds, and H. Liu. "Quantum dot optoelectronic devices: lasers, photodetectors and solar cells." *J. Phys. D: Appl. Phys.* **48**, 363001 (2015).

[91] M. Cirillo, T. Aubert, R. Homes, R. V. Deun, P. Emplit, *et al*. "Flash synthesis of CdSe/CdS core-shell quantum dots." *Chem. Mater.* **26**, 1154 (2014).

[92] J.-S. Lee, M. V. Kovalenko, J. Huang, D. S. Chung, and D. V. Talapin. "Band-like transport, high electron mobility and high photoconductivity in all-inorganic nanocrystal arrays." *Nat. Nanotechnol.* **6**, 348 (2011).

[93] B. Y. Zhang, T. Liu, B. Meng, X. Li, G. Liang, *et al*. "Monolayer graphene photodetector." *Nat. Commun.* **4**, 1811 (2013).

[94] H. Liu, Z. Zhang, L. Hu, N. Gao, L. Sang, *et al*. "New UV-A photodetector based on individual potassium niobate nanowires with high performance." *Adv. Optical. Mater.* **2**, 771 (2014).

[95] D. Wu, Y. Jiang, X. Yao, Y. Chang, Y. Zhang, *et al*. "Construction of crossed heterojunctions from p-ZnTe and n-CdSe nanoribbons and their photoresponse properties." *J. Mater. Chem. C* **2**, 6547 (2014).

[96] W. Gao, Q. Jiang, Y. Kawano, and R. H. Hauge. "Carbon Nanotube Terahertz Detector." *Nano. Lett.* **14**, 3953 (2014).

[97] G. Konstantatos, M. Badioli, L. Gaudreau, J. Osmond, M. Bernechea, *et al*. "Hybrid graphene – quantum dot phototransistors with ultrahigh gain." *Nat. Nanotechnol.* **7**, 363 (2012).

[98] D.-S. Tsai, C.-A. Lin, W.-C. Lien, H.-c. Chang, Y.-l. Wang, *et al*. "Ultra-high-responsivity broadband detection of Si metal–semiconductor–metal Schottky photodetectors improved by ZnO nanorod arrays." *ACS Nano* **5**, 7748 (2011).

[99] I. Vurgaftman, J. R. Meyer, and L. R. Ram-Mohan. "Band parameters for III – V compound semiconductors and their alloys Band parameters for III – V compound semiconductors and their alloys." *J. Appl. Phys.* **5815**, 5815 (2003).

[100] X. Dai, S. Zhang, Z. Wang, G. Adamo, H. Liu, *et al*. "GaAs/AlGaAs Nanowire Photodetector." *Nano Lett.* **14**, 2688 (2014).

[101] S. A. Dayeh, A. Fontcuberta i Morral, and C. Jagadish. *Semiconductor Nanowires II: Properties and Applications*, vol. 94. 1 ed. Elsevier (2016).

[102] X. Wang, Y. Zhang, X. Chen, M. He, C. Liu, *et al*. "Ultrafast, superhigh gain visible-blind UV detector and and optical logic gates based on nonpolar *a*-axial GaN nanowire." *Nanoscale* **6**, 12009 (2014).

[103] J. Miao, W. Hu, N. Guo, Z. Lu, X. Zou, *et al*. "Single InAs nanowire room-temperature near-infrared photodetectors." *ACS Nano* **28**, 3628 (2014).

[104] X. Dai, S. Zhang, Z. Wang, G. Adamo, H. Liu, *et al*. "GaAs/AlGaAs nanowire photodetector." *Nano Lett.* **14**, 2688 (2014).

[105] Y.-S. No, R. Gao, M. N. Mankin, R. W. Day, H.-G. Park, *et al*. "Encoding active device elements at nanowire tips." *Nano Lett.* **16**, 4713 (2016).

[106] K. Peng, P. Parkinson, Q. Gao, J. L. Boland, Z. Li, *et al*. "Single n+-i-n+ InP nanowires for highly sensitive terahertz detection." *Nanotechnology* **28**, 125202 (2017).

[107] P. Senanayake, A. Lin, G. Mariani, J. Shapiro, C. Tu, *et al*. "Photoconductive gain in patterned nanopillar photodetector arrays." *Appl. Phys. Letts.* **97**, 203108 (2010).

[108] H. Pettersson, I. Zubritskaya, N. T. Nghia, J. Wallentin, M. Borgstrom, *et al*. "Electrical and optical properties of InP nanowire ensemble p^+–i–n^+ photodetectors." *Nanotechnology* **23**, 135201 (2012).

[109] S. Zhao, H. Pham, T. Nguyen, and Z. Mi. "Near-infrared InN nanowire optoelectronic devices on Si." *2014 IEEE Photonics Society Summer Topical Meeting Series* **1**, 208 (2014).

[110] W. Wei, X.-y. Bao, C. Soci, Y. Ding, Z.-l. Wang, *et al*. "Direct Heteroepitaxy of vertical InAs nanowires on Si substrates for broadband photovoltaics and photodetection." *Nano. Letts.* **9**, 2926 (2009).

[111] S. Lei, F. Wen, L. Ge, S. Najmaei, A. George, *et al*. "An atomically layered InSe avalanche photodetector." *Nano. Letts.* **15**, 3048 (2015).

[112] Z. Liu, J. Xu, D. Chen, and S. Guozhen. "Flexible electronics based on inorganic nanowires." *Chem. Soc. Rev.* **44**, 161 (2015).

[113] I. Aberg, G. Vescovi, D. Asoli, U. Naseem, J. P. Gilboy, *et al*. "A GaAs nanowire array solar cell with 15.3% efficiency at 1 sun." *IEEE J. Photovoltaics* **6**, 185 (2016).

[114] N. Anttu. "Shockley-Queisser Detailed Balance Efficiency Limit for Nanowire Solar Cells." *ACS Photonics* **2**, 446 (2015).

[115] W. Shockley, and H. J. Queisser. "Detailed Balance Limit of Efficiency of p-n Junction Solar Cells." *J. Appl. Phys.* **32**, 510 (1961).

[116] Y. Hishikawa, W. Warta, M. A. Green, D. H. Levi, J. Hohl, *et al*. "Solar cell efficiency tables (version 50)." *Prog. Photovolt. Res. Appl.* **25**, 668 (2017).

[117] A. Polman, M. Knight, E. C. Garnett, B. Ehrler, and W. C. Sinke. "Photovoltaic materials – present efficiencies and future challenges." *Science* **352**, 307 (2016).

[118] D. Zhang, Y. Yang, Y. Bekenstein, Y. Yu, N. A. Gibson, *et al*. "Synthesis of composition tunable and highly luminescent cesium lead halide nanowires through anion-exchange reactions." *J.Am.Chem.Soc* **138**, 7236 (2016).

[119] J.-h. Im, J. Luo, M. Franckevic, N. Pellet, P. Gao, *et al*. "Nanowire perovskite solar cell." *Nano. Letts.* **15**, 2120 (2015).

[120] Q. Jiang, X. Sheng, Y. Li, X. Feng, and T. Xu. "Rutile TiO_2 nanowire-based perovskite solar cells." *Chem. Commun.* **50**, 14720 (2014).

[121] J. Du, Z. Du, J.-s. Hu, Z. Pan, Q. Shen, *et al*. "Zn-Cu-In-Se Quantum Dot Solar Cells with a Certified Power Conversion Efficiency of 11.6%." *J. Am. Chem. Soc.* **138**, 4201 (2016).

[122] P. V. Kamat. "Quantum dot solar cells. *The next big thing* in photovoltaics." *J. Phys. Chem. Letts.* **4**, 908 (2013).

[123] X. Liu, Y. Feng, H. Cui, F. Liu, X. Hao, *et al*. "The current status and future prospects of kesterite solar cells: a brief review." *Prog. Photovolt. Res. Appl.* **24**, 879 (2016).

[124] M. Yao, N. Huang, S. Cong, C.-Y. Chi, M. A. Seyedi, *et al*. "GaAs nanowire array solar cells with axial p-i-n junctions." *Nano Lett.* **14**, 3293 (2014).

[125] G. Otnes, and M. T. Borgström. "Towards high efficiency nanowire solar cells." *Nano Today* 1–15 (2016).

[126] D. van Dam, N. J. J. van Hoof, Y. Cui, P. J. van Veldhoven, E. P. A. M. Bakkers, *et al*. "High-efficiency nanowire solar cells with omnidirectionally enhanced absorption due to self-aligned indium–tin–oxide mie scatterers." *ACS Nano* **10**, 11414 (2016).

[127] X. Li, and Y. Zhan. "Enhanced external quantum efficiency in rectangular single nanowire solar cells." *Appl. Phys. Lett.* **102**, 1 (2013).

[128] T. Mårtensson, P. Carlberg, M. Borgstrom, L. Montelius, W. Seifert, *et al*. "Nanowire Arrays Defined by Nanoimprint Lithography." *Nano. Letts.* **4**, 699 (2004).

[129] H. He, X. Yu, Y. Wu, X. Mu, H. Zhu, *et al*. "13.7% Efficiency graphene–gallium arsenide Schottky junction solar cells with a P3HT hole transport layer." *Nano Energy* **16**, 91 (2015).

[130] G. Liang, X. Hu, X. Yu, Y. Shen, L. H. Li, *et al*. "Integrated Terahertz Graphene Modulator with 100% Modulation Depth." *ACS Photonics* **2**, 1559 (2015).

[131] T. Suzuki, M. Nagai, and Y. Kishi. "Extreme-sensitivity terahertz polarizer inspired by an anisotropic cut-through metamaterial." *Opt. Lett.* **41**, 325 (2016).

[132] S. S. Dhillon, M. S. Vitiello, E. H. Linfield, A. G. Davies, M. C. Hoffmann, *et al*. "The 2017 terahertz science and technology roadmap." *J. Phys. D: Appl. Phys.* **50**, 043001 (2017).

[133] M. Tonouchi. "Cutting-edge terahertz technology." *Nat. Photonics* **1**, 97 (2007).

[134] B. Ferguson, and X.-C. Zhang. "Materials for terahertz science and technology." *Nature Mater.* **1**, 26 (2002).

[135] R. Ulbricht, E. Hendry, J. Shan, T. F. Heinz, and M. Bonn. "Carrier dynamics in semiconductors studied with time-resolved terahertz spectroscopy." *Rev. Mod. Phys.* **83**, 543 (2011).

[136] J. Shan, and T. F. Heinz. "Terahertz radiation from semiconductors." *Ultrafast Dyn. Process. Semicond.* **59**, 1 (2004).

[137] M. Kress, T. Löff, S. Eden, M. Thomson, and H. G. Roskos. "Terahertz-pulse generation by photoionization of air with laser pulses composed of both fundamental and second-harmonic waves." **29**, 1120 (2004).

[138] K. Suto, and J. Nishizawa. "Widely frequency-tunable terahertz wave generation and spectroscopic application." *Int. J. Infrared Milli.* **1**, 63 (2005).

[139] M. B. Johnston, A. Corchia, A. Dowd, E. H. Linfield, A. G. Davies, *et al*. "Magnetic-field-induced enhancement of terahertz emission from III-V semiconductor surfaces." *Physica E* **13**, 896 (2002).

[140] Y. C. Shen, P. C. Upadhya, H. E. Beere, E. H. Linfield, a. G. Davies, *et al*. "Generation and detection of ultrabroadband terahertz radiation using photoconductive emitters and receivers." *Appl. Phys. Lett* **85**, 164 (2004).

[141] M. B. Johnston, A. Dowd, R. Driver, E. H. Linfield, a. G. Davies, *et al*. "Emission of collimated THz pulses from photo-excited semiconductors." *Semicond. Sci. Technol.* **19**, S449 (2004).

[142] J. Faist, F. Capasso, D. L. Sivco, C. Sirtori, A. L. Hutchinson, *et al*. "Quantum cascade laser." *Science* **264**, 553 (1994).

[143] K. Reimann. "Table-top sources of ultrashort THz pulses." *Rep. Prog. Phys.* **70**, 1597 (2007).

[144] A. Nahata, D. H. Auston, T. F. Heinz, and C. Wu. "Coherent detection of freely propagating terahertz radiation by electro-optic sampling." *Appl. Phys. Lett* **68**, 150 (1996).

[145] J. Dai, J. Liu, and X.-c. Zhang. "Terahertz wave air photonics: Terahertz wave generation and detection with laser-induced gas plasma." *IEEE J. Sel. Top. Quantum Electron.* **17**, 183 (2011).

[146] Y. Cai, I. Brener, J. Lopata, J. Wynn, L. Pfeiffer, *et al*. "Coherent terahertz radiation detection: Direct comparison between free-space electro-optic sampling and antenna detection." *Appl. Phys. Lett* **73**, 444 (1998).

[147] K. Peng, P. Parkinson, L. Fu, Q. Gao, N. Jiang, *et al*. "Single nanowire photoconductive terahertz detectors." *Nano Lett.* **15**, 206 (2015).

[148] K. Peng, P. Parkinson, J. L. Boland, Q. Gao, Y. C. Wenas, *et al*. "Broadband phase-sensitive single InP nanowire photoconductive terahertz detectors." *Nano. Letts.* **16**, 4925 (2016).

[149] J. L. Boland, S. Conesa-Boj, P. Parkinson, G. Tütüncüoglu, F. Matteini, *et al*. "Modulation doping of GaAs/AlGaAs core–shell nanowires with effective defect passivation and high electron mobility." *Nano. Letts.* **15**, 1336 (2015).

[150] J. L. Boland, A. Casadei, F. Matteini, C. L. Davies, F. Jabeen, *et al*. "Increased photoconductivity lifetime in GaAs nanowires by controlled n-type and p-type doping." *ACS Nano* **10**, 4219 (2016).

[151] C. Beard, M.C., Turner, G.M., Schmuttenmaer. "Terahertz Spectroscopy." *J. Phys. Chem. A* **106**, 6427 (2002).

[152] A. Nahata, A. S. Weling, and T. F. Heinz. "A wideband coherent terahertz spectroscopy system using optical rectification and electro-optic sampling." *Appl. Phys. Lett* **69**, 2321 (1996).

[153] L. Duvillaret, F. Garet, and J.-L. L. Coutaz. "A reliable method for extraction of material parameters in terahertz time-domain spectroscopy." *IEEE J. Sel. Top. Quantum Electron.* **2**, 739 (1996).

[154] D. M. Mittleman, M. Gupta, R. Neelamani, R. G. Baraniuk, J. V. Rudd, *et al*. "Recent advances in terahertz imaging." *Appl. Phys. B* **68**, 1085 (1999).

[155] J. B. Jackson, M. Mourou, J. F. Whitaker, I. N. Duling, S. L. Williamson, *et al*. "Terahertz imaging for non-destructive evaluation of mural paintings." *Opt. Commun.* **281**, 527 (2008).

[156] J. Shu, C. Qiu, V. Astley, D. Nickel, D. M. Mittleman, *et al*. "High-contrast terahertz modulator based on extraordinary transmission through a ring aperture." *Opt. Express* **19**, 26666 (2011).

[157] S. Zhang, J. Zhou, Y.-S. Park, J. Rho, R. Singh, *et al*. "Photoinduced handedness switching in terahertz chiral metamolecules." *Nature Commun.* **3**, 942 (2012).

[158] N. Grady, J. E. Heyes, D. R. Chowdhury, Y. Zeng, M. T. Reiten, *et al*. "Metamaterials for broadband linear polarization conversion and near-perfect anomalous refraction." *Science* **340**, 1 (2013).

[159] C. M. Watts, D. Shrekenhamer, J. Montoya, G. Lipworth, J. Hunt, *et al*. "Terahertz compressive imaging with metamaterial spatial light modulators." *Nature Photon.* **8**, 605 (2014).

[160] W. L. Chan, H. T. Chen, A. J. Taylor, I. Brener, M. J. Cich, *et al*. "A spatial light modulator for terahertz beams." *Appl. Phys. Lett* **94**, 3 (2009).

[161] K. U. R.Kersting, G. Strasser. "Terahertz phase modulator." *Electron. Lett.* **36**, 1156 (2000).

[162] T. Kleine-Ostmann, K. Pierz, G. Hein, P. Dawson, M. Marso, *et al*. "Spatially resolved measurements of depletion properties of large gate two-dimensional electron gas semiconductor terahertz modulators." *J. Appl. Phys.* **105**, 0 (2009).

[163] C.-F. Hsieh, Y.-C. Lai, R.-P. Pan, and C.-L. Pan. "Polarizing terahertz waves with nematic liquid crystals." *Opt. Lett.* **33**, 1174 (2008).

[164] C.-F. Hsieh, R.-P. Pan, T.-T. Tang, H.-L. Chen, and C.-L. Pan. "Voltage-controlled liquid-crystal terahertz phase shifter and quarter-wave plate." *Opt. Lett.* **31**, 1112 (2006).

[165] I. Yamada, K. Takano, M. Hangyo, M. Saito, and W. Watanabe. "Terahertz wire-grid polarizers with micrometer-pitch Al gratings." *Opt. Lett.* **34**, 274 (2009).

[166] Y. Ma, a. Khalid, T. D. Drysdale, and D. R. S. Cumming. "Direct fabrication of terahertz optical devices on low-absorption polymer substrates." *Opt. Lett.* **34**, 1555 (2009).

[167] S. Li, Z. Yang, J. Wang, and M. Zhao. "Broadband terahertz circular polarizers with single- and double-helical array metamaterials." *J. Opt. Soc. Am. A* **28**, 19 (2011).

[168] M. Hochberg, T. Baehr-Jones, G. Wang, M. Shearn, K. Harvard, *et al*. "Terahertz all-optical modulation in a silicon-polymer hybrid system." *Nature Mater.* **5**, 703 (2006).

[169] H. T. Chen, S. Palit, T. Tyler, C. M. Bingham, J. M. O. Zide, *et al*. "Hybrid metamaterials enable fast electrical modulation of freely propagating terahertz waves." *Appl. Phys. Lett.* **93**, 7 (2008).

[170] O. Paul, C. Imhof, B. Lägel, S. Wolff, J. Heinrich, *et al*. "Polarization-independent active metamaterial for high-frequency terahertz modulation." *Opt. Express* **17**, 819 (2009).

[171] M. Unlu, M. R. Hashemi, C. W. Berry, S. Li, S.-H. Yang, *et al*. "Switchable scattering meta-surfaces for broadband terahertz modulation." *Sci. Rep.* **4**, 5708 (2014).

[172] J. E. Heyes, W. Withayachumnankul, N. K. Grady, D. R. Chowdhury, A. K. Azad, *et al*. "Hybrid metasurface for ultra-broadband terahertz modulation." *Appl. Phys. Lett* **105**, 181108 (2014).

[173] H.-T. Chen, W. J. Padilla, M. J. Cich, A. K. Azad, R. D. Averitt, *et al*. "A metamaterial solid-state terahertz phase modulator." *Nature Photon.* **3**, 148 (2009).

[174] J. Mork, Y. Chen, and M. Heuck. "Photonic crystal fano laser: Terahertz modulation and ultrashort pulse generation." *Physical Review Lett.* **113**, 1 (2014).

[175] N. Born, M. Scheller, M. Koch, and J. V. Moloney. "Cavity enhanced terahertz modulation." *Appl. Phys. Lett.* **104**, 2014 (2014).

[176] B. Sensale-Rodriguez, R. Yan, M. M. Kelly, T. Fang, K. Tahy, *et al*. "Broadband graphene terahertz modulators enabled by intraband transitions." *Nature Commun.* **3**, 780 (2012).

[177] S. Shi, B. Zeng, X. Hong, H. S. Jung, A. Zettl, *et al*. "Optimizing broadband terahertz modulation with hybrid graphene/ metasurface structures." *Nano Lett.* **15**, 372 (2015).

[178] H. K. Choi, S. H. S. Lee, C.-G. Choi, S.-Y. Choi, X. Zhang, *et al*. "Switching terahertz waves with gate-controlled active graphene metamaterials." *Nature Mater.* **11**, 936 (2012).

[179] L. Ren, C. L. Pint, L. G. Booshehri, W. D. Rice, X. Wang, *et al*. "Carbon nanotube terahertz polarizer." *Nano Lett.* **9**, 2610 (2009).

[180] J. Kyoung, E. Y. Jang, M. D. Lima, H. R. Park, R. O. Robles, *et al*. "A reel-wound carbon nanotube polarizer for terahertz frequencies." *Nano Lett.* **11**, 4227 (2011).

[181] N. Karl, K. Reichel, H. T. Chen, A. J. Taylor, I. Brener, *et al*. "An electrically driven terahertz metamaterial diffractive modulator with more than 20 dB of dynamic range." *Appl. Phys. Lett.* **104**, 1 (2014).

[182] S. Z. Chen, J. F. Liu, H. J. H. Chen, and F. S. Huang. "Study of nanoimprint pattern transfer on hydrogen silsesquioxane." *J. Vac. Sci. Technol. B Microelectron. Nanom. Struct.* **24**, 1934 (2006).

[183] X. Liu, E. P. J. Parrott, B. S.-Y. Ung, and E. Pickwell-MacPherson. "Exploiting total internal reflection geometry for efficient optical modulation of terahertz light." *APL Photonics* **1**, 071603 (2016).

[184] Y. Harada, M. S. Ukhtary, M. Wang, S. Srinivasan, E. Hasdeo, *et al*. "Giant terahertz-wave absorption by monolayer graphene in a total internal reflection geometry." *ACS Photonics* **4**, 121 (2017).

[185] J. Jean, A. Wang, and V. Bulović. "In situ vapor-deposited parylene substrates for ultra-thin, lightweight organic solar cells." *Org. Electron.* **31**, 120 (2016).

[186] Y. Galagan, J.-E. J. M. Rubingh, R. Andriessen, C.-C. Fan, P. W. M. Blom, *et al*. "ITO-free flexible organic solar cells with printed current collecting grids." *Sol. Energy Mater. Sol. Cells* **95**, 1339 (2011).

[187] A. Nathan, A. Ahnood, M. T. Cole, Y. Suzuki, P. Hiralal, *et al*. "Flexible Electronics: The Next Ubiquitous Platform." *Proc. IEEE* **100**, 1486 (2012).

[188] K. Takei, T. Takahashi, J. C. Ho, H. Ko, A. G. Gillies, *et al*. "Nanowire active-matrix circuitry for low-voltage macroscale artificial skin." *Nat. Mater.* **9**, 821 (2010).

[189] X. Dai, A. Messanvi, H. Zhang, C. Durand, J. Eymery, *et al*. "Flexible Light-Emitting Diodes Based on Vertical Nitride Nanowires." *Nano Lett.* **15**, 6958 (2015).

[190] P. Zhu, S. Gu, X. Shen, N. Xu, Y. Tan, *et al*. "Direct conversion of perovskite thin films into nanowires with kinetic control for flexible optoelectronic devices." *Nano Lett.* **16**, 871 (2016).

[191] M. C. Mcalpine, R. S. Friedman, S. Jin, K.-h. Lin, W. U. Wang, *et al*. "High-Performance Nanowire Electronics and Photonics on Glass and Plastic Substrates." *Nano Lett.* **3**, 1531 (2003).

[192] F. Nickel, T. Haas, E. Wegner, D. Bahro, S. Salehin, *et al*. "Mechanically robust, ITO-free, 4.8% efficient, all-solution processed organic solar cells on flexible PET foil." *Sol. Energy Mater. Sol. Cells* **130**, 317 (2014).

[193] Lux Research. "The coming crack-up in the wearable electronics market." (2015). http://blog.luxresearchinc.com/blog/2015/08/the-coming-crack-up-in-the-wearable-electronics-market-2/.

[194] Pulse.ng. "Body-adapted wearable electronics." (2014). http://www.pulse.ng/news/politics/emerging-technologies-2014-1-body-adapted-wearable-electronics-id2785849.html.

[195] B. Fagioli. "LG mass-produces first-ever flexible OLED smartphone display." (2013). https://betanews.com/2013/10/07/lg-mass-produces-first-ever-flexible-oled-smartphone-display/.

[196] R. Arthur. "Tommy Hilfiger's Solar-Powered Jacket - Wearable Tech in Review." (2014). https://www.forbes.com/sites/rachelarthur/2014/11/20/tommy-hilfigers-solar-powered-jacket-wearable-tech-in-review/#57ed54df566b.

[197] Plastics Today. "The cutting edge: Sensors stretch and remain flexible." (2011). https://www.plasticstoday.com/content/cutting-edge-sensors-stretch-and-remain-flexible/98142107715826.

[198] F. R. Fan, W. Tang, and Z. L. Wang. "Flexible Nanogenerators for Energy Harvesting and Self-Powered Electronics." *Adv. Mater.* **28**, 4283 (2016).

[199] A. Nadarajah, R. C. Word, J. Meiss, and R. Könenkamp. "Flexible inorganic nanowire light-emitting diode." *Nano Lett.* **8**, 534 (2008).

[200] F. C. Krebs, and M. Jørgensen. "High carrier mobility in a series of new semiconducting PPV-type polymers." *Macromolecules* **36**, 4374 (2003).

[201] S. B. Hacène, and T. Benouaz. "Influence of charge carrier mobility and surface recombination velocity on the characteristics of P3HT: PCBM organic solar cells." *Phys. Status. Solidi. A* **211**, 862 (2014).

[202] P. P. Boix, J. Bisquert, M. Sessolo, and H. J. Bolink. "Solar energy materials & solar cells Simultaneous determination of carrier lifetime and electron density-of-states in P3HT:PCBM organic solar cells under illumination by impedance spectroscopy." *Sol. Energy. Mater. Sol. Cells.* **94**, 366 (2010).

[203] W. Gaynor, G. F. Burkhard, M. D. McGehee, and P. Peumans. "Smooth nanowire/polymer composite transparent electrodes." *Adv. Mater.* **23**, 2905 (2011).

[204] M. F. L. D. Volder, S. H. Tawfick, R. H. Baughman, and A. J. Hart. "Carbon Nanotubes: Present and Future Commercial Applications." *Science* **339**, 535 (2013).

[205] X. Chen, C. K. Y. Wong, C. A. Yuan, and G. Zhang. "Nanowire-based gas sensors." *Sensors Actuators B. Chem.* **177**, 178 (2013).

[206] P. Judeinstein, and C. Sanchez. "Hybrid organic-inorganic materials: a land of multidisciplinarity." *J. Mater. Chem.* **6**, 511 (1996).

[207] C. H. Lee, D. R. Kim, and X. Zheng. "Fabricating nanowire devices on diverse substrates by simple transfer-printing methods." *Proc. Natl. Acad. Sci. U. S. A.* **107**, 9950 (2010).

[208] P. K. Mohseni, A. Behnam, J. D. Wood, X. Zhao, K. J. Yu, *et al*. "Monolithic III-V nanowire solar cells on graphene via direct Van der Waals epitaxy." *Adv. Mater.* **26**, 3755 (2014).

[209] R. Yerushalmi, Z. A. Jacobson, J. C. Ho, Z. Fan, and A. Javey. "Large scale, highly ordered assembly of nanowire parallel arrays by differential roll printing Large scale, highly ordered assembly of nanowire parallel arrays by differential roll printing." *Appl. Phys. Lett* **91**, 203104 (2007).

[210] B. Park, I.-G. Bae, and Y. H. Huh. "Aligned silver nanowire-based transparent electrodes for engineering polarisation-selective optoelectronics." *Sci. Rep.* **6**, 19485 (2016).

[211] J. B. Cui, C. P. Daghlian, U. J. Gibson, R. Püsche, P. Geithner, *et al*. "Low-temperature growth and field emission of ZnO nanowire arrays." *J. Appl. Phys.* **97** (2005).

[212] Z. Fan, H. Razavi, J.-w. Do, A. Moriwaki, O. Ergen, *et al*. "Three-dimensional nanopillar-array photovoltaics on low-cost and flexible substrates." *Nat. Mater.* **8**, 648 (2009).

[213] M. T. Hessmann, T. Kunz, T. Ahmad, D. Li, S. Wittmann, *et al*. "O pen Solar cell fabricated on welded thin flexible silicon." **60302** (2015).

[214] F. Yang, M. E. Messing, K. Mergenthaler, M. Ghasemi, J. Johansson, *et al*. "Zn-doping of GaAs nanowires grown by aerotaxy." *J. Cryst. Growth* **414**, 181 (2015).

[215] J. Song, J. Li, J. Xu, and H. Zeng. "Super-stable transparent conductive Cu-Cu_4Ni nanowire elastomer composites against oxidation, bending, stretching and twisting for flexible and stretchable optoelectronics." *Nano Lett.* **14**, 6298 (2014).

[216] A. Gang, N. Haustein, L. Baraban, W. Weber, T. Mikolajick, *et al*. "Microfluidic alignment and trapping of ID nanostructures – a simple fabrication route for single-nanowire field effect transistors." *RSC* **5**, 94702 (2015).

[217] S. Wu, K. Huang, E. Shi, W. Xu, Y. Fang, *et al*. "Soluble polymer-based, blown bubble assembly of single and double-layer nanowires with shape control." *ACS Nano* **8**, 3522 (2014).

[218] M. C. M. C. Alpine, H. Ahmad, D. Wang, and J. R. Heath. "Highly ordered nanowire arrays on plastic substrates for ultrasensitive flexible chemical sensors." **23** (2007).

[219] D. Li, Y. Wang, and Y. Xia. "Electrospinning Nanofibers as Uniaxially Aligned Arrays and Layer-by-Layer Stacked Films." *Adv. Mater.* **16**, 361 (2004).

[220] T. Haggren, A. Shah, A. Autere, J.-P. Kakko, V. Dhaka, *et al*. "Nanowire encapsulation with polymer for electrical isolation and enhanced optical properties." *Nano Research* **10**, 2657 (2017).

[221] T. B. Singh, and N. S. Sariciftci. "Progress in Plastic Electronics Devices." *Annu. Rev. Mater. Res.* **36**, 199 (2006).

[222] A. C. E. Chia, and R. R. LaPierre. "Contact planarization of ensemble nanowires." *Nanotechnology* **22**, 245304 (2011).

[223] X. Yuan, P. Caroff, J. Wong-leung, L. Fu, and H. H. Tan. "Tunable polarity in a III–V nanowire by droplet wetting and surface energy engineering." *Adv. Mater.* **27**, 6096 (2015).

[224] A. G. Emslie, F. T. Bonner, and L. G. Peck. "Flow of a viscous liquid on a rotating disk." *J. Appl. Phys.* **29**, 1 (1958).

[225] N. Sahu, B. Parija, and S. Panigrahi. "Fundamental understanding and modelling of spin coating process: A review." *Indian J. Phys.* **83**, 493 (2009).

[226] P. Marchand, S. Sathasivam, B. A. D. Williamson, D. Pugh, S. M. Bawaked, *et al*. "A single-source precursor approach to solution processed indium arsenide thin films." *J. Mater. Chem. C* **4**, 6761 (2016).

[227] S. Choubak, P. L. Levesque, E. Gaufres, M. Biron, P. Desjardins, *et al*. "Graphene CVD : Interplay Between Growth and Etching on Morphology and Stacking by Hydrogen and Oxidizing Impurities." *J. Phys. Chem.* **118**, 21532 (2014).

[228] M. Wang, X. Wang, P. Moni, A. Liu, D. H. Kim, *et al*. "CVD Polymers for Devices and Device Fabrication." *Adv. Mater.* **29** (2017).

[229] S. H. Baxamusa. "Conformal polymer cvd." (2014).

[230] T. Duan, C. Liao, T. Chen, N. Yu, Y. Liu, *et al*. "Single crystalline nitrogen-doped InP nanowires for low-voltage fi eld-effect transistors and photodetectors on rigid silicon and fl exible mica substrates." *Nano Energy* **15**, 293 (2015).

[231] C. K. Jeong, K.-I. Park, J. H. Son, G.-T. Hwang, S. H. Lee, *et al*. "Self-powered fully flexible light-emitting system enabled by flexible energy harvester." *Energy Environ. Sci.* **7**, 4035 (2014).

[232] S. V. Ribu, and M. A. Ravi. "Design and optimization of a doubly clamped piezoresistive acceleration sensor with an integrated silicon nanowire piezoresistor." *Microsyst. Technol.* **23**, 3525 (2017).

[233] K. Endo, H. Sato, Y. K, T. Mizukoshi, T. Yoshizawa, *et al*. "Fabrication of intrinsic Josephson junctions on BSCCO superconducting films grown by MOCVD." *Physica C. Superconductivity* **372–376**, 1075 (2002).

[234] P. Parkinson, H. J. Joyce, Q. Gao, H. H. Tan, X. Zhang, *et al*. "Carrier lifetime and mobility enhancement in nearly defect-free core-shell nanowires measured using time-resolved terahertz spectroscopy." *Nano Lett.* **9**, 1 (2009).

[235] K. Norrman, and N. B. Larsen. "Studies of spin-coated polymer films." *Annu. Rep. Prog. Chem. Sect. C* **101**, 174 (2005).

[236] J. Charmet, J. Bitterli, O. Sereda, M. Liley, P. Renaud, *et al.* "Optimizing Parylene C Adhesion for MEMS Processes: Potassium Hydroxide Wet Etching." *J. Microelectromechanical Syst.* **22**, 855 (2013).

[237] Big Chemical Encyclopedia. "Parylene deposition." (1999). http://chempedia.info/info/71298/.

[238] ACMAL. "Energy dispersive spectrometer." (2017). http://mcff.mtu.edu/acmal/electronmicroscopy/MA_EDS_Basic_Science.htm.

[239] J. Valícek. "Measurement of titanium surface roughness created by non-conventional cutting technology." *Res. Agr. Eng.* **57**, S57 (2011).

[240] Nunez group research. "Biophysics of bacterial biofilms." (2017). https://www.mtholyoke.edu/~menunez/ResearchPage/AFM.html.

[241] Y. Jusman, S. C. Ng, and N. A. A. Osman. "Investigation of CPD and HMDS sample preparation techniques for cervical cells in developing computer-aided screening system based on FE-SEM/EDX." *Hindawi* **1**, 289817 (2014).

[242] W. F. Gorham. "A New, General Synthetic Method for the Preparation of Linear Poly-p-xylylenes." *J. Polym. Sci. Part A-1 Polym. Chem.* **4**, 3027 (1966).

[243] Obducat. "Obducat product porfolio." (2018). http://www.obducat.com/products/product-portfolio/product/eitre-3/.

[244] A. Jilani, A. S. Abdel-Wahab, and A. H. Hammad. "Advance deposition techniques for thin film and coating." (2018). https://www.intechopen.com/books/modern-technologies-for-creating-the-thin-film-systems-and-coatings/advance-deposition-techniques-for-thin-film-and-coating.

[245] MIT. "Sol power processing." (2010). https://stuff.mit.edu/afs/athena.mit.edu/course/3/3.082/www/team2_f02/Pages/processing.html.

[246] N. Yasrebi, B. Bagheri, P. Yazdanfar, B. Rashidian, and P. Sasanpour. "Optimization of sputtering parameters for the deposition of low resistivity indium tin oxide thin films." (2014). https://link.springer.com/article/10.1007/s40195-014-0048-0.

[247] Newport. "Solar simulators." (2018). https://www.newport.com/f/solar-simulator-accessories.

[248] T. V. Lvova, A. L. Shakhmin, I. V. Sedova, and M. V. Lebedev. "Sulfur passivation of InSb(1 0 0) surfaces: Comparison of aqueous and alcoholic ammonium sulfide solutions using X-ray photoemission spectroscopy." *Appl. Surf. Sci.* **311**, 300 (2014).

[249] S. Baig. *Optoelectronic Devices Made From Polymer Encapsulated III-V Semiconductor Nanowires*. Cambridge University (2014).

[250] Y. S. Jeong, B. Ratier, a. Moliton, and L. Guyard. "UV-visible and infrared characterization of poly(p-xylylene) films for waveguide applications and OLED encapsulation." *Synth. Met.* **127**, 189 (2002).

[251] SCS. "Properties." (2019). https://scscoatings.com/wp-content/uploads/2017/09/02-SCS-Parylene-Properties-1016.pdf.

[252] C. D. Lee, and E. Meng. "Mechanical properties of thin-film parylene–metal–parylene devices." *Frontiers in Mechanical Engineering* **1**, 10 (2015).

[253] H. J. Joyce, J. L. Boland, C. L. Davies, H. J. Joyce, C. J. Docherty, *et al*. "Electronic properties of GaAs , InAs and InP nanowires studied by terahertz spectroscopy." *Nanotechnology* **7**, 214006 (2013).

[254] T. Kleine-Ostmann, and T. Nagatsuma. "A Review on Terahertz Communications Research." *J Infrared Milli Terahz Waves* **32**, 143 (2011).

[255] W. Gao, J. Shut, K. Reichel, D. Nickel, X. He, *et al*. "High-Contrast terahertz wave modulation by gated graphene enhanced by extraordinary transmission through ring apertures." *Nano Lett.* **14**, 1242 (2014).

[256] H.-T. Chen, W. J. Padilla, A. C. Zide, Joshua M. O. Gossard, A. J. Taylor, and R. D. Averitt. "Active terahertz metamaterial devices." *Nature* **444**, 597 (2006).

[257] J.-H. Kang, Q. Gao, H. J. Joyce, H. H. Tan, C. Jagadish, *et al*. "Defect-free GaAs/AlGaAs core–shell nanowires on Si substrates." *Cryst. Growth Des.* **11**, 3109 (2011).

[258] L. V. Titova, T. B. Hoang, H. E. Jackson, L. M. Smith, J. M. Yarrison-Rice, *et al*. "Temperature dependence of photoluminescence from single core-shell GaAs–AlGaAs nanowires." *Appl. Phys. Lett* **89**, 173126 (2006).

[259] P. Parkinson, H. J. Joyce, Q. Gao, H. H. Tan, X. Zhang, *et al*. "Carrier lifetime and mobility enhancement in nearly defect-free core–shell nanowires measured using time-resolved terahertz spectroscopy." *Nano Lett.* **9**, 3349 (2009).

[260] H. J. Joyce, J. Wong-Leung, C. K. Yong, C. J. Docherty, S. Paiman, *et al*. "Ultralow surface recombination velocity in InP nanowires probed by terahertz spectroscopy." *Nano Lett.* **12**, 5325 (2012).

[261] C. K. Yong, K. Noori, Q. Gao, H. J. Joyce, H. H. Tan, *et al*. "Strong carrier lifetime enhancement in GaAs nanowires coated with semiconducting polymer." *Nano Lett.* **12**, 6293 (2012).

[262] Y. Zhang. "The Tao of microelectronics." (2014). http://iopscience.iop.org/book/978-1-6270-5453-9/chapter/bk978-1-6270-5453-9ch2.

[263] Encyclopaedia Britannica. "Diode." (2018). https://www.britannica.com/technology/diode.

[264] F. Rizzi, N. J. van Eck, and M. Frey. "The production of scientific knowledge on renewable energies: Worldwide trends, dynamics and challenges and implications for management." *Renew. Energy* **62**, 657 (2014).

[265] C. J. Novotny, E. T. Yu, and P. K. L. Yu. "InP nanowire/polymer hybrid photodiode." *Nano Lett.* **8**, 775 (2008).

[266] A. C. E. Chia, and R. R. LaPierre. "Analytical model of surface depletion in GaAs nanowires." *J. Appl. Phys.* **112**, 63705 (2012).

[267] J. Li, D. Wang, and R. LaPierre. *Advances in III-V semiconductor nanowires*, vol. 1. 1 ed. Bentham books (2011).

[268] R. Schlaf, H. Murata, and Z. Kafafi. "Work function measurements on indium tin oxide films." *J. Electron Spectros. Relat. Phenomena* **120**, 149 (2001).

[269] W. F. Wei, and W. J. Leivo. "Photoelectric emission and work function of semiconducting diamonds." *Carbon N. Y.* **13**, 425 (1975).

[270] P. A. Tipler, and R. A. Llewellyn. *Modern Physics*. 3 ed. W.H. Freeman (1999).

[271] F. Schmitt, N. Susa, N. Shibata, H. Ikoma, A. Funyu, *et al*. "X-Ray photoelectron spectroscopic study of oxidation of InP." *Jpn. J. Appl. Phys.* **31**, 3976 (1992).

[272] Q. Li, K. W. Ng, and K. M. Lau. "Growing antiphase-domain-free GaAs thin films out of highly ordered planar nanowire arrays on exact (001) silicon." *Appl. Phys. Lett.* **106**, 072105 (2015).

[273] J. Zhang, A. C. E. Chia, and R. R. LaPierre. "Low resistance indium tin oxide contact to n-GaAs nanowires." *Semicond. Sci. Technol.* **29**, 054002 (2014).

[274] W. S. Koh, C. H. Gan, W. K. Phua, Y. a. Akimov, and P. Bai. "The potential of graphene as an ITO replacement in organic solar cells: An optical perspective." *IEEE J. Sel. Top. Quantum Electron.* **20** (2014).

[275] P. Arnou, J. W. Bowers, and J. M. Walls. "Aluminium-doped zinc oxide deposited by ultrasonic spray pyrolysis for thin film solar cell applications." *IEEE Proc. PVSC* **1**, 308 (2014).

[276] A. Sharma, V. Singh, T. L. Bougher, and B. A. Cola. "A carbon nanotube optical rectenna." *Nat. Nanotechnol.* **10**, 1027 (2015).

[277] R. Yan, D. Gargas, and P. Yang. "Nanowire photonics." *Nat. Photonics* **3**, 569 (2009).

Appendix A

Preliminary work on a solar cell based on SAE grown nanowires

Appendix A refers to initial studies in the developing the fabrication process for a flexible solar based on nanowire arrays grown by SAE (selective area epitaxy) which have been specially optimised for solar cell device applications.

A.1 SAE InP nanowire growth process

A 30 nm thick SiO_2 layer was deposited on (111)A p+ InP substrate by plasma enhanced chemical vapor deposition (PECVD) at 300 °C. After SiO_2 deposition, holes were patterned using electron beam lithography: Hexamethyldisilazane (HMDS) was spin-coated at 500 rpm for 5 s and then at 4000 rpm for 45 s, followed by ZEP 520A resist, spin-coated using the exact same procedure. The resist was then exposed to a pattern consisting of hexagonal array of holes defined using a Raith 150 electron beam lithography (EBL) system. After development of the resist, oxygen plasma (300 watts, 2 min, 300 sccm O_2 flow) was used to remove the footage residues of the resist prior to etching of the pattern in a solution of 48% hydrofluoric acid diluted 1:45 in ammonium fluoride (75 s). ZEP stripper was used to remove the ZEP and oxygen plasma was again used to clean the surface. Since the exposed InP surface could have been damaged during the SiO_2 deposition process, 10% H_2O_2 was first used to oxidize the InP layer for 2 minutes. Then a clean InP surface was prepared by etching off the oxide layer with 10% H_3PO_4 solution for 2 minutes. These steps were repeated sequentially for 5 times. After this trim etch, the sample was immediately transferred into the metal-organic vapor-phase epitaxy (MOVPE) reactor for NW growth.

The patterned array of PIN InP NWs were grown for 1.5 minutes(p), 5 minutes (i) and 1.5 minutes (n). The flow rate of PH_3, TMIn, SiH_4 and DEZn was $4.911\,x10^{-4}$ mol/min, $3.436\,x10^{-5}$ mol/min, $3.079\,x10^{-7}$ mol/min and $2.031\,x10^{-5}$ mol/min respectively. The V/III

ratio: 80.9 and the nanowires were grown at 730 °C. The nanowires were grown by Dr Qian Gao at Professor Jagadish's lab at the Australian National University.

A.2 Suggested device fabrication process

After optimising the fabrication process for test devices for a flexible nanowire solar cell, as described in Chapter 8, further work began to develop an analagous process for high quality pin junction InP nanowires that were specifically designed for use in solar cell devices. A PIN structure was used, to ensure the depletion region ran across most of the length of the nanowire, which reduces the chance of recombination in axial structures, and the nanowires were grown in dense arrays patterned by SAE [21].

A similar process to the one developed in Chapter 5 was envisioned - Parylene C would be deposited onto the nanowire substrate, and peeled off yielding nanowire array thin films. Furthermore, it was also thought that the nanowires could be removed selectively, leaving behind the dielectric mask which could potentially be used for subsequent growths, as per Figure A.1. Given that the EBL (electron beam lithography) and ALD (atomic layer deposition) steps needed for mask fabrication are time consuming and only suitable for small areas, the scope for reuse of the growth mask was a big positive.

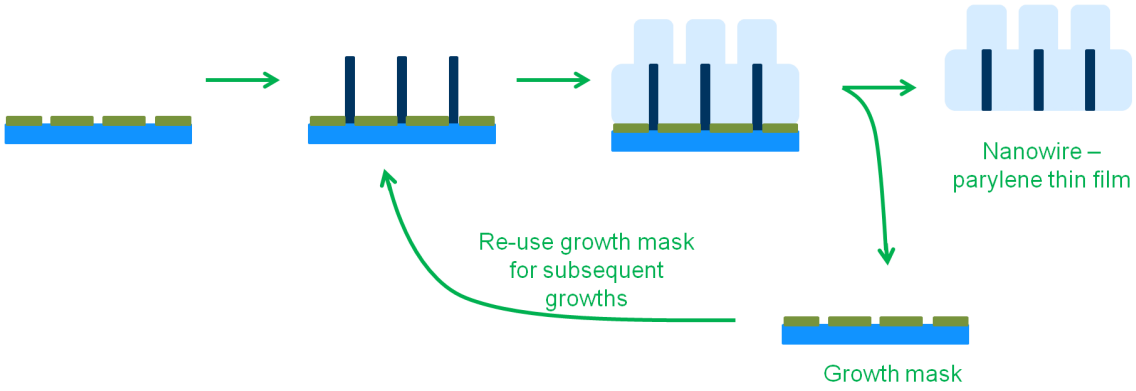

Fig. A.1: Schematic of SAE-nanowire-Parylene C thin films. Initially it was thought that the SAE grown nanowires could be coated with Parylene C and the nanowires would be removed selectively whilst the dielectric mask remained on the surface. The dielectric mask could then be reused for subsequent nanowire growths, which is currently not possible

SAE grown InP nanowires were not cleaved due to risk of damaging the array with debris. Hence, the entire substrate was coated with a 3 µm layer of Parylene C, peeled off and the excess Parylene C was trimmed using scissors, then backed onto a tacky PDMS slide for subsequent processing.

Samples consisting of spacings 400 nm apart and 800 nm apart were used for thin film fabrication tests. The nanowire density of the SAE defined nanowires was far greater then that of the VLS (vapour-liquid solid) defined nanowires. Interestingly, it was found that it was

difficult to lift off the samples consisting of 400 nm spacing — presumably because the nanowire density and effective surface area was so high, resulting in greater adhesion of the thin film to the substrate. It was much easier to lift off the nanowires that were spaced 800 nm apart.

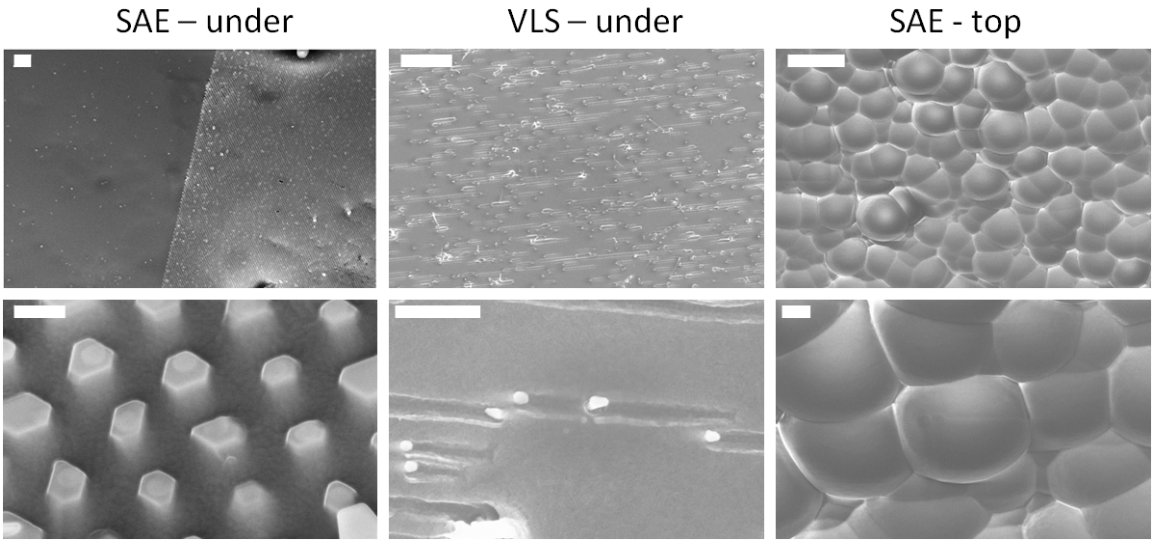

Fig. A.2: SEM images comparing parylene coated VLS and SAE nanowires. SAE-under shows the underside of the SAE nanowire film (in contact with the substrate). When compared to VLS-under, the two films look very different: VLS - under shows what the underside of the VLS nanowire film should look like with slight tears as the nanowire-film was removed from the substrate. SAE-top shows the top view of the nanowire film, which is comparable with other SEM images of nanowires coated with Parylene C.

In Figure A.2, while it is clear through the SEM image that the nanowires have been encapsulated in the Parylene C, and have been successfully listed off the substrate, it is unclear if the dielectric mask has also been removed. When comparing the thin films of the SAE nanowires with the thin films fabricated from VLS nanowires, it was immediately apparent that two looked different. The 'top' side of the films (as opposed to the substrate side) has a 'bubbly' textured appearance arising from the conformal nature of the coating, which was to be expected for both films. However, when examining the substrate side of the two films, they looked very different. The VLS film has obvious tears, which most likely arise from the resistance of the nanowires when they are being removed from the growth substrate. However, with the VLS film, these tears are not visible - which could indicate that the nanowires are stabilised in dielectric mask, which may have also been lifted off. thus preventing tears in the Parylene C film.

As shown in Figure A.3, EDS (energy dispersive spectroscopy was then carried out to deduce if the mask had been lifted off. However, this result was also inconclusive as the signal from the carbon arising from the Parylene C is so strong, it obscures the signal from the silicon and oxygen. Further characterisation such as AFM needs to be carried out to deduce if the mask has indded been lifted off.

Mask removal opens up several interesting possibilities for alternative device fabrication. Selectively contacting the core and shell elements of core-shell nanowires is difficult to do, and

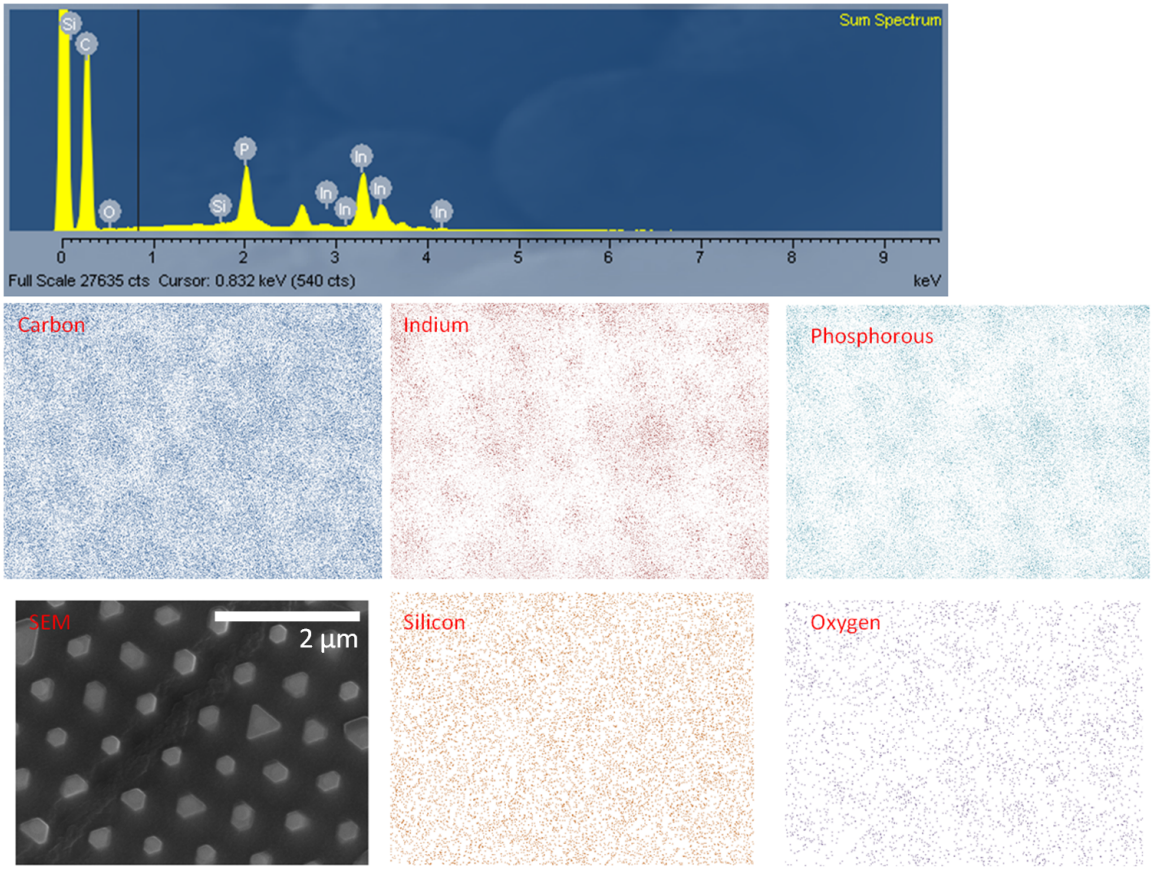

Fig. A.3: EDS (Energy-dispersive spectroscopy) spectra of the parylene coated SAE nanowires. Elemental maps were acquired to understand the presence of selected elements on the surface. Carbon arises from the polymer, indium and phosphorous arise from the nanowires, silicon arises from the dielectric mask, oxygen should arise from the dielectric mask but also indicates the presence of a surface oxide layer. Due to the strong signal of the carbon (from the Parylene), this elemental map is inconclusive.

often it is easy to contact both the core and shell, which results in short circuiting of the device. Current methods demonstrated in the literature are impractical - these include an *in situ* HCl etch during nanowire growth which prevents short circuiting arising from radial overgrowth [2]; careful post-growth etching of the n and i layers [32]; or by ensure that during growth, the shell does not completely cover the core nanowire[48].

If the mask has been successfully lifted off, it would make it much easier to selectively contact the core and shell components as seen in Figure A.4, as the mask essentially prevents contacting to the shell.

A.3 Device characterisation

It was found that the device have been short circuited, as shown in Figure A.5. For future devices, care needs to be taken to ensure that the Parylene is not overetched to exponse the I region, and is only etched enough to expose the N region for selective contacting.

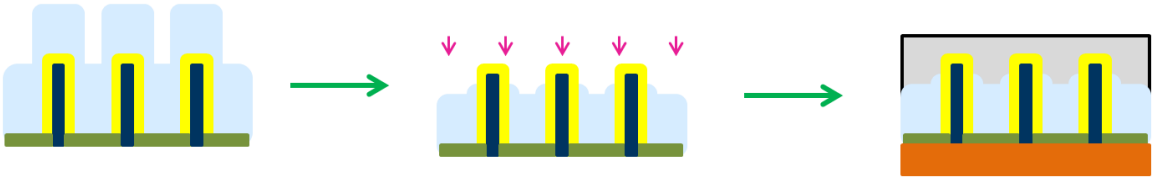

Fig. A.4: Schematic depicting how selective contacting of core-shell nanowire structures may be achieved if the dielectric mask is also removed from the substrate. Presence of the mask means that only the core material is exposed at the bottom of the device and hence can be selectively contacted. Growth of the shell material means that only the shell can be contacted by the top contact.

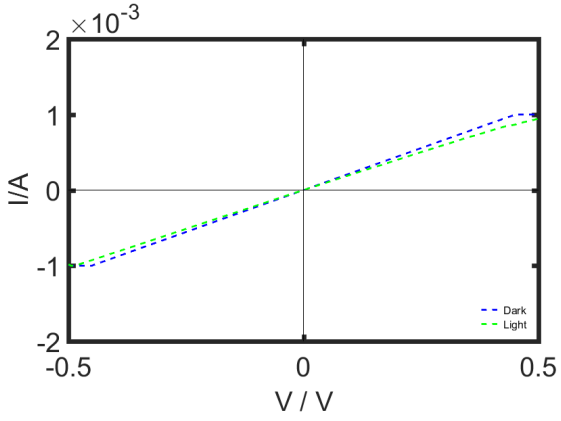

Fig. A.5: IV curve of solar cell based in SAE-defined nanowires. The device has been short circuited, presumably due to overetching of the Parylene C.

Appendix B

Preliminary studies on a single nanowire photodetector

Appendix B presents a fabrication method for a vertically aligned single nanowire photodetector. Here, the devices remains on the growth substrate, the fabrication method means that several single nanowire devices may be fabricated in tandem on the same substrate.

B.1 Nanowire growth and single nanowire photodetector fabrication

Electrically insulated vertically aligned MOCVD (metal-organic chemical vapour deposition) grown InP nanowires were used for accurate comparison to other single nanowire devices that are wholly removed from the growth substrate. This was achieved by spacing the nanowires sufficiently far apart so there was no cross talk between them. Unpublished FDTD (finite difference time domain) simulation work within the group showed that for a nanowire diameter of 150 nm, a minimum spacing of 1.6 μm was needed. The nanowires were grown by Dr Qian Gao at Professor Jagadish's lab at the Australian National University.

A schematic diagram of device fabrication is given in Figure B.1. The nanowires were planarised using BCB (benzocyclobutene) and etched using a highly localised FIB (focussed ion beam) milling technique to expose the tip of a single nanwoire. RIE (reactive ion etching) was not suitable in this case as the objective was to only isolate one single nanowire tip. Gold and ITO pads were deposited using sputter coating, and the Ti/Au back contacts were deposited using electron beam evaporation. The advantage of using the vertically aligned geometry is that several single nanowire photodetector devices can be fabricated quickly on a single wafer, after which they could be encapsulated using Parylene C and removed from the substrate.

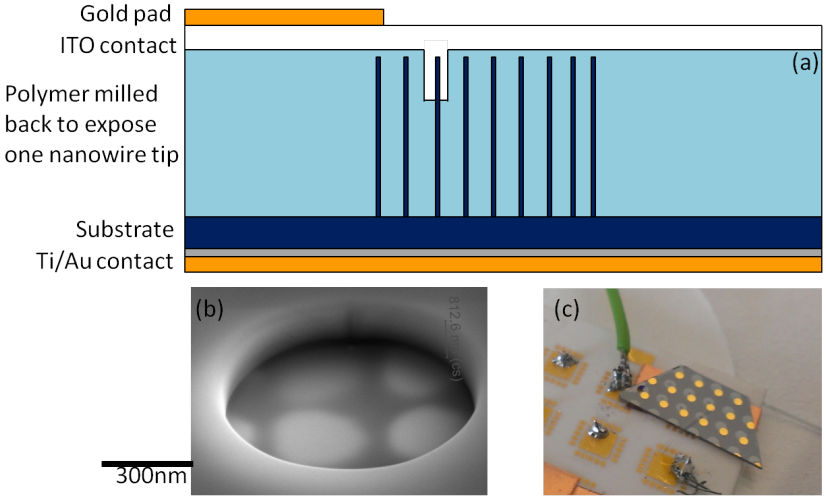

Fig. B.1: (a) Schematic of a vertically aligned nanowire photodetector device. (b) SEM (scanning electron microscope) image showing milling using FIB to expose nanowire (c) Photograph of finished device

B.2 Single nanowire photodetector characterisation

The FIB system was used to selectively expose single nanowire tips, using gallium ion beam milling. A small area was etched away quickly at a higher voltage and current until it was possible to see the nanowires below the surface of the polymer. The voltage and current was then turned down to etch away the material slowly and carefully to expose the nanowire tip. Finally, a gentle cleaning step was carried out to remove the last remnants of the polymer.

Exposure of the nanowire tips was confirmed using elemental mapping in Figure B.2. Dark spots indicate no material, whereas bright spots indicate an abundance of material. Compared to the SEM (scanning electron microscope) image, the bright spots in the indium and phosphorus maps and the dark spots in the carbon and silicon maps correspond to the exposed nanowire tips. However, it was noticed that gallium droplets were being deposited onto the sample and was confirmed using EDX (energy dispersive X-ray spectroscopy) and SEM, as shown in Figure B.2. Using lower/higher beam currents and voltages did little to avoid gallium droplet deposition. After etching, the rest of the device was fabricated

After contacting, the IV curves of the photodetector were taken. Unfortunately, as shown by the IV characteristics in Figure B.3, the device had short circuited. This may have occured due to unwanted metal contact through voids in the polymer layer. In addition, gallium contamination could have caused defects and traps, which could result in random generation of electron hole pairs which contributes to the dark current.

It would be interesting to repeat this experiment using Parylene C encapsulation instead of BCB, and using the insights gained from Chapter 8 regarding annealing-free ohmic contact formation.

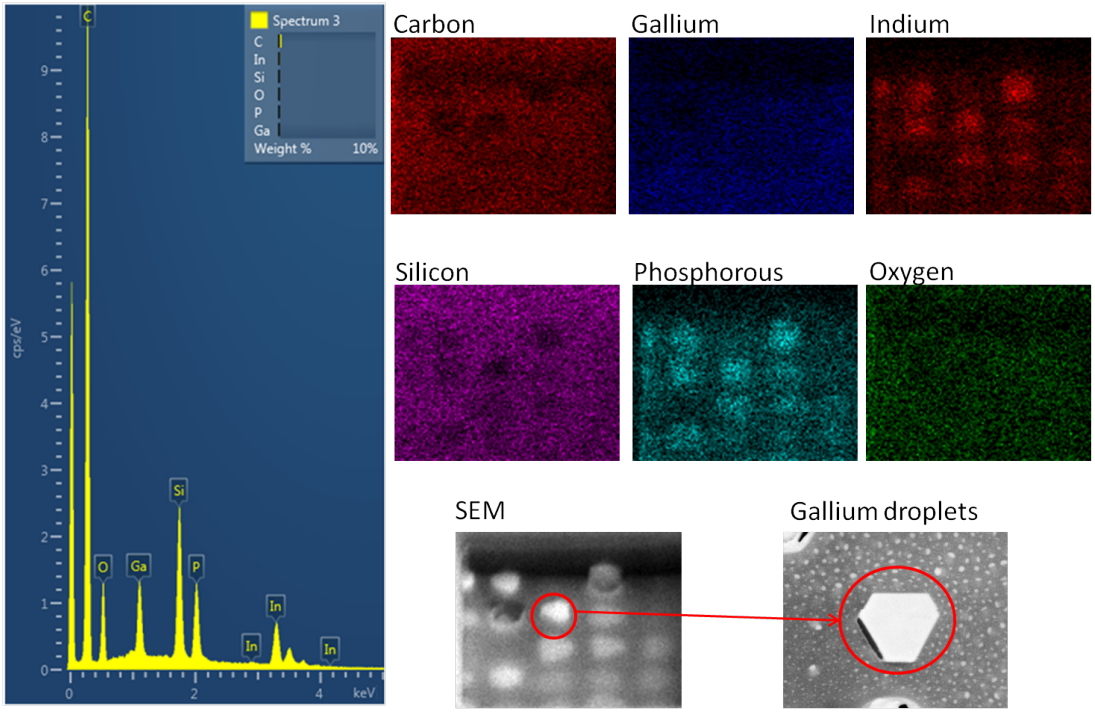

Fig. B.2: EDX spectra and elemental mapping showing gallium contamination following FIB milling. The bright spots in the maps show an adundance of material, the dark spots show a lack of material. The bright spots in the In and P maps and the dark spots in the C and Si maps correspond to the nanowire tips in the SEM images. The magnified SEM images also shows the gallium droplets deposited around the nanowire.

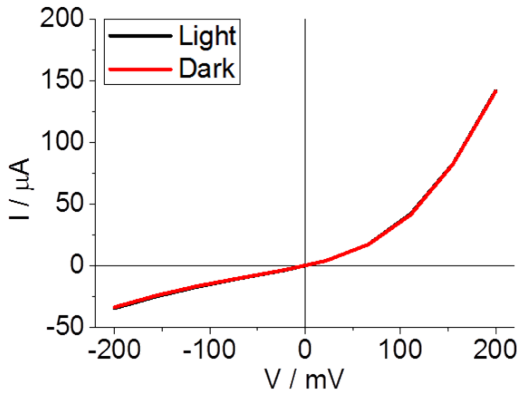

Fig. B.3: IV curves of the single nanowire photodetector. The device has short circuited, which is why there is no light photocurrent response

Appendix C

FDTD Simulations

Appendix C details initial FDTD (finite difference time domain) simulation studies for optimum nanowire geometries for light absorption

C.1 Simulation parameters

FDTD (finite difference time domain) simulations are used extensively in the literature to understand the interaction of a nano object with light [22]. The basic operation of an FDTD simulation is that the electric field and the magnetic field vectors are solved in an instance of time for a unit cell consisting of the nano object, subject to specific boundary conditions. This process is repeated for a different instances of time until the desired electromagnetic behaviour is found. As discussed extensively in Chapter 2, optical simulation work is of utmost importance when designing an optoelectronic device as different devices require different nanowire dimensions, materials, spacings etc. [21, 23, 57, 62]. Lumerical software was used to carry out the simulations.

For the single nanowire simulations, the materials were used as given in the Lumerical materials database without any further modification. 'GaAs–Palik' or 'InP–Palik' were used. Perfectly matched layers (PML) were used as boundary conditions in the *x,y,z* directions. As these are absorbing layers, they are used to simulate a single nanowire environment. A total-field scattered-field (TFSF) source was used as this source separates the computation region into the two: one that contains the total field, the other contains the scattered field. This is useful when studying the scattered field, as the two are separated. The source injection direction was in the z direction. The cross section analysis group was used to calculate the scattering and absorption cross sections. The absorption cross section monitor was placed inside the source region, whereas the scattering cross section monitor was placed outside the source. The wavelength range of the source was 450-850nm. The background index was set to 1 for air and 1.63 for Parylene C simulations. Nanowire diameter, length, material, volume and the background index were varied.

For the array simulations, the materials and background index parameters were set to the same as the single nanowire simulations. Periodic boundary conditions (PBC) were used in the x and y directions to simulate a 2D array of nanowires. PML boundary conditions were used in the z direction to absorb reflections that would lead to misleading simulation results. A plane wave source was used, as the TFSF source was unsuitable to be used in conjunction with periodic boundary conditions - the TSFS source can only be used where scattering in zeroeth order direction is of interest. Of course, this is not the case with nanowires, hence a plane wave source is used instead, with an injection axis in the z axis. Transmission and reflection monitors were used to calculate absolute transmission and reflection, and were placed below the nanowire and above the source respectively. Unit cell size was varied to investigate the effect of nanowire spacing on reflection and transmission measurements.

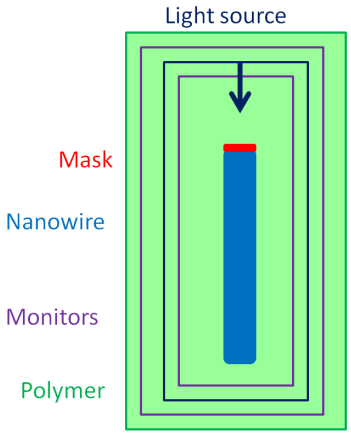

Fig. C.1: Schematic diagram outlining FDTD simulation unit cell

C.2 Single nanowire simulations

A single GaAs or InP nanowire of varying lengths and radii was embedded in Parylene C and air. This was to investigate the effect of embedding a nanowire in Parylene C, compared to air and to deduce the effect of the nanowire dimensions on the scattering and absorption cross sections.

For Figure C.2, the GaAs nanowire length was varied. A GaAs nanowire was set to have a radius of 100 nm, and lengths of 1 μm, 1.5 μm and 2 μm. Figure C.2 shows that the peak height of the absorption and scattering cross sections increased with the length of the nanowire. This was to be expected as a longer nanowire would have a greater probability of absorption and scattering events taking place. When comparing a nanowire embedded in Parylene C to a nanowire in air, the peak heights of both the scattering and absorptions cross sections are lower for the Parylene C simulations. This is to be expected as the refractive index of the nanowire ($n = 3.52$) is closer that of Parylene C ($n = 1.64$) than air ($n = 1$), resulting in less scatter at the Parylene C–nanowire interface.

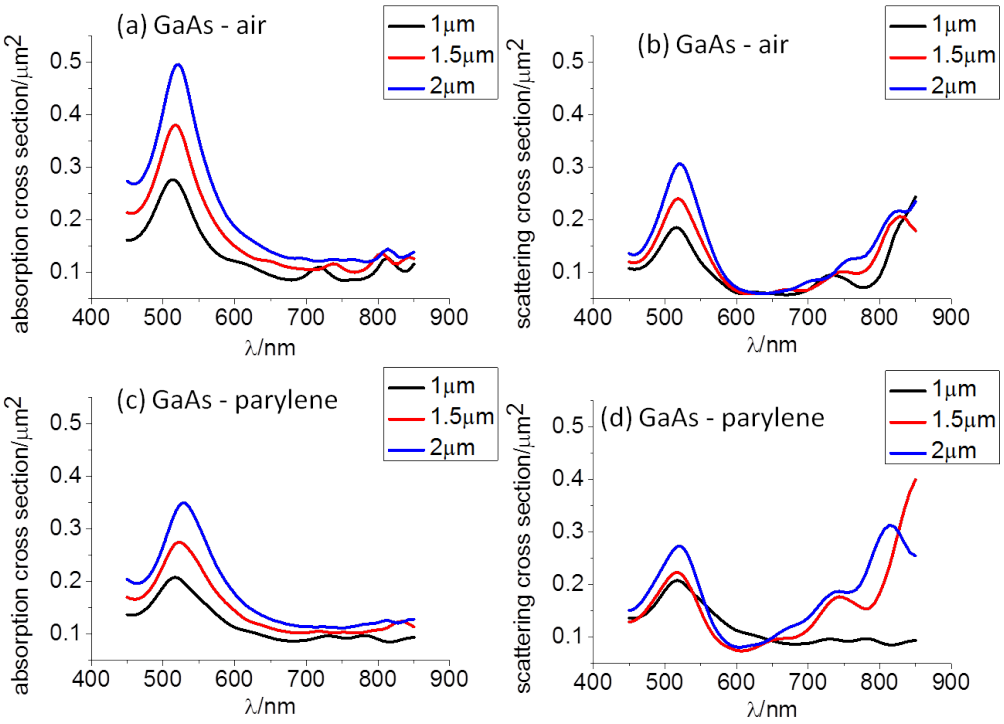

Fig. C.2: Single nanowire GaAs simulation varying nanowire length (1 μm, 1.5 μm, 2 μm). (a): Absorption cross section of GaAs in air. (b): Scattering cross section of GaAs in air. (c): Absorption cross section of GaAs in Parylene C. (d): Scattering cross section of GaAs in Parylene C

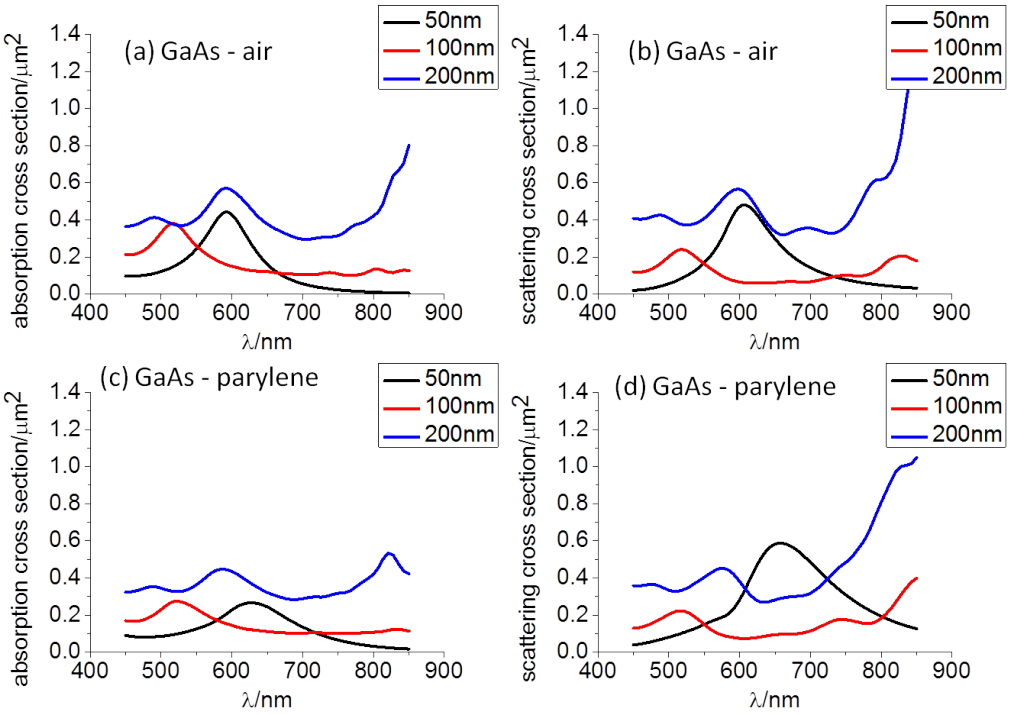

Fig. C.3: Single nanowire GaAs simulation varying nanowire radius (50 nm, 100 nm, 200 nm). (a): Absorption cross section of GaAs in air. (b): Scattering cross section of GaAs in air. (c): Absorption cross section of GaAs in Parylene C. (d): Scattering cross section of GaAs in Parylene C

For Figure C.3, the nanowire radius was varied. A single GaAs nanowire had its length set to 1.5 μm and the radius set to 50 nm, 100 nm and 200 nm. There is no clear correlation between the radius of the nanowire and the peak height of the absorption and scattering cross sections. Furthermore, when comparing the Parylene C and the air simulations for the 50 nm nanowire, the peak height of the scattering cross section curve increases in Parylene C. This is contrary to what is expected as a smaller difference in refractive index should result in less scatter. This may be due to evanescent waves increasing the perceived cross section of the nanowire, which enhances scattering due to resonant modes [277]. Finally, there is a change in the peak wavelength for the different nanowire radius, with no obvious correlation to the radius.

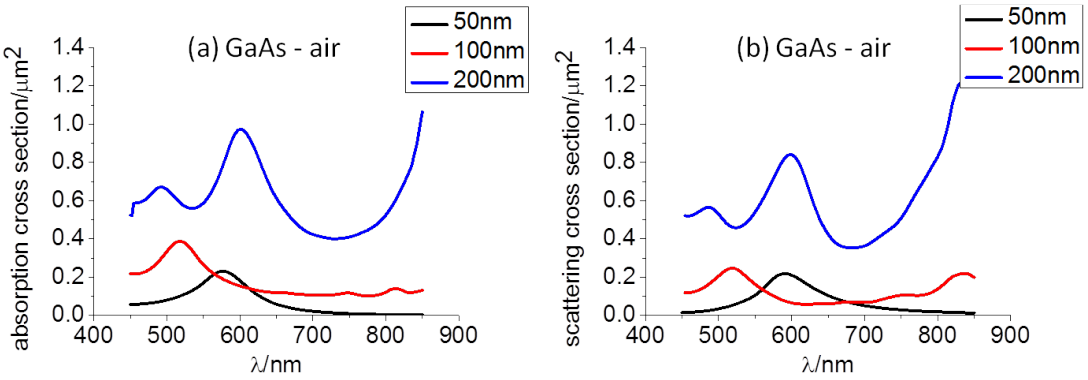

Fig. C.4: Single nanowire GaAs simulation maintaining nanowire aspect ratio but changing the nanowire size (radius/length values were 50 nm/1.5 μm, 100 nm/3 μm and 200 nm/6 μm). Graph (a): Absorption cross section of GaAs in air. Graph (b): Scattering cross section of GaAs in air.

The next simulation looked at maintaining the same aspect ratio, (50 nm/1.5 μm, 100nm/3 μm, 200 nm/1.5 μm) at different radii. There was a general increase of peak height with increasing nanowire radii. When comparing Figure C.4 with Figure C.3, the peak wavelength (λ_{max}) remained the same for each nanowire radius (r). For $r = 50$ nm, $\lambda_{max} = 580$ nm, $r = 100$ nm, $\lambda_{max} = 510$ nm, $r = 200$ nm, $\lambda_{max} = 590$ nm in both Figures C.3 and C.4. This may show that the peak wavelength for the absorption and scattering cross sections have a dependence on the nanowire radius.

For the next two simulations, the behaviour of InP was studied. Figure C.5 shows simulations where the nanowire length has been varied. A single InP nanowire had its radius set to 100 nm and lengths were 1 μm, 1.5 μm and 2 μm - analagous to the GaAs simulation (Figure C.2). As was expected, the peak height of the scattering and absorption cross section curves increased with nanowire length, due to increased probability of scattering and absorption events occuring. For the 2 μm nanowire, there was also a change in the peak wavelength and increased scatter at wavelengths close to the band gap. Scattering and absorption cross sections also decreased for the Parylene C samples with respect to air as the nanowire refractive index is closer to Parylene C refractive index.

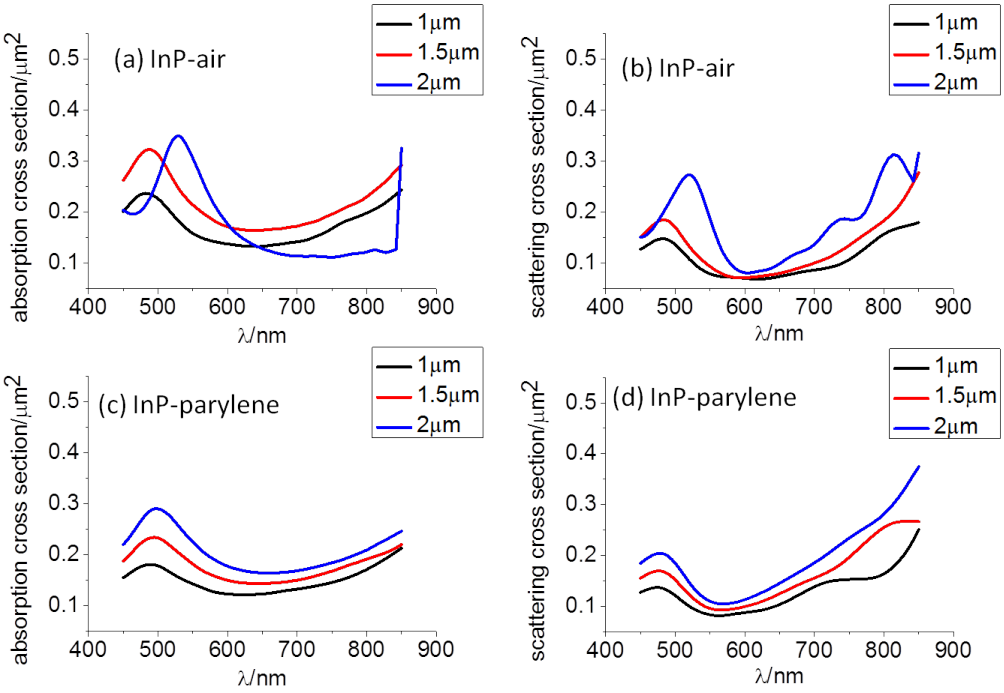

Fig. C.5: Single nanowire InP simulation varying nanowire length (1 μm, 1.5 μm, 2 μm). (a): Absorption cross section of InP in air. (b): Scattering cross section of InP in air. (c): Absorption cross section of InP in Parylene C. (d): Scattering cross section of InP in Parylene C

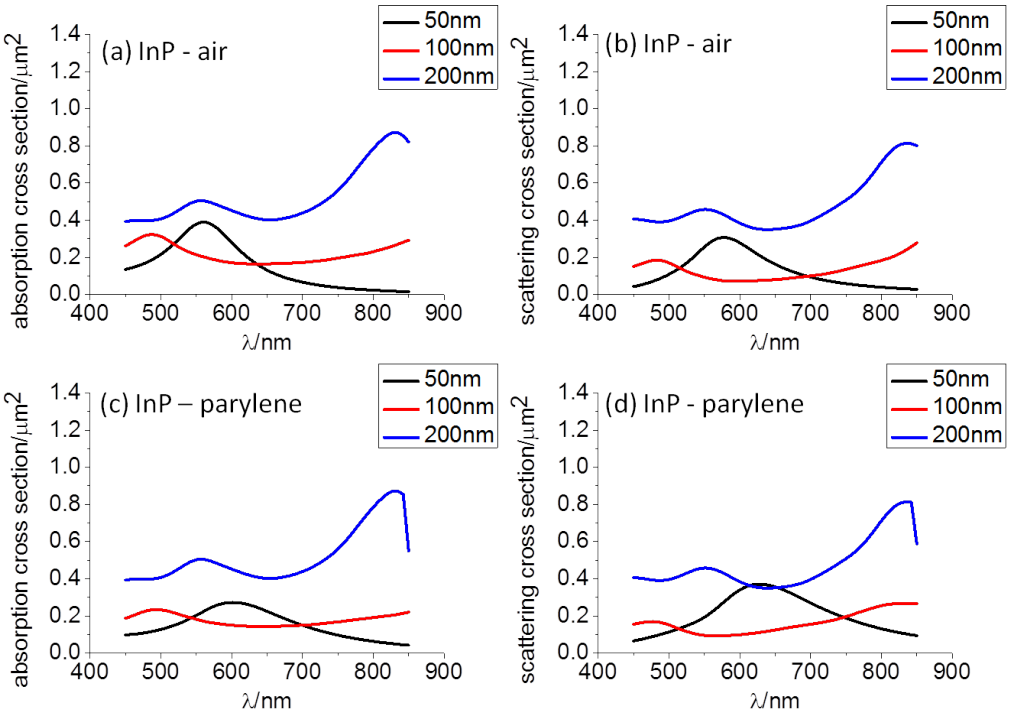

Fig. C.6: Single nanowire InP simulation varying nanowire radius (50 nm, 100 nm, 200 nm). (a): Absorption cross section of InP in air. (b): Scattering cross section of InP in air. (c): Absorption cross section of InP in Parylene C. (d): Scattering cross section of InP in Parylene C

For Figure C.5, the nanowire radii were varied. A single InP nanowire had its length set to 1.5 μm and the nanowire radius was set to 50 nm, 100 nm to 200 nm. This exhibited some interesting results, consistent with was was viewed with the GaAs results. There was also no clear trend between the nanowire radius and the scattering and absorption cross section peak heights, and there was also a shift in the peak wavelength with different radii.

C.3 Nanowire array simulations

Nanowire arrays simulations were carried out for GaAs. The objective of this was to investigate the effect of the nanowire spacing on transmission and reflection of light through a vertically aligned nanowire film. The radius and the length of the nanowires were kept at 50 nm and 1.5 μm, with the background index varied for air and Parylene C.

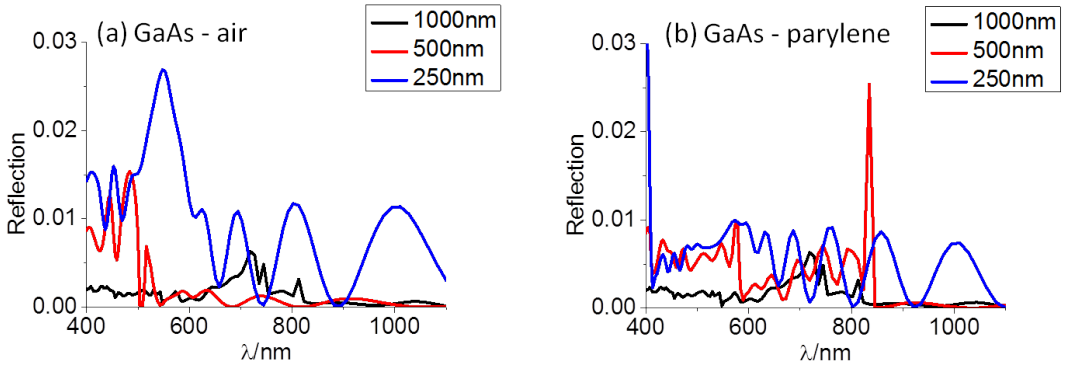

Fig. C.7: GaAs nanowire array simulation showing how reflection varies with unit cell size. Graph (a): Reflection from a nanowire array in air. Graph (b): Reflection from a Parylene C–nanowire film

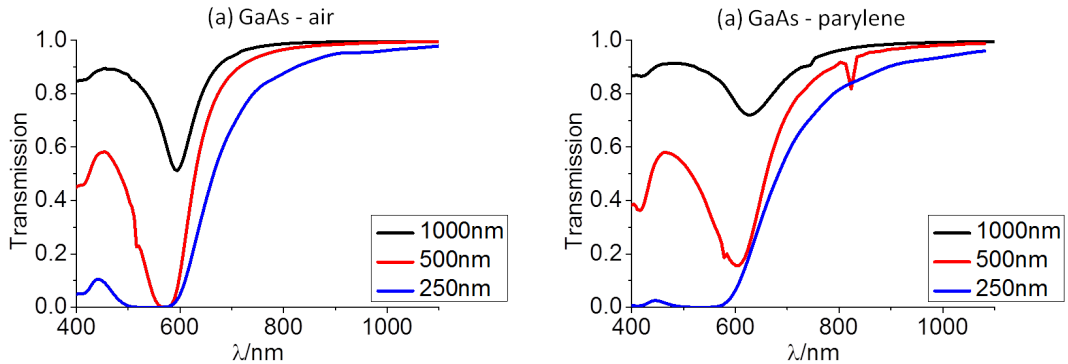

Fig. C.8: GaAs nanowire array simulation showing how transmission varies with unit cell size. Graph (a): Transmission through nanowire array in air. Graph (b): transmission through a Parylene C–nanowire film

The nanowire spacing was varied from 1000 nm, 500 nm and 250 nm. As shown by Figure C.7, this has a significant effect on reflection of the nanowires. Firstly, the reflection response of

the nanowires is absolutely minimal compared to the transmission (Figures C.7 and C.8). This may be due to light trapping effects from the nanowires, resulting in very little light escaping the array. Interestingly, wider spaced nanowires (1000 nm) seem to reflect less, perhaps due to reduced scatter between the nanowires. In addition, with decreased nanowire spacing (250 nm), there were increased periodic reflections arising. This is due to the regular structure of the array: when light enters the array, it scatters and interferes constructively and deconstructively periodically. This effect is more pronounced with decreased spacing of the nanowires, as this would result in increased density of nanowires, resulting in increased scatter. A way to reduce these periodic reflections is to model randomly spaced/height/radius nanowires.

Figure C.8 shows nanowires spaced further apart (1000 nm) seem to transmit the most light, with the minimum transmission occuring near the peak of the absorption cross section, as seen in Fig 8.1. This indicates that the loss in transmission may be due to absorption. This is also consistent with the Parylene C samples. The band gap of GaAs is 827 nm, and for wavelengths longer than this, minimal light is absorbed as it is of lower energy than the band gap and consequently just transmitted through. There is less transmission in Parylene C, which may be due to a small amount of parisitic absorption from the Parylene C which is causing a decrease in transmission[250].

In conclusion, it is very clear to see that GaAs and InP nanowires exhibit interesting optical properties, with nanowire dimensions, background index and material all having a significant role. There are some unexplained trends which need further investigation - most notably, the effect of nanowire radius and aspect ratio on the absorption and scattering cross section peak wavelength and peak height. The array simulations need to be carried out with InP for a comparison with GaAs. Lumerical is a very powerful software tool - it is possible to carry out electrical simulations using the DEVICE package. It is also possible to import results from the optical simulations into this package. Two further challenges will be modelling the inherent incoherance of sunlight and modelling random height/dimension nanowire arrays.

Appendix D

Extraction of parameters from OPTP spectroscopy data

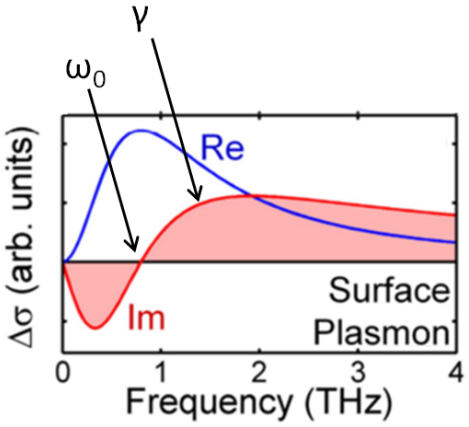

Fig. D.1: Parameter extraction from photoconductivity spectra - The frequency at which $\delta\sigma = 0$ is the resonant frequency ω_0, and the peak of the imaginary photoconductivity component is where $\omega = \gamma$.

OPTP spectroscopy measures the relative photoinduced change in transmission $\Delta T/T$ through the nanowire polariser, which is directly related to the change in photoconductivity $\Delta\sigma$. Such a calculation requires consideration of sample geometry, the absorption depth of the photoexcitation pulse and the propagation of the THz pulse through the sample.

The photoinduced change in transmission is related to the THz electric field $\Delta E/E$ by:

$$\frac{\Delta T}{T} = \frac{\Delta E}{E} = \frac{E_{on} - E_{off}}{E_{off}}, \tag{D.1}$$

where E_{on} and E_{off} refer to the THz electric field transmitted through sample with and without photoexcitation respectively. The photoinduced change in photoconductivity $\Delta\sigma$ is directly proportional to the fractional measured change in transmission

$$\Delta\sigma = \frac{\varepsilon_0 c(1+n_{parylene})}{d_{parylene}} \frac{\Delta T}{T}, \tag{D.2}$$

where ε_0 is the dielectric permittivity of free space, $d_{parylene}$ is the Parylene C thickness, c is the speed of light in a vacuum, $n_{parylene}$ is the frequency dependant complex refractive index of the Parylene C layer.

This is a very useful aspect of OPTP spectroscopy as it is possible to extract parameters relating to charge transport in nanowires from the photoconductivity spectra. Physical parameters such as the momentum scattering rate γ, charge carrier mobility μ photoexcited carrier density N_p may call be obtained by fitting the measured spectra with physical models that describe the relationship between the conductivity and these physical parameters.
The Drude model is a relatively simple, classical model describing the motion of charge carriers under an applied alternating electric field. This gives the frequency dependant conductivity of metals and semiconductors by the following equation:

$$\sigma(\omega) = \frac{Nq^2}{m_e^*} \frac{i}{\omega + i\gamma}, \tag{D.3}$$

where N is the charge carrier density, q is elementary charge, m_e^* is the effective mass of an electron, i is a complex number and ω is the angular frequency. The typical spectral shape of the Drude model is useful in describing the conductivity of bulk samples, but does not reproduce the spectra obtained for nanowire samples. Experimental nanowire spectra features a negative imaginary component which cannot be fitted with the Drude model. Therefore a modification of the Drude model is needed.
The surface plasmon model, proposed by Ninhuys and Sundstrom, is used to describe the THz conductivity spectra of particles that are small compared to the THz wavelength where charge carriers cannot travel beyond the boundaries of the particles[41]. Under the applied THz electric field, electrons and holes are driven in opposite direction, resulting in dipole formation where there is a net excess of positive charge on one side of the particle, and a net excess of positive charge on the other side of particle. The electric field associated with the dipole opposes the electric field and is known as the depolarisation field. This depolarisation field acts as an electrostatic restoring force, which results in the carried undergoing a harmonic oscillation - a surface plasmon response. This approximation can also be used to describe nanowires.

Surface plasmons may be described using a Lorentzian function. The modified Drude response that follows a Lorentzian function is

$$\sigma = \frac{iNq^2\omega}{m_e^*(\omega^2 - \omega_0^2 + i\omega\gamma)}, \tag{D.4}$$

where ω_0 is the resonant frequency. The experimental photoconductivity spectra of nanowires exhibits a Lorentzian lineshape characteristic of a plasmon response, and can therefore be fitted

with the above function. As stated above, it is possible to extract useful physical parameters by fitting the experimentally derived spectra to the Drude-Plasmon function in Equation D.4 above. The frequency at which $\Delta\sigma = 0$ is the resonant frequency ω_0, and the peak of the imaginary photoconductivity component is where $\omega = \gamma$. This is illustrated in Figure D.1.